



**HAL**  
open science

# Spin-photons interface and quantum gates for spins in carbon nanotubes

Benoît Neukelmance

► **To cite this version:**

Benoît Neukelmance. Spin-photons interface and quantum gates for spins in carbon nanotubes. Quantum Physics [quant-ph]. Sorbonne Université, 2024. English. NNT : 2024SORUS186 . tel-04719374

**HAL Id: tel-04719374**

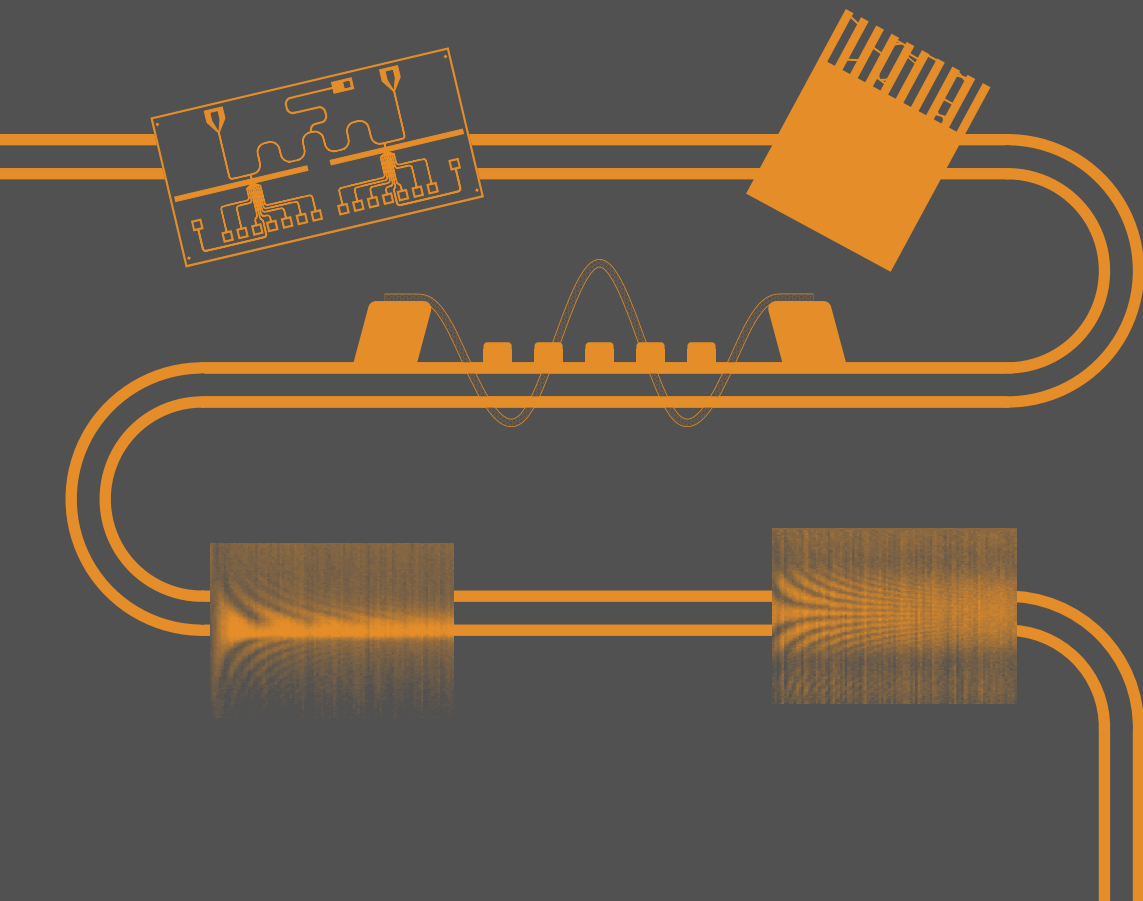
**<https://theses.hal.science/tel-04719374v1>**

Submitted on 3 Oct 2024

**HAL** is a multi-disciplinary open access archive for the deposit and dissemination of scientific research documents, whether they are published or not. The documents may come from teaching and research institutions in France or abroad, or from public or private research centers.

L'archive ouverte pluridisciplinaire **HAL**, est destinée au dépôt et à la diffusion de documents scientifiques de niveau recherche, publiés ou non, émanant des établissements d'enseignement et de recherche français ou étrangers, des laboratoires publics ou privés.

In this thesis, we study the implementation of a ferromagnetic spin qubit. A carbon nanotube is used as a coherent conductor to trap an isolated electron spin in which quantum information is encoded providing long coherence time. This quantum dot circuit is embedded in a circuit quantum electrodynamics (cQED) architecture offering great assets for qubit readout, manipulation and long-range coupling. The spin-photon coupling is enabled through a spin-charge hybridization: the electron being trapped in a double potential well with different spin quantization axis in each of the two dots. This key ingredient is here implemented by non collinear ferromagnetic contact electrodes and their respective magnetic field. Enhancing the spin-photon coupling is however inevitable to outreach the proof of concept. Increasing the resonator impedance with disordered superconductors is one possible solution which has been explored in this work using granular aluminum. Preliminary investigations have also been carried out for a suitable multi-qubit integration deploying a bulk "2.5D" cavity. The main results of this thesis have been obtained with a standard architecture where microsecond lived quantum states have been observed. The manipulation with cavity photons has yielded non-conventional Rabi chevrons hiding a multi-level dynamics. Standard qubit characterization could have nevertheless been done, showing coherence time exceeding those of quantum dot circuits in cQED architectures and the ones of carbon nanotube based devices by one and two orders of magnitude.

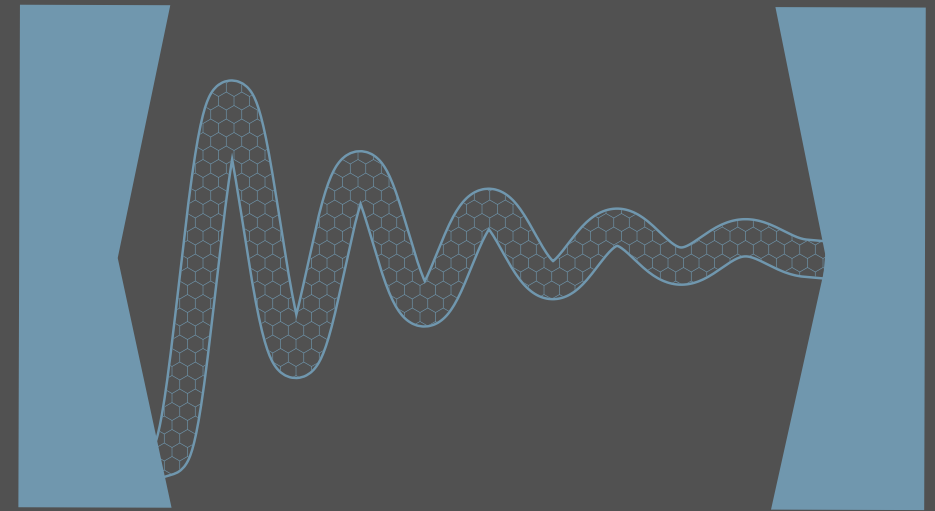


Benoît Neukelmance

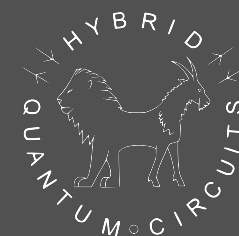
Spin-photon interface and quantum gates for spins in carbon nanotubes

2024

## Spin-photon interface and quantum gates for spins in carbon nanotubes



Benoît Neukelmance



C12

# **SORBONNE UNIVERSITÉ**

**THÈSE de DOCTORAT préparée à l'ÉCOLE NORMALE SUPÉRIEURE**

**Spécialité : Physique**

**École doctorale n° 564 : Physique en Île-de-France**

présentée par

**Benoît NEUKELMANCE**

pour obtenir le titre de

**DOCTEUR de SORBONNE UNIVERSITÉ**

Sujet de la thèse :

**SPIN-PHOTON INTERFACE AND QUANTUM GATES  
FOR SPINS IN CARBON NANOTUBES**

Soutenue le 15 Mars 2024 devant le jury composé de :

<b>M.</b>	<b>Georgios KATSAROS</b>	<b>Rapporteur</b>
<b>M.</b>	<b>Romain MAURAND</b>	<b>Rapporteur</b>
<b>Mme.</b>	<b>Natalia ARES</b>	<b>Examinatrice</b>
<b>M.</b>	<b>Dimitri RODITCHEV</b>	<b>Examineur</b>
<b>M.</b>	<b>Takis KONTOS</b>	<b>Directeur de thèse</b>
<b>M.</b>	<b>Matthieu DELBECQ</b>	<b>Membre invité</b>



*À mes grands-parents*

# Abstract

In this thesis, we study the implementation of a ferromagnetic spin qubit. A carbon nanotube is used as a coherent conductor to trap an isolated electron spin in which quantum information is encoded providing long coherence time. This quantum dot circuit is embedded in a circuit quantum electrodynamics (cQED) architecture offering great assets for qubit readout, manipulation and long-range coupling. The spin-photon coupling is enabled through a spin-charge hybridization: the electron being trapped in a double potential well with different spin quantization axis in each of the two dots. This key ingredient is here implemented by non collinear ferromagnetic contact electrodes and their respective magnetic field. Enhancing the spin-photon coupling is however inevitable to outreach the proof of concept. Increasing the resonator impedance with disordered superconductors is one possible solution which has been explored in this work using granular aluminum. Preliminary investigations have also been carried out for a suitable multi-qubit integration deploying a bulk "2.5D" cavity. The main results of this thesis have been obtained with a standard architecture where microsecond lived quantum states have been observed. The manipulation with cavity photons has yielded non-conventional Rabi chevrons hiding a multi-level dynamics. Standard qubit characterization could have nevertheless been done, showing coherence time exceeding those of quantum dot circuits in cQED architectures and the ones of carbon nanotube based devices by one and two orders of magnitude.

# Résumé

Dans cette thèse, on s'intéresse à l'implémentation d'un qubit de spin dit ferromagnétique. Un nanotube de carbone est utilisé comme conducteur cohérent pour piéger un spin électronique dans lequel est encodé l'information quantique assurant des longs temps de cohérence. Ce circuit à base de boîtes quantiques est intégré à une architecture d'électrodynamique quantique sur puce procurant de grands atouts pour la lecture, la manipulation et un couplage à distance. Le couplage spin-photon existe grâce à une hybridation spin-charge : l'électron étant piégé dans un double puit de potentiel avec différents axes de quantification du spin pour chacune des boîtes quantiques. Cet ingrédient clef est ici implémenté avec des électrodes de contacts ferromagnétiques non colinéaires et leur champ magnétique respectif. Augmenter le couplage spin-photon est toutefois nécessaire pour dépasser la preuve de concept. Pour cela il est possible d'accroître l'impédance du résonateur avec des supraconducteurs désordonnés, ce qui a été exploré dans ce travail avec de l'aluminium granulaire. Des travaux d'investigations ont également été menés pour une intégration multi-qubits avec une cavité usinée dite "2.5D". Les résultats principaux de cette thèse ont été obtenus dans une architecture standard où des états quantiques cohérents jusqu'à la microseconde ont été observés. La manipulation avec des photons de la cavité a conduit à des chevrons de Rabi non conventionnels cachant une dynamique multi-niveaux. La caractérisation standard des qubits a toutefois pu être réalisée et a montré des temps de cohérence dépassant ceux des circuits de boîtes quantiques en cavité d'un ordre de grandeur et ceux des dispositifs à base de nanotubes de carbone de deux ordres de grandeur.

# Acknowledgements

On imagine souvent une thèse comme une longue quête solitaire. C'est en effet un travail de longue haleine avec des embuches : "that's life in the big city", mais il a toujours été possible d'avancer grâce aux discussions, aux collaborations et à l'aide que j'ai pu avoir au cours de ma thèse. Je tiens donc à remercier toutes ces personnes, grâce à qui je peux aujourd'hui mettre un point final à ce manuscrit.

First of all, I would like to thank the jury members : Romain Maurand, Georgios Katsaros, Natalia Ares and Dimitri Roditechev for having taken the time reviewing my thesis manuscript with constructive remarks and for their interest during the defense.

Je remercie ensuite bien évidemment mon directeur de thèse, Takis Kontos, qui a su insuffler son optimisme tout au long de ma thèse, même dans les situations les plus frustrantes. Il faut en effet savoir se "shaoliniser" pour s'attaquer aux nanotubes de carbone. Cela a été un réel plaisir de travailler durant ces quatre années au sein de l'équipe HQC que Takis anime avec sa mythique "funkiness", son art de raconter les histoires et ses imitations (très niches). J'ai également énormément appris à ses côtés, de sa riche expérience allant de la plomberie des cryostats à la théorie derrière les systèmes quantiques hybrides : en grand écart facial comme Jean-Claude Van Damme. Je tiens également à remercier Matthieu Delbecq qui, avec Takis, ont encadré cette thèse de façons très complémentaires. Leur grande disponibilité a été extrêmement agréable et les nombreuses discussions m'ont permis de ne jamais être à court d'idées. L'enthousiasme et l'énergie que Matthieu apporte au labo, j'ai aussi pu en profiter en courant le midi avec lui (sauf pendant son fameux tour rapide). Je remercie également Audrey Cottet pour son apport à la compréhension théorique de ces systèmes quantiques hybrides.

En arrivant en stage, j'ai été encadré puis formé jusqu'à la fin de ma première année par William Legrand. J'ai donc énormément appris grâce à lui sur tous les différents aspects expérimentaux que comportent la manip et de sa façon de travailler au sein d'un laboratoire de recherche : avec une grande patience. En milieu de deuxième année, j'ai à mon tour pu transmettre ces connaissances à Benjamin Hue qui a rejoint l'équipe HQC et le fameux projet de la cavité 2.5D. Après s'être approprié le sujet à une vitesse impressionnante, il a su faire profiter l'équipe et les différents stagiaires de sa pédagogie et de ses vastes connaissances scientifiques. Cela a été plus que motivant de travailler en binôme avec lui et sa constante bonne humeur jusqu'à la fin de ma thèse. Les résultats expérimentaux présentés dans ce

manuscrit sont donc aussi les siens ! Je n'oublierai pas le finish en apothéose aux Houches avec panorama sur le Mont Blanc depuis le jacuzzi. Je remercie également les autres membres de l'équipe HQC : Lucas Jarjat qui a toujours apporté son aide précieuse ; Arnaud Théry accompagnant le labo au piano comme à la voix ; Jules Craquelin qui repousse les limites des nanotubes de carbone et Chloé Fruy continuant la quête de la matière noire. Merci pour la si bonne ambiance au labo rythmée par les discussions autour de la machine à café (fabuleuse machine et meilleur café de Paris soit dit en passant), les évaps en salle blanche, les goûters rue Mouffetard et les courses à pied au jardin du Luxembourg.

Je remercie Matthieu et Pierre Desjardins pour la confiance qu'ils m'ont accordée en me prenant en thèse au tout début de l'aventure C12 Quantum Electronics. I also thank all the C12 people and especially the ones I have worked or interacted with during my PhD: Quentin Schaeverbeke, Arthur Larrouy, Joey Sulpizio, Gubi Abulizi, Sergio De Bonis, Maria El Abbassi, Louis Virey, Davide Stefani, Jeanne Becdelièvre, Sandrine Lopes, Juliette Ginies, Romaric Le Goff, Frederik Van Veen, Alice Castan, Louis Godet, Nicolas Hauseux, Farah Ourak, Matthieu Lebard, Aziz Rifi, Lorenzo Vistoli and Elisa Passalacqua. I am very excited to continue this scientific journey at C12 !

Au début de ma thèse, nous partagions le sous-marin (surnom du labo) avec l'équipe Quantic. Je remercie Marius Villiers qui venait volontiers apporter ses fines connaissances en circuits RF, Alvisse Borgognoni, Ulysse Réglade, Camille Berdou, Matthieu Praquin (le maître du pinball), Vincent Lienhard, Erwan Roverch, Clark Smith, Aron Vanselow, Adrien Bocquet, Briec Beauseigneur, Zaki Leghtas et Philippe Campagne-Ibarcq. Je remercie également les différentes équipes du LPENS et notamment celle de la salle blanche (pour y avoir passé une bonne partie de ma thèse) : Michael Rosticher, José Palomo et Aurélie Pierret mais aussi le bureau d'étude avec l'aide de Pascal Morfin dans la conception de la cavité 2.5D, la cryogénie avec Florent Perrin et Olivier Andrieu qui nous ont permis de garder la manip à froid tout au long des mois de mesure, les électroniciens avec Anne Denis et Philippe Pace, l'atelier mécanique avec Matthieu Sardin et l'équipe administrative avec Delphine Rolland et Olga Hodges. Je suis aussi reconnaissant envers Chéryl Feuillet-Palma et Gabriel Hétet pour leur disponibilité et le suivi des avancées de ce projet de thèse.

Pour finir, je tiens également à exprimer ma gratitude pour le soutien que j'ai eu en dehors du laboratoire. Merci à Thomas, Killian, Valentine, Clémentine, Flavien, Lucie, Marguerite et Frédéric pour tous les bons moments de déconnexion avec vous ces quatre dernières années. Je remercie la famille de Coline qui a suivi tout mon parcours de thésard. Merci à mon parrain, à ma marraine et à mon papi d'avoir été à mes côtés le jour de la soutenance. Merci

à mon frère Clément et à ma sœur Agathe à qui je souhaite de pouvoir vivre une aventure scientifique aussi passionnante que l'a été ma thèse. Je remercie mes parents, Olivier et Fabienne, qui m'ont pleinement soutenu tout au long de mes études et sans qui je ne serais pas arrivé là. Enfin, je remercie Coline qui partage ma vie et m'a aidé, à travers son soutien quotidien, à trouver un équilibre durant ces années riches et intenses.

# Contents

<b>Abstract</b>	<b>ii</b>
<b>Acknowledgements</b>	<b>iv</b>
<b>Acronyms</b>	<b>1</b>
<b>Introduction</b>	<b>3</b>
<b>1 Shaping the spectrum of hybrid quantum systems</b>	<b>11</b>
1.1 Carbon nanotubes for quantum dots circuits . . . . .	12
1.1.1 A promising material for quantum systems . . . . .	12
1.1.2 Trapping electrons in carbon nanotubes . . . . .	15
1.2 Double quantum dot as a charge qubit . . . . .	17
1.2.1 Electrical model . . . . .	17
1.2.2 Stability diagram . . . . .	19
1.2.3 Charge qubit . . . . .	21
1.3 Spin qubits . . . . .	24
1.3.1 Various types of implementation . . . . .	24
1.3.2 The ferromagnetic spin qubit . . . . .	31
1.3.3 Various architectures enabling spin-photon coupling . . . . .	35
<b>2 Addressing individual hybrid quantum systems with mesoscopic QED</b>	<b>39</b>
2.1 Coupling quantum dot circuits to a microwave cavity . . . . .	41
2.1.1 From cavity QED to mesoscopic QED . . . . .	41
2.1.2 Microscopic description . . . . .	42
2.2 Hybrid light-matter system . . . . .	45
2.2.1 Different coupling regimes . . . . .	46
2.2.2 Two qubits coupled to a cavity . . . . .	48

2.2.3	Qubit manipulation . . . . .	50
2.3	Measuring with a microwave cavity . . . . .	50
2.3.1	Input-output theory . . . . .	51
2.3.2	Qubit readout . . . . .	54
2.3.3	Two-tone spectroscopy . . . . .	57
<b>3</b>	<b>Experimental methods</b>	<b>61</b>
3.1	Nanofabrication . . . . .	62
3.1.1	Sample fabrication overview . . . . .	62
3.1.2	Gold precontacts and alignment crosses . . . . .	65
3.1.3	Niobium mesoscopic QED architecture . . . . .	66
3.1.4	Gates and contacts electrodes . . . . .	67
3.1.5	Trenches . . . . .	68
3.2	Carbon nanotubes fabrication and integration . . . . .	69
3.2.1	Carbon nanotube growth and selection . . . . .	69
3.2.2	Stapling carbon nanotubes . . . . .	71
3.3	Measurement techniques . . . . .	77
3.3.1	Isolating the device from the outside world . . . . .	78
3.3.2	DC measurements . . . . .	79
3.3.3	RF measurements . . . . .	82
<b>4</b>	<b>Towards new mesoscopic QED architectures</b>	<b>91</b>
4.1	Increasing the spin-photon coupling with high impedance resonators . . . . .	92
4.1.1	Coplanar waveguide resonators . . . . .	93
4.1.2	High impedance resonators . . . . .	95
4.1.3	Preliminary developments using granular aluminum . . . . .	97
4.2	Multiplexing with a "2.5D cavity" . . . . .	103
4.2.1	Motivations . . . . .	103
4.2.2	Designing a "2.5D cavity" . . . . .	103
4.2.3	Experimental realization . . . . .	106
<b>5</b>	<b>Observation of microsecond lived quantum states in carbon-based circuits</b>	<b>113</b>
5.1	Shaping and highlighting the ferromagnetic spin qubit . . . . .	114
5.1.1	Working principle . . . . .	114
5.1.2	Device fabrication . . . . .	115
5.1.3	Tuning the double quantum dot . . . . .	117
5.1.4	Two-tone spectroscopy . . . . .	117

---

5.2	Quantum manipulation of the system . . . . .	119
5.2.1	Rabi manipulation . . . . .	119
5.2.2	Qubit characterization . . . . .	121
5.2.3	Decoherence budget . . . . .	123
5.3	Multi-level quantum dynamics . . . . .	124
5.3.1	Four-level spectrum . . . . .	124
5.3.2	Eight-level spectrum . . . . .	127
	<b>Conclusion</b>	<b>129</b>
<b>A</b>	<b>Charging energies extraction for detuning axis energy conversion</b>	<b>131</b>
A.1	Charging energies . . . . .	131
A.2	Detuning energy axis . . . . .	133
<b>B</b>	<b>Detailed fabrication recipes</b>	<b>135</b>
B.1	Ferromagnetic spin qubit chip nanofabrication . . . . .	135
B.2	CNT fabrication . . . . .	148
	<b>Bibliography</b>	<b>151</b>



# Acronyms

AFM	Atomic force microscope
AWG	Arbitrary waveform generator
CNT	Carbon nanotube
CPW	Coplanar waveguide
cQED	Circuit quantum electrodynamics
CVD	Chemical vapor deposition
DC	Direct current
DQD	Double quantum dot
EDSR	Electric-dipole spin resonance
ESR	Electron spin resonance
IF	Intermediate frequency
IPA	Isopropanol
LO	Local oscillator
MFM	Magnetic force microscope
MIBK	Methyl-iso-butyl ketone
MWNT	Multi-wall carbon nanotube
PCB	Printed circuit board
PMMA	Poly methyl methacrylate
QD	Quantum dot
QND	Quantum nondemolition
RF	Radio frequency
RIE	Reactive ion etching
SEM	Scanning electron microscope
SQD	Single quantum dot
SWNT	Single-wall carbon nanotube
TMR	Tunneling magneto-resistance
UHV	Ultra high vacuum
VNA	Vector network Analyser
2DEG	Two-dimensional electron gas



# Introduction

What kind of computer are we going to use to simulate physics ? It is around this issue, in 1981, that scientists have gathered for the Physics of Computation conference. In this context, Richard Feynman explains that: “Nature isn’t classical, dammit, and if you want to make a simulation of nature, you’d better make it quantum mechanical, and by golly it’s a wonderful problem, because it doesn’t look so easy”. This opens thus the field of quantum computation [1]. The building block of a classical computer (a bit) used to store the information and perform operations is now replaced by its quantum version: a quantum bit (qubit) encoded for example in a two-level system.

Building a quantum computer is indeed not an easy task since by nature it embodies a paradox. On the one hand, there is a need for long coherence time for the qubits to remain “quantum” all along the computation, implying thus isolation from the environment. On the other hand, the qubit state must be able to be changed very rapidly for fast operations which is possible via a very strong coupling to the outside world. Quantum computing has first been let in the scope of science fiction until the end of the nineties with two game changer contributions provided by Peter Shor. First, he proposed a polynomial-time quantum algorithm for integer factorization [2] making the RSA crypto-system vulnerable which has logically aroused interest outside of the scientific community. Furthermore, quantum computing then spans a much larger scope than just simulating physics as it opens the path for solving certain hard problems exponentially faster than classical computing. Second, he introduced the concept of quantum error correction [3], which in the case of quantum computer with a physical error rate below a certain threshold, can suppress the logical error rate to arbitrarily low levels. This helped the field to mature from hobby side projects to structured academic research ones with the realization of a fault-tolerant quantum computer in their sights.

Information is physical. Whereas classical bits are encoded in silicon-based transistors, none of the various physical platforms used for hosting qubits have won unanimous support yet. Trapped ions, cold atoms, photonic circuits, semiconductor quantum dots and superconduct-

ing circuits are part of the possible implementations with somehow the last being for now a step head. Their integration in a circuit quantum electrodynamics (cQED) architecture [4] notably offers scale-up perspectives which has convinced big tech companies like Google and IBM. They have recently demonstrated some hints of quantum advantage with a 53-qubit processor over a classical supercomputer [5] and shown the potential of noisy intermediate-scale quantum (NISQ) computer with a 127-qubit processor [6]. Despite the substantial advances over the last twenty years, today's challenge remains in increasing coherence time. For this purpose, the community agrees on the need of better qubits. This is within this framework that my thesis work falls. It is question of benefiting from the cQED architecture with a highly coherent qubit encoded in an isolated spin hosted in a carbon nanotube [7].

## Quantum bit

In a classical computer, the information is stored and processed in bits that can either take the value 0 or 1. In a quantum computer, this bit turns in a qubit which can be in the state  $|0\rangle$  or  $|1\rangle$  but also in any superposition  $|\psi\rangle = \alpha|0\rangle + \beta|1\rangle$  such that  $|\alpha|^2 + |\beta|^2 = 1$ , with  $\alpha$  and  $\beta$  complex numbers. The associated density matrix  $\rho = |\psi\rangle\langle\psi|$  can be decomposed over the Pauli matrices  $\hat{\sigma}_x$ ,  $\hat{\sigma}_y$  and  $\hat{\sigma}_z$  resulting in a vector pointing towards the surface of the so-called Bloch sphere. For simplicity, we will consider the quantum state instead of its density matrix. In this representation, the  $|0\rangle$  and  $|1\rangle$  states figure at the north and south pole and  $|\psi\rangle$  which is represented in figure 1 can be re-expressed as:

$$|\psi\rangle = \cos\left(\frac{\theta}{2}\right)|0\rangle + e^{i\varphi}\cos\left(\frac{\theta}{2}\right)|1\rangle \quad (1)$$

This form highlights the two types of information incorporated in a qubit: the bit one characterized by the angle  $\theta$  and the phase one characterized by the angle  $\varphi$ . As a result, two different types of error can occur when manipulating quantum information: bit flips which also occur in a classical computer and phase flips which are purely quantum. The first one comes out of energy exchange with the environment and is characterized experimentally by measuring the associated relaxation time  $T_1$ . The second type of error results from fluctuations of the energy separating the  $|0\rangle$  or  $|1\rangle$  states described by the pure dephasing time  $T_\varphi$ . This last is not directly measured but deduced from the coherence time  $T_2^*$  that encompasses both mechanisms.

Performing quantum operations requires to bring the vector anywhere on the Bloch sphere surface. Such a manipulation is made possible by physically interacting with the qubit. The Bloch vector then rotates at a frequency  $\Omega_R$  called the Rabi frequency setting the speed of

the one qubit gate which has to be maximized. There is nevertheless a trade-off with the coherence time which is shortened for a qubit strongly coupled to the environment. This is why it is more relevant to focus on the gate fidelity: a dimensionless quantity encompassing both features.

After the manipulation, the information has to be readout. By the probabilistic nature of quantum mechanics, the outcome will be 0 or 1 with a probability  $|\alpha|^2$  or  $|\beta|^2$ . The measurement projects the qubit state on the z axis making then the final state perfectly discernible but also different from the initial one. Such a scenario refers to strong measurement: the measurement apparatus being strongly coupled to the qubit. It differs from weak measurement, where the measurement apparatus gets very little information about the qubit state without nearly affecting it. As a counterpart, this requires a lot of averaging to finally discriminate the two states. The readout also distinguishes if whether or not it destroys the quantum property of the qubit. If the observable being measured commutes with the Hamiltonian describing the qubit it is question of quantum nondemolition (QND) measurement.

Finally, measuring a single qubit does not provide more information than with a classical one. The quantum advantage starts to be visible by considering  $N \geq 2$  qubits. Quantum superposition and entanglement are used to perform massively parallel operations in a single step that would require  $2^N$  on a classical computer. Despite the readout only enables to access one over the  $2^N$  terms defining the complex quantum state, special quantum algorithms allow for taking advantage of the exponential depth of the associated Hilbert space. In order to run such an algorithm, the quantum computer implementation should satisfy certain conditions. David DiVincenzo formulated this in five criteria [8]:

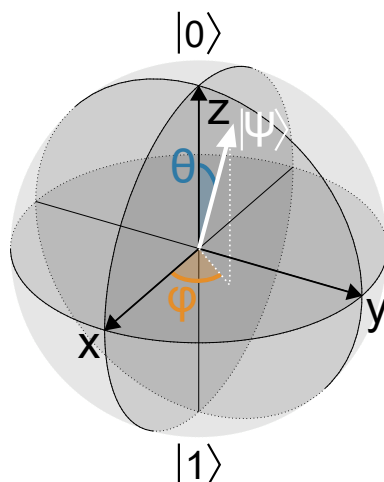


Figure 1: **Qubit representation with the Bloch sphere**

- A scalable physical system with well characterized qubits
- The ability to initialize the state of the qubits to a simple fiducial state, such as  $|000\dots\rangle$
- Long relevant decoherence times, much longer than the gate operation time
- A “universal” set of quantum gates
- A qubit-specific measurement capability

We further introduce the different concepts used for their fulfillment.

## Semiconductor spin qubits

Quantum mechanics describes the microscopic world. But how small do we really need to be to see emerging the effects of quantum mechanics ? Nanofabrication advances have enabled to fabricate smaller and smaller devices which has notably highlighted the quantization of the electrical conductance [9, 10]. This opens up the path towards mesoscopic physics with systems of intermediate scale. Such electronic circuits enable to tune quantum properties with macroscopic buttons. As an example, one can trap electrons thanks to nanometer-sized electrodes with tunable DC potentials to form a quantum dot [11]. This results in a discrete energy spectrum for the electrons such as the ones orbiting an atomic nucleus. Such a realization is then also designated as an artificial atom.

In 1998, Daniel Loss and David DiVincenzo propose to use the spin states of coupled single-electron quantum dots for implementing quantum computation [12]. The electron spin is indeed a natural way to encode quantum information being up or down. It also has the good taste of being weakly coupled to the environment offering long coherence time. Such a qubit is somehow sensitive to magnetic field fluctuations which arise from the surrounding nuclear spin bath. This last is more or less perturbative depending on the host material. This huge isolation from the outside world makes as a counterpart the qubit hard to address. To counter this, spin-orbit coupling have been introduced to enable fast electrical driving via electric-dipole spin resonance (EDSR) [13, 14]. As a result, fidelities above 99.9% have been measured for the one qubit gate [15, 16]. Finally, recent implementations of four [17] (see figure 2.a) and six [18] qubit processor have confirmed the potential of semiconductor spin qubits towards the realization of a large scale quantum computer.

In this thesis work, we opt for carbon nanotubes as material host which offer great perspectives. They can indeed be suspended reducing impact of stray charges and can be grown with

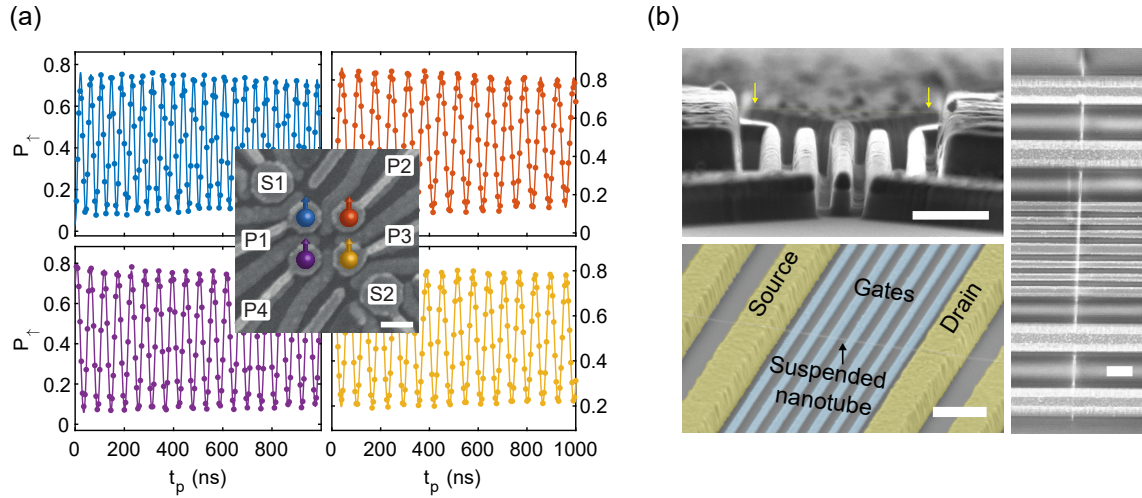


Figure 2: **Quantum dot devices:** (a) Four Ge hole spin qubits device with associated coherent Rabi oscillations. Single qubit gate fidelities all exceed 99%. [17] (b) Scanning electron microscope images of various ultraclean quantum dot devices integrating a suspended carbon nanotube. The scale bars are 400 nm. [19, 20]

isotopically purified  $^{12}\text{C}$ , offering a nuclear spin free environment for electronic spin qubits. Their integration to nanoscale circuits is somehow challenging but constantly improving to reach an ultraclean environment (see figure 2.b).

## Circuit quantum electrodynamics and beyond

Few years after the first demonstration of quantum manipulation [21] and coherence [22] in superconducting circuits, have been introduced circuit quantum electrodynamics (cQED) [4] which enables the coupling with microwave photons of a cavity. Inspired from cavity quantum electrodynamics [23] which studies the light-matter interaction at the most elementary level, this architecture is now the leading platform for superconducting qubits. Circuit QED is indeed appealing for quantum computing perspectives as it notably provide a fast readout and the possibility to couple distant qubits [24, 25]. This architecture is then scalable as confirmed by the growing number of superconducting qubits integrated on a single chip [5, 6] which has recently enabled the implementation of quantum error correction [26, 27].

Circuit QED turned out to be crucial for the superconducting qubits community but its impact is much bigger with the opening of new research directions. The superconducting circuit can indeed be replaced by other systems such as nanomechanical oscillator, ferromagnetic crystal or semiconducting quantum dots. This last is particularly appealing providing both new probes for condensed matter phenomena and attractive architecture for semiconductor

spin qubits. Mesoscopic quantum electrodynamics has in the first instance enabled to couple the quantum dot circuits to microwave photons via the charge degree of freedom [28, 29]. A single spin is indeed far too weakly coupled to the cavity magnetic field to hope benefiting from the cQED architecture. Tricks have somehow been found to finally reach the strong spin-photon coupling [30–32]. Finally, the coupling between distant spins [33, 34] and very recently the demonstration of a two qubit iSWAP gate [35] place circuit-QED as a possible platform for scaling up semiconductor spin qubits.

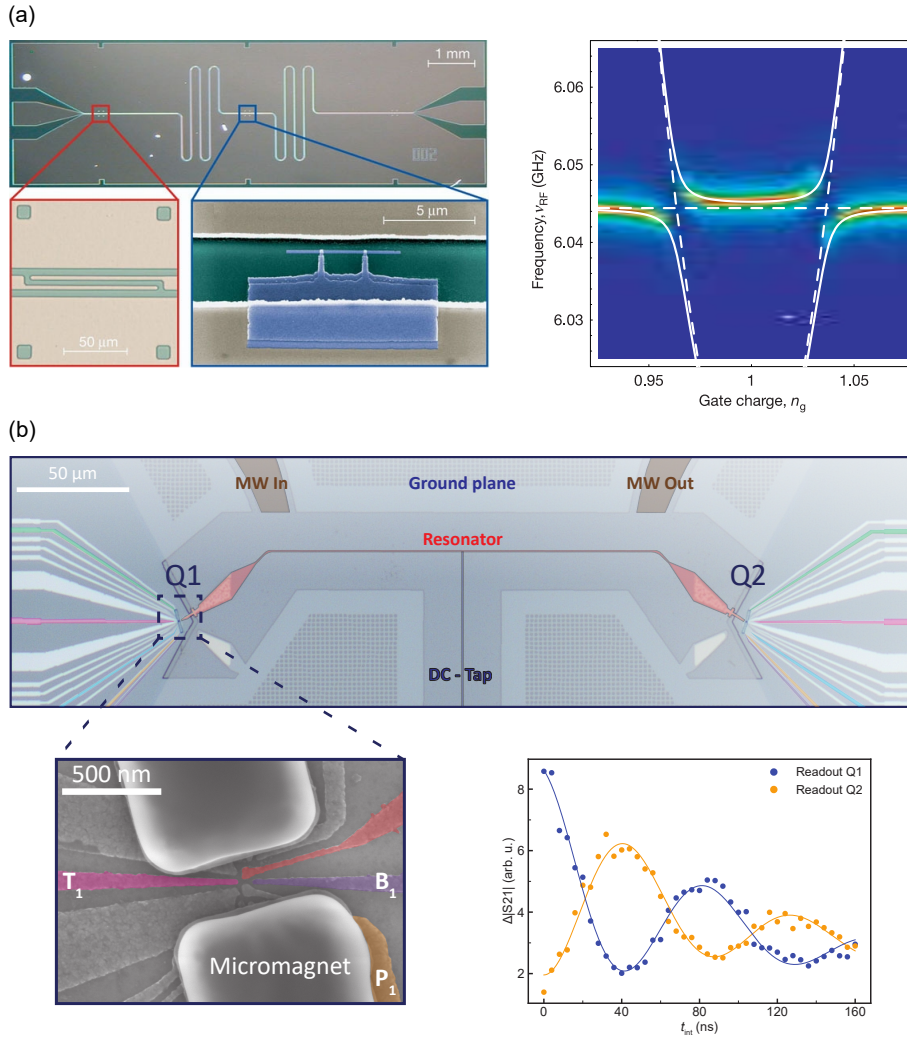


Figure 3: **From cQED to mesoscopic QED:** (a) False colour electron micrograph of a Cooper pair box coupled to a superconducting niobium coplanar waveguide resonator (left). The use of cQED enabled to reach strong coupling regime (left). The resonator transmission as a function of the probe frequency and the gate charge reveals avoiding crossing between the two systems energy states. [4] (b) Mesoscopic QED device embedding two spin qubits (Q1 and Q2) with a dedicated micromagnet (left) that are coupled to the same high impedance resonator. Such a device enables to reach the strong spin-photon coupling and have high-lighted iSWAP oscillations between two distant spin qubits (right). [35]

## Thesis outline

This thesis is organized as follows: the first chapter presents quantum dot circuits considering carbon nanotubes as material host. The various spin qubit implementations are then exposed with a focus on the architecture studied in this work: the ferromagnetic spin qubit. It ends up by exploring the possible solutions enabling spin-photon coupling. The second chapter first explains the physical phenomena involved for coupling a quantum dot circuit to a microwave cavity. It then exposes the consequences of such a coupling on the whole system and explains how to take advantage of this for quantum computing perspectives. Lastly, the second chapter focuses on how to probe the resulting mesoscopic QED system. Chapter three describes the various experimental techniques used in this work including in particular the nanofabrication of the devices and the measurement setup used for low temperature measurements. Chapter four shows that our current mesoscopic QED device limits both the spin-photon coupling strength and the inter-qubit connectivity. Two ways of improving the architecture are explored to tackle individually those issues with preliminary results. Finally, chapter five highlights the first observation of microsecond lived quantum states in carbon-based circuits.



## Chapter 1

# Shaping the spectrum of hybrid quantum systems

Nanofabrication progress has enabled miniaturization of solid state devices opening the field of mesoscopic physics. Between the micrometer and the nanometer scale, systems start to behave quantum mechanically at low temperatures [9,10]. In such devices, it has been possible to confine electrons in all space dimensions to realize what is called a quantum dot. Unlike atoms which have an essentially immutable discrete energy spectrum, the one of quantum dots can be shaped which makes them attractive for quantum computing perspectives [36].

The aim of this chapter is to introduce the different concepts required to shape the ideal spectrum of the ferromagnetic spin qubit [7]. The first part presents the physics of carbon nanotubes and explains the motivations of using them as a qubit host material. The key element enabling quantum information encoding, namely quantum dots are also introduced in this part. The next one focuses on a more complex quantum dot circuit: double quantum dots which are at the heart of the ferromagnetic spin qubit as it can implement a charge qubit. Finally the last part reviews the interest of spin qubits with their main different architectures which includes the ferromagnetic spin qubit.

## 1.1 Carbon nanotubes for quantum dots circuits

### 1.1.1 A promising material for quantum systems

A carbon nanotube (CNT) can be seen as a graphene sheet wrapped around itself forming a cylinder. More complex CNT can be composed of several graphene sheets forming concentric cylinders these are called multi-wall nanotube (MWNT) as opposed to single-wall nanotube (SWNT). Its diameter is typically 1-5 nm and its length can vary from several nm to hundreds of  $\mu\text{m}$ . CNT can thus be considered as a one-dimensional nanoconductor. The hexagonal lattice of carbon atoms can be wrapped in different ways leading to various structures. The main consequence of this is that depending on its structure the CNT can be either metallic or semiconducting.

The different structures are defined by the vector going around the circumference of the CNT: the chiral vector  $\vec{C}$  (figure 1.1). The electronic bandstructure of a carbon nanotube can be deduced from the one of graphene with the assumption that the cylindrical shape of the CNT does not affect it except for adding a BVK boundary condition:  $\vec{k} \cdot \vec{C} = 2p\pi$ , with p an integer. This is the zone folding approximation. This implies the quantization of the transverse wave vector:  $k_{\perp} \cdot D = 2p$ , with p an integer and D the diameter of the CNT ( $D = \|\vec{C}\|/\pi$ ). As a consequence, the first Brillouin of the CNT is an ensemble of parallel lines in the first Brillouin zone of graphene. The CNT bandstructure is therefore determined by the intersection between the Dirac cones and the plan corresponding to the quantified

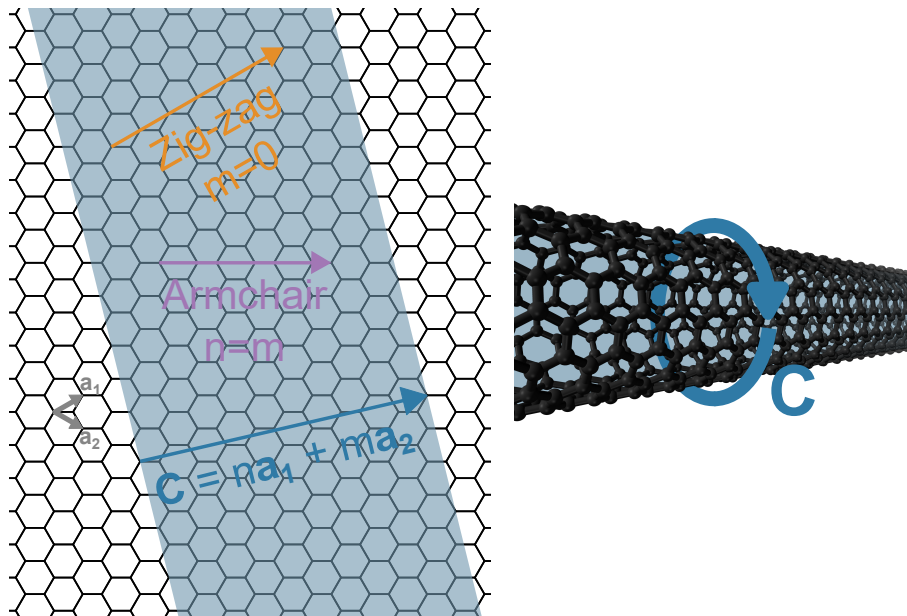


Figure 1.1: **From graphene to carbon nanotube:** Carbon nanotubes can be seen as an enrolled graphene sheet which leads to many possibilities. Those different configurations are depicted by a vector going around the cylinder perimeter : the chiral vector  $\vec{C} = n\vec{a}_1 + m\vec{a}_2$  (with  $n$  a positive integer and  $m$  an integer such that:  $-n/2 < m \leq n$ ). One can distinguish three different types of configuration : zig-zag ( $m=0$ ), armchair ( $n=m$ ) and chiral presenting no symmetry.

value of  $k_{\perp}$  (figure 1.2.b). If the lines cross the Dirac point  $K/K'$  then the CNT is metallic. Otherwise it opens up a gap  $E_G = \hbar v_F/3D$  where  $v_F$  is the Fermi velocity: the CNT is then semiconducting. One can show that a CNT is metallic if  $m-n=3k$ , with  $k$  an integer. The zone folding approximation does not take into account the curvature of the CNT. This results in a displacement  $\Delta k^{cv} \ll \Delta k_{\perp}$  of the Dirac points in the reciprocal space. It introduces therefore a small bandgap to CNT initially predicted metallic<sup>1</sup>: those CNT are called narrow gap. As for graphene, the electronic bandstructure entails two valleys  $K$  and  $K'$ . This degree of freedom can be seen as the clockwise and counter-clockwise motion of the electrons around the CNT. This degeneracy completing the one of spin can be lifted with a magnetic field applied along the nanotube. Those degeneracies can nevertheless be lifted at zero magnetic field in some cases. Spin-orbit coupling arises from the curvature of the nanotube with two contributions. The Zeeman-like contribution shifts the Dirac cones vertically (in opposite direction for each spin) and the orbital-like shifts them horizontally. The magnitude of the splitting ranges from  $\Delta_{SO} = 0.37$  meV [38] to  $\Delta_{SO} = 3.4$  meV [39]. The origin of intervalley scattering is not well understood but one suspects very local electrical disorder. A mixing term can be introduced empirically and ranges from  $\Delta_{KK'} = 25$   $\mu$ eV [40] to  $\Delta_{KK'} = 700$   $\mu$ eV [41]. Those degrees of

<sup>1</sup>except for armchair where the Dirac points are shifted along the parallel lines

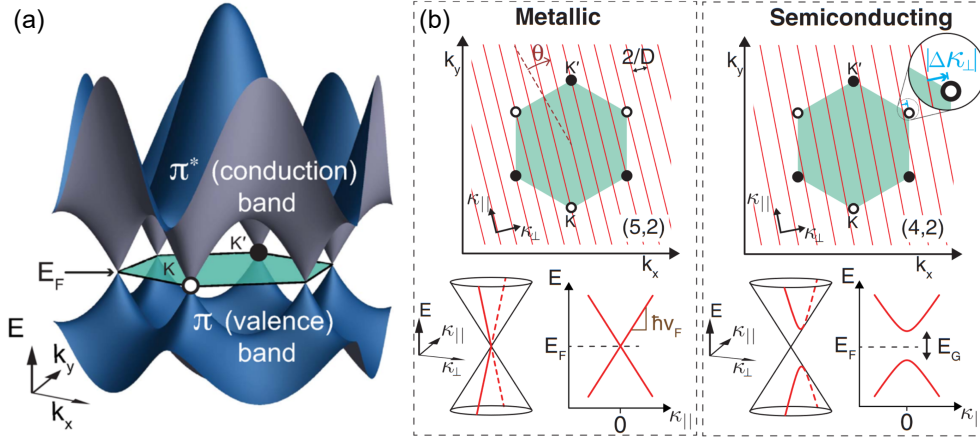


Figure 1.2: **From graphene bandstructure to CNT bandstructure:** (a) Graphene bandstructure contains 6 Dirac cones close to the Fermi energy. The first Brillouin zone shows 6 symmetry points  $K/K'$ . (b) CNT bandstructure can be deduced from the graphene one with the zone folding approximation. The boundary condition leads to a first Brillouin zone composed of parallel lines. If those lines cross the Dirac points (left case), the nanotube is metallic. If not (right case), the nanotube is semiconducting. Source: [37]

freedom can be used to encode quantum information [42]. Moreover CNT are composed of 99% of  $^{12}\text{C}$  atoms in which the nuclear spin is zero and  $\sim 1\%$  of  $^{13}\text{C}$  atoms which possesses a nuclear spin. Alike silicon, CNT can be isotopically purified to tend towards a nuclear spin free material. As the hyperfine interaction could be suppressed in such a CNT, it is predicted to be the best material host in terms of coherence properties with an associated spin qubit coherence time:  $T_2^* \sim 350 \mu\text{s}$  [43]. Carbon nanotubes are thus really appealing for quantum technologies perspectives.

With their high Fermi velocity  $v_F \sim 8.10^5 \text{m.s}^{-1}$ , electrons move ballistically in carbon nanotubes. As in graphene, the electron contributing to transport occupies a  $p_z$  orbital which is perpendicular to the graphene sheet. It is therefore possible to connect a CNT to metal electrodes and envision transport experiments. Carbon nanotubes have been observed for the first time in 1991 [44]. Since then it has been possible to select and measure SWNT [45, 46], to build a CNT-based transistor [47, 48], to develop spintronics devices [49, 50], or to suspend the carbon nanotube like a guitar string [51] to study for example its mechanical mode [52]. As nanotubes are one dimensional nanoconductor, by applying a DC voltage one can trap electrons such that they are confined in the three dimensions of space resulting in a quantized energy spectrum. This realization is called a quantum dot (QD) and can be seen as an artificial atom.

### 1.1.2 Trapping electrons in carbon nanotubes

As opposed to real atoms with properties determined by nature, quantum dots can be tuned with design and DC voltages. This is the whole idea of quantum systems: tuning quantum properties with macroscopic buttons. In a quantum dot circuit, the trapped electrons can be exchanged with the reservoirs commonly named source and drain at a rate  $\Gamma_{S/D}$  (figure 1.3.a). Trapping electrons is commonly done using semiconductor heterostructure such as GaAs/AlGaAs or Si/SiGe. Electrons are thus confined in a plane forming a two-dimensional electron gas (2DEG) and can be trapped with gate electrodes [53,54] that can reach sub 100 nm width thanks to nanofabrication progress. The quantum dot energy spectrum is determined by two phenomena setting the energy required to add the  $N^{\text{th}}$  electron in the QD. The first one is due to both Coulomb repulsion and electrostatic environment responsible of the charging energy  $E_c = e^2/C_\Sigma$  [11]. The second one is due to the confinement in all directions: the orbital energies  $\epsilon_i$  are quantized and determined by  $\Delta E_{\text{conf}} = \hbar v_F/2L \sim 17$  meV [46], with  $v_F \sim 8.10^5 \text{m.s}^{-1}$  the Fermi velocity for CNT and  $L \sim 100$  nm the size of the dot. These two contributions give the quantum dot filled with  $N$  electrons the following energy :

$$E(N) = \frac{-(N - N_0)|e| + C_g V_g)^2}{2C_\Sigma} + \sum_{i=1}^N \epsilon_i \quad (1.1)$$

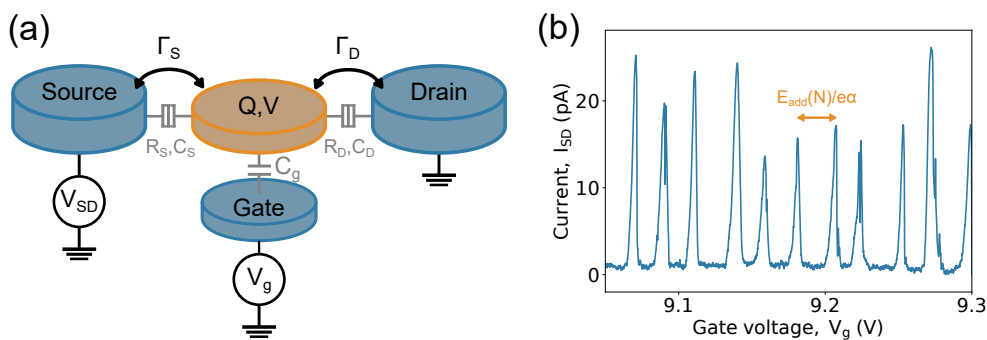


Figure 1.3: **Trapping electrons in a single quantum dot:** (a) Schematic of a single quantum dot (orange) and its electrostatic environment (blue). The quantum dot is connected to source and drain by tunnel junctions (represented here by a resistor  $R_{S/D}$  and a capacitor  $C_{S/D}$  in parallel) and a to a gate by a capacitor  $C_g$ . Applying a bias voltage  $V_{SD}$  on the source moves its chemical potential with respect to the Fermi energy and opens thus a bias window. Whenever an energy state of the quantum dot finds in this bias window, electrons can flow from source to drain. This is set by the gate potential  $V_g$ . (b) Measurement of the current  $I_{SD}$  in a carbon nanotube as a function of the gate voltage  $V_g$  at  $V_{SD} = 3.5$  mV and  $T = 300$  mK. For given values of  $V_g$  corresponding to a state in the bias window, electrons flow from source to drain : one measures electrical current. This leads to Coulomb peaks separated by the addition energy  $E_{\text{add}}(N)$  renormalized by the lever arm of the gate :  $\alpha = C_g/C_\Sigma$ . (device v3-a4)

where  $C_\Sigma = C_L + C_R + C_g$  is the total capacitance of the QD and  $N_0$  is the number of electrons in the QD when all the voltage sources are zero. Equation 1.1 takes places in the linear transport regime ( $V_{SD} \approx 0$ ). The energy required to add the  $N^{\text{th}}$  electron in the dot is the chemical potential:  $\mu(N) = E(N) - E(N - 1)$  and the energy cost for adding one electron is therefore:  $E_{\text{add}}(N) = \mu(N + 1) - \mu(N)$  and reads :

$$E_{\text{add}}(N) = \frac{e^2}{C_\Sigma} + \epsilon_{N+1} - \epsilon_N \quad (1.2)$$

This energy inversely related with the size of the quantum dot  $L$  can be experimentally measured in the Coulomb blockade regime [55, 56] (figure 1.3.b) where  $\Gamma_{S/D}, k_B T \ll E_C$ , which implies  $T \ll 20$  K.  $\Gamma_{S/D}$  can be tuned with gates between the quantum dot and the reservoirs but in the simplest QD design  $\Gamma_{S/D}$  is fully determined by the tunneling resistance  $R_t$  between the nanoconductor and the reservoir which needs to be much higher than the resistance quantum :  $R_t \gg R_Q = e^2/h \approx 25.813$  k $\Omega$  [11]. In the first order, electronic transport occurs if a discrete state of the quantum dot is aligned with the Fermi energy. In practice a small bias voltage  $V_{SD}$  is applied to the source, tuning the gate voltage scrolls the discrete energy spectrum and Coulomb peaks are measured only for finite periodic gate voltages corresponding to a state in the bias window (figure 1.3.b). The full characterization is done by sweeping the bias voltage  $V_{SD}$  and the gate voltage  $V_g$ . The Coulomb peaks broaden with the bias voltage as the QD energy level figures in the bias window for a bigger span in gate voltage. This forms what is called Coulomb diamonds. In carbon nanotubes, with the four-fold degeneracy (spin and valley) this transport measurement shows an extra four-fold periodicity as every four electron there is an extra cost  $\Delta E$  to  $E_{\text{add}}(N)$  [57]. Furthermore, if the CNT is semiconducting it is possible to identify the 1 electron and 1 hole states which corresponds to the first Coulomb peak after and before the gap [51]. By lifting the spin degeneracy with a magnetic field, the first electron states (spin up and spin down) can be used to encode quantum information. Quantum dots constitute then a promising platform for quantum bits realization [36].

The characteristics energies of the QD circuit can be tuned differently from the Coulomb blockade regime. In the Fabry-Perot regime where  $E_C, k_B T \ll \Gamma_{S/D}$ , the electrons behave as plane waves [58, 59]. In between one finds the Kondo regime where  $k_B T \ll \Gamma_{S/D} \lesssim E_c$  which shows an enhancement of the conductance at zero bias because of scattering events [60, 61].

One presented here the building block of quantum dot circuits which can be duplicated to build double quantum dots (DQD) [62], triple quantum dots [63] or even quadruple quantum dots [64, 65]. These different cases with  $N_e$  electrons in  $N$  quantum dots can be described by

the Hubbard Hamiltonian :

$$H_{Hub} = \sum_{i=1}^N \left( \frac{E_{c_i}}{2} n_i (n_i - 1) + \epsilon_i n_i \right) + \sum_{\langle i,j \rangle} E_{c_m,ij} n_i n_j + \sum_{\sigma=\uparrow,\downarrow} (t_{ij} c_{i\sigma}^\dagger c_{j\sigma} + h.c.) \quad (1.3)$$

where  $c_{i\sigma}^\dagger/c_{i\sigma}$  is the creation/annihilation operator for an electron in quantum dot  $i$  with spin  $\sigma$ ,  $\epsilon_i$  is the orbital energy in the dot  $i$ ,  $E_{c_i}$  is the charging energy of dot  $i$ ,  $E_{c_m,ij}$  is the mutual charging energy between the dots  $i$  and  $j$  and  $n_i = \sum_{\sigma} c_{i\sigma}^\dagger c_{i\sigma}$  is the number operator. This Hamiltonian captures exchange interaction which is crucial for spin qubit implementation (see section 1.3).

## 1.2 Double quantum dot as a charge qubit

In the same way as single quantum dots (SQD) can be seen as artificial atoms, multiple quantum dots can be seen as artificial molecules. Building quantum dots with multiple sites can be interesting for quantum computing perspectives [18] but also to study topological matter [66]. This section focuses on double quantum dots that present a new feature compare to SQD: the interdot transition.

### 1.2.1 Electrical model

A double quantum dot (DQD) consists of two single quantum dots coupled to each other. Electrons can thus tunnel from one dot to the other at a tunnel rate  $t$  typically ranging from 1 GHz to several tens of GHz. Similarly to the SQD, the left (resp. right) dot is connected to the source (resp. drain) through a tunnel barrier and exchange electrons a rate  $\Gamma_L$  (resp.  $\Gamma_R$ ) (figure 1.4). One can also derive the addition energy  $E_{\text{add}}(N)$  of each dot from the electrostatic and orbital energies. It is supposed to be dominated by the charging energy whose derivation is detailed in [62]. The double quantum dot model gives also rise to the mutual charging energy  $E_{C_m}$  which describes how one dot is affected when an electron is added to the other one due to their coupling:

$$E_{C_L} = \frac{e^2}{C_{\Sigma_L}} \left( 1 - \frac{C_m^2}{C_{\Sigma_L} C_{\Sigma_R}} \right)^{-1} \quad (1.4)$$

$$E_{C_R} = \frac{e^2}{C_{\Sigma_R}} \left( 1 - \frac{C_m^2}{C_{\Sigma_L} C_{\Sigma_R}} \right)^{-1} \quad (1.5)$$

$$E_{C_m} = \frac{e^2}{C_m} \left( \frac{C_{\Sigma_L} C_{\Sigma_R}}{C_m^2} - 1 \right)^{-1} \quad (1.6)$$

where  $C_{\Sigma_{L/R}} = C_{L/R} + C_{g_{L/R}} + C_m$  is the total capacitance of the left/right dot. Extracting those energies gives insights on the double quantum dot behavior. Moreover it enables to have an absolute energy axis which is very useful to extract parameters such as the interdot tunnel coupling  $t$ . The gate voltages that are applied are indeed not the potential felt in the DQD due to their physical spacing, screening effects and cross capacitances. As for the SQD (1.3.b), the gate voltage axis  $V_{g_i}$  has to be re-scaled by a factor  $e\alpha_i = eC_{g_i}/C_{\Sigma_i}$  to be an absolute energy axis. A procedure of energy calibration is presented in appendix A for the case we are interested in.

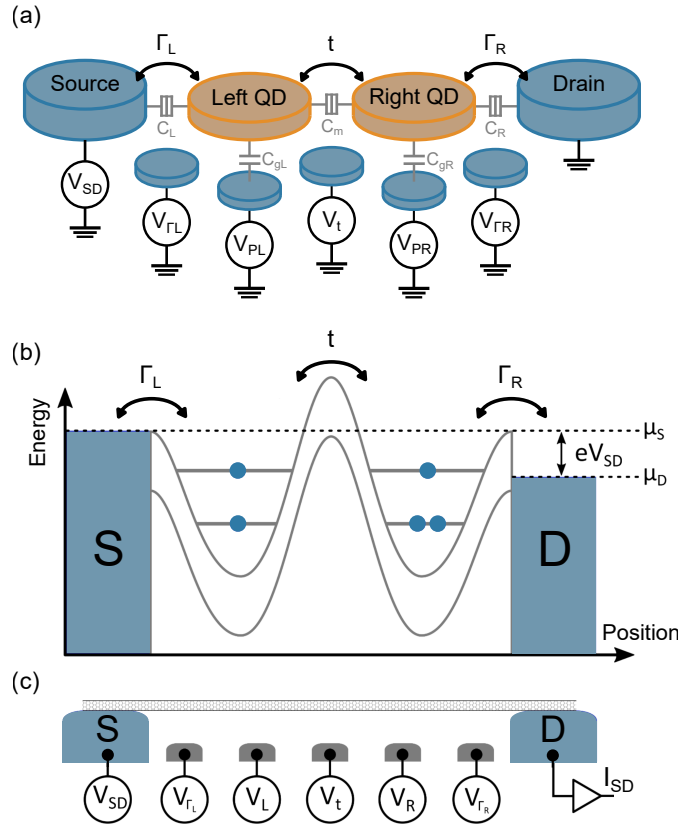


Figure 1.4: **Double quantum dot:** (a) Equivalent electrical circuit. The electrons trapped in the dot can tunnel to the other one or to the neighboring reservoir. The tunnel barriers can be tuned with the gate voltages  $V_{\Gamma_L}$ ,  $V_{\Gamma_R}$  and  $V_t$ . The plunger gate voltages  $V_{P_L}$  and  $V_{P_R}$  scrolls the energy levels of the left and right dot. This model is idealized as the cross capacitance are not considered. (b) Representation of the double quantum dot electrostatic potential felt by the electrons in a semiconducting nanoconductor. In this situation electronic transport happens as the two states are aligned in the bias window (set by  $V_{SD}$ ) (c) Representation of a carbon nanotube contacted to source and drain and suspended over the five gates shaping the DQD.

For the ferromagnetic spin qubit implementation (described in section 1.3.2), one should have a charge dipole isolated from its environment. This can be done with  $\Gamma_L, \Gamma_R \ll k_B T \ll t$  which can be in principle electrostatically tuned with the gate voltages  $V_{\Gamma_L}, V_{\Gamma_R}$  and  $V_t$ . In this situation the electron is delocalized over the two dots forming molecular orbitals.

Double quantum dots have been measured in semiconductor heterostructure [67, 68] and also in carbon nanotubes [69, 70]. However as opposed to SQD fully characterized with a two dimensional scan (Coulomb diamonds), DQD would require a six dimensional scan (five gates values and one bias voltage) which is not suitable. Double quantum dots are commonly characterized with the stability diagram which is much more convenient [71].

### 1.2.2 Stability diagram

As for the single quantum dot, sweeping the gate voltage varies the number of electrons trapped in the dot. In a double quantum dot, measuring the current  $I_{SD}$  at a fixed bias voltage  $V_{SD} \ll k_B T$  as a function of the plunger gate voltages  $V_{P_L}$  and  $V_{P_R}$  (figure 1.4) reveals a honeycomb pattern called the stability diagram. It highlights indeed equilibrium areas which have an hexagonal shape where there is a fixed number of electrons in each dot ( $N_L, N_R$ ) (figure 1.5.a,b). For some borderline cases the equilibrium areas are not hexagonal anymore. On the one hand, the two dots can be decoupled from each other ( $C_m \rightarrow 0$ ), sweeping  $V_{P_L}$  will not affect the right dot and vice-versa. This gives rise to rectangular areas (figure 1.5.d). On the other hand, the two dots can behave as a single one with  $N_L + N_R$  electrons if their coupling is the dominant one ( $C_m \gg C_{L/R}, C_{g_{L/R}}$ ). This gives rise to oblique parallel lines (figure 1.5.e). Measuring the stability diagram gives therefore insights on the behavior of the double quantum dot. This measurement over a wide range of plunger gate voltages is nevertheless time consuming especially since it can be done for any value of  $V_{\Gamma_L}, V_{\Gamma_R}$  and  $V_t$ . Some efforts are put towards converging faster to the proper DQD regime with tuning protocols [20, 72], computer automation [73–75] or machine learning approach [76, 77]. A quantitative approach of the stability diagram provides the charging energies of the DQD (appendix A).

The lines delimiting the hexagons can be seen in transport measurements only with sufficiently high tunnel rates  $\Gamma_L, \Gamma_R$  and  $t$ . In the linear regime ( $V_{SD} \ll k_B T$ ), electrons flow from source to drain only if the 2 dots ground state electrochemical potentials are aligned to the one of the reservoir that are set to the Fermi energy. This condition is satisfied at the triple points in the  $V_{P_L} - V_{P_R}$  plane (figure 1.5.c). In the non-linear regime (at finite bias voltage), triangles extend next to the triple points as  $V_{SD}$  is increased (figure 1.6). Multiple discrete energy levels can indeed enter the bias window. As excited states can now contribute to transport,

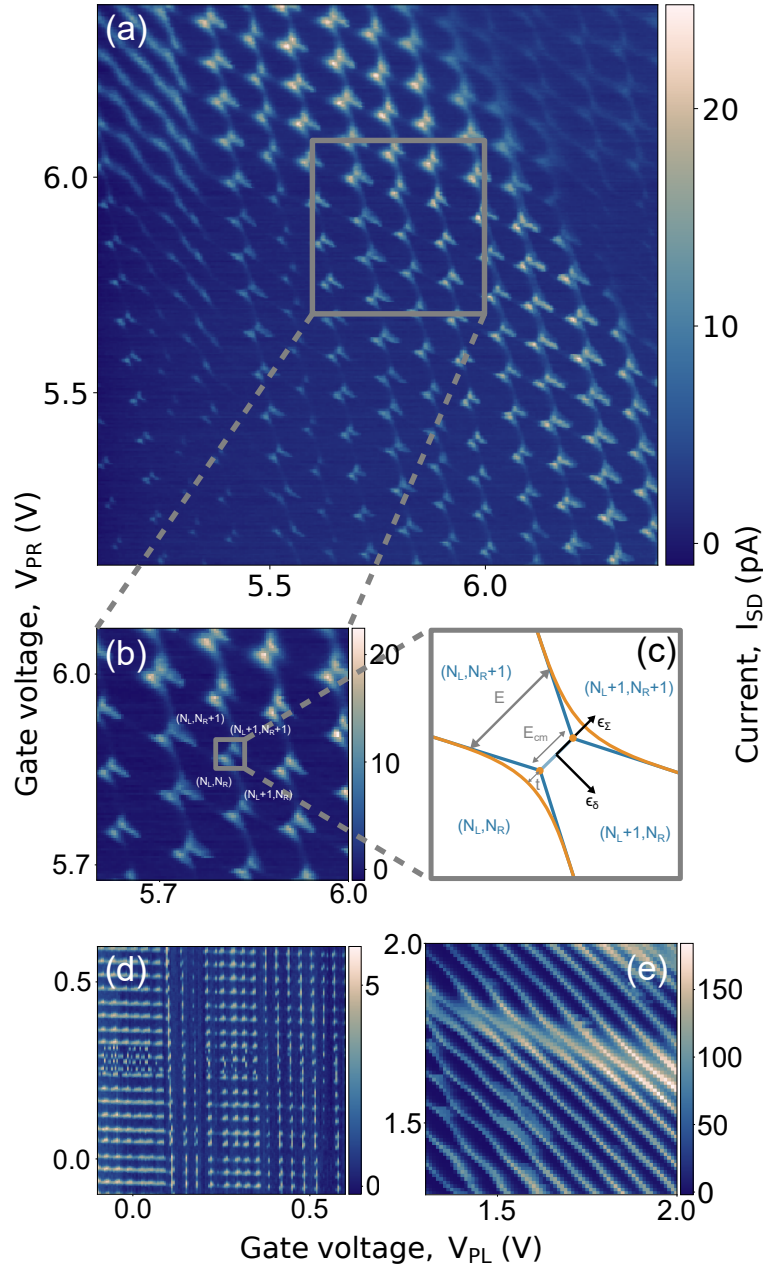


Figure 1.5: **Stability diagram:** (a) Current  $I_{SD}$  as a function of the plunger gate voltages  $V_{PL}$  and  $V_{PR}$  showing a honeycomb pattern. The carbon nanotube in which is formed the double quantum dot has been afterwards identified as a bundle. (device B2) (b) Zoom on (a): the hexagonal equilibrium areas have a given number of electrons in each dot. (c) Schematic of the region around an interdot transition. The orange circles are the triple points showing a maximum current. Changing the detuning value  $\epsilon_\delta$  affects how the electron is localized in the dots. At  $\epsilon_\delta = 0$  the electron is delocalized over the two dots. (d) Stability diagram showing two uncoupled dots. The equilibrium areas are rectangles. (device SpinQMag5R) (e) Stability diagram showing two overcoupled dots that behave like a single dot. An electron is added to the single dot as an oblique line is crossed. (device B2)

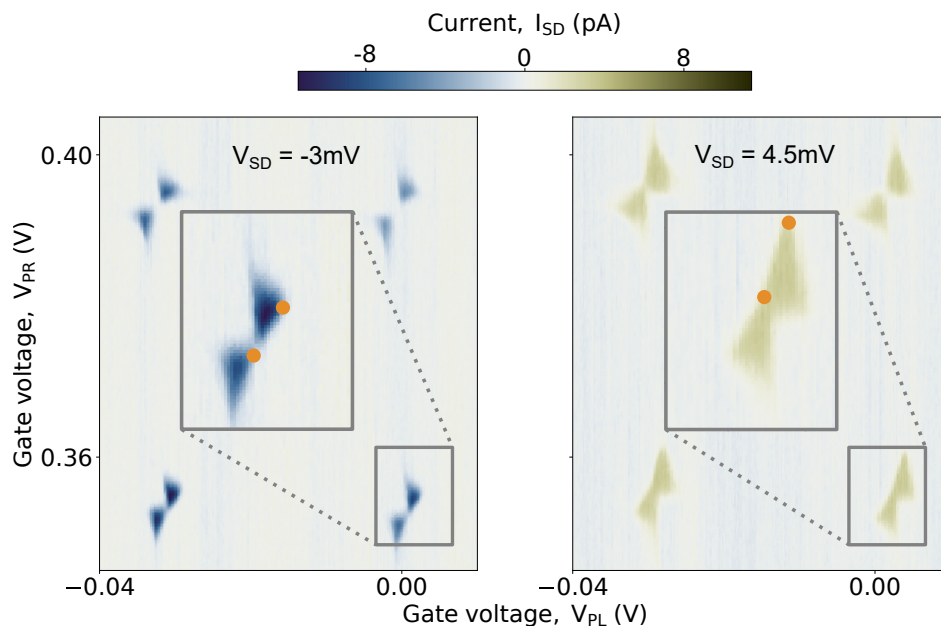


Figure 1.6: **Bias triangles:** Current  $I_{SD}$  as a function of the plunger gate voltages  $V_{PL}$  and  $V_{PR}$  in the non-linear regime ( $V_{SD} = 4.5$  mV on the left panel and  $V_{SD} = -3$  mV on the right panel). Transport occurs in triangles whose size is proportional to the bias voltage. They are located next to the triple points represented here with orange circles. (device SpinQMag5R)

triangles provides a spectroscopy of the system. Furthermore, this measurement is useful for a lever arm calibration (appendix A).

In practice, the electrostatic potential landscape felt by the electrons is not entirely determined by the applied gate potentials. Strong local modifications of the potential can arise from the presence of impurities. A textbook stability diagram highlights then the cleanliness of the device. In the case of multi-wall carbon nanotubes or multiple tubes touching each other (bundles), transport is more complex and gives rise to additional complexity in the stability diagram. To implement the ferromagnetic spin qubit, one wants to identify the area corresponding to one electron trapped in the double quantum dot. A clean narrow gap single-wall carbon nanotube should reveal such a region in the stability diagram. The gap delimits indeed four different regimes giving a reference for counting electrons and holes in the dots.

### 1.2.3 Charge qubit

As mentioned previously, the stability diagram reveals zones where an interdot transition occurs (figure 1.5.c). In the picture of a single orbital in each dot, the electron tunnels from one dot to the other at a rate  $t$ . This provides a two level system that can be used to encode

quantum information. Depending on the detuning value  $\epsilon_\delta = \epsilon_R - \epsilon_L$ , the electron is either in the left dot with corresponding state  $|L\rangle = |1, 0\rangle$  or in the right dot with corresponding state  $|R\rangle = |0, 1\rangle$ . In this basis  $\{|L\rangle, |R\rangle\}$ , the Hamiltonian of the system can be deduced from equation 1.3 and reads:

$$H = \begin{pmatrix} \epsilon_L & t \\ t & \epsilon_R \end{pmatrix} \quad (1.7)$$

This gives rise to the following eigenstates :

$$|+\rangle = u |L\rangle + v |R\rangle \quad |-\rangle = v |L\rangle - u |R\rangle \quad (1.8)$$

where  $u = \sqrt{\frac{1}{2} - \frac{1}{2} \frac{\epsilon_\delta}{\sqrt{\epsilon_\delta^2 + 4t^2}}}$  and  $v = \sqrt{\frac{1}{2} + \frac{1}{2} \frac{\epsilon_\delta}{\sqrt{\epsilon_\delta^2 + 4t^2}}}$ .

Close to charge degeneracy point ( $\epsilon_\delta \sim 0$ ), the electron is fully delocalized over the two dots. The  $|-\rangle$  and  $|+\rangle$  states are called bonding and anti-bonding states and are the logical states of the qubit :  $|B\rangle = 1/\sqrt{2} (|1, 0\rangle + |0, 1\rangle)$  and  $|AB\rangle = 1/\sqrt{2} (|1, 0\rangle - |0, 1\rangle)$  with corresponding energy  $E_\pm = 1/2 (\epsilon_\Sigma \pm \sqrt{\epsilon_\delta^2 + 4t^2})$  where  $\epsilon_\Sigma = \epsilon_R + \epsilon_L$  (figure 1.7.a,b). The spacing between those energies sets the qubit frequency and reads:

$$\hbar\omega_q = \sqrt{\epsilon_\delta^2 + 4t^2} \quad (1.9)$$

It is worth noticing that the charge qubit frequency is in principle entirely tunable with the gate voltages  $V_{P_L}$ ,  $V_{P_R}$  and  $V_t$ . Adjusting  $V_{\Gamma_L}$  and  $V_{\Gamma_R}$  is also important to isolate the qubit from the reservoirs and thus obtain a closed system.

The charge qubit can be initialized with the gate voltage control which can be pulsed to be faster. It is manipulated with a modulation of the detuning at the qubit frequency which enables rotations in the Bloch sphere (figure 1.7.c). Finally the readout can be done via transport measurement [78], charge sensing [79, 80] or using a cQED architecture [81, 82].

At  $\epsilon_\delta = 0$ , the charge qubit is insensitive to charge noise at first order ( $\partial\omega_q/\partial\epsilon_\delta = 0$ ) (figure 1.7.b). Charge noise is directly linked to the fluctuations of localized charge defects in the semiconductor leading to fluctuations in the local electric field. [83]. Charge qubits have therefore poor coherence times :  $T_2^* = 7$  ns in GaAs [80],  $T_2^* = 2.1$  ns in Si/SiGe [84] and  $T_2^* = 5$  ns in carbon nanotube [85]. However in the recent years the measured coherence times have increased up to  $T_2^* = 220$  ns [82]. To limit charge noise, the qubit should be isolated from its environment [78]. The use of suspended carbon nanotube would go in this direction. Another approach is to hybridize the charge with the spin which is expected to

be much more isolated from its environment to form a spin-orbit qubit (see section 1.3.3). Ideally it gets the best of the two worlds resulting in a tunable and addressable qubit with a long coherence time.

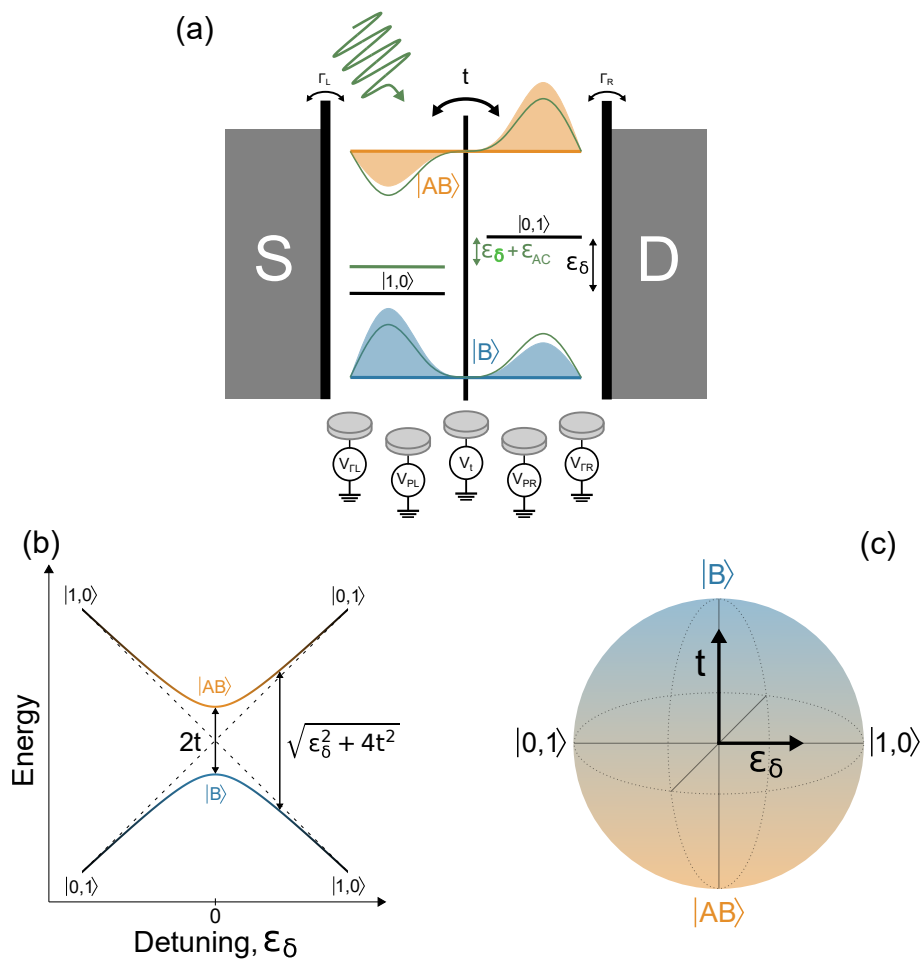


Figure 1.7: **Charge qubit in a double quantum dot:** (a) Schematic of the DQD in the closed regime with one electron. Close to  $\epsilon_\delta = 0$  the eigenstates are the bonding and anti-bonding states that are encoding the logical states of the charge qubit. Varying  $\epsilon_\delta$  changes the wave function overlap over the two dots. (b) Energy spectrum of the charge qubit. Around  $\epsilon_\delta = 0$  an avoiding crossing is observed. The bonding and anti-bonding states are separated in energy by  $2t$ . (c) A two level system can be represented with a Bloch sphere. The north and south pole are the  $|0\rangle$  and  $|1\rangle$  logical states. Qubit manipulation can be performed with a modulation of the detuning at the qubit frequency : the qubit state vector rotates around the  $\epsilon_\delta$  axis.

## 1.3 Spin qubits

The spin degree of freedom naturally provides a two-level system which can be used as a qubit [36]. Using the spin to encode quantum information presents several advantages. It is weakly coupled to the environment and thus high coherence time can be envisioned. On the one hand, the spin is insensitive to the electric field. On the other hand, the magnetic noise coming from the interaction with the nuclear spin bath can be drastically reduced by the choice of host material. The use of isotopically purified silicon with  $^{28}\text{Si}$  which has no nuclear spin has led to record coherence times [86, 87]. It is likely to be the same with  $^{12}\text{C}$ . Semiconductor spin qubits reviewed in this section benefit from available industrial infrastructures. By adding the fact that their small size opens the door for scaling up, semiconductor spin qubits are highly competitive candidate for scalable solid-state quantum information processing.

### 1.3.1 Various types of implementation

#### Loss-DiVincenzo spin qubit

In 1998, Loss and DiVincenzo proposed a qubit realization with a direct mapping on the spin of an electron in a quantum dot [36]. A single electron can be trapped in a quantum dot (section 1.1.2) and the spin degree of freedom can be lifted by applying an external magnetic field  $B_z$ . This results in two states that can be isolated to work in the following computational basis:  $\{|\uparrow\rangle, |\downarrow\rangle\}$ . The Hamiltonian and the associated qubit frequency read:

$$H_{LD} = \frac{1}{2}g\mu_B B_z \hat{\sigma}_z \quad (1.10)$$

$$\hbar\omega_q = g\mu_B B_z \quad (1.11)$$

where  $g$  is the electron  $g$ -factor ( $g \approx 2$ ) and  $\mu_B$  is the Bohr magneton. Those quantities define the electron gyromagnetic ratio  $\gamma_e$  as follows:  $\gamma_e = g\mu_B/\hbar \approx 28 \text{ GHz/T}$ .

The readout of this qubit has been firstly demonstrated with a spin to charge conversion technique [88]: depending on its spin, the electron can whether or not tunnel to the reservoir. Such a technique requires to optimize the tunnel rate for a fast readout with still the possibility to detect the signal. Readout fidelities above 99% have been obtained in Si/SiGe [89]. However the spin to charge conversion affects the qubit states and is therefore not a quantum nondemolition (QND) technique. To remedy this, an ancilla can be conditionally rotated and measured [90, 91] or a cQED architecture can be used with a different qubit encoding [30, 31].

The first manipulation has been done using electron spin resonance (ESR) in a singlet-triplet qubit [92]. This technique has been afterwards implemented for a single spin manipulation [93, 94]. With an applied transverse AC magnetic field at the qubit frequency, in the rotating frame the Hamiltonian becomes:  $H = g\mu_B B_{x, AC} \hat{\sigma}_x$ . This enables rotations between the spin up and down states at a frequency:  $\hbar\Omega_{\text{Rabi}} = g\mu_B B_{x, AC}$ . Rabi frequencies are thus obtained with a transverse magnetic field modulated at high frequency (RF) with an amplitude of few mT in parallel with high static B field. In these conditions, it is technically challenging to avoid heating and mechanical oscillations [95]. Furthermore in the case of several qubits, selective manipulation is problematic. An alternative way consists in driving electrically the spin qubit through a gate electrode. As the spin does not couple to the electric field, spin-charge hybridization is required to perform what is called electric-dipole spin resonance (EDSR). One possibility is to exploit the intrinsic spin-orbit coupling of the host material [13, 96]. Hole spins are also attractive as they carry large spin-orbit coupling [97–99]. Another possibility is to induce a magnetic field gradient which is mostly implemented with a Co micromagnet [14, 15, 100, 101]. Those techniques are also crucial in the perspective of integrating a cQED architecture (see section 1.3.3).

Realizing two-qubit gates can be achieved with an electric control of the exchange interaction [36]. In the case of  $N_e$  electrons in  $N$  quantum dots if  $N_e = N$ , the Hubbard model says that spins behave as an Heisenberg spin chain. Equation 1.3 becomes then :

$$H_{\text{Heisenberg}} = \sum_{\langle i,j \rangle} J_{ij} \hat{S}_i \hat{S}_j \quad (1.12)$$

where  $J_{ij}$  is the exchange interaction and  $\hat{S}_{i/j}$  is the spin operator for the electron  $i/j$  in QD  $i/j$ .  $\langle i,j \rangle$  indicates that the sum is restricted to nearest neighbors. The electric control of exchange interaction has been firstly demonstrated in a singlet-triplet architecture [102] and later on with distinct readout of each spin [103]. The drawback is that it only couples nearest neighbors which is a hurdle for developing large-scale quantum processors. Several strategies are thus studied to enable long-range coupling between distant spins. A first approach consists in a physical transport of the electron spin via surface acoustic waves [104, 105] or single-electron shuttling [106–108]. An auxiliary quantum dot array can be implemented to provide superexchange [109]. In the case of spin-orbit qubits one can benefit from capacitive and electric dipole-dipole coupling [110]. One can take advantage of this to integrate the cQED tool box which have widely proved its worth for superconducting qubits [24, 25].

The various implementations of the Loss and DiVincenzo spin qubit have shown long coherence times [111], the highest being  $T_2^* = 120 \mu s$  [112, 113]. The Rabi frequency can be

damped with hyperfine interaction and hence the use of isotopically purified silicon which has demonstrated one and two qubit gate fidelities above 99% [16, 114]. It constitutes an important milestone as it is the threshold for the quantum error correction surface code. Recently, a four qubit [115] and a six qubit [18] quantum processor have been implemented which hold promise for scalable network of spin qubits.

### Donor spin qubit

In the same idea than the Loss and DiVincenzo proposal, Kane suggested to use nuclear spins of  $^{31}\text{P}$  in silicon [116]. Using the nuclear spin instead of the electron one increases again the coherence time. Their gyromagnetic ratio differs indeed by three order of magnitude:  $\gamma_n \approx 17.2 \text{ MHz/T}$  (for  $^{31}\text{P}$  nucleus) and  $\gamma_e \approx 28 \text{ GHz/T}$ . To this can be added the fact that nuclear spins have no mobility in the semiconductor which prevents spin-orbit coupling and thus charge noise. Finally, as mentioned before, silicon can be purified to obtain a nuclear spin free material [117].  $^{31}\text{P}$  donors positioning must be very accurate and is thus demanding in terms of nanofabrication. They are placed with a masked ion-implantation method [118] or using scanning tunneling microscope lithography [119].

Two types of gates are implemented on the chip: above the donor sites the gates tune the nuclear spin resonance frequency and between the donor sites the gates control the nuclear spin exchange coupling. A coupled electron spin is used for the nuclear spin readout with a spin to charge conversion technique which is here QND [117, 120]. Storing quantum information in the nuclear spin provides the best coherence time ever reported in semiconductor spin qubits [111] :  $T_2^* = 2.4 \text{ ms}$  [121]. The qubit manipulation is done using ESR technique. One and two qubit gates have recently shown high fidelities values [122].

### Singlet-triplet spin qubit

Using the spin of a single electron is the natural way to implement a qubit. The logical states have opposed magnetic quantum number:  $S_z = \pm 1/2$  and the qubit frequency is set by the external magnetic field. Small magnetic field fluctuations affects therefore the qubit associated energies differently and then the qubit frequency yielding dephasing. To remedy this, the qubit can be encoded with more complex states spaced by an energy that is not affected by global magnetic noise. The singlet-triplet qubit satisfies this condition [123]. It is implemented with two electrons in a double quantum dot close to the (0,2)/(1,1) interdot transition [102] (figure 1.8.a), with  $(N_L, N_R)$  the number of electrons in the left and right dot. It is thus question of the case  $N_e = 2$  electrons in  $N=2$  quantum dots (left and right) of the Hamiltonian presented in equation 1.3. In the (0,2) charge configuration the ground state is

the singlet  $|S_{(0,2)}\rangle = 1/\sqrt{2}(|\uparrow_R\downarrow_R\rangle - |\downarrow_R\uparrow_R\rangle)$  and is the only one considered here. The triplet states are indeed far away in the energy spectrum as one of the two electron occupies a higher orbital due to the Pauli exclusion principle. In the (1,1) charge configuration the ground state is the singlet  $|S_{(1,1)}\rangle = 1/\sqrt{2}(|\uparrow_L\downarrow_R\rangle - |\downarrow_L\uparrow_R\rangle)$  and triplet states read :  $|T_{+(1,1)}\rangle = |\uparrow_L\uparrow_R\rangle$ ,  $|T_{0(1,1)}\rangle = 1/\sqrt{2}(|\uparrow_L\downarrow_R\rangle + |\downarrow_L\uparrow_R\rangle)$  and  $|T_{-(1,1)}\rangle = |\downarrow_L\downarrow_R\rangle$ . The index L/R indicates if the spin is in the left or right dot. With an external magnetic field  $B_z$ , the  $T_+$  ( $S_z = +1$ ) and  $T_-$  ( $S_z = -1$ ) triplet states repel each other with respect to  $T_0$  ( $S_z = 0$ ) which is not affected. With the tunnel coupling, the charge states (0,2) and (1,1) hybridize around  $\epsilon_\delta = 0$ . As the spin quantum number is conserved as the electron tunnels from one dot to the other, the energy spectrum only shows an avoiding crossing between the singlet states  $|S_{(0,2)}\rangle$  and  $|S_{(1,1)}\rangle$  [54] (figure 1.8.b). The singlet-triplet qubit states are :

$$|S\rangle = \alpha |S_{(0,2)}\rangle + \beta |S_{(1,1)}\rangle \quad |T_0\rangle = |T_{0(1,1)}\rangle \quad (1.13)$$

With  $\alpha$  and  $\beta$  complex numbers such that  $|\alpha|^2 + |\beta|^2 = 1$ . Finally both states do have a magnetic quantum number equal to zero resulting in a qubit insensitive to  $B_z$  noise. As mentioned earlier, as  $N_e = N$ , the system can be described by the Heisenberg Hamiltonian (see equation 1.12). The exchange energy  $J(\epsilon_\delta)$  sets the qubit frequency and can be electrostatically tuned as it depends on the detuning  $\epsilon_\delta$  and the tunnel coupling rate  $t$ :

$$\hbar\omega_q = J(\epsilon_\delta) \approx \frac{4t^2 E_c}{E_c^2 - \epsilon_\delta^2} \quad (1.14)$$

where one assumes that both quantum dots have the same charging energy:  $E_{cL} = E_{cR} = E_c$ . As the two states of the singlet-triplet qubit have different orbital wave functions, they experience a different magnetic environment. This magnetic field difference  $\Delta B_z$  couples the two states and provides therefore a full control of the qubit:

$$H_{S-T} = J(\epsilon_\delta)\hat{\sigma}_z + g\mu_B\Delta B_z\hat{\sigma}_x \quad (1.15)$$

In practice,  $\Delta B_z$  has a finite value thanks to inhomogeneous nuclear magnetic field (as in GaAs [102, 124]) coming at the price of good coherence properties. To counter this, a micromagnet can be integrated to a chip without nuclear field [125].

The qubit initialization is done by setting the detuning to large negative values where the ground state is  $|S_{(0,2)}\rangle$ . Then the detuning is increased to prepare a  $|S\rangle$  state. The readout of the singlet-triplet qubit relies on Pauli spin blockade. As mentioned previously, tunneling conserves spin. Thus, depending if the electrons form a singlet state  $|S_{(1,1)}\rangle$  ( $S=0$ ) or a triplet

state  $|T_{0(1,1)}\rangle$  ( $S=1$ ), the electron of the left dot can tunnel or not to the right one as the only available state is the singlet  $|S_{(0,2)}\rangle$  ( $S=0$ ). This tunneling event can be detected with a charge sensor [102] or direct transport measurement [126]. Although being non QND, this technique enables a rapid and accurate readout [127]. The qubit manipulation can be performed as  $\Delta B_z$  has a finite value and thus drives rotations between the  $|S\rangle$  and  $|T_0\rangle$  states. For a singlet-triplet qubit, the highest coherence time classified [111] is  $T_2^* = 12 \mu s$  [59]. High one qubit gate fidelities have been reported [59, 128, 129] and a two qubit gate with a 90% fidelity has been performed by coupling capacitively two singlet triplet qubit [130].

Although this qubit is protected from global  $B_z$  noise, the non-diagonal term in the Hamiltonian makes it sensitive to local magnetic fluctuations. Encoding quantum information in more complex spin states can lead to a qubit insensitive to both local and global field fluctuations. Such a system is generally called a decoherence-free subspace.

### Exchange-only spin qubit

Obtaining a decoherence-free subspace can be achieved by using three electrons in a triple quantum dot [131]. The system can be described by Hamiltonian presented in equation 1.3 with  $N_e = 3$  electrons in  $N = 3$  quantum dots. The spin Hilbert space is formed of a quadruplet ( $S=3/2$ ) and two degenerate doublet ( $S=1/2$ ) subspaces. Restricting to the  $S=1/2$  and  $S_z = +1/2$  (or equivalently  $S_z = -1/2$ ) subspace gives eight states of which two are in the (1,1,1) configuration: have one electron in each dot (figure 1.9.a). Those two states defines the exchange-only (EO) qubit and read [132, 133]:

$$|0\rangle = (|\uparrow_1\uparrow_2\downarrow_3\rangle - |\downarrow_1\uparrow_2\uparrow_3\rangle)/\sqrt{2} \quad (1.16)$$

$$|1\rangle = (|\uparrow_1\uparrow_2\downarrow_3\rangle + |\downarrow_1\uparrow_2\uparrow_3\rangle - 2|\uparrow_1\downarrow_2\uparrow_3\rangle)/\sqrt{6} \quad (1.17)$$

As  $N_e = N$ , the system can once again be described with an Heisenberg Hamiltonian:

$$H_{Heisenberg} = \frac{J_L(\epsilon)}{4} \hat{S}_1 \hat{S}_2 + \frac{J_R(\epsilon)}{4} \hat{S}_2 \hat{S}_3 \quad (1.18)$$

With  $J_{L/R}(\epsilon)$  the exchange energy between the left/right dot and the middle one (figure 1.9.b). It can be rewrite in the qubit basis as follows:

$$H_{EO} = -\frac{1}{4}(J_R(\epsilon) + J_L(\epsilon))\hat{\sigma}_z - \frac{\sqrt{3}}{4}(J_R(\epsilon) - J_L(\epsilon))\hat{\sigma}_x \quad (1.19)$$

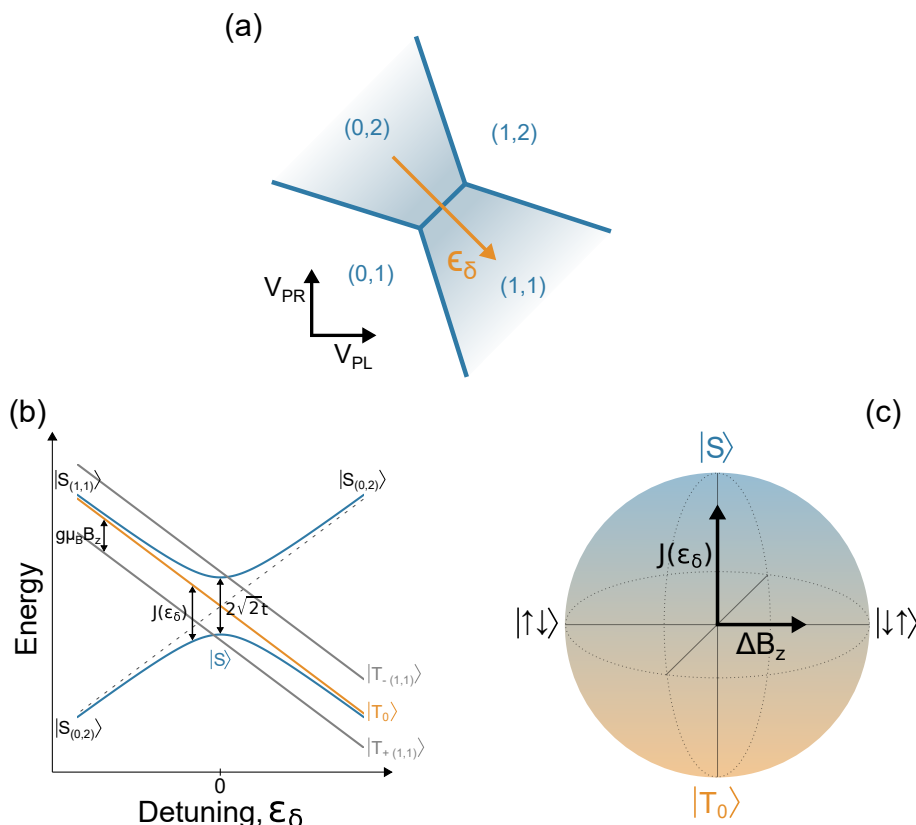


Figure 1.8: **Singlet-triplet spin qubit:** (a) The qubit is formed from two electrons in a double quantum dot close to the (0,2)/(1,1) interdot transition. (b) Energy spectrum of the singlet-triplet qubit. The two singlet states shows an avoiding crossing at  $\epsilon_\delta = 0$ . The triplet states are separated from each other with an external magnetic field  $B_z$ . The qubit energy  $J(\epsilon_\delta)$  can be tuned through the plunger gate voltages  $V_{PL}$  and  $V_{PR}$ . (c) Representation of the qubit states in the Bloch sphere. If  $J(\epsilon_\delta) \ll \Delta B_z$ , the eigenstates become  $|\downarrow\uparrow\rangle$  and  $|\uparrow\downarrow\rangle$ . Modulation of  $J(\epsilon_\delta)$  induces then oscillations between those states.

As its name implies, the qubit can be fully operated through exchange interaction which is electrostatically tunable.  $J_L(\epsilon)$  and  $J_R(\epsilon)$  pulses are not separately driving rotations in the Bloch sphere. Therefore the rotation axis forms a  $120^\circ$  angle (figure 1.9.c). The qubit frequency depends also only on exchange interactions and reads:

$$\hbar\omega_q = \sqrt{J_L(\epsilon)^2 + J_R(\epsilon)^2 + J_L(\epsilon)J_R(\epsilon)} \quad (1.20)$$

As for the singlet-triplet qubit, the exchange-only qubit can be readout using Pauli spin blockade [134]. One qubit gates are performed by pulsing the detuning  $\epsilon$  which modifies the exchange interactions  $J_L(\epsilon)$  and  $J_R(\epsilon)$ . As those quantities also depend on the tunnel rates  $t_L$  and  $t_R$ , one qubit gates can also be performed at a fixed detuning by playing on the tunnel rates to limit charge noise. It is referred to the symmetric operation point [135, 136]. The

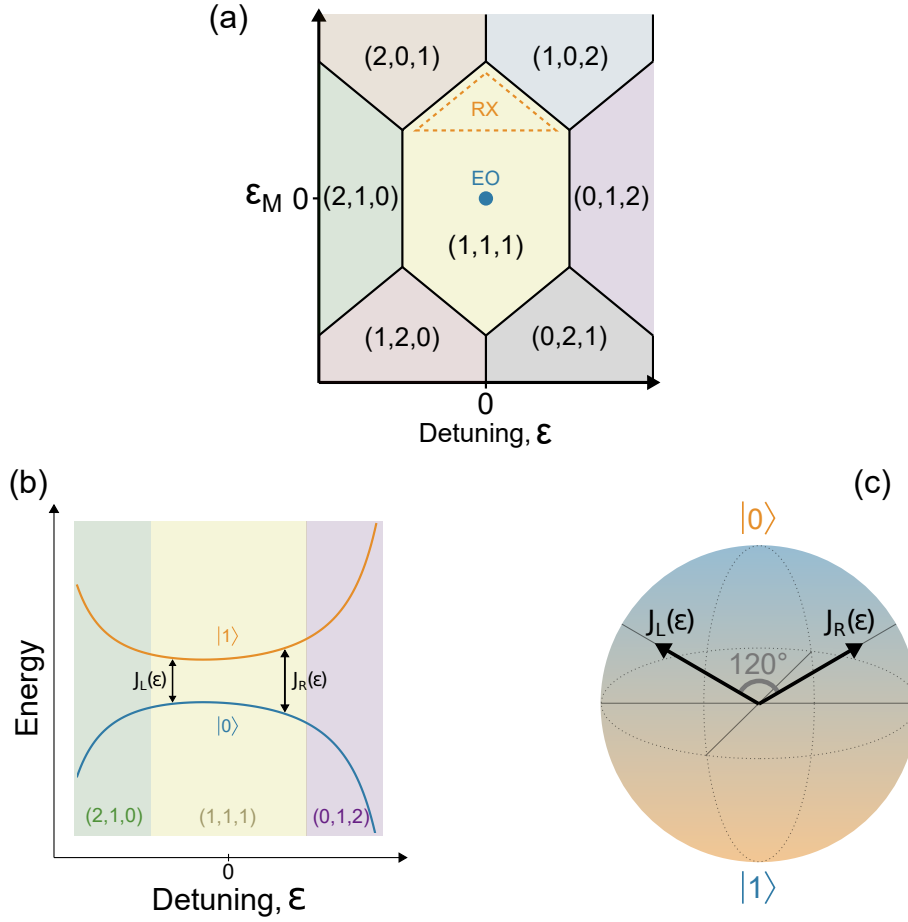


Figure 1.9: **Exchange-only spin qubit:** (a) Charge stability diagram of a triple quantum dot as a function of  $\epsilon = (\epsilon_1 - \epsilon_3)/2$  and  $\epsilon_M = \epsilon_2 - (\epsilon_1 + \epsilon_3)/2$ . The sweet spot of the exchange-only qubit figures in the middle of the (1,1,1) zone and the one of the resonant exchange qubit is delimited with the orange dashed line. (b) Energy spectrum of the exchange-only qubit. The spacing between the two energy states is controlled via the exchanges energies  $J_L(\epsilon)$  and  $J_R(\epsilon)$ . The asymmetry with respect to the detuning ensue from different tunnel coupling rates  $t_L$  and  $t_R$ . (c) Representation of the qubit states in the Bloch sphere. The rotations axis form a  $120^\circ$  angle.

maximum reported [111] coherence time is  $T_2^* \approx 2\mu\text{s}$  [137]. High one qubit gate fidelities have been reached [137, 138] and a 97.1% two qubit gate fidelity has been measured in a six quantum dot array [139].

The resonant exchange (RX) qubit is a slightly different version of the EO qubit. It is operated at a different working point where the exchange interactions are always turned on (figure 1.9.a). This results in a large qubit splitting which can be strongly modulated electrically leading to very short gate times [140]. In this regime, the readout can also be done by implementing a cQED architecture [32].

### 1.3.2 The ferromagnetic spin qubit

Circuit quantum electrodynamics which will be discussed in details in chapter 2 constitutes an appealing tool for quantum computation processing. It can indeed enhance qubit lifetime, allows high fidelity QND measurements of multiple qubits and enables entanglement of qubits separated by macroscopic distances [141]. This toolbox is widespread in the superconducting qubit field [4,5,24,142] and much more tricky to implement for a spin qubit. Even though the coupling between the spin and the cavity magnetic field have recently been enhanced from  $g \approx 10$  Hz [143] to  $g \approx 3$  kHz [144], it is still four orders of magnitude below suitable values. To circumvent this, a key ingredient is to hybridize the spin and charge degrees of freedom to couple to the electric field of the cavity. In those conditions, the qubit is a spin-orbit qubit of which the ferromagnetic spin qubit [7] is part. The specificity of this qubit is an all electric manipulation without any external applied magnetic field thanks to ferromagnetic contacts.

#### Overview

This qubit can be realized with many different nanoconductor. This work focuses on carbon nanotubes as they present many advantages (see section 1.1). A charge dipole can be obtained in a double quantum dot circuit with an electron delocalized over the two dots (see section 1.2). This provides coupling to the electric field of the cavity. The qubit spectrum is spin polarized with non-collinear ferromagnetic contacts. The spin quantization axis is then different in the two dots leading to spin dependent tunneling. This can be seen as an artificial spin orbit coupling.

#### Ferromagnetic interface-induced exchange fields

The ferromagnetic contacts polarize the electron spin trapped in the DQD via three different mechanisms [49,145]. One can first mention the stray field generated by the ferromagnet itself. This phenomenon is not dominant which is convenient for the cQED superconducting design. In the non-interacting limit, electronic transport in a coherent nanoconductor contacted to ferromagnetic contacts can be described with the scattering matrix formalism with transmission and reflection probabilities (figure 1.11.a). The second mechanism exists for finite transmission probability and is similar to proximity effect [146]. The electronic wave function then overlaps the ferromagnet and hybridize with its first atomic layer. Concretely the transmission probability depends on the contact quality of the nanoconductor on the ferromagnetic contact and can be electrically tuned with the closest gate electrode to the interface [147–150]. However for qubit perspective, one is looking for a closed system; having a finite transmission probability opens thus the way towards decoherence. The last mecha-

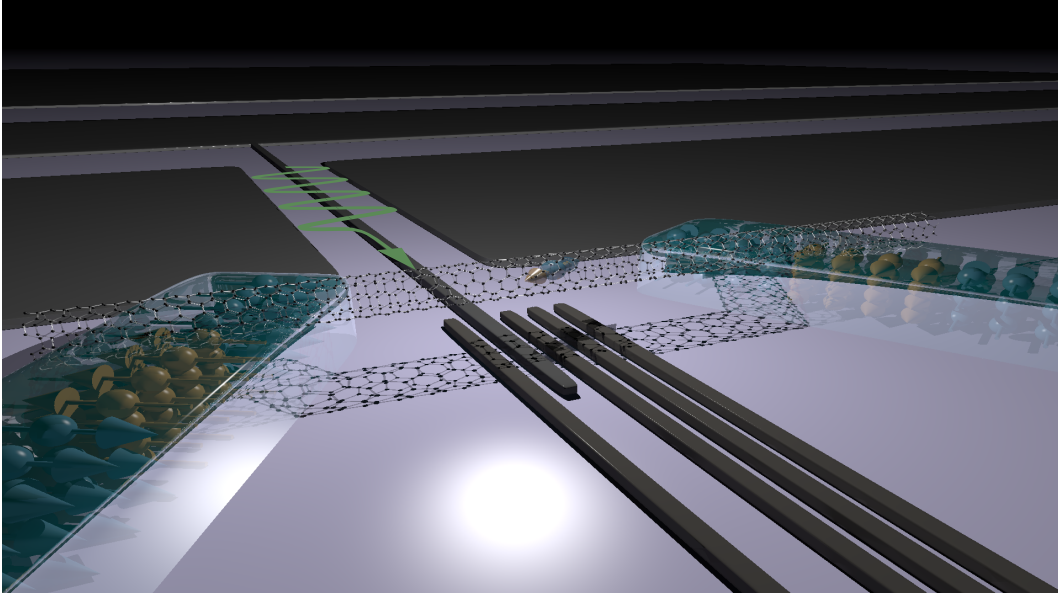


Figure 1.10: **Implementation of the ferromagnetic spin qubit:** A single electron in a carbon nanotube is trapped in a double quantum dot circuit. The non colinear ferromagnetic electrodes on which the nanotubes is contacted hybridize the spin and the charge degrees of freedom. This allows the spin to couple to photons of the microwave cavity.

nism does not require non opaque barrier and arises from spin dependent phase shift that is acquired by the electron. This leads to an effective Zeeman field in the nanoconductor itself called the confinement-induced exchange field [49]:

$$2\delta = \frac{\hbar v_F}{2L}(\varphi_{\uparrow} - \varphi_{\downarrow}) \quad (1.21)$$

where  $v_F \sim 8.10^5 \text{ m.s}^{-1}$  is the Fermi velocity of CNT,  $L$  is the length of the dot and  $\varphi_{\uparrow/\downarrow}$  is a spin dependent interfacial phase shift. This energy that defines the ferromagnetic spin qubit frequency is in principle electrically tunable with  $V_{\Gamma_{L/R}}$ .

To ensure the proper functioning of the ferromagnetic contacts, one can realize a magnetic force microscope (MFM) characterization. Such image and details on the fabrication are given in section 3.1. Once the device is fabricated and cooled down, one can perform Tunneling Magneto-Resistance (TMR) measurements [147, 150, 151]. The system implements a double quantum dot spin valve. Applying an external magnetic field generates a competition between the anisotropy energy of the ferromagnetic electrode and the interaction with the external field. The contact magnetization flips when the external magnetic field reaches its coercitive field. This results in a change of conductance captured in transport measurements (figure 1.11.b).

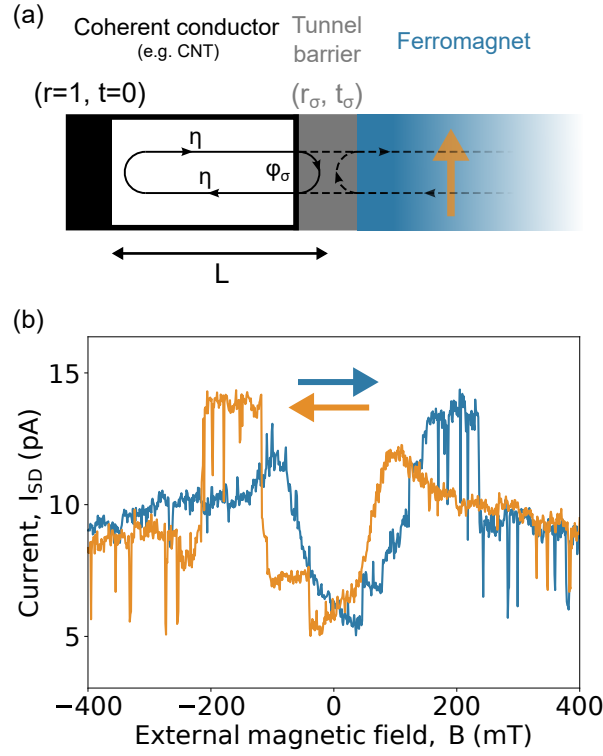


Figure 1.11: **Ferromagnetic interface and characterization:** (a) The confinement-induced exchange field originates from the interface with the ferromagnetic contact modeled with a tunnel barrier. An electron reflecting on the interface results in a spin-dependent phase shift  $\varphi_\sigma$  that adds to the phase acquired with the electronic path  $\eta$  over a distance  $L$  in the coherent conductor. (b) TMR measurement: Current through the double quantum dot is measured while sweeping the external magnetic field with a bias voltage  $V_{SD} = 5$  mV. (device v3-a4)

### Qubit characteristics

Owing the spin-charge hybridization, the system involves four states :  $|\uparrow, 0\rangle$ ,  $|\downarrow, 0\rangle$ ,  $|0, \nearrow\rangle$ , and  $|0, \searrow\rangle$ . By taking into account the valley degree of freedom of electrons in carbon nanotubes this would imply eight states but here K and K' are considered degenerate. By assuming a symmetric contact-induced effective spin splitting between the left and right dot:  $\delta_L = \delta_R = \delta$ , the Hamiltonian reads:

$$H_{ferro} = -\frac{\epsilon\delta}{2}\hat{\tau}_z\hat{\sigma}_0 + t\hat{\tau}_x\hat{\sigma}_0 - 2\delta\left(\hat{\sigma}_z\frac{\hat{\tau}_0 + \hat{\tau}_z}{2} + (\cos(\theta)\hat{\sigma}_z + \sin(\theta)\hat{\sigma}_x)\frac{\hat{\tau}_0 - \hat{\tau}_z}{2}\right) \quad (1.22)$$

where  $\hat{\tau}_i$  and  $\hat{\sigma}_i$  are the Pauli matrices (or the identity if  $i=0$ ) for the orbital and spin degree of freedom.  $\theta$  is the angle between the magnetizations of the left and right dot. The term preceded by  $\sin(\theta)$  provides the spin-charge hybridization. For any transition, a change in the orbital part of the wavefunction affects its spin part and vice-versa: this results in an

artificial spin-orbit coupling (see figure 1.12.a). The spin-charge hybridization is controlled by the angle  $\theta$  fixed by design and the detuning  $\epsilon_\delta$  which is electrically tunable. With  $\theta = \pi/2$  the hybridization to the charge is maximum as well as the coupling to the cavity which is attracting. However, it comes at the cost of charge noise. There is therefore a trade-off to find. The angle has been fixed in this work to  $\theta = \pi/6$  accordingly to calculations (see figure 1.13) and previous results of the group [152]. One can also play on the detuning to find an optimum between being sufficiently coupled to the cavity with minimal charge noise (see figure 1.13). A first possibility is to go at sufficiently large detuning still being coupled to the cavity (labeled "ON"): the 01 transition is here mostly "spin-like" (see figure 1.12.b). In this regime, the qubit frequency is not affected by small changes of the detuning. However the coupling to the cavity is drastically reduced. The later can still be turned completely "OFF" by increasing again the detuning towards a pure spin transition. In those conditions, the qubit coherence time is maximal and can thus be used as a quantum memory. Switching from "ON" and "OFF" without affecting the qubit frequency is furthermore required for implementing the two qubit iSWAP gate and can be done via gate voltage pulses. The second working point is at zero detuning where similarly to the charge qubit,  $\partial\omega_q/\partial\epsilon_\delta = 0$  at first order. At zero detuning, the electron is delocalized over the two dots resulting in a maximum charge dipole that couples to the cavity electric field. As the spin-charge hybridization is maximum at this working point (see figure 1.12.b), the most spin-like transition is the 02 which is used to form the qubit.

Important milestones towards the implementation of the ferromagnetic spin qubit have been achieved in the recent years. The first crucial ingredient for the readout was to observe coupling [28] and strong coupling [146] between a photon in a microwave cavity and an electron in a quantum dot circuit. This has led to the demonstration of the readout of the spin via the microwave cavity [151]. This technique will be discussed in chapter 2. Another key feature was to set and identify the qubit. The 01 transition has been highlighted through microwave spectroscopy [152]. As predicted, the linewidth of the transition narrows with increasing detuning to reach a minimum value setting the decoherence rate  $\gamma_s \leq 2\pi \times 249$  kHz. Finally, a full characterization of the qubit requires time domain measurements. The modulation of the detuning changes the overlapping of the wave function over the two dots. As their exchange field have a different contribution the effective magnetic field is now tilted resulting in a transverse component in the Bloch sphere (see figure 1.12.c). Modulating the detuning at the qubit frequency enables thus rotations on the Bloch sphere. Chapter 5 presents such manipulations highlighting microsecond lived quantum states.

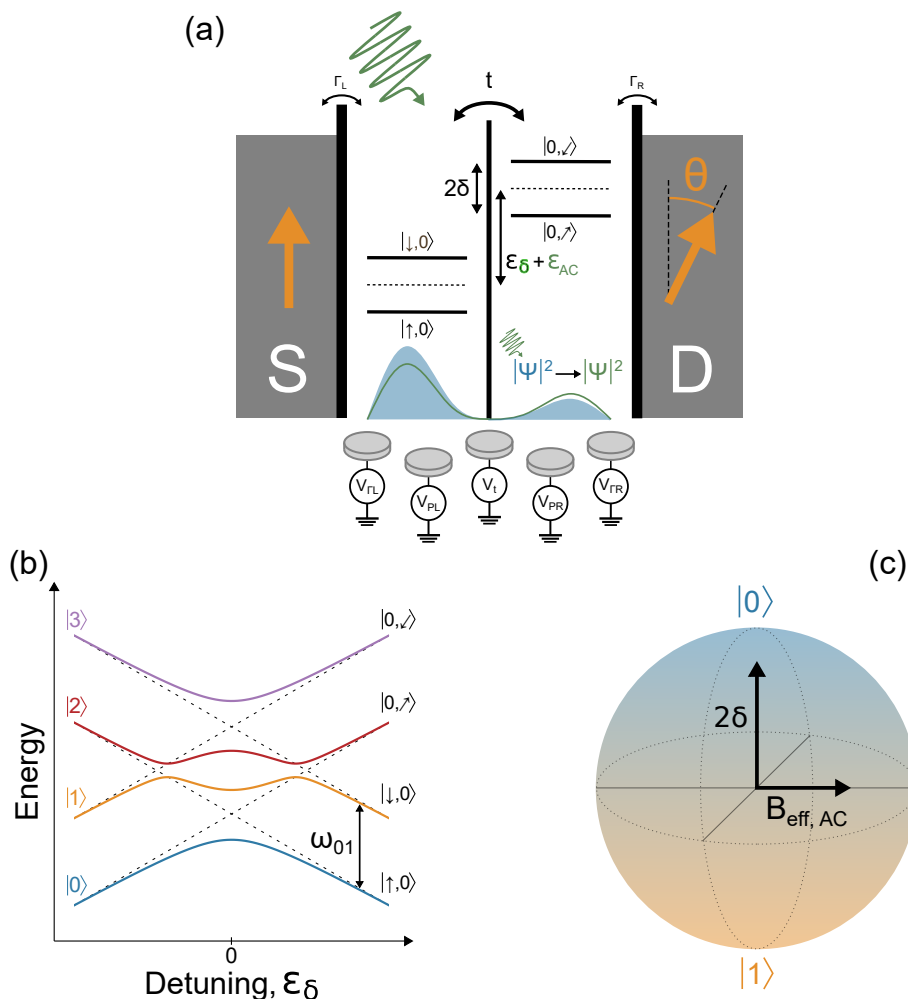


Figure 1.12: **Ferromagnetic spin qubit in a double quantum dot:** (a) Schematic of the DQD in the closed regime with one electron. The ferromagnetic contacts lift the spin degeneracy by  $2\delta$ . The non-collinear electrode magnetization sets two different spin quantization axis in the two dots resulting in an artificial spin-orbit coupling which enables a spin-photon coupling. Modifying the detuning  $\epsilon_\delta$  changes the orbital part of the wave function and therefore also the spin part. (b) Ideal energy spectrum of the ferromagnetic spin qubit as function of the detuning. The spin-charge hybridization is maximum at  $\epsilon_\delta = 0$ . At reasonably high detuning, the 01 transition is mostly spin like and still coupled to the cavity: a possible qubit working point. (c) Bloch sphere representation of the qubit encoded in the  $|0\rangle$  and  $|1\rangle$  states of the energy spectrum. Qubit manipulation can be performed with a modulation of the detuning at the qubit frequency. It indeed modifies the wavefunction overlap over the two dots resulting in an AC transverse component of the effective magnetic field.

### 1.3.3 Various architectures enabling spin-photon coupling

One of the main motivations of the ferromagnetic spin qubit is its compatibility with the cQED toolbox. Nevertheless, this is not the only implementation enabling a spin-photon

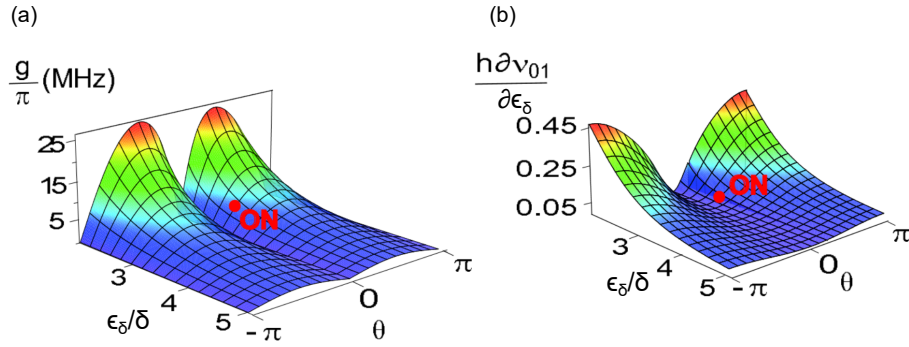


Figure 1.13: **Trade-off between spin-photon coupling and charge noise:** (a) Spin-photon coupling as a function of the angle and the detuning. The maximum value is obtained for  $\theta = \pm\pi/2$  and  $\epsilon_\delta = 0$ . The spin-photon coupling decreases drastically with the detuning and is suppressed for  $\theta = 0$ . (b) Charge noise of the 01 transition captured by the partial derivative of transition frequency with respect to the detuning which decreases with  $\theta$  and  $\epsilon_\delta/\delta$ . A sweet spot is found at  $\epsilon_\delta = 2.8\delta$  and  $\theta = \pi/6$  [7].

coupling. The latter have first been realized to overcome the issues of ESR for qubit manipulation by implementing EDSR [153]. The main options consist in using a magnetic field gradient, the intrinsic spin-orbit coupling or multiple spin states.

### Micromagnet

The magnetic field gradient generated by Co micromagnets in the presence of external magnetic field hybridizes the spin and orbital degree of freedom. This technique is now widespread in the spin qubit community and has notably led to high fidelities [15] and a six-qubit quantum processor [18]. In such a situation, a single electron in a double quantum dot shows an equivalent Hamiltonian to equation 1.22 which is expressed in equation 5.1. The total magnetic field can indeed be decomposed into a symmetric part that lifts the spin degeneracy and an anti-symmetric part responsible for the spin-charge hybridization. This design has led to the observation of strong spin-photon coupling in silicon [30, 31].

One major advantage of micromagnets is their reliability and the possibility to simulate the stray field of a given geometry: [154, 155]. Furthermore, it does not restrict the choice of material host. Nuclear spin free materials can thus be used. Finally, this implementation has led to the most significant results namely coupling distant spins via microwave photons [33, 156] and the realization of a two qubit iSWAP gate [35]. A drawback of the micromagnets is that it constitutes an additional element on the chip. This complicates the nanofabrication with an additional step potentially leading to misalignment. Furthermore micromagnets are an obstacle for the microwave design of the circuit. Applying external magnetic field also affects the quality factor of the microwave cavity and vortices in the superconducting film

constitute an ensemble of two level system causing decoherence. As it is, micromagnets are not compatible with the carbon nanotube integration used in this works but it could be adapted by burying them [155].

### Magnetic gates

An alternative to an additional micromagnet is to directly integrate the magnetic texture in the DC gates removing the constraint on compatibility with CNT integration. This is thus investigated as an alternative to ferromagnetic contacts. A first possibility is to rely on plunger gates stray field formed by several layers of Pt/Co. This has already been used with one and two gates [157, 158]. It relaxes the external magnetic field constraint but is very challenging in terms of nanofabrication. Such a device (SpinQMag5R) has been measured along this work but did not show any effect of the magnetic gates. The outcome was a need of 20 Pt/Co layers instead of 5 for sufficient stray field which was not considered suitable. Another possibility that is currently investigated by the C12 team is to magnetize a Co tunnel gate. As for all the other implementation, a finite external magnetic field is then required but it relaxes the constraint on nanofabrication. Both approaches are supported by micromagnetic simulations. However the Landé g-factor in carbon nanotubes varies a lot from sample to sample. This can be compensated with a very large external magnetic field ( $B_{\text{ext}} > 1\text{T}$ ) but makes the superconducting cavity inoperable. Ferromagnetic contacts can solve this issue as they provide a local and sufficiently high effective magnetic field [147, 159].

### Intrinsic spin-orbit coupling

Instead of adding magnetic elements for an artificial spin-orbit coupling, one possibility is to directly use a host material with intrinsic spin-orbit coupling. Firstly demonstrated with electrons in GaAs [13], it can also be realized in InAs [96] and InSb [160] or with holes in Si [161], Ge [98] and Ge/SiGe [17]. Such systems have been embedded in a cQED architecture: spin-photon coupling has been highlighted in an InAs nanowire [162] and the strong coupling regime bordering the ultra-strong coupling limit has been reached in a silicon MOS device [163].

Using intrinsic spin-orbit coupling simplifies the device nanofabrication but limits the choice of materials. Carbon nanotubes are not in the list but by bending the CNT, it has shown sufficiently large spin-orbit coupling to enable EDSR [42]. In those conditions, the nanotube touches the substrates bringing charge noise.

### Multiple spin states

As mentioned in section 1.3.1, a resonant exchange qubit can be coupled to cavity photons. Unlike the exchange-only spin qubit which is in the (1,1,1) charge configuration, the resonant exchange qubit states are also mixed with the (2,0,1) and (1,0,2) charge configurations leading to an electric charge dipole enabling a coupling with the cavity [164]. With this type of qubit, strong spin-photon coupling has also been demonstrated [32].

This approach differs from the other as more gates are required to form a triple quantum dot. As it does not depend on the host material it could be implemented with carbon nanotubes. Nevertheless, tuning a triple quantum dot to the desired regime would be challenging. Recent results have similarly shown the strong spin-photon coupling within the framework of a singlet-triplet spin qubit [165].

## Chapter 2

# Addressing individual hybrid quantum systems with mesoscopic QED

Cavity quantum electrodynamics has enabled the study of light-matter interaction at the most elementary level. Pioneer experiments have been realized with Rydberg atoms and microwave photons of a superconducting cavity [23]. These experiments have also proved to be important for quantum computation perspectives. Basic concepts have indeed been demonstrated such as the deterministic entanglement of atoms and the realization of quantum gates using atoms and photons as quantum bits. Subsequently, this has given rise to the field of circuit QED (cQED) where a superconducting circuit encoding a qubit is coupled to an on-chip microwave cavity [4, 141].

Circuit QED is particularly appealing for quantum computing perspectives for several reasons. As superconducting microwave cavities constitute a high quality bandpass filter, they can enhance qubit lifetime with strong inhibition of spontaneous emission [166]. The resonance frequency of those cavities are in the GHz range: similar to the what can be set for the qubit. They provide a sensitive readout whose speed notably depends on their quality factor. Finally the cQED architecture is scalable: it provides high fidelity QND measurements of multiple qubits [167, 168] and enables entanglement of qubits separated by macroscopic distances [24, 25]. A crucial result towards this implementation is to achieve the strong coupling regime between the qubit and the cavity [4].

One can envision to replace the superconducting circuit of a cQED architecture by any hybrid quantum circuit that interacts with microwave photons giving rise to mesoscopic QED [169, 170]. Cavity photons can thus be used both in the artificial atom limit for quantum information perspectives and in the open system limit to study electronic transport [61] or condensed matter phenomena [157, 158]. This work focuses on the artificial atom limit where the on-chip microwave cavity is coupled to a ferromagnetic spin qubit [7] (see section 1.3.2). As the spin shows very weak coupling to the cavity magnetic field ( $g \approx 10$  Hz [143]), it is hybridized with the charge degree of freedom. Interdot transitions in a double quantum dot circuit can indeed be coupled to the cavity electric field [28, 29] up to enter the strong coupling regime [146, 171, 172]. Photon-mediated interaction between distant quantum dots has also been highlighted [173, 174]. The same key results have been obtained afterwards with the implementation of artificial spin-orbit coupling namely the spin-photon coupling [151, 162], the strong coupling regime [30–32] and the distant coupling [33, 156].

This chapter focuses on the charge-photon coupling which enables the spin-photon coupling through the spin-charge hybridization already discussed previously. The first part focuses on what physically enables the coupling between cavity photons and an atom, a superconducting circuit or a quantum dot circuit. The second part describes the consequences of this coupling

on the system and how to take advantage of this for quantum computing perspectives. Finally, the last part introduces the ingredient bridging the classical and the quantum world to enable readout of the qubit state: the transmission line.

## 2.1 Coupling quantum dot circuits to a microwave cavity

Coupling a quantum dot circuit to a microwave cavity is not trivial. Adding electric connections for contacts and gate electrodes is done at the cost of ground plane continuity which affects the cavity quality factor. It also provides a channel for photons to leak out from the cavity. The chip should therefore be designed carefully to prevent these issues as much as possible. This technical aspects will be discussed in chapter 4 to focus here on the physical description of the coupling.

### 2.1.1 From cavity QED to mesoscopic QED

Cavity QED studies the interaction between electrons in the atomic orbitals of a flying atom and the photons trapped inside superconducting mirror cavity (figure 2.1.a). One focuses thus on the coherent cavity electric field which can be considered constant in the region of the atom: this is the electric-dipole approximation. In those conditions, the light-matter interaction reads:  $\hat{H}_{\text{int}} = -\vec{E}_0 \cdot \vec{d}$  where  $\vec{E}_0$  is the constant quantized electric field of the cavity in the region of the atom and  $\vec{d}$  is the atomic electric dipole.

In circuit QED, the different ingredients are transferred on a chip to form a solid-state physics device. The atom is replaced by a superconducting circuit which can encode a qubit [21, 22] and the mirror cavity by a superconducting coplanar waveguide (CPW) resonator [175, 176]. The superconducting circuit is placed close to the central conductor of the CPW resonator which has ground planes on both sides (figure 2.1.b). With the superconducting circuit, it is not question anymore of the orbital degree of freedom as the rigidity of the superconducting phase makes macroscopic collective degree of freedom dominant. Furthermore the superconducting circuit influences a lot the electric field distribution which is thus not constant around it. It is localized in areas where metallic elements are highly capacitively coupled. A physical description of circuit QED is then provided by an equivalent lumped element circuit with constant electric field at its nodes.

Mesoscopic QED focuses on any hybrid quantum circuit coupled to a microwave cavity. One can implement various types of nanoconductors such as 2DEG [29], nanowires [162] or carbon nanotubes [28] and the contacts electrodes can be made of normal, superconducting [146] or ferromagnetic [151] metal. Mesoscopic QED figures in between the cavity and circuit QED

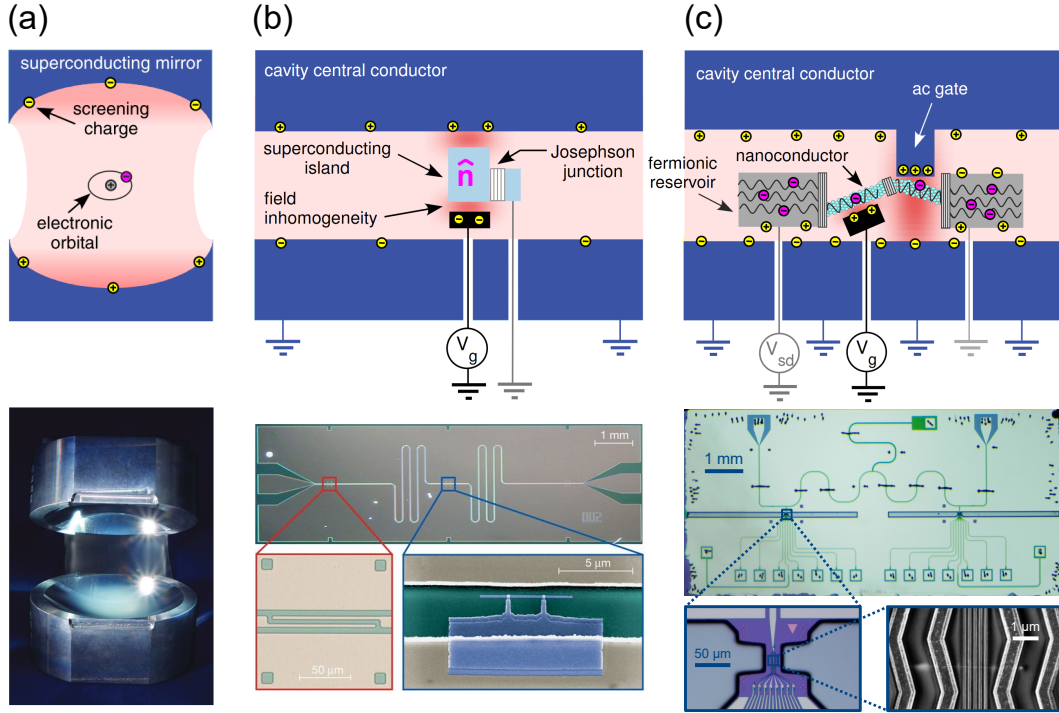


Figure 2.1: **Schematic of different quantum systems coupled to cavity photons:** (a) Cavity QED: an atom in a superconducting mirror cavity stands in a constant photonic field. (b) Circuit QED: a superconducting circuit is placed close to the cavity central conductor. The cavity electric field concentrates between metallic elements highly capacitively coupled (c) Mesoscopic QED: the cavity electric field is brought to the circuit with an AC gate. Sources: [4, 170, 179]

cases. On the one hand, quantum dots energy spectrum is indeed influenced by the quantization of the orbital levels. On the other hand the quantum dots electrostatic environment modifies drastically the electric field. An equivalent lumped element circuit can be derived in the case of a cavity resonance frequency much smaller than all characteristic frequencies of the QD [177, 178]. The cavity electric field can nevertheless not be described in this low frequency picture.

## 2.1.2 Microscopic description

### General case

In order to describe the electric field of the microwave cavity in the presence of a quantum dot circuit, the Hodge decomposition can be used [170, 180]. The electric field is then separated into a transverse part  $\vec{E}_\perp(\vec{r}, t)$  that has no divergence, a longitudinal part  $\vec{E}_\parallel(\vec{r}, t)$  that has no rotational and a harmonic part  $\vec{E}_{\text{harm}}(\vec{r})$  that has none:  $\vec{E}(\vec{r}, t) = \vec{E}_\perp(\vec{r}, t) + \vec{E}_\parallel(\vec{r}, t) + \vec{E}_{\text{harm}}(\vec{r})$ .  $\vec{E}_\perp(\vec{r}, t)$  corresponds to the photonic mode,  $\vec{E}_\parallel(\vec{r}, t)$  is set by the charge

distribution in the nanoconductor and  $\vec{E}_{\text{harm}}(\vec{r})$  is set by the boundary conditions on the conductors including plasmonic modes.  $\vec{E}_{\perp}(\vec{r}, t)$  is therefore the part of the electric field that can be quantized. With a similar quantization approach than in cavity QED and by neglecting the magnetic effects of photons, the coupling part of the mesoscopic QED Hamiltonian [170] reads :

$$H_{\text{int}} = -e \int dr^3 V_{\perp}(\vec{r}) \hat{\psi}^{\dagger}(\vec{r}) \hat{\psi}(\vec{r}) (\hat{a} + \hat{a}^{\dagger}) \quad (2.1)$$

where  $\hat{\psi}^{\dagger}(\vec{r}) / \hat{\psi}(\vec{r})$  is the field operator associated to the creation/annihilation of an electron in the nanoconductor,  $\hat{a}^{\dagger} / \hat{a}$  is creation/annihilation operator of a photon in the cavity and  $V_{\perp}(\vec{r})$  is the photonic pseudo-potential. The latter can describe both the cavity QED boundary case where the dipolar electric approximation gives:  $V_{\perp}(\vec{r}) = \vec{E}_0 \cdot \vec{r}$  and the circuit QED boundary case where the photonic potential is constant at each node of the equivalent electrical circuit. Coupling a quantum dot circuit to microwave cavity is therefore possible if the photonic pseudo-potential felt by the conduction electrons in the nanoconductor is non zero. Concretely this can be achieved with an AC gate directly connected or highly capacitively coupled to the central conductor of the CPW microwave cavity which is brought close enough to the nanoconductor.

### Tunneling process in quantum dots circuits

Equation 2.1 describes the general case of the electron-photon coupling in mesoscopic QED. Sections 1.1.2 and 1.2 have shown how important tunneling events are in the physics of quantum dot circuits. Hamiltonian 2.1 can therefore be expressed differently in order to highlight tunneling processes. To do so, the field operator can be linked to the different orbital levels:  $\hat{\psi}^{(\dagger)}(\vec{r}) = \varphi_n^{(*)}(\vec{r}) \hat{c}_n^{(\dagger)}$ , where  $\hat{c}_n^{\dagger} / \hat{c}_n$  is the creation/annihilation operator of an electron in orbital n with associated energy  $\epsilon_n$ . With this consideration, Hamiltonian 2.1 can be re-expressed as follows:

$$\tilde{H}_{\text{int}} = \left( \sum_n g_n \hat{c}_n^{\dagger} \hat{c}_n + \sum_{n \neq n'} (\gamma_{n,n'} \hat{c}_{n'}^{\dagger} \hat{c}_n + h.c.) \right) (\hat{a} + \hat{a}^{\dagger}) \quad (2.2)$$

with:

$$g_n = -e \int dr^3 V_{\perp}(\vec{r}) |\hat{\varphi}_n(\vec{r})|^2 \quad (2.3)$$

$$\gamma_{n,n'} = -e \int dr^3 V_{\perp}(\vec{r}) \hat{\varphi}_n^*(\vec{r}) \hat{\varphi}_{n'}(\vec{r}) \quad (2.4)$$

The first sum of equation 2.2 describes a modification of the orbital energies through the cavity photons.  $g_n$  expression shows that the electron-photon coupling is proportional to the overlap between the pseudo-photon potential and the square modulus of the orbital wavefunction. In the case of a constant photonic potential in the vicinity of the orbital wavefunction, the coupling can be seen, as in circuit QED, as a capacitive one with the CPW central conductor. The second sum of equation 2.2 shows that cavity photons couples different orbitals together. One identifies two types of photon-induced transitions. The first one couples orbitals from the same circuit element. It is similar to orbital transitions of an atom and is thus the coupling mechanism in cavity QED. The other one couples orbitals in different circuit element such as different dots reminding photon-assisted tunneling. However in mesoscopic QED, wavefunctions of different orbitals are spatially separated resulting in weak overlap. This results in :  $\gamma_{n,n'} \ll g_n$  and one can thus only consider the first sum of equation 2.2 for the following development.

### Interdot transitions in a double quantum dot

It is now possible to focus on the artificial atom limit case which is the one of interest in this work. As explained in section 1.3.2, the use of the circuit QED toolbox with the ferromagnetic spin qubit requires to couple a charge qubit to the cavity. By considering one orbital in each of the left and right dot of the DQD as in Hamiltonian 1.7, equation 2.2 becomes:

$$\tilde{H}_{int,DQD} = (g_L \hat{n}_L + g_R \hat{n}_R)(\hat{a} + \hat{a}^\dagger) \quad (2.5)$$

where  $\hat{n}_i = \hat{c}_i^\dagger \hat{c}_i$  is the number operator with  $i = \{L, R\}$ . The eigenstates of the charge qubit are the  $|+\rangle$  and  $|-\rangle$  states (see equation 1.8). In this case, the charge-photon coupling strength  $g$  can be expressed as follows:

$$g(\hat{a} + \hat{a}^\dagger) = \langle + | \tilde{H}_{int,DQD} | - \rangle \quad (2.6)$$

and reads:

$$g = \frac{2t}{\sqrt{\epsilon_\delta^2 + 4t^2}} g_c \quad (2.7)$$

with:

$$g_c = \frac{g_L - g_R}{2} = -\frac{e}{2} \int dr^3 V_\perp(\vec{r}) (|\hat{\varphi}_L(\vec{r})|^2 - |\hat{\varphi}_R(\vec{r})|^2) \quad (2.8)$$

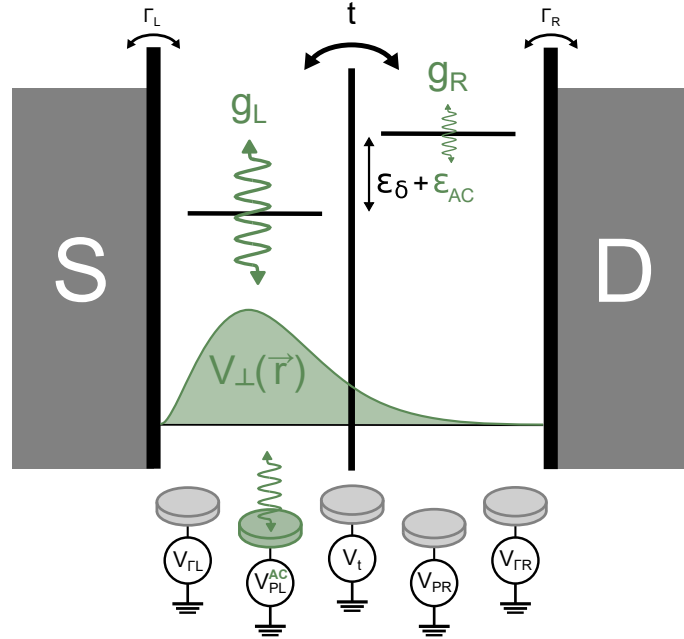


Figure 2.2: **Coupling a double quantum dot to a cavity:** The AC gate (here the plunger left) creates a strong gradient of electric potential over the two dots. One thus obtains a finite value for  $g_c$  as  $g_L \gg g_R$ . This results in a modulation of the detuning  $\epsilon_\delta$  which enables to address the interdot transition with light.

where  $g_c$  is the charge-photon bare coupling strength. The important feature to highlight is that a similar coupling between the left and right dot and the cavity ( $g_L \sim g_R$ ) does not couple the charge qubit to the cavity ( $g_c \sim 0$ ). In order to obtain a finite coupling, one dot has to be coupled to the cavity much more than the other one. This is possible if the photonic pseudo-potential  $V_\perp(\vec{r})$  varies strongly between the left and right dot as shown as in figure 2.2. Such a gradient can be obtained with an AC gate which concentrates the electric field in a very small region. One of the two plunger gates is therefore used for this purpose as it is ideally the closest to the dot. A reliable field distribution in the vicinity of the double quantum dot is however challenging to engineer. A simulation software such as Ansys HFSS could in principle handle the problem but the huge gap between characteristic scales of the device (1 mm to 100 nm) makes the simulation very tricky.

## 2.2 Hybrid light-matter system

The previous section has given insights on the physical phenomena enabling a quantum dot circuit to couple to a microwave cavity. This section focuses on the consequences of this coupling on the system and on how to take advantage of this for quantum computing perspectives.

### 2.2.1 Different coupling regimes

The quantum dot circuit considered here is a double quantum dot encoding a charge qubit. In the artificial limit, the Rabi Hamiltonian describes the light-matter interaction:

$$H_{Rabi} = \hbar\omega_c \hat{a}^\dagger \hat{a} + \frac{\hbar\omega_q}{2} \hat{\sigma}_z + \hbar g (\hat{a} + \hat{a}^\dagger) \hat{\sigma}_x \quad (2.9)$$

where  $\omega_c$  is the cavity resonance frequency and  $\omega_q$  is the qubit frequency defined in equation 1.9 for the charge qubit case. The last term describes the light matter interaction characterized by the coupling strength  $g$ . In this picture, as the coupling axis ( $\hat{\sigma}_x$ ) is orthogonal to the qubit quantization axis ( $\hat{\sigma}_z$ ), it is question of transverse coupling. This coupling scheme is widely used in circuit QED for its straightforward implementation [4] but using longitudinal coupling ( $\hat{\sigma}_z$  as coupling axis) can also be envisioned [181]. It provides a pure QND read-out and is particularly appealing for scale up perspectives [182]. One can define the raising and lowering operators acting on the qubit as:  $\hat{\sigma}_\pm = 1/2 (\hat{\sigma}_x \pm i\hat{\sigma}_y)$  and re-express equation 2.9. By assuming  $g \ll \omega_c$  and  $|\omega_c - \omega_q| \ll \omega_c + \omega_q$ , the counter rotating terms rapidly averages out and can be neglected (rotating-wave approximation). This leads to the well-known Jaynes-Cummings Hamiltonian [183]:

$$H_{JC} = \hbar\omega_c \hat{a}^\dagger \hat{a} + \frac{\hbar\omega_q}{2} \hat{\sigma}_z + \hbar g (\hat{a} \hat{\sigma}_+ + \hat{a}^\dagger \hat{\sigma}_-) \quad (2.10)$$

The last term describes the coherent exchange of a single quantum between light and matter resulting in vacuum Rabi oscillations. In absence of the coupling  $g$ , the qubit-photon states are labeled  $|\sigma, n\rangle$ , where  $\sigma = \{g, e\}$  for the ground or excited qubit state and  $n$  the photon number in the cavity. With a finite coupling  $g$ , the two systems hybridize and a diagonalization of the Jaynes-Cummings Hamiltonian leads the ground state  $|g, 0\rangle$  and the excited dressed states:

$$|+, n\rangle = \cos(\theta_n) |e, n\rangle + \sin(\theta_n) |g, n+1\rangle \quad (2.11)$$

$$|-, n\rangle = -\sin(\theta_n) |e, n\rangle + \cos(\theta_n) |g, n+1\rangle \quad (2.12)$$

with:

$$\tan(2\theta_n) = \frac{2g\sqrt{n+1}}{\Delta_{qc}} \quad (2.13)$$

where  $\Delta_{qc} = \omega_q - \omega_c$  is the qubit-cavity detuning.

In the resonant regime:  $|\Delta_{qc}| \ll g$ , light and matter are maximally hybridized. The energy

spectrum forms the Jaynes-Cummings ladder that scales non-linearly. The dressed states are indeed separated in energy by  $2g\sqrt{n+1}$ : this is the vacuum Rabi splitting. To observe this splitting experimentally, being in the resonant regime is not sufficient. The coupling to the environment has indeed not been taken into account yet. A more realistic model considers that photons leak out from the cavity and that the qubit decoheres. Those effects are quantified respectively by  $\kappa$  which defines the cavity quality factor as:  $Q = \omega_c/\kappa$  and by the decoherence rate  $\Gamma_2$ . This results in spectroscopic peaks of linewidth  $(\kappa + \Gamma_2)/2$  which are then not distinguishable until  $g > \kappa, \Gamma_2$ . Such a regime where the coupling strength overwhelms the qubit and cavity decay rates is called the strong-coupling regime. This was achieved with various qubits encoding [4, 31, 171] and is crucial for quantum computing perspectives. Vacuum Rabi oscillations which capture the coherent qubit-photon exchange present a dynamic with frequency  $2g$  for the first doublet. This has thus to be faster than the decay rates to perform notably quantum states transfer [25].

In the dispersive regime:  $|\Delta_{qc}| \gg g$ , the two systems are weakly entangled. The coherent exchange of quanta is not resonant and is only allowed via virtual photon processes. A good description of this regime can be obtained by applying the unitary transformation  $U = e^X$ , with  $X = g/\Delta_{qc} (\hat{a}\hat{\sigma}_+ - \hat{a}^\dagger\hat{\sigma}_-)$  to the Jaynes-Cummings Hamiltonian 2.10 with the Baker-Campbell-Hausdorff formula up to the second order<sup>1</sup> [181]:

$$H_{JC}^{disp} = UH_{JC}U^\dagger \approx \hbar(\omega_c + \chi_{disp}\hat{\sigma}_z)\hat{a}^\dagger\hat{a} + \frac{\hbar}{2}(\omega_q + \chi_{disp})\hat{\sigma}_z \quad (2.14)$$

This expression highlights a change of the cavity resonance frequency by a quantity depending on the qubit state:  $\Delta\omega_c = \chi_{disp}\langle\hat{\sigma}_z\rangle$ , where  $\chi_{disp} = \frac{g^2}{\Delta_{qc}}$  is the dispersive charge susceptibility. This regime can then be used to readout the qubit state through a cavity transmission measurement (see section 2.3.2). Moreover, this readout is almost QND as the approximation of  $H_{disp}$  (equation 2.14) commutes with the observable that is measured:  $\hat{\sigma}_z$ .

Alternatively, equation 2.14 can be re-arranged to exhibit the reciprocal effect:

$$H_{JC}^{disp} \approx \frac{\hbar}{2}\left(\omega_q + 2\chi_{disp}\left(\hat{a}^\dagger\hat{a} + \frac{1}{2}\right)\right)\hat{\sigma}_z + \hbar\omega_c\hat{a}^\dagger\hat{a} \quad (2.15)$$

The qubit frequency is then modified by a quantity depending on the number of photons in the cavity  $n = \langle\hat{a}^\dagger\hat{a}\rangle$ :  $\Delta\omega_q = 2\chi_{disp}n$ . This is the AC-Stark shift [184] (see figure 2.4) coming with a Lamb shift corresponding to the factor 1/2.

---

<sup>1</sup> $UHU^\dagger = H + [X, H] + \frac{1}{2!}[X, [X, H]] + \dots$



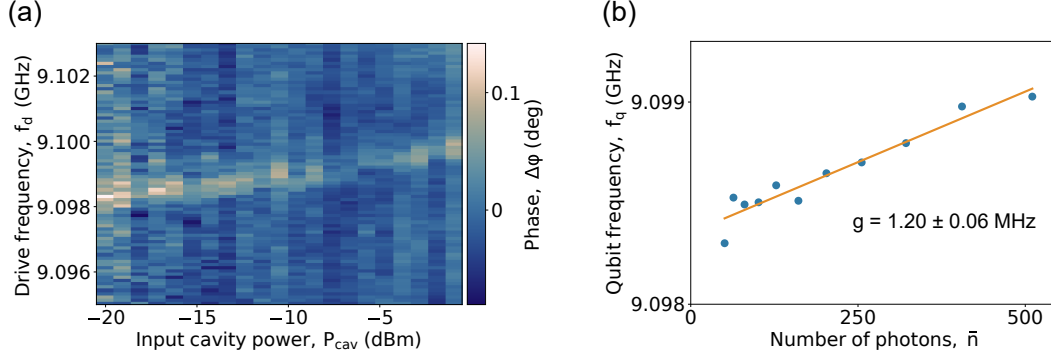


Figure 2.4: **AC-stark shift:** (a) Two-tone spectroscopy as a function of the power sent into the cavity  $P_{\text{cav}}$ . It reveals the qubit frequency which is proportional to the number of photons in the cavity  $\bar{n}$  (b) Formula 2.33 enables to convert  $P_{\text{cav}}$  into the number of photons inside the cavity  $\bar{n}$ . The slope is then  $\Delta\omega_q = 2\chi_{\text{disp}}\bar{n}$ . As the cavity and qubit frequencies are known ( $f_c = 7.031$  GHz and  $f_q \simeq 9.098$  GHz), the coupling strength can be extracted (here  $g = g_c$  as  $\epsilon_\delta = 0$ ). The fit is done with  $P_{\text{cav}} \in [-20.5, -10.5]$  dBm. (device W11-A)

so that the direct qubit-qubit exchange interaction is ignored. Such a system is described by the Tavis-Cummings model with the associated Hamiltonian [183]:

$$H_{TC} = \hbar\omega_c \hat{a}^\dagger \hat{a} + \sum_{i=\{1,2\}} \frac{\hbar\omega_{q_i}}{2} \hat{\sigma}_{z_i} + \hbar g_i (\hat{a} \hat{\sigma}_{+i} + \hat{a}^\dagger \hat{\sigma}_{-i}) \quad (2.16)$$

It is thus possible to swap the quantum state of the qubit 1 to qubit 2. To do so, the first qubit is tuned on resonance with the cavity for half a vacuum Rabi oscillation cycle in order to transfer the qubit state to the resonator. Qubit 1 is then set off resonance and qubit 2 on resonance to enable the coherent exchange. The cavity plays therefore the role of a quantum bus [25]. However, this sequence is not an entangling two-qubit gate.

To remedy this, a possibility is to work in the dispersive regime with both qubits:  $|\Delta_{q_i c}| \gg g_i$  by only virtually populating the resonator. Similarly to the one qubit case, it is possible to obtain an effective expression for Hamiltonian 2.16, considering here the unitary transformation  $U = e^X$ , with  $X = \sum_i g_i / \Delta_{q_i c} (\hat{a} \hat{\sigma}_{+i} - \hat{a}^\dagger \hat{\sigma}_{-i})$ :

$$H_{TC}^{\text{disp}} \approx \hbar \left( \omega_c + \sum_{i=\{1,2\}} \chi_{\text{disp}_i} \hat{\sigma}_{z_i} \right) \hat{a}^\dagger \hat{a} + \sum_{i=\{1,2\}} \frac{\hbar\omega_{q_i}}{2} \hat{\sigma}_{z_i} + \hbar J (\hat{\sigma}_{-1} \hat{\sigma}_{+2} + \hat{\sigma}_{-2} \hat{\sigma}_{+1}) \quad (2.17)$$

with:

$$J = \frac{g_1 g_2}{2} \left( \frac{1}{\Delta_{q_1 c}} + \frac{1}{\Delta_{q_2 c}} \right) \quad (2.18)$$

where  $\chi_{\text{disp}_i} = \frac{g_i^2}{\Delta_{q_i c}}$  is the dispersive charge susceptibility associated to qubit<sub>*i*</sub> and  $\Delta_{q_i c} = \omega_{q_i} - \omega_c$  is the qubit<sub>*i*</sub> – cavity detuning. The first term of equation 2.17 shows that a dispersive readout of both qubits through the same cavity is possible. The last term describes an exchange interaction of strength *J* between the two qubits. When the two qubits are resonant with each other:  $|\omega_{q_1} - \omega_{q_2}| \ll J$ , an excitation in qubit 1 can be transferred to qubit 2 by virtually becoming a photon. This enables the implementation of the  $\sqrt{\text{iSWAP}}$  gate which is universal.

### 2.2.3 Qubit manipulation

With this hybridized light-matter system, one can envision quantum manipulation of the qubit. To do so, a coherent drive tone of time dependent amplitude  $\varepsilon_d(t)$ , of frequency  $\omega_d$  and of phase  $\phi_d$  can be applied to the cavity. It can be modeled by the following Hamiltonian:

$$H_{\text{drive}} = \hbar\varepsilon_d(t)(a^\dagger e^{-i(\omega_d t + \phi_d)} + a e^{i(\omega_d t + \phi_d)}) \quad (2.19)$$

The system is now described by:  $H = H_{\text{JC}} + H_{\text{drive}}$  (equations 2.10 and 2.19). The same unitary transformation that leads to equation 2.14 and 2.15 can be used. In the rotating frame at the frequency  $\omega_d$ , it leads to the effective one-qubit gate Hamiltonian:

$$H_{1q} = \frac{\hbar\delta}{2}\hat{\sigma}_z + \hbar\frac{g\varepsilon_d(t)}{\Delta_{qc}}(\cos(\phi_d)\hat{\sigma}_x + \sin(\phi_d)\hat{\sigma}_y) + \hbar(\omega_c - \omega_d)\hat{a}^\dagger\hat{a} \quad (2.20)$$

where  $\delta = \omega_q + 2\chi_{\text{disp}}(\hat{a}^\dagger\hat{a} + \frac{1}{2}) - \omega_d$ . If  $\delta = 0$ , it enables qubit rotations around the x axis ( $\phi_d = 0$ ) or y axis ( $\phi_d = \pi/2$ ) (figure 2.5) at a frequency  $\Omega_R = g\varepsilon_d/\Delta_{qc}$  called the Rabi frequency. A high coupling strength *g* and a weak dispersive regime then help to obtain high fidelities for the one qubit gate. Moreover, the Rabi frequency can be controlled with the amplitude of the drive tone  $\varepsilon_d(t)$  with a linear scaling. Fast manipulation can also be implemented by applying the driving tone through a fast line instead of the cavity to get rid of the denominator term  $\Delta_{qc}$  in the Rabi frequency expression.

## 2.3 Measuring with a microwave cavity

The previous section described the light-matter system with the Jaynes-Cummings Hamiltonian (equation 2.10). However, from an experimental point of view, one needs to access the system state. A possibility is to couple the cavity to a transmission line which can be measured. One focuses then on how the transmission is modified with the presence of a quantum dot circuit or more specifically of the qubit.

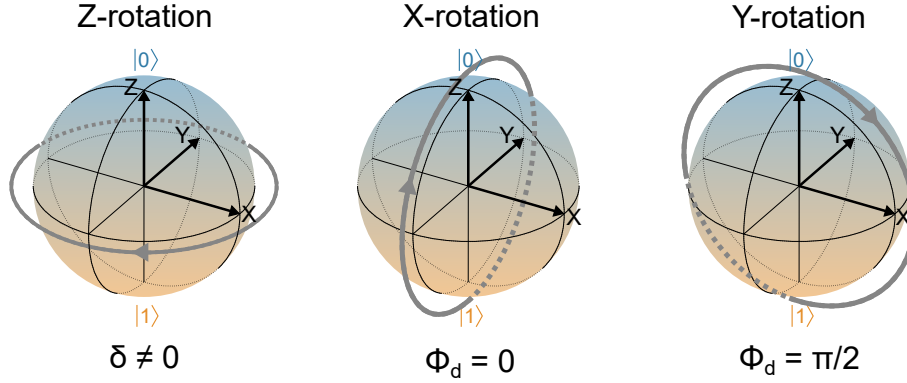


Figure 2.5: **One-qubit gate:** Any rotation on the Bloch sphere can be performed with a specific driving field

### 2.3.1 Input-output theory

From now on, the microwave cavity is considered coupled to a transmission line and thus to the environment. The cavity transmission can be derived from an equivalent lumped element circuit with scattering theory [177,178] however this does not give access to the whole dynamic of the system. This is why one introduces here the quantum version of the scattering theory: the input-output theory [185]. The system can be described with the internal cavity mode  $\hat{a}$  and the external bath modes  $\hat{b}$  (see figure 2.6.a). For a high Q cavity the system can be described with the following Hamiltonian:

$$H_{sys} = H_{cav} + H_{bath} + H_{cav-bath} \quad (2.21)$$

with:

$$H_{cav} = \hbar\omega_c \hat{a}^\dagger \hat{a} \quad (2.22)$$

$$H_{bath} = \sum_{k,i} \hbar\omega_k \hat{b}_{k,i}^\dagger \hat{b}_{k,i} \quad (2.23)$$

$$H_{cav-bath} = -i\hbar \sum_{k,i} f_{k,i} \hat{a}^\dagger \hat{b}_{k,i} - f_{k,i}^* \hat{a} \hat{b}_{k,i}^\dagger \quad (2.24)$$

where  $\hat{b}_{k,i}^\dagger / \hat{b}_{k,i}$  creates/annihilates a photon in mode  $k$  of frequency  $\omega_k$  in bath  $i = \{1, 2, L\}$ .  $H_{cav}$  describes the cavity as a harmonic oscillator and  $H_{bath}$  the external bath modes.  $H_{cav-bath}$  represents the interaction between the two systems within the rotating-wave approximation. A photon in bath  $i$  and mode  $k$  can be converted into a cavity photon with transition am-

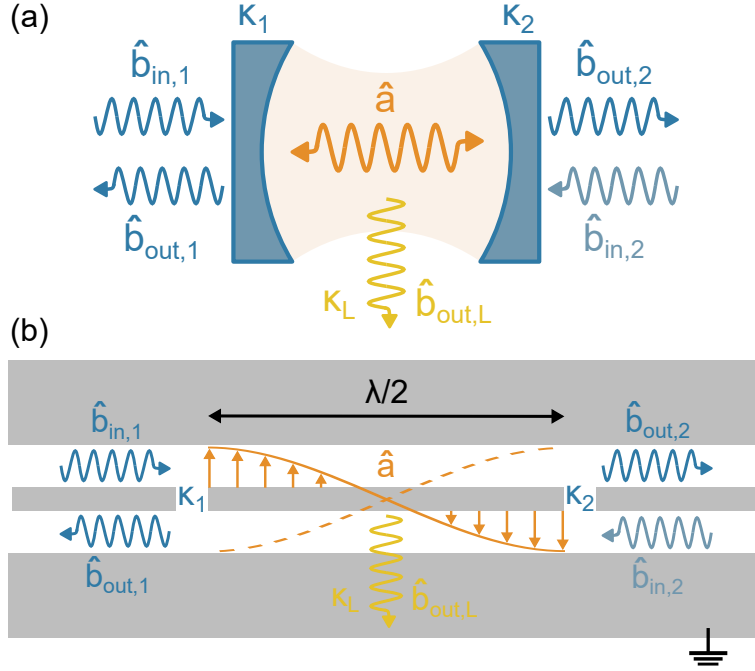


Figure 2.6: **Input-output formalism:** (a) A solution to probe the cavity mode  $\hat{a}$  is to send an ingoing mode  $\hat{b}_{in,1}$  on port 1 and measure the outgoing mode  $\hat{b}_{out,2}$  from port 2. One performs then a transmission measurement of the cavity. Each port is characterized by a coupling  $\kappa_i$ .  $\kappa_L$  describes the internal losses. (b) Schematic of a necklace-type  $\lambda/2$  resonator. The cavity is an open-circuited  $\lambda/2$  coupled to two baths at the two ends which are transmission-line waveguides.

plitude  $f_{k,i}$  and vice-versa. The goal is now to define as shown as in figure 2.6 an input and output mode to express the cavity transmission. To do so, one can derive the Heisenberg equation of motion of each operator:

$$\frac{d}{dt}\hat{a}(t) = \frac{i}{\hbar}[H_{sys}, \hat{a}] = -i\omega_c\hat{a}(t) - \sum_{k,i} f_{k,i}\hat{b}_{k,i}(t) \quad (2.25)$$

$$\frac{d}{dt}\hat{b}_{k,i}(t) = \frac{i}{\hbar}[H_{sys}, \hat{b}_{k,i}] = -i\omega_k\hat{b}_{k,i}(t) + f_{k,i}^*\hat{a}(t) \quad (2.26)$$

In order to solve equation 2.26, one introduces the time  $t_0 < t$  associated to well-known initial conditions. The solution then reads:

$$\hat{b}_{k,i}(t) = e^{-i\omega_k(t-t_0)}\hat{b}_{k,i}(t_0) + \int_{t_0}^t d\tau e^{-i\omega_k(t-\tau)} f_{k,i}^*\hat{a}(\tau) \quad (2.27)$$

By considering  $\hat{a}(\tau) \simeq e^{i\omega_c(t-\tau)}\hat{a}(t)$ , the second term of equation 2.25 can then be re-expressed as:

$$\sum_{k,i} f_{k,i} \hat{b}_{k,i}(t) = \sum_{k,i} f_{k,i} e^{-i\omega_k(t-t_0)} \hat{b}_{k,i}(t_0) + \hat{a}(t) \sum_{k,i} |f_{k,i}|^2 \int_{t_0}^t d\tau e^{-i(\omega_k - \omega_c)(t-\tau)} \quad (2.28)$$

One can consider the transition amplitude to be constant over the range of frequencies relevant to the cavity:  $f_{k,i} = f_i$  (Markov approximation). This quantity can be linked to the coupling rate between a cavity photon and the bath  $i$   $\kappa_i$  as:  $\kappa_i = 2\pi|f_i|^2\rho_i$  with  $\rho_i$  the density of states for bath  $i$  considered constant. By defining the input mode on port 1 as:  $\hat{b}_{in,1}(t) \doteq \frac{1}{\sqrt{2\pi\rho_1}} \sum_k e^{-i\omega_k(t-t_0)} \hat{b}_{k,1}(t_0)$ , equation 2.25 becomes [185]:

$$\frac{d}{dt}\hat{a}(t) = -i\omega_c\hat{a}(t) - \frac{\kappa}{2}\hat{a}(t) - \sqrt{\kappa_1}\hat{b}_{in,1}(t) \quad (2.29)$$

where  $\kappa = \kappa_1 + \kappa_2 + \kappa_L$  is the cavity decay rate and  $\hat{b}_{in,1}(t)$  is the input mode corresponding to bath 1. As opposed to  $\hat{b}_{k,i}$  and  $\hat{a}$ , this input mode operator is non-dimensionless:  $\dim(\hat{b}_{in,1}(t)) = T^{1/2}$ . As one drives the cavity through port 1, one considers  $\hat{b}_{in,2}(t) = 0$ .

A similar reasoning can be done with a time  $t_1 > t$  to introduce the output mode  $\hat{b}_{out,2}(t)$ . In this work, one uses a necklace-type  $\lambda/2$  resonator (figure 2.6.b) with a  $\pi$  phase shift of the cavity mode at the two ends leading to the following input-output relations [186]:

$$\hat{b}_{out,1}(t) = \hat{b}_{in,1}(t) + \sqrt{\kappa_1}\hat{a}(t) \quad (2.30)$$

$$\hat{b}_{out,2}(t) = -\sqrt{\kappa_2}\hat{a}(t) \quad (2.31)$$

By moving this set of equation to the mean value and applying a Fourier transformation on equation 2.29, one can derive the cavity transmission:

$$T(\omega) \doteq \frac{\langle \hat{b}_{out,2}(t) \rangle}{\langle \hat{b}_{in,1}(t) \rangle} = \frac{\sqrt{\kappa_1\kappa_2}}{-i(\omega - \omega_c) + \kappa/2} \quad (2.32)$$

Unsurprisingly, the transmission has a Lorentzian shape centered on the resonance frequency  $\omega_c$ . Another quantity interesting to express is the average number of photons in the cavity  $\bar{n}$ . This value can then be determined experimentally since all the parameters on which it depends are accessible (see chapter 3). For a symmetric cavity-bath coupling ( $\kappa_1 = \kappa_2 = \kappa$ ),

it reads:

$$\bar{n} \hat{=} \langle \hat{a}^\dagger(t) \hat{a}(t) \rangle_{\omega=\omega_c} = \frac{2\sqrt{P_{in}P_{out}}}{\hbar\omega_c\kappa} \quad (2.33)$$

where  $P_{in} = \hbar\omega \langle \hat{b}_{in,1}^\dagger(t) \hat{b}_{in,1}(t) \rangle$  and  $P_{out} = \hbar\omega \langle \hat{b}_{out,2}^\dagger(t) \hat{b}_{out,2}(t) \rangle$ .

### 2.3.2 Qubit readout

#### Introducing qubit decoherence

In the previous section, one has introduced the input-output theory to derive an expression for the cavity transmission which can be measured experimentally. We have so far considered a bare cavity but the same reasoning can be done with Hamiltonian 2.10 describing a qubit coupled to a cavity. Nevertheless, the Jaynes-Cummings model describes a closed system which is not what is experimentally measured. Dissipation processes has then to be considered. It can arise from coupling with fermions in the contacts, phonon modes, fluctuators or also photonic modes of the cavity. Similarly to the cavity case (equation 2.21), the non-closed qubit system can be described by introducing a bath that couples to the qubit. The qubit can couple in two different ways with the environment. One introduces then a transverse coupling term and a longitudinal one with their associated bath. The Hamiltonian describing the qubit as an open system reads:

$$H_{open\ qubit} = \frac{\hbar\omega_q}{2} \hat{\sigma}_z + H_{bath,t} + H_{qubit-bath,t} + H_{bath,l} + H_{qubit-bath,l} \quad (2.34)$$

where:

$$H_{bath,t} = \sum_t \hbar\omega_t \hat{b}_t^\dagger \hat{b}_t \quad (2.35)$$

$$H_{qubit-bath,t} = \sum_t \hbar g_t (\hat{b}_t^\dagger \hat{\sigma}_- + \hat{b}_t \hat{\sigma}_+) \quad (2.36)$$

$$H_{bath,l} = \sum_l \hbar\omega_l \hat{d}_l^\dagger \hat{d}_l \quad (2.37)$$

$$H_{qubit-bath,l} = \sum_l \hbar g_l (\hat{d}_l^\dagger + \hat{d}_l) \hat{\sigma}_z \quad (2.38)$$

The equations of motion of the different involved operators read:

$$\frac{d}{dt}\hat{\sigma}_-(t) = -i\omega_q\hat{\sigma}_- + i\hat{\sigma}_z \sum_t g_t \hat{b}_t - 2i\hat{\sigma}_- \sum_l g_l (\hat{d}_l^\dagger + \hat{d}_l) \quad (2.39)$$

$$\frac{d}{dt}\hat{\sigma}_z(t) = 2i \sum_t g_t (\hat{b}_t^\dagger \hat{\sigma}_- - \hat{b}_t \hat{\sigma}_+) \quad (2.40)$$

$$\frac{d}{dt}\hat{b}_t(t) = -i\omega_t \hat{b}_t - ig_t \hat{\sigma}_- \quad (2.41)$$

$$\frac{d}{dt}\hat{d}_l(t) = -i\omega_l \hat{d}_l - ig_l \hat{\sigma}_z \quad (2.42)$$

As here it is question of fermions, a similar reasoning than in the previous section does not enable to demonstrate the expected results. Using density matrix theory [187], it can be shown that:

$$\frac{d}{dt}\langle\hat{\sigma}_-(t)\rangle = -(i\omega_q + \frac{\Gamma_1}{2} + \Gamma_\varphi)\langle\hat{\sigma}_-(t)\rangle \quad (2.43)$$

$$\frac{d}{dt}\langle\hat{\sigma}_z(t)\rangle = -\Gamma_1(\langle\hat{\sigma}_z(t)\rangle + \sigma_0) \quad (2.44)$$

Equation 2.43 enables then to define the qubit decoherence rate:

$$\Gamma_2 = \frac{\Gamma_1}{2} + \Gamma_\varphi \quad (2.45)$$

The decoherence rate comprises both transverse and longitudinal noise.  $\Gamma_1$  describes depolarization along the qubit quantization axis and is often seen as energy relaxation. Resonant energy exchange with the environment can indeed result in a bit flip:  $|0\rangle \leftrightarrow |1\rangle$ . Conversely,  $\Gamma_\varphi$  describes depolarization in the equatorial plane of the Bloch sphere. This results from random fluctuations of the qubit frequency  $\omega_q$ . Pure dephasing occurs with noise at any frequency.

### Cavity response

Now that the qubit-environment interaction have been introduced, the measured system can be well-described by the following Hamiltonian:

$$H_{\widetilde{sys}} = H_{JC} + H_{bath} + H_{cav-bath} + H_{bath,t} + H_{qubit-bath,t} + H_{bath,l} + H_{qubit-bath,l} \quad (2.46)$$

where  $H_{JC}$  is the Jaynes-Cummings Hamiltonian (equation 2.10) describing the closed qubit-cavity system. For each operator, a Heisenberg equation of motion can be expressed, the useful ones read:

$$\frac{d}{dt}\hat{a}(t) = \frac{i}{\hbar}[H_{\widetilde{sys}}, \hat{a}] = -i\omega_c\hat{a}(t) - ig\sigma_-(t) - \frac{\kappa}{2}\hat{a}(t) - \sqrt{\kappa_1}\hat{b}_{in,1}(t) \quad (2.47)$$

$$\frac{d}{dt}\hat{\sigma}_-(t) = \frac{i}{\hbar}[H_{\widetilde{sys}}, \hat{\sigma}_-] = -(\Gamma_2 + i\omega_q)\sigma_- + ig\sigma_z\hat{a} \quad (2.48)$$

Considering equation 2.31 and a similar approach than in section 2.3.1 give the following expression for the cavity transmission:

$$T(\omega) = \frac{\langle \hat{b}_{out,2}(t) \rangle}{\langle \hat{b}_{in,1}(t) \rangle} = \frac{\sqrt{\kappa_1\kappa_2}}{-i(\omega - \omega_c) + \kappa/2 - i\chi(\omega)\langle \sigma_z \rangle} \quad (2.49)$$

where  $\chi(\omega)$  is the charge susceptibility of the system:

$$\chi(\omega) = \frac{g^2}{\omega - \omega_q + i\Gamma_2} \quad (2.50)$$

$\omega_q = \sqrt{\epsilon_\delta^2 + 4t^2}$  is the charge qubit frequency,  $g = 2t/\omega_q \times g_c$  is the charge-photon coupling strength and  $\Gamma_2$  is the associated qubit decoherence rate arising from its coupling to the baths. The transmission of the cavity do depend on the qubit state  $\langle \sigma_z \rangle$ : one implemented thus the dispersive readout. In the closed system picture ( $\kappa = \Gamma_2 = 0$ ), one recovers the dispersive shift of the cavity frequency (see section 2.2.1). Here the cavity shift reads:  $\Delta\omega_c = \text{Re}(\chi(\omega))\langle \sigma_z \rangle$ .

To benefit its high sensitivity, the cavity is driven at its resonance frequency ( $\omega = \omega_c$ ) so that it cancels out the denominator first term of equation 2.49. The transmission is a complex quantity with a given amplitude and phase and the signals measured experimentally are the phase shift  $\Delta\varphi$  and amplitude shift  $\Delta A$  defined as follows:

$$T(\omega_c) = (A_0 + \Delta A)e^{i(\varphi_0 + \Delta\varphi)} \quad (2.51)$$

where  $A_0$  and  $\varphi_0$  are the reference amplitude and phase taken for a cavity that does not see the qubit ( $\chi(\omega) = 0$ ).  $\Delta\varphi$  captures then the dispersive shift whereas  $\Delta A$  reflects the dissipation processes and read:

$$\Delta\varphi = \frac{\Delta\omega_c}{\kappa/2} = \frac{\text{Re}(\chi(\omega))}{\kappa/2} \langle\sigma_z\rangle \quad (2.52)$$

$$\frac{\Delta A}{A_0} = \frac{\Delta(\kappa/2)}{\kappa/2} = \frac{\text{Im}(\chi(\omega))}{\kappa/2} \langle\sigma_z\rangle \quad (2.53)$$

With a simple cavity transmission measurement, the qubit remains almost in its ground state<sup>2</sup> ( $\langle\sigma_z\rangle = -1$ ). However, measuring the cavity transmission enables to find the proper working point and provides information on the qubit frequency. In the same spirit than in section 1.2.2, one can perform a stability diagram measurement by looking at the phase and amplitude of the cavity instead of the current trough the double quantum dot circuit. This should highlights the areas where interdot transitions occurs with oblique resonant lines (figure 2.7.e,f) as the coupling strength  $g$  depends on the detuning  $\epsilon_\delta$  (equation 2.7). One distinguishes two cases which reflect in the resonant lines structure. In the non-resonant case ( $2t > \omega_c$ ), the charge qubit frequency is always higher than the cavity one (figure 2.7.a). On the contrary if  $2t < \omega_c$ , the charge qubit frequency meets the cavity for two opposed detuning values (figure 2.7.b). These measurements can be useful to extract the characteristic parameters of the system: the charge qubit decoherence rate  $\Gamma_2$ , the tunnel rate  $t$  and the charge-photon bare coupling strength  $g_c$ .

### 2.3.3 Two-tone spectroscopy

The system coupled to the cavity has been considered in this part as a two-level system but several transitions can be coupled to the cavity. The measured phase includes then the effect of each transition through the sum of their associated dispersive shift. In order to address individually the different transitions, a second tone (described by Hamiltonian 2.19) can be applied. Such a system is described by the Hamiltonian:  $H_{2\text{-tone}} = H_{\text{sys}} + H_{\text{drive}}$ . Once again, the equation of motion can be derived [178]. The cavity transmission is given by equation 2.49 with the qubit state  $\langle\sigma_z\rangle$  depending on the drive frequency  $\omega_d$ :

$$\langle\sigma_z\rangle(\omega_d) = \frac{-1}{1 + \frac{4\Omega_R^2}{\Gamma_1} \frac{\Gamma_2}{\Gamma_2^2 + \delta}} \quad (2.54)$$

---

<sup>2</sup>it can start to move away from a given input power on the cavity [81]

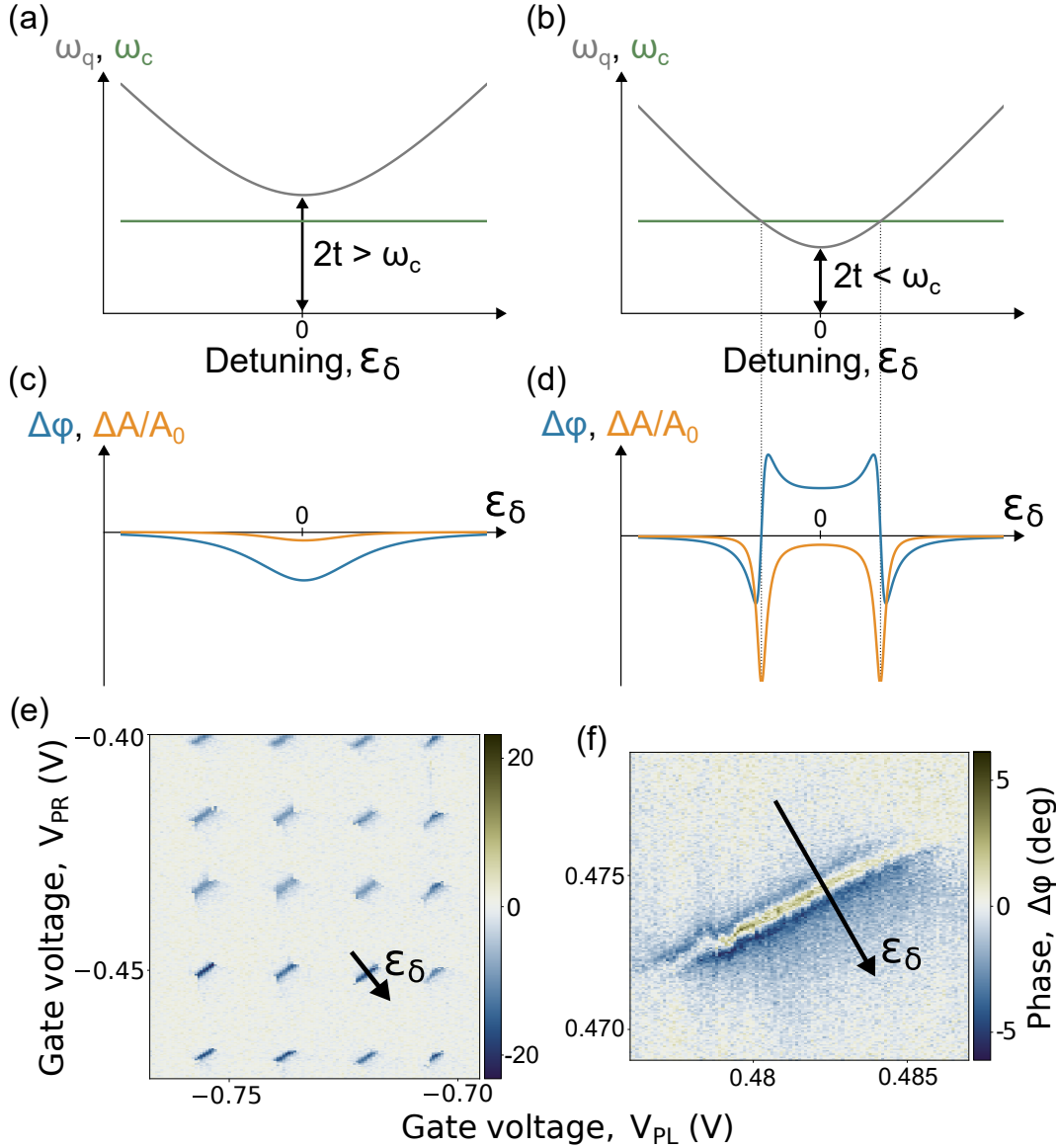


Figure 2.7: **Cavity readout** in the case where  $2t > \omega_c$  (left) and where  $2t < \omega_c$  (right): (a, b) Charge qubit and cavity energy spectrum as a function of the detuning  $\epsilon_\delta$ . (c, d) Phase and Amplitude signals around an interdot transition as a function of the detuning  $\epsilon_\delta$ . (e, f) Stability diagram measurement of the phase  $\Delta\phi$  as a function of the plunger gate voltages  $V_{PL}$  and  $V_{PR}$  revealing (an) interdot transition(s). (device Spin21Q11L)

where  $\delta = \omega_q + 2\chi_{\text{disp}}(\hat{a}^\dagger \hat{a} + \frac{1}{2}) - \omega_d$  and  $\Omega_R = g\varepsilon_d/\Delta_{qc}$  is the Rabi frequency. Measuring the cavity at  $\omega = \omega_c$  while sweeping the drive frequency  $\omega_d$  informs on the transition frequency  $\omega_q$  and on the qubit decoherence rate  $\Gamma_2$ . It indeed results in a Lorentzian centered around  $\omega_q$  of full width at half maximum:  $\Delta\omega_{\text{FWHM}} = 2\pi\Delta f_{\text{FWHM}} = 2\Gamma_2$  [111]. In practice, one observes a broadening of the peak with an increasing drive amplitude  $\varepsilon_d$  (see figure 2.8) up to  $\Delta\omega_{\text{FWHM}} = 2\sqrt{\Gamma_2^2 + \Omega_R^2\Gamma_2/\Gamma_1}$  [181]. Such a measurement constitutes a sanity check

for discriminating relevant system transitions from parasitic effects and reveals the upper bound of the decoherence rate  $\Gamma_2$ . A non ambiguous way consists in performing a Ramsey interferometry measurement from which one can extract the qubit coherence time  $T_2^* = 1/\Gamma_2$  (see chapter 5).

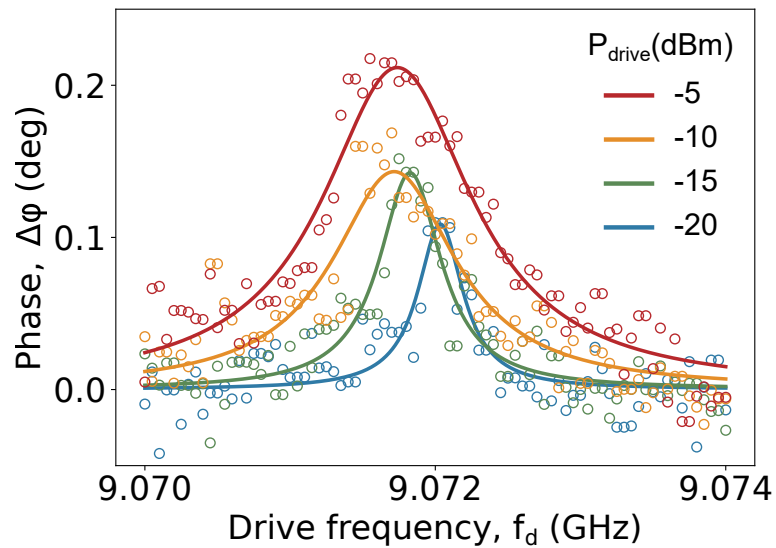


Figure 2.8: **Power broadening of the qubit line:** Two-tone spectroscopy for different powers on the drive. (device W11-A)



## Chapter 3

# Experimental methods

In order to measure the physical phenomena described in the two first chapters, there is beforehand a long journey towards the realization of a device. The goal of this chapter is to describe the different experimental methods concerning the realization of the ferromagnetic spin qubit. The first part goes through the different nanofabrication steps required to fabricate the device. The second part focuses on the carbon nanotube production and integration. Finally, the last part describes the measurement setup and techniques required to highlight the physical phenomena of interest.

## 3.1 Nanofabrication

This section presents the general idea of the chip and describes the steps and techniques involved in its fabrication. A detailed recipe is given in appendix B.

### 3.1.1 Sample fabrication overview

This journey starts in the ENS clean room where all the samples mentioned in this thesis have been fabricated. There is nevertheless a preliminary step consisting in designing the circuit chip. This is done with a package enabling to draw circuits using python: HFSSdrawpy which has been developed by the Quantic team. The design and fabrication process described here gave the results presented in chapter 5. This has however barely changed compared to previous work [188] except for the alternative strategies presented in chapter 4. Different elements are required to implement the ferromagnetic spin qubit described in section 1.3.2:

- 5 DC gates
- 2 non-collinear ferromagnetic contacts: namely source and drain
- 1 suspended carbon nanotube
- 1 microwave cavity coupled to a transmission line
- 1 AC gate connected to the cavity
- 1 fast RF gate (optional)

The 2 gates carrying a RF signal have a floating DC potential which stands in the vicinity of the double quantum dot. This constraint needs to be taken into account afterwards for the electrical tuning of the device which makes it more tricky. It indeed imposes new boundary conditions which complicates the realization of the electrostatic double potential well. Furthermore, it can lead to the formation of additional undesired dots. To remedy this,

in the design considered here (figure 3.1), the AC gate and the fast RF gate both also carry a DC potential which sets the plunger gate voltages  $V_{PL}$  and  $V_{PR}$ . The three other gates namely the tunnel one, the gamma left and the gamma right only have a DC component.

The carbon nanotube is not introduced on the chip during the nanofabrication process but transferred afterwards in a vacuum chamber [188, 189]. The growth is indeed done on a separated cantilever chip (see section 3.2). This transfer process named stapling requires two different elements added during the nanofabrication process. First, one has to dig the circuit chip to create a hosting zone for the cantilever chip containing the CNTs during the transfer: it constitutes the trenches. Then, two additional contact electrodes need to be implemented: one next to the source and one next to the drain. These are called the cut electrodes and their utility will make sense in section 3.2.2.

To fabricate this chip, one starts with a 4" diameter and 500  $\mu\text{m}$  thick undoped silicon wafer of high resistivity ( $\rho = 10 \text{ k}\Omega\cdot\text{cm}$ ) that is covered by 500 nm of silicon oxide ( $\text{SiO}_2$ ). It is diced with a circular saw into 9.9 mm  $\times$  9.9 mm square chip which can contain two devices. This step can already contaminate the chip. It is therefore important to protect the wafer beforehand with a resist that remains after this dicing procedure. Most of the following steps consist in patterning the chip with a given metal. To do so, it exists two distinct procedures:

#### **Lift-off procedure:**

A first possibility is to cover the chip with a photoresist or an electrosensitive resist. Photons or electrons are then used to pattern the chip with laser or e-beam lithography. The chip is afterwards put in an developer solution that removes the exposed (resp. unexposed) resist of the chip in case of a positive (resp. negative) resist. The laser lithography resolution is limited by the laser wavelength which enable to pattern structures down to  $\sim 2 \mu\text{m}$ . The e-beam lithography enables to go down to smaller structures ( $\sim 50 \text{ nm}$ ). In this work, only the e-beam lithography was used to standardize the process with the only use of one resist. The bigger structures of the chip are in return longer to pattern. Once we have this chip covered by a patterned resist, metal can be deposited on its whole surface in an evaporator. The last step is the lift-off which consists in removing the resist and thus the metal above in a solution. It results in a chip with a metal film where the resist was previously removed (figure 3.2.a). The drawback of this technique is an irregular shape on the side of the metallic film. Industrial processes use thus another technique.

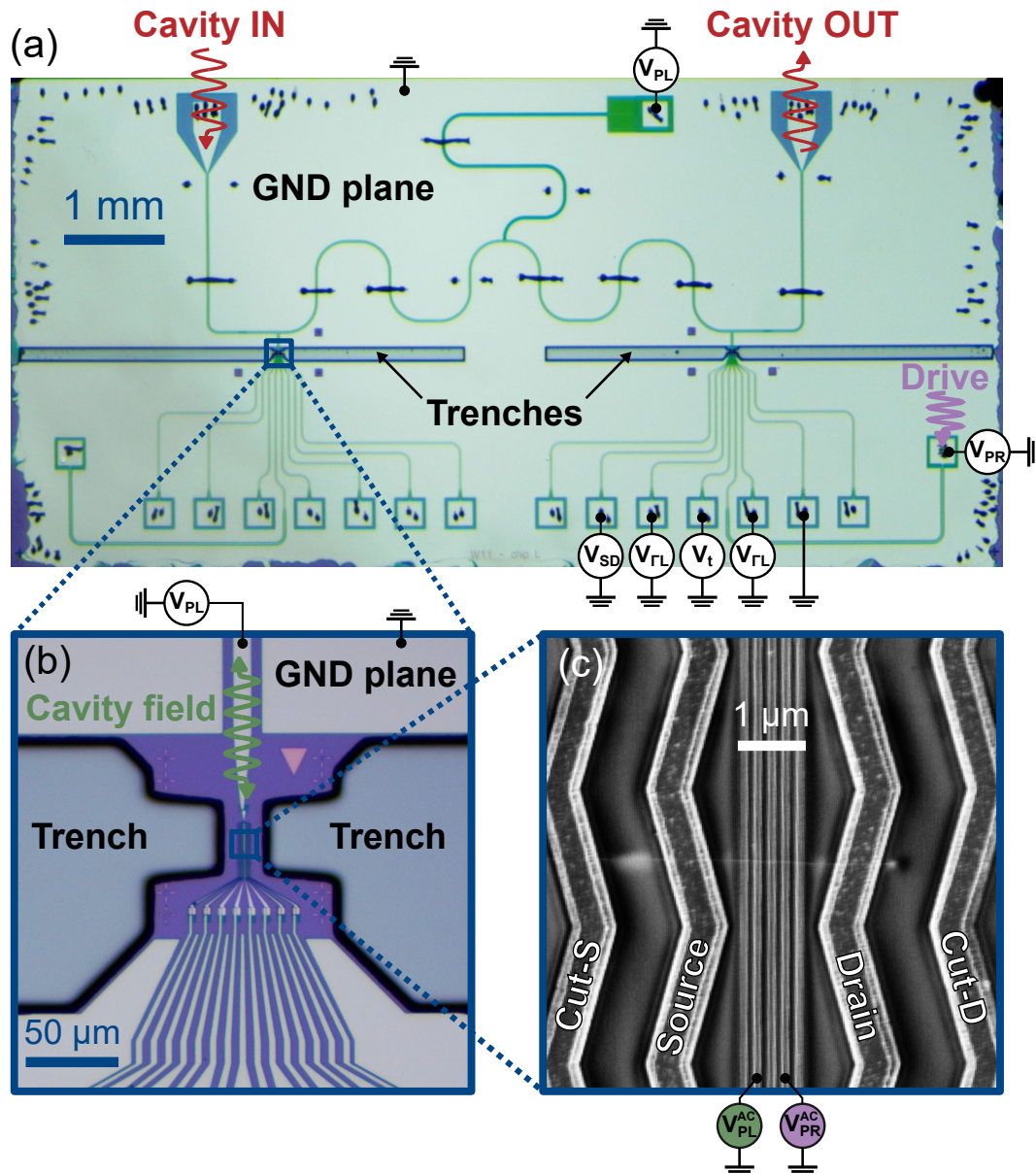


Figure 3.1: **Chip overview:** (a) Optical image of the  $5\text{ mm} \times 10\text{ mm}$  chip. Two double quantum dot circuits are implemented. They are coupled to the same microwave cavity itself coupled to a transmission line. The trenches are  $15\text{ }\mu\text{m}$  deeper than the rest of the chip to host the chip containing CNTs. The bounding pads at the edge of the chip are wire bounded to a corresponding DC or RF line on the sample holder PCB. (b) Optical image centered on the area where is transferred the CNT. The cavity central conductor sharpen towards this region to couple to the double quantum dot circuit. (c) Scanning electron microscope (SEM) image centered on a CNT contacted between the source and drain electrodes. Underneath, five DC gates shape the double quantum dot electrostatic potential: gamma left, plunger left, tunnel, plunger right and gamma right. Plunger left and right gates also carry respectively the cavity electric field (represented in green) and the driving tone (represented in violet).

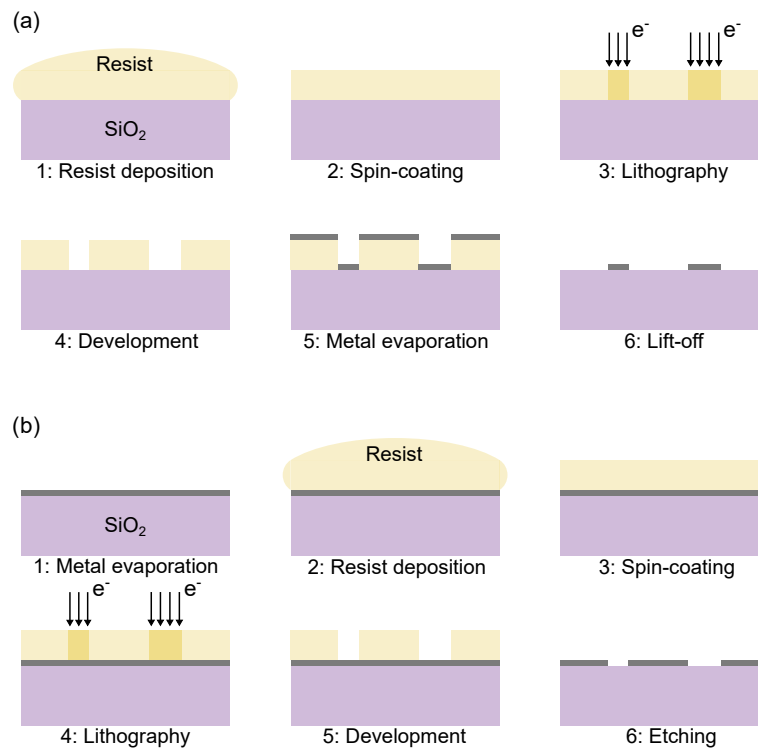


Figure 3.2: **Electronic lithography steps with a positive resist:** (a) Lift-off procedure. (b) Etching procedure

### Etching procedure:

The second possibility is to directly start with the metal evaporation. The resist is deposited afterwards and patterned similarly as in the lift-off procedure. The metal that is not protected by the resist is then removed with the etching process (figure 3.2.b). The etching can either be physical or chemical. In this work, the etching is achieved with a plasma in a reactive ion etching chamber (RIE). One critical aspect is to make sure the etching recipe does not consume the resist entirely.

### 3.1.2 Gold precontacts and alignment crosses

The previous section highlighted the need of several steps to fabricate the chip. This poses a challenge for a good electrical contact between two metallic thin films. The first one indeed oxidizes before the next one is evaporated. In our case, one evaporates the small structures (contact and gate electrodes) after the big metallic structures (cavity and electric lines) in Niobium. Having a good electrical continuity at this interface is therefore crucial to measure properly the current across the CNT, to avoid heating in the lines, to set the right DC voltage in each gate and to ensure a good coupling with the cavity field. To remedy this, we introduce

gold precontacts at this interface fabricated with a lift-off procedure. As gold does not oxidize, each of two different lines can have a good electrical contact with the gold precontact and therefore a good electrical contact between them. Gold is not a superconducting metal which is then a drawback for the precontact bridging the cavity central conductor and the AC gate. The electrical cavity field can therefore dissipate in the precontact which lower the cavity quality factor and the cavity-DQD coupling. It is thus important to make it small and thin. An alternative to the use of precontacts is to perform a gentle argon etching in the vacuum transfer airlock of the evaporator. This enables to remove the oxide of the first metal film before evaporating the other one. This solution has not been implemented in this work.

For the next lithography steps, one needs to realign with very high precision. This can be achieved by introducing alignment crosses which set global and local references. As it has to be done in the first step, they are here made of gold which make them easily distinguishable during the e-beam lithography settings.

### 3.1.3 Niobium mesoscopic QED architecture

The design of the cavity is quite standard and is greatly inspired from what have been developed in the circuit QED community [175]. The length of the central conductor  $L = \lambda/2$  should be designed for a fundamental mode in a range of frequencies suitable with the different RF components (4-8 GHz). In this design,  $L \simeq 8.46$  mm corresponds to a measured resonance frequency  $f_c = 6.975$  GHz. The impedance of the CPW lines should match the one of the RF sources and cables ( $Z_0 = 50 \Omega$ ) to avoid unwanted reflections. A track width  $w = 10.2 \mu\text{m}$  and a gap width  $s = 5.17 \mu\text{m}$  satisfy this constraint.

The specificity of the mesoscopic QED architecture is the need of both DC and RF signals in the qubit location. There is thus an undesired coupling to handle between the cavity and the DC electrodes which lower considerably its quality factor  $Q$ . This is even more problematic for the cavity which is DC biased to avoid floating potentials in the DQD region. To avoid leakage of the cavity electric field through its connected DC line several strategies are implemented. First, the DC line is connected at the node of the cavity mode where the electric field is minimum. It is designed with a different impedance ( $Z \simeq 80 \Omega$ ) than the cavity and a corresponding length  $\lambda/4$  to minimize the transmission through this line [190]. Finally, an interdigitated low pass filter is added at the end of the line. This filter could be added to all DC lines. High quality factor have been reached with this design:  $Q=5150$ . The fast RF line also shares DC signal but is less tricky to implement as parasitic leakage can be to some extent compensated with the input power of the RF source.

For this nanofabrication step, as nearly the whole chip surface ends up covered by superconducting metal, it is convenient to use an etching procedure. It also provides smoother edges than lift-off which contributes to low internal losses for the cavity. For this design, one works with niobium: a material that has already proved itself to achieve coupling hybrid systems to a microwave cavity [4, 28, 151, 171]. It has a high superconducting critical temperature ( $T_c \sim 9$  K) and is relatively resilient to in plane magnetic field. However in the recent years, the widely used niobium have have started to be replaced by disordered superconducting materials. The motivations of their use will be discussed in chapter 4. The 100 nm thick niobium film is deposited on the chip surface in a ultra high vacuum (UHV) evaporator. A solid piece of niobium is targeted by an electron gun that sublime the metal. As Niobium belongs to the class of refractory metals, it implies a very high temperature to make it evaporate. This increases the pressure in the chamber from the vacuum that is usually reached which limits the quality of the niobium film. To remedy this, an efficient cooling of the evaporator enclosure is implemented to reach the standard UHV pressure ( $P_E \lesssim 1.10^{-9}$  mbar). It is done with a circulation of liquid nitrogen  $\sim 30$  mn before and during the evaporation. To avoid this issue, the deposition of niobium is thus commonly done by sputtering which guarantee a high purity of the film.

### 3.1.4 Gates and contacts electrodes

The gates and contact electrodes are the smallest structures of the device. They are defined with an e-beam lithography in a lift-off procedure. These structures fit in a  $100 \mu\text{m} \times 100 \mu\text{m}$  zone which the scanning electron microscope (SEM) can expose without any mechanical displacement. This ensures an accurate alignment which is essential to avoid merging between the gates and contacts electrodes. The gates are 80 nm wide and spaced by 120 nm. For their part, contacts electrodes are 600 nm wide and the spacing between the source or drain and its associated cut is  $1 \mu\text{m}$ . In this design, the idea is to suspend the CNT over the gates. No oxide is then deposited on the gates to electrically detect a non-suspended CNT. To perform this implementation, the contacts electrodes have to be thicker than the gates electrodes (see figure 3.3.a). A 185 nm Ti thick film is used for that purpose.

The ferromagnetic spin qubit requires ferromagnetic contacts. It is implemented with a 35 nm thick film of PdNi whose magnetization direction is set by the electrode shape [191] (see figure 3.3.b). The magnetization is orthogonal to the electrode longitudinal direction. Non-collinear ferromagnetic electrodes lead then to different spin quantization axis in the two dots. In this design, the source and drain electrodes are tilted by an angle  $\theta = \pi/6$  with respect to each other. One can check the electrodes magnetization with Magnetic Force Microscope

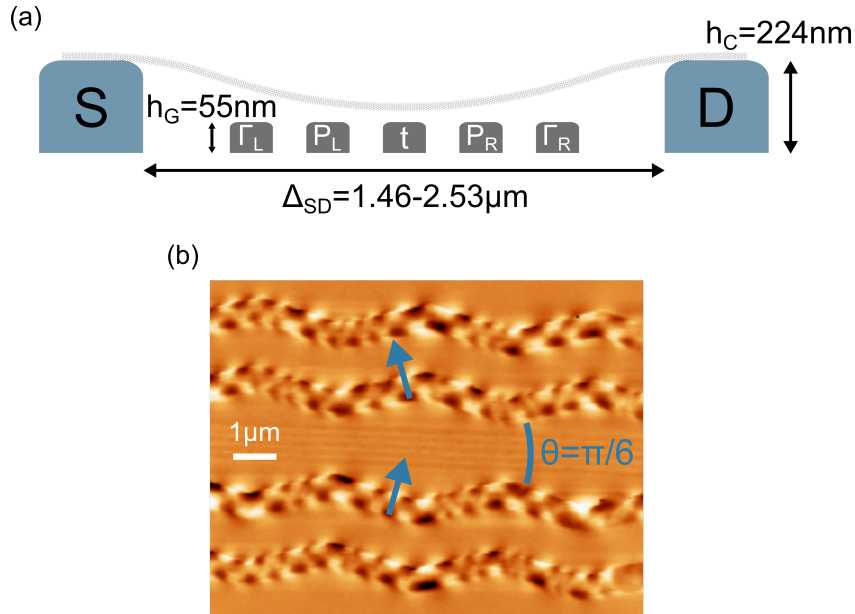


Figure 3.3: **Gates and contacts layout:** (a) Double quantum dot circuit schematic (not to scale) with characteristic lengths enabling a suspended CNT. (b) Magnetic force microscope (MFM) image of the PdNi contact electrodes. Their associated cut electrode is also magnetized as it is done at the same step.

(MFM) imaging (figure 3.3.b).

Finally, the choice of metal in contact with the CNT is determinant. A semiconducting nanotube-metal junction behaves as a Schottky barrier [192] which is then problematic to tune the device at low bias voltage. Nevertheless as the size of the Schottky barrier depends on the difference between the nanotube and metal work functions, it can be reduced up to an ohmic contact [193]. Contacts electrodes made of Pd have enabled this [194] as its work function ( $\Phi_{\text{Pd}} = 5.1 \text{ eV}$ ) is close to the one of carbon nanotubes [195]. A 4 nm thick film of Pd is then deposited on top of the contacts electrodes.

### 3.1.5 Trenches

A specificity of this design is the way carbon nanotubes are integrated on the device. This will be fully described in the next section but this has to be considered for the device nanofabrication. CNT are indeed grown on a dedicated cantilever chip. In order to enable the CNT transfer from the cantilever chip to the device, this last needs a hosting zone for the cantilever chip: the trenches. The trenches (see figure 3.1) are  $\sim 15 \mu\text{m}$  deeper than the rest of the chip surface. This is obtained by etching the  $\text{SiO}_2$  and the silicon with a very thick resist ( $\sim 3 \mu\text{m}$ ) protecting the rest of the chip. Trenches constitute then a big hole in the ground plane which complicates the RF chip design.

## 3.2 Carbon nanotubes fabrication and integration

Once the chip is fabricated the only missing component is the carbon nanotube. This section describes how carbon nanotubes are fabricated, selected and integrated into the sample.

### 3.2.1 Carbon nanotube growth and selection

The widespread technique to fabricate carbon nanotubes that is used for almost three decades is to grow them by Chemical Vapor Deposition (CVD) [196, 197]. A catalyst containing metallic nanoparticles is deposited on a chip before the growth in a furnace at 900°C in a controlled atmosphere (see figure 3.4.a). The gas directly responsible of the carbon nanotube formation is CH<sub>4</sub> which contains 99% <sup>12</sup>C and ~ 1% <sup>13</sup>C which possess a nuclear spin. One can tend towards nuclear spin-free carbon nanotubes by using isotopically purified <sup>12</sup>CH<sub>4</sub>. In this work, standard methane has been used for the CNT growth. The catalyst and growth recipes have been here optimized to produce single-wall carbon nanotubes and largely inspired from what has been developed in Basel university [198]. The details of the recipe are given in appendix B.2. The specific CNT integration (see section 3.2.2) requires a customized chip for the growth. The cantilever chip is indeed composed of combs separated by 30 μm. To enable the transfer, carbon nanotubes have to grow at the tip of this cantilever chip and bridge two combs (see figure 3.4.b). The amount of catalyst has then to be optimized to have enough CNT satisfying this condition but not too much to avoid several CNTs at the same location. Even though the recipe has been optimized, there is still a lot a variability. The transferable carbon nanotubes has then to be selected.

After the growth, the tip of the cantilever chips are imaged under SEM to select the transferable CNTs. Ideally the nanotube is the only one between two given combs to avoid the simultaneous transfer of several nanotubes. The closer to the tip the CNT is located, the easier the transfer is. If it is too far ( $d \gtrsim 20\mu\text{m}$ ), the transfer becomes tricky or even impossible as the cantilever chip is touching the bottom of the trenches before the CNT reaches the contact electrode surface. This SEM imaging also enables to discriminate several tubes crossing each other: bundles. However it does not provide any information on the tube itself such as its bandgap or the presence of defects. Those information can be provided by Raman spectroscopy which enables then to select clean carbon nanotubes with small bandgap.

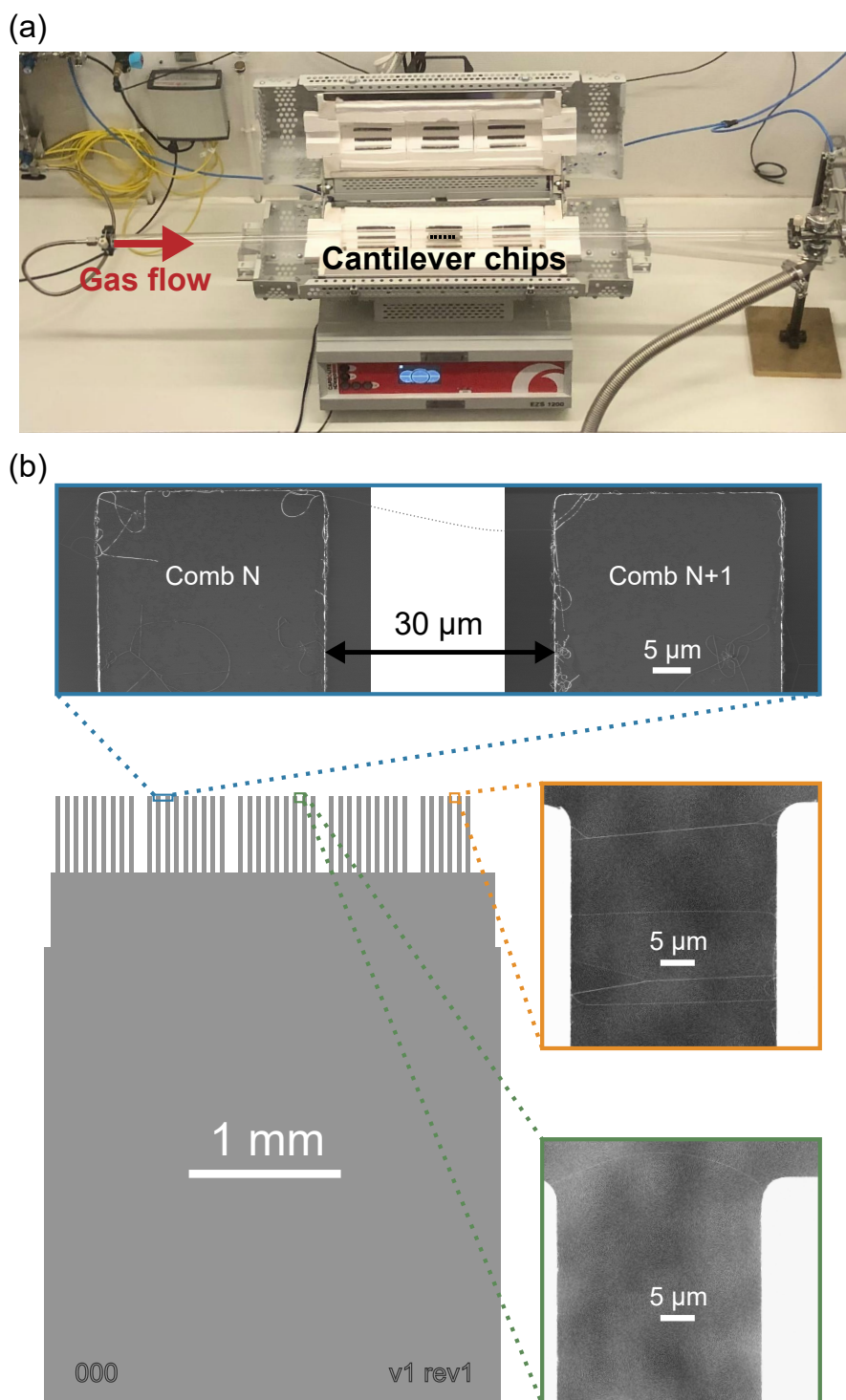


Figure 3.4: **CNT growth and characterization:** (a) The cantilever chips are placed in a quartz tube with a controlled gas flow. The furnace enables to reach the  $900^{\circ}\text{C}$  temperature required for the growth. (b) Each comb of the cantilever chips is imaged with SEM. The middle section is not exposed to avoid deposition of amorphous carbon (blue panel). One can guess if it is question of bundles (orange panel) or looking single-wall (green panel).

### 3.2.2 Stapling carbon nanotubes

#### Various CNT integration

The integration of the carbon nanotube can be thought is several different ways. It can indeed be added on the circuit chip at different steps of its nanofabrication. The simplest way consists in growing carbon nanotubes on the bare circuit chip and fabricate contact and gate electrodes afterwards on top of a well chosen CNT [45,199]. In this approach, the CNT is not suspended and the whole nanofabrication process can introduce disorder. To circumvent this, the CNT growth can be done directly on the circuit chip with catalyst deposited on the electrodes [19,46,51]. The choice of metal for the contacts electrode is almost limited to Pt as it has to handle a 900°C temperature during the CNT growth. It is thus also incompatible with our Nb mesoscopic QED architecture. Finally, this technique has small yield and many devices are then required to obtain a working device.

An alternative technique has been developed to obtain a suspended CNT without post growth contamination and compatible with various circuit chip architectures [200]. In this approach, the CNTs are grown on a dedicated chip and transferred afterwards onto the circuit chip [20,201–203]. In the HQC group, such a transfer technique has firstly been developed by J. Viennot: the stamping [204]. The CNT is here stamped close to the cavity gate and the contact and gate electrodes are fabricated afterwards. This allow to adapt the design depending on the CNT location resulting in high quality factors for the microwave cavity. Nevertheless the CNT is then subject to contamination as it undergoes nanofabrication processes. Furthermore the CNT is not suspended which increases charge noise. To get rid of these issues, the nanotube can be transferred on a complete circuit chip and measured directly after. Inspired from the one used at the Weizmann Institute [20], such a technique has been developed by T. Cubaynes: the stapling [189]. This is what has been used in this work.

#### The stapler

The circuit chip is beforehand embedded in a sample holder (see section 3.3.1) to package the circuit chip and to play the intermediary role between cables and sample lines. For the stapling procedure, the sample holder is placed in a vacuum chamber and connected to some electronics (see figure 3.5). The cantilever chip is glued with PMMA on a mechanical part which can move in the three direction of space thanks to a micro-manipulator stage and a piezo-motor stage for coarse motion and fine positioning. The stapler also includes an Ar gun to remove the thin oxide layer on the contacts electrodes before integrating the CNT. When

using it, the cantilever chip can be protected in an isolated buffer chamber. The Ar gun can also be used to remove a non suitable CNT and start with a new one. However with this physical etching, even though the CNT may not be electrically detectable, it can still lay in the vicinity and complicate the system. A chemical etching with  $O_2$  in a plasma cleaner is used to really get rid of an undesired CNT. In order to align the two chips with respect to each other, a window enables a top view with an optical microscope connected to a camera.

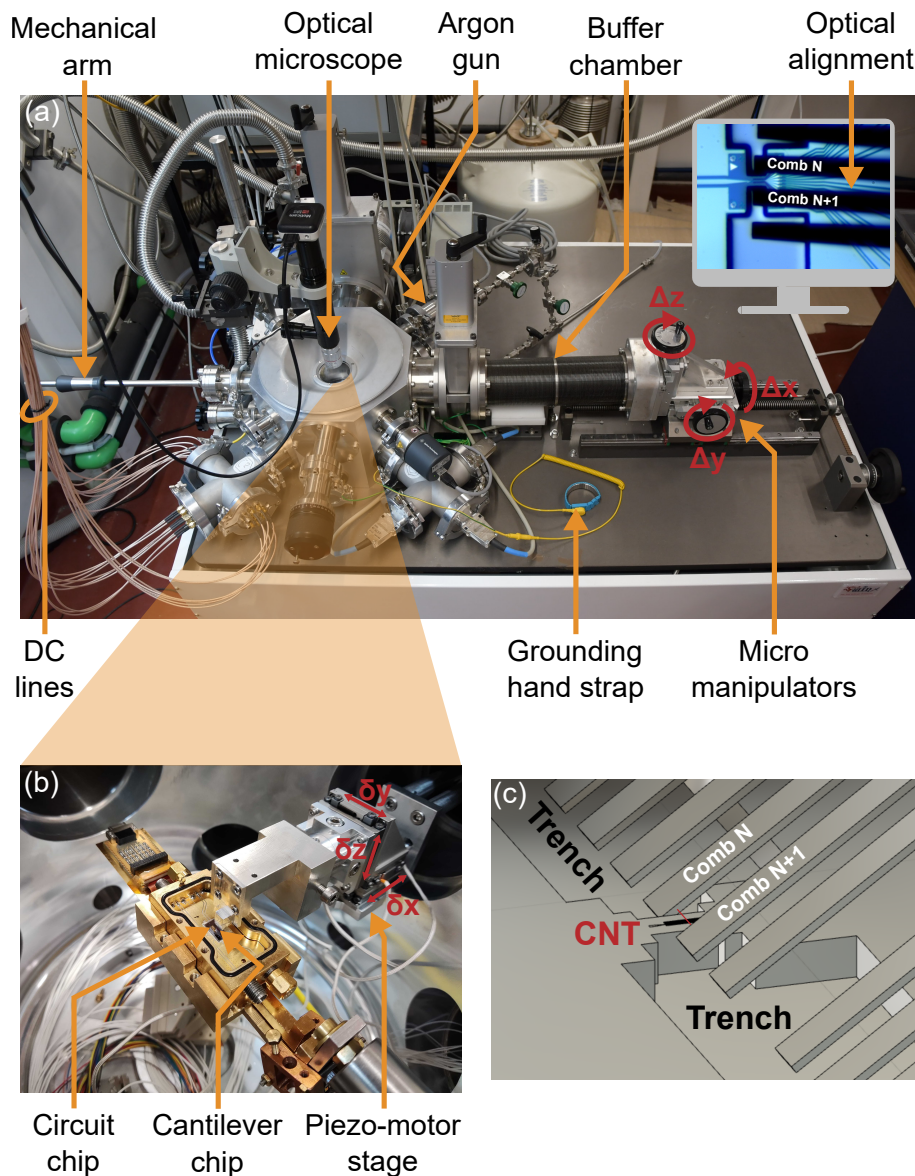


Figure 3.5: **Stapler setup:** (a) The system lies on an air-cushion table to limit vibrations. (b) Inside of the transfer vacuum chamber. (c) Schematic of a CNT bridging two combs of the cantilever chip being transferred on the circuit chip.

### Stapling protocol

The general idea of the stapling is to bring a predefined CNT of the cantilever chip towards the circuit chip while measuring the current flowing between the contact electrode and its associated cut electrode. If a current is measured the CNT has reached the electrode surface.

- Loading

Ideally, carbon nanotubes should not see the ambient atmosphere after their growth as they have a high adsorption rate. It is thus important to transfer the CNT rapidly after their growth and characterization with a storage in a vacuum chamber. Once both cantilever and circuit chips are ready, they can be loaded in the stapler. The cantilever chip surface forms a  $45^\circ$  angle with the one of the circuit chip to see both the combs and the circuit electrodes with the camera. The cantilever chip is also rotated by a few degrees with respect to the arm axis such that the carbon nanotubes are not transferred all at the same time. One should also load the sample holder cover embedded in a metallic part with the associated allen key for the closing enabling the vacuum transfer.

The stapler is equipped with a turbo pump that enables to reach vacuum down to  $P_E \lesssim 1.10^{-6}$  mbar. The Ar cleaning is usually done at  $P_{Ar} = 2.10^{-5}$  mbar during 3 mn. The pressure should then be beforehand ten times smaller to make sure the majority gas in the stapler is indeed Ar. Before starting the CNT transfer, one can check that the chip does not present any electrical short with the "chip health" procedure. This consists in applying a voltage (typically  $V_{bias} = 2$  V) on the circuit chip line  $i$ , grounding line  $j$  and measuring the current. One should only measure noise as nothing is supposed to connect the two of them. A switching matrix implemented by the C12 team automatizes the chip health procedure for any pairs of lines.

- CNT detection

To enable the CNT electrical detection, one applies a bias voltage on the two cut electrodes ( $V_{bias} = 2$  V) while the source and drain are grounded (see figure 3.6). A pair of two combs selected during the cantilever chip characterization is brought towards the chip surface, in the  $100 \mu\text{m} \times 100 \mu\text{m}$  area containing contacts electrodes while measuring the current. This is firstly done by adjusting the micro-manipulator up to the point where the tip of the combs and the chip surface have roughly the same focus. At this point, one should use the piezo-motor stage for a fine tuning of the cantilever chip position. By lowering the combs again and again, if the transfer happens as it should, at some point a current is measured. One can set a detection current which advertised the user when a bigger current is measured. One typically

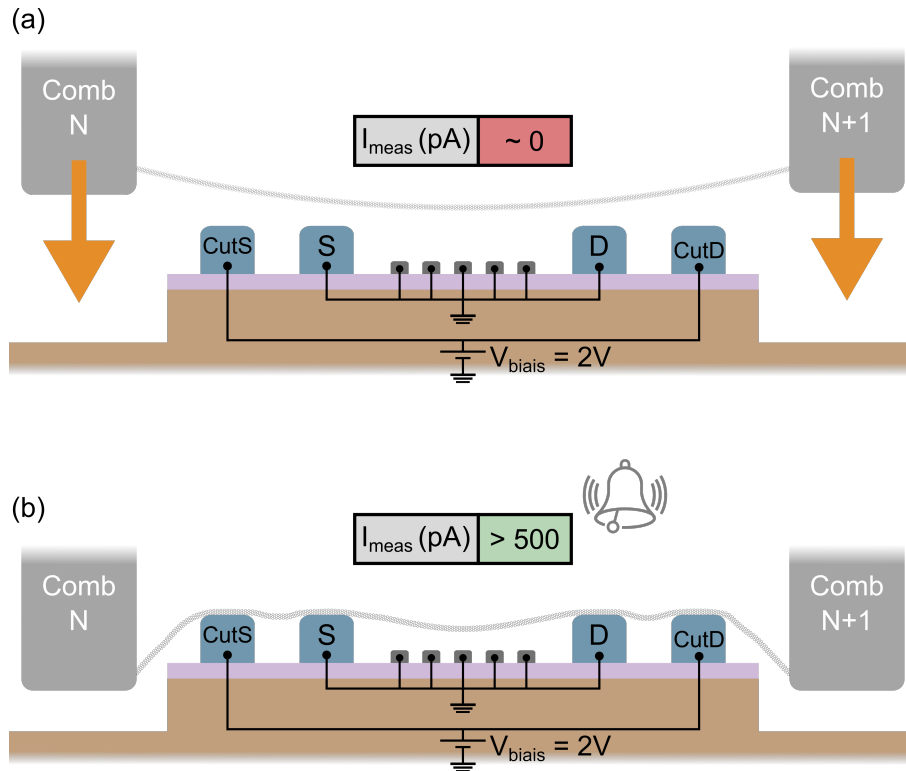


Figure 3.6: **CNT electrical detection:** (a) Two combs with a suitable bridging CNT are brought closer and closer to the circuit chip while measuring the current. (b) When the CNT touches the electrodes surface, current can flow between the contact and its associated cut electrode.

sets  $I_{\text{detection}} = 500 \text{ pA}$  which corresponds to a detection resistance  $R_{\text{detection}} = 4 \text{ G}\Omega$ . If no current has been measured when the combs touch the bottom of the trench it is not worth to continue. SEM images have shown that in such a situation the CNT has really been transferred but then with a bad electrical contact most probably caused by high Schottky barriers. In this detection method, the measured current is the sum of the current flowing in the two sides sections:  $I_{\text{meas}} = I_{\text{CutS-Source}} + I_{\text{CutD-Drain}}$ . One should then check them individually to make sure the CNT is electrically contacted with both the source and drain electrodes.

- CNT cutting

Once the CNT has been electrically detected with the source and drain electrodes, the cantilever chip has to be moved away from the circuit chip. However the CNT is still attached to the combs. The cut electrodes have been introduced on the chip design to solve this issue. By applying an increasing bias voltage  $V_{\text{bias}}$  on the CutS (resp. CutD), more and more current is flowing in the CutS-Source (resp. CutD-Drain) section up to a threshold value  $I_{\text{threshold}}$

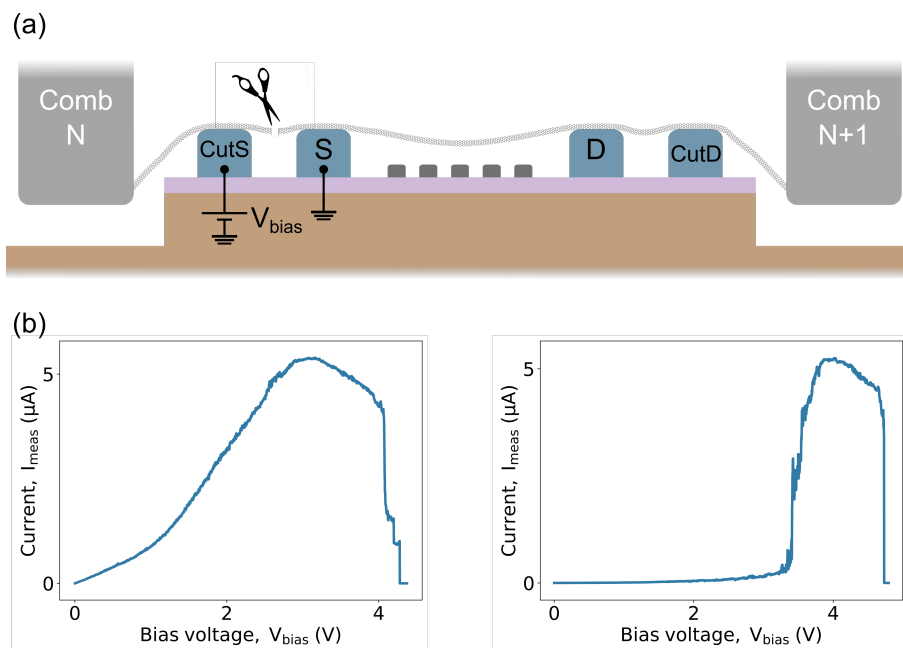


Figure 3.7: **CNT cutting procedure:** (a) The side section of the CNT can be cut by Joule heating with a sufficiently high current. (b) Measurement of the current  $I_{\text{meas}}$  as a function of the applied voltage  $V_{\text{bias}}$  for the source side (left) and drain side (right). When the current falls down to zero, the CNT is cut.

before falling down to zero meaning the CNT is cut (see figure 3.7). This is supposed to be due to Joule heating [20, 205] which is consistent with the cut occurring in the middle of the section. The electrodes indeed behave as thermal heat sink. After this procedure, the CNT is bridging the source and drain electrodes and not connected anymore to the cantilever chip which can be moved away.

Besides, this cutting procedure provides information on the CNT. The value of  $I_{\text{threshold}}$  depends indeed on the current carrying capacity of the CNT which is smaller for single-wall nanotubes (SWNTs) than for multiwall nanotubes (MWNTs) or bundles [206]. For the section length of our design, SWNTs show  $I_{\text{threshold}} \sim 5 - 7 \mu\text{A}$  and CNTs with  $I_{\text{threshold}} \sim 15 - 30 \mu\text{A}$  are classified as MWNTs or bundles. When reaching  $I_{\text{threshold}}$ , the current falls down abruptly to zero for a SWNT whereas it happens in several steps for a MWNT or a bundle corresponding to the burning of its different constituent components. A decrease of the current can also be observed before falling down to zero (see figure 3.7.b). This negative differential conductance is a positive feature since it is due to electron-phonon scattering which occurs for a suspended CNT. Finally, without local disorder, the cutting IV curves are expected to be similar on both sides.

The last benefit of the cutting procedure is to act as an annealing procedure. This consid-

erably decreases the resistance of the circuit which enables afterwards at low temperature to tune the double quantum dot through transport measurements. After the CNT has cut, it is sometimes still possible to measure current. It can be due to the CNT side section that touches both the cut electrode and the silicon substrate as it is not insulating at room temperature. This configuration is not problematic and can easily be confirmed with an IV curve with opposite polarization which should this time present no current.

- CNT characterization

When the cantilever has been removed one can already characterize the device at room temperature. The first thing we can do is to measure the resistance between the source and drain electrodes at low bias. Ideally, one obtains a non noisy linear IV curve and the resistance is  $R_{\text{CNT}} \lesssim 2\text{M}\Omega$  at  $V_{\text{SD}} = 10 \mu\text{V}$ . If this criteria is not satisfied one can try an annealing procedure consisting in sending more and more current directly between the source and drain electrodes. One should be very careful not to reach the threshold current corresponding to this section length which is then smaller than  $I_{\text{threshold}}$ . For this, the stapler electronics enables to set a compliance value for the current  $I_{\text{compliance}}$ : the applied voltage is then adapted in real time to satisfy  $I_{\text{SD}} \leq I_{\text{compliance}}$ .

The other possible room temperature characterization is the gate dependence. Measuring  $I_{\text{SD}}$  as a function of the gate voltages  $V_g$  at a fixed bias voltage  $V_{\text{SD}}$  gives information on the CNT bandgap size. The gate potential indeed bends the conduction and valence bands which affects the current depending whether or not the CNT chemical potential is in the bandgap. This measurements enables to distinguish between metallic, semiconducting (figure 3.8.a) and

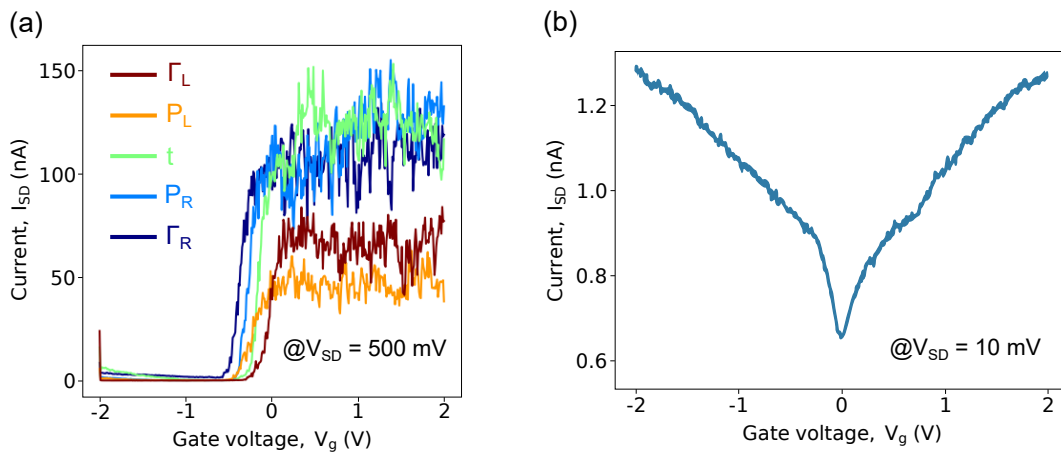


Figure 3.8: **Gate dependence characterization** : (a) Individual sweep of each of the five gates showing similar influence on the CNT identified here as semiconducting. (b) Global sweep with the five gate voltages simultaneously highlighting a narrow gap CNT.

narrow gap CNTs (figure 3.8.b). It can be done by sweeping the five gates all together but also with each of them individually to check their proper functioning. Similar gate dependencies also captures the cleanliness of the CNT.

This room temperature characterization gives insights on the potential of the device but reliable information are provided by low temperature measurements. Interesting physics phenomena can indeed be observed with a non ideal room temperature characterization (see chapter 5). Nevertheless, if after the room temperature characterization the device is considered not suitable, it is possible to remove the CNT with an O<sub>2</sub> plasma and to start again the stapling process.

- From the stapler to the cryostat

The challenge is now to transfer the device from the stapler to the cryostat alive. One has to be very careful during this step as the CNT can blow as a fuse with the electrostatic discharge. To prevent this issue, one should pay attention to ground everything in contact with the device all together: the stapler, the cryostat and the user. The electrical DC lines of the device are at floating potentials during the transfer as the sample holder includes filtering (see section 3.3.1). To limit the current in the CNT, 10 MΩ resistors are added to the cryostat DC lines associated to source and drain. It has been shown that the breakdown of CNT occurs at lower  $I_{\text{threshold}}$  in the presence of O<sub>2</sub> [205]. Transferring the device under vacuum is then useful to reduce the influence of electrical discharge and also limits the potential CNT contamination. To make this possible, the sample holder embedding the circuit chip has been designed to be vacuum tight. It can be closed in the stapler at  $P_E \lesssim 1.10^{-6}$  mbar with a mechanical arm ending with a wrench. It first holds the sample holder cover which can be properly placed at the end of the room temperature characterization. The second step consists in catching an allen key to tighten the sample holder cover. A non adiabatic venting of the chamber enables the inside of the sample holder to stay under vacuum during the transfer to the cryostat.

### 3.3 Measurement techniques

Now that the CNT has been integrated on the circuit chip, the device can be measured. This section describes the different measurement techniques and associated setup.

### 3.3.1 Isolating the device from the outside world

#### Embedding of the chip in the sample holder

The chip sample holder has several utilities. First, it plays the intermediary between the macroscopic cables and the microscopic circuit lines. The circuit chip is glued with PMMA resist to the sample holder and is micro-bonded to a surrounding Printed Circuit Board (PCB) (see figure 3.9). As it has to convey both RF and DC signals a multi-layer PCB is used to suppress cross-talk.

The sample holder also isolates the circuit chip from external noise sources. It is question of a gold plated copper box acting as a Faraday cage. The electromagnetic environment is then defined by the shape of the box. This results in package modes that can interact with the sample modes of interest. The JAWS has been designed by M. Villiers [207] to avoid this issue and greatly inspired the sample holder used in this work. An alternative consists in using the fundamental box mode as the cavity mode in a 3D design instead of the CPW one [208] (see chapter 4). The box volume:  $40 \text{ mm} \times 17 \text{ mm} \times 5 \text{ mm}$  sets the fundamental box mode to  $f_{110} \gtrsim 9.5 \text{ GHz}$  (see section 6.3 of [176]). As the chip is covered by Nb and lies on an metallic surface, another type of package mode exists in the chip volume. The chip size  $10 \text{ mm} \times 5 \text{ mm} \times 0.5 \text{ mm}$  sets the fundamental parasitic mode to  $\tilde{f}_{110} \approx 9.8 \text{ GHz}$ . It can be pushed away spatially from the chip at higher frequency by opening a vacuum gap below the chip [207]. Finally, once the CNT is contacted to the circuit chip, one needs to prevent electrical discharges. A filtering PCB with Pi filters is implemented to the sample holder for that purpose. As mentioned in section 3.2.2, the sample holder needs to be vacuum tight not to expose the CNT to ambient atmosphere during the transfer from the stapler to the cryostat. The main challenge consists in bringing all the DC lines which is overcome with an electrical flat ribbon sandwiched between two indium joints.

#### Measuring at low temperature

Reaching low temperatures is important for several purposes. First, it is mandatory to reveal the physical phenomena of interest. In order to form a double quantum dot,  $k_B T \ll E_{C_L}, E_{C_R}, E_{C_m} \sim 0.5 - 2.5 \text{ meV}$  [152] which can be achieved with  $T \ll 10 \text{ K}$ . Concerning the realization of the ferromagnetic spin qubit, the smallest energy scale which has to be resolved is the qubit frequency expected at  $\omega_{q_{th}} \sim 7.68 \text{ GHz}$  [7] and already measured at  $\omega_{q_{exp}} \sim 6.506 \text{ GHz}$  [152] which corresponds to  $T \sim 312 \text{ mK}$ . Furthermore to fully benefit from the mesoscopic QED architecture, the cavity should not be thermally populated:  $\bar{n} = (e^{\hbar\omega_c/k_B T} - 1)^{-1} \ll 1 \leftrightarrow T \ll 500 \text{ mK}$  for a  $7 \text{ GHz}$  cavity resonance frequency. Finally, the temperature should be

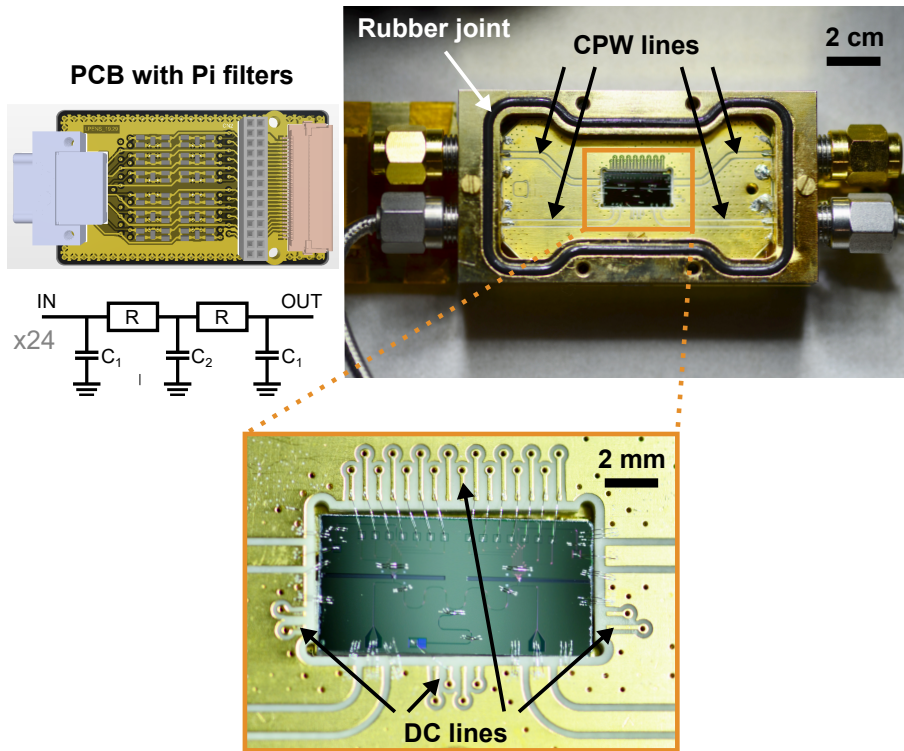


Figure 3.9: **Circuit chip embedded in the sample holder:** The PCB contains 24 DC lines and 4 CPW lines for RF signals. Each DC line has a Pi filter:  $R = 1 \text{ k}\Omega$ ,  $C_1 = 1 \text{ nF}$  and  $C_2 = 2.2 \text{ nF}$ . A rubber joint ensures the tightness when closing the sample holder with its cover inside the stapler.

lower than the critical temperatures of the different superconducting metals involved in the design:  $T_C(\text{Nb}) = 9.26 \text{ K}$ ,  $T_C(\text{Al}) = 1.2 \text{ K}$  and  $T_C(\text{Ti}) = 0.39 \text{ K}$ .

At the very beginning of this work, the measurements were carried out in a dry dilution fridge refrigerator with a base temperature of 20 mK but nearly all of what is shown in this thesis has been measured in a  $^3\text{He}$  cryostat with a base temperature of 280 mK. The RF and DC wiring of this cryostat has been done by M.M. Desjardins whose thesis provides the details [209]. It includes 12 DC lines, one RF input line and one RF output line (see figure 3.10). The base temperature is obtained by pumping on  $^3\text{He}$  liquid contained in a closed circuit with an charcoal pump. This temperature is maintained over  $\sim 20 - 30$  hours before the  $^3\text{He}$  fully evaporates.

### 3.3.2 DC measurements

Once the cryostat is under vacuum with the circuit chip loaded we can check if the CNT is still connected between the source and drain electrodes. Similar characteristics as in the stapler<sup>1</sup>

<sup>1</sup>Contact resistance and gate dependence notably

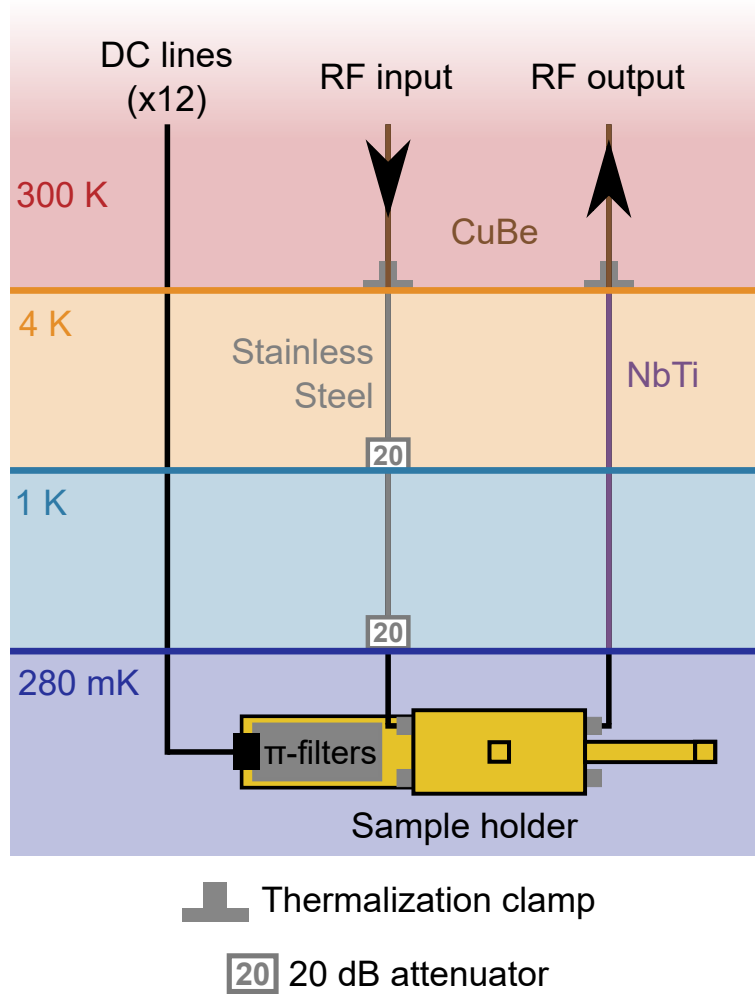


Figure 3.10: **<sup>3</sup>He cryostat wiring:** The attenuators thermalizes both the outer and inner part of the coaxial cable and reduce thermal noise. The NbTi line provides very few attenuation to the RF output line. The signal to noise ratio could be increased by implementing a cryogenic amplifier.

reflects the smooth completion of the transfer. This section presents the setup (figure 3.11) enabling this first characterization and further transport measurements at low temperature as shown as in section 1.2. The electric lines associated to the source and the five gates are connected to a dedicated Yokogawa GS200 DC source which has a  $10 \mu\text{V}$  and  $100 \mu\text{V}$  resolution for the used 1 V and 10 V source range. In order to measure very small current in the CNT (typically  $10 - 100 \text{ pA}$ ), the drain electrode is connected to a  $10^7$  gain current amplifier which has been designed by J. Viennot and the ENS electronic team [178]. The voltage is then read with a Keithley 2000 multimeter with an acquisition time of  $\tau_a = 20 \text{ ms}$ . In this work, the transport measurements are obtained with a  $3\tau_a = 60 \text{ ms}$  integration time. This characteristic time has to be taken into account for the implementation of filtering

on the lines connected to DC sources. Introducing RC low pass filters of cutoff frequency  $f_{\text{cutoff}} = 2\pi/RC$  involves indeed another characteristic time  $\tau_{\text{cutoff}} = 1/f_{\text{cutoff}}$ . The line in the vicinity of the device will reach 99% of the instruction value after  $5\tau_{\text{cutoff}}$  which has to be much smaller than  $3\tau_a = 60$  ms to measure a system set according to the instruction values. In this work, the low pass filter has a cutoff frequency  $f_{\text{cutoff}} = 1.6$  kHz ( $R = 1$  M $\Omega$  and  $C = 100$  pF) which satisfies the condition:  $5\tau_{\text{cutoff}} = 3.1$  ms  $\ll$   $3\tau_a = 60$  ms. This filtering aims at minimizing the electrical noise just like the factor 1000 voltage divider placed on the source line. Finally as mentioned previously, two  $R = 10$  M $\Omega$  resistors are placed on the source and drain lines to limit the current in the CNT and thus protecting it during the transfer and cool down procedure. The one on the drain side is kept for measurements as well as it increases the signal to noise ratio.

During the cool-down procedure, one can monitor a gate dependence measurement to check how the gap is affected. When reaching the base temperature, each gate can be tested individually to see whether or not they all have the same influence on the CNT. The regular spacing of Coulomb peaks and an four-fold degeneracy informs on the cleanliness of the CNT [210]. In practice, this behavior is often only seen for a specific range of gate voltages which constitutes an interesting zone to focus on. The identification of a gap is also important to work afterwards with only electron in the double quantum dot. Tuning the circuit into a DQD can be done with a stability diagram measurement (see section 1.2.2). Rough settings can be quickly obtained with a one-dimensional scan with both plunger gate voltages which is equivalent to a diagonal cut in the stability diagram.

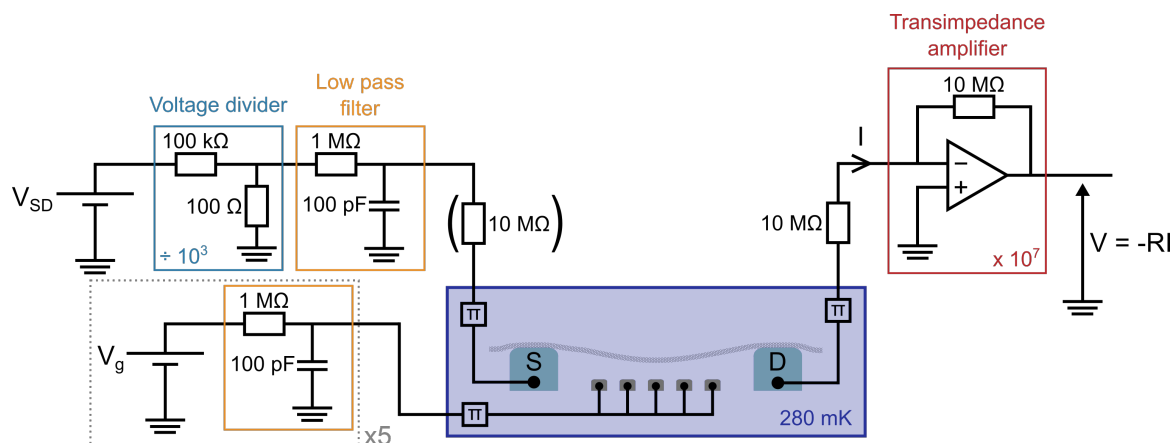


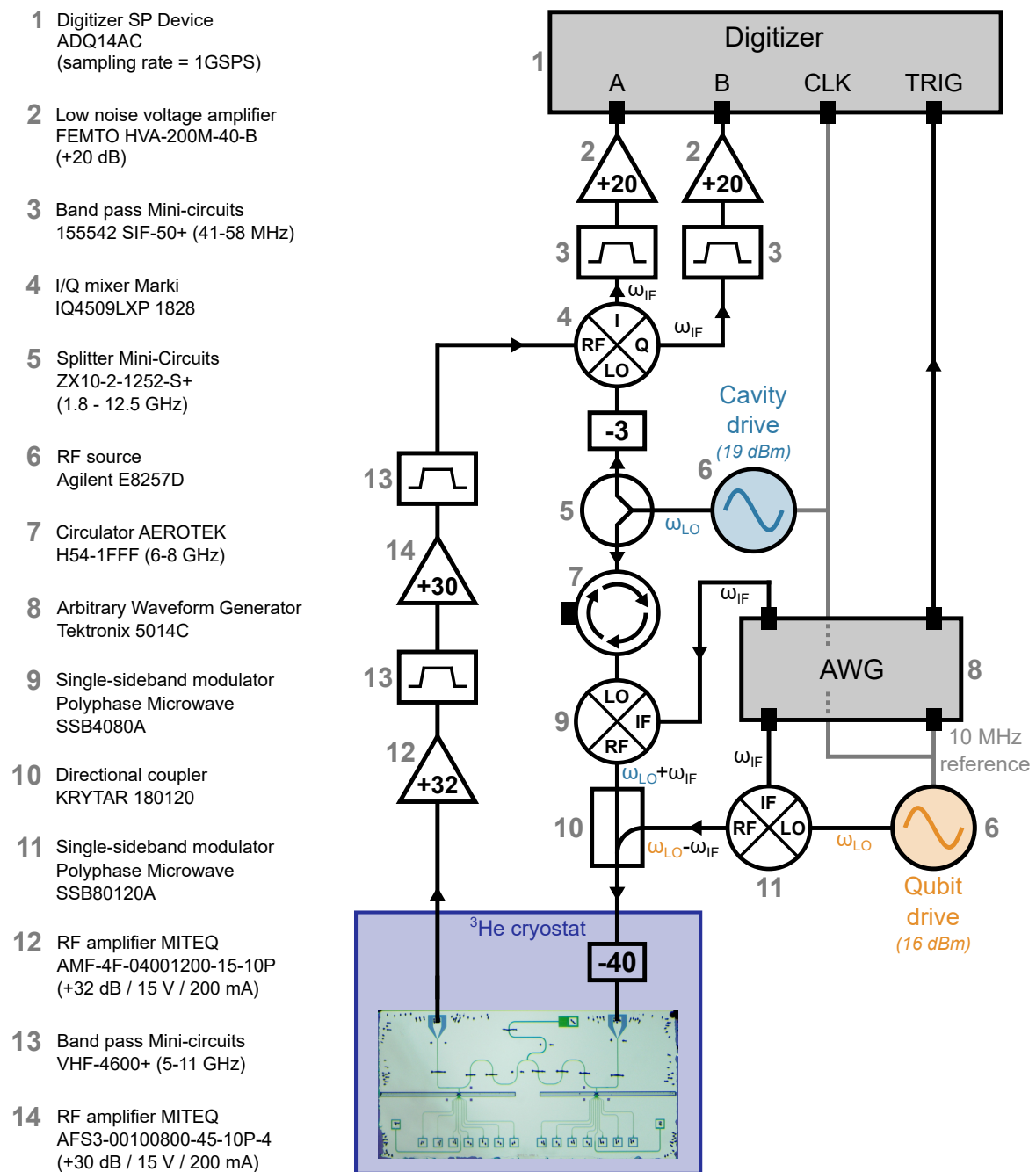
Figure 3.11: **DC measurement setup:** The voltage divider reduces the bias voltage  $V_{\text{SD}}$  by a factor of 1000. The current going out of the cryostat is amplified by a factor  $10^7$  by a low noise I-V converter.

### 3.3.3 RF measurements

#### RF measurement setup

The simplest way to measure a microwave cavity consists in connecting its two ports to a Vector Network Analyzer (VNA) that can handle signals in the GHz range. This has been widely used in this work for rapid tests but also for continuous measurements. The limit of this setup occurs if we want to perform time domain measurements. For that purpose, pulses have to be generated which is not possible with the VNA. With the development of quantum technologies, it is now possible to find instruments that both generate and handle pulse sequences in the GHz range.

In this work, the signal is generated and handled by different instruments in a setup based on heterodyne detection [181,211] (see figure 3.12). The cavity drive tone ( $\sim 7$  GHz) called Local Oscillator (LO) is generated by an RF source. In parallel, a 50 MHz signal called Intermediate Frequency (IF) is generated by an Arbitrary Waveform Generator (AWG) which can generate pulse sequences. The LO and IF signals are then mixed in a single-sideband modulator with an output signal at  $\omega_{\text{LO}} \pm \omega_{\text{IF}}$  depending if it is an upper or lower sideband. The direct transmission at  $\omega_{\text{LO}}$  and the unwanted sideband at  $\omega_{\text{LO}} \mp \omega_{\text{IF}}$  are internally suppressed by 30 dB and 40 dB. The power of the resulting signal is fixed by the IF signal set on the AWG. The power of the LO signal set by the RF source still has to be well chosen to satisfy both I/Q mixer and single-sideband accepted input powers. This output signal is then sent to the cavity input port in the cryostat. The output signal which now carries information on the device through the I and Q quadratures is amplified and filtered before being demodulated with an I/Q mixer which also takes the LO signal as input. This LO signal is either used as it is or  $90^\circ$  phase shifted and filtered resulting in two signals at  $\omega_{\text{IF}}$  on the I and Q ports of the I/Q mixer of which several traces ( $\sim 10^4$ ) are collected by the digitizer (see figure 3.13.a). The I and Q quadratures can then be obtained by averaging the signals multiplied by  $\cos(\omega_{\text{IF}}t)$  and  $\sin(\omega_{\text{IF}}t)$ . From those physical quantities one can access the phase and amplitude of the RF signal (see figure 3.13.b). The use of an I/Q mixer is not mandatory as a basic one would be sufficient to calculate both the I and Q quadratures. However, this supplementary output enables to multiply the signal to noise ratio by 2 (see appendix D in [188]). For now the RF setup only enables to measure the cavity. A second drive is then integrated to manipulate the qubit. As for the cavity drive, the qubit drive is composed of a LO and IF signals that are mixed in a single-sideband. The device includes a dedicated line for the qubit drive but the  $^3\text{He}$  cryostat only has one input RF line. The drive has thus to be applied through the cavity. To do so, a directional coupler brings the two signals together in the same line.



### Continuous wave measurements

Once the device has reached the base temperature, one can check the proper functioning of the cavity. As described in section 2.3.1, the transmission of the transmission line as a function of the cavity drive frequency should result in a Lorentzian centered around the cavity resonance frequency  $f_c$ . Some parasitic package mode can couple to the cavity mode

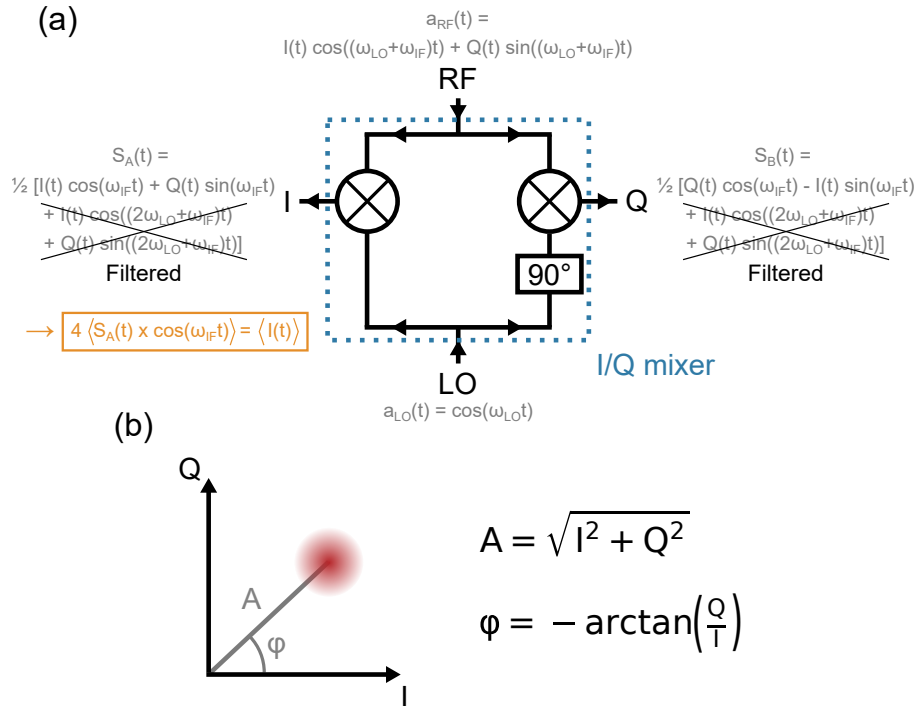


Figure 3.13: **Heterodyne detection for microwave measurements:** (a) The I/Q mixer enables to calculate the I (in orange) and Q quadratures which carries information on the device. (b) These two quantities informs on the amplitude and phase of the output signal.

which results in distorted Fano-shaped resonances (see section 4.5 of [178] and figure 3.14). From this measurement, one can extract the cavity quality factor:  $Q = f_c / \Delta f_{-3\text{dB}}$  which usually ranges from 2000 to 8000 for this chip design and similar ones. After this cavity characterization, the cavity drive tone is set to the cavity resonance frequency to maximize the sensitivity of the RF measurements. The goal is now to couple to interdot transitions of the double quantum dot circuit resulting in oblique resonant lines in the stability diagram (see section 2.3.2). It is however also possible to couple to dot-lead transitions which can be circumvented by closing the DQD from the reservoirs with the gamma gate voltages.

The highlighted resonant lines correspond to a sum of dispersive shifts induced by potentially several different transitions. The two-tone spectroscopy aims at deconvoluted all of this. The second tone enables indeed to address and characterize individually the different transitions. One can obtain information on the transition with the dispersion of its frequency with respect to the detuning  $\epsilon_\delta$  (figure 3.15), the external magnetic field, the cavity drive power (figure 2.4) or the qubit drive power (figure 2.8). This also provides information such as the associated coupling strength  $g$  or the decoherence rate  $\Gamma_2$ . With this continuous spectroscopy, the qubit is brought out of its ground state (see equation 2.54). However bringing the qubit anywhere on the Bloch sphere requires to drive it for a finite amount of time.

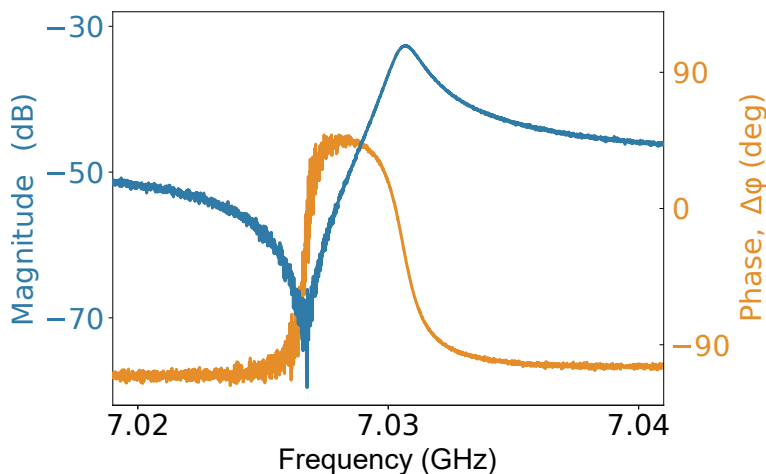


Figure 3.14: **Cavity transmission measurement:** This exhibits a Fano-shaped transmission. One can extract the cavity resonance frequency  $f_c = 7.031$  GHz and the associated bandwidth  $\Delta f_{-3\text{dB}} = 1.365$  MHz which define the cavity quality factor  $Q = f_c/\Delta f_{-3\text{dB}} = 5150$ . (device W11A)

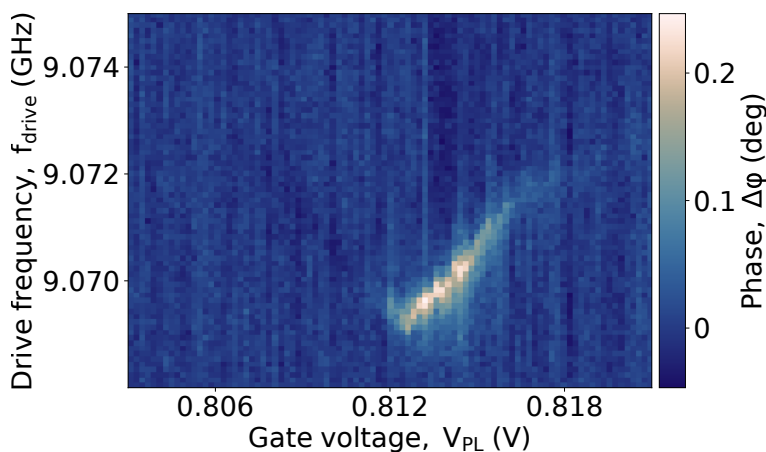


Figure 3.15: **Continuous two-tone spectroscopy as a function of the plunger gate voltage  $V_{\text{PL}}$ :** The x axis can be related to the detuning  $\epsilon_\delta$ . The dispersion shows similarities with the one expected for the 01 transition of the ferromagnetic spin qubit. (device W11A)

### Time domain measurements

- Calibration

The next step is then to perform time domain measurements which is possible with our RF setup (figure 3.12). This type of measurement is harder to implement as it involves several timings which have to be calibrated according to the experimental RF setup and the measured system. The different powers are also critical and can be a limiting factor to perform such measurements. In time domain measurements, the qubit is driven for a given amount of time

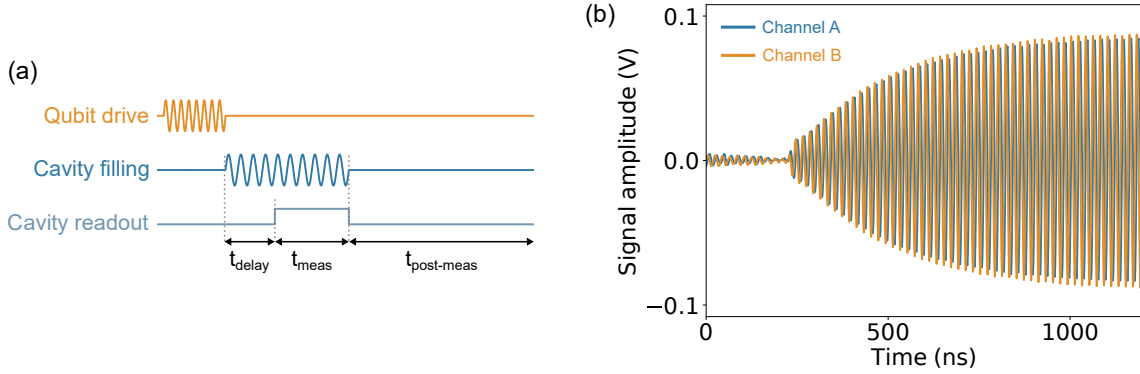


Figure 3.16: **Pulse sequence calibration:** (a) Representation of the different timings to calibrate in the pulse sequence. (b) Collected signals on the channels A and B of the digitizer after starting to fill the cavity. In the first  $\sim 250$  ns, nearly no signal is being collected representing then the time required for the signal to travel through the cables.

After  $\sim 250$  ns, one observes an exponential increase characterized by a time  $\tau = 1/\kappa$ .

and the cavity is filled and measured afterward (figure 3.16.a). This prevents measurement induced dephasing. The quantum fluctuation around the average number of photons in the cavity gives indeed rise to fluctuations of the qubit frequency through AC-stark shift [184,211] (see section 2.2.1). As we start with an empty cavity, we need to wait a finite time  $t_{\text{delay}}$  after it has been started to be filled for the signal to arrive at the digitizer. This time which depends on the cable length and on the cavity quality factor can be determined by filling the cavity while monitoring the signal acquired by the digitizer (figure 3.16.b). One could wait to reach a maximum output signal before measuring the cavity but the qubit lifetime has to be considered to still obtain information about it. Similar constraints have to be considered for the time we measure the cavity  $t_{\text{meas}}$ . A too short  $t_{\text{meas}}$  would provide relevant information on the qubit but the associated signal is too noisy to reveal it whereas a too long  $t_{\text{meas}}$  would not provide information on the qubit as it exceeds its lifetime. The Signal to Noise Ratio (SNR) can be increased to some extent with the number of traces collected by the digitizer. Given the qubit lifetime  $T_1 \sim 1.1 \mu\text{s}$ , the cavity filling dynamic and the SNR the measurements presented in chapter 5 where acquired such that  $t_{\text{delay}} + t_{\text{meas}} \lesssim T_1$ , with  $t_{\text{delay}} = 400$  ns and  $t_{\text{meas}} = 600$  ns and by collecting 150k traces. With those considerations, a qubit with relaxation time  $T_1$  can not be measured this way if the cavity quality factor is in comparison too high: we should have  $T_1 > \tau = 1/\kappa$ . After the cavity measurement, both qubit and cavity have to be reset to their ground state to always start the measurement in the same conditions. For this purpose, we define a time  $t_{\text{post-meas}}$  in the pulse sequence to make the two systems relax. We need to ensure  $t_{\text{delay}} + t_{\text{meas}} + t_{\text{post-meas}} \gtrsim 3 - 5 T_1$  and  $t_{\text{post-meas}} \gtrsim 3 - 5 \tau$ . We have set  $t_{\text{post-meas}} = 2.85 \mu\text{s}$ . The pulse sequence represented on figure 3.16.a is a pulsed spectroscopy of the qubit and can be used to tune the different timings.

- Qubit characterization

**Rabi oscillations:** Once the pulse sequence timings are set, one can start to characterize the qubit. The first measurement to perform is the Rabi experiment which enables to characterize how fast we can manipulate the qubit by determining the Rabi frequency  $\Omega_R$ . This quantity is crucial to know as it defines the  $\pi$  and  $\pi/2$  pulse durations required for further characterization. In this measurement, the qubit is driven during a varying time  $t_{burst}$  resulting in rotations of the qubit around the X axis of the Bloch sphere: the qubit oscillates between its ground and excited states at a frequency  $\Omega_R$ . These oscillations last for a finite amount of time before the qubit ends up in a statistical mixture at the center of the Bloch sphere (see figure 3.17.a). Experimentally we observe exponentially damped oscillations characterized by a decay time  $T_R$ . For accurate insight on the system, it is important to perform this measurement not only at the transition frequency  $\omega_q$  but on a larger span of driving frequencies  $\omega_d$ . One obtains what is called a Rabi chevron pattern which can indeed capture a more complex behavior than a simple two-level system [212]. The probability for a qubit to be in the excited state  $|1\rangle$  reads:

$$P_{0 \rightarrow 1}(t_{burst}, \omega_d) = \frac{\Omega_R^2}{(\omega_d - \omega_q)^2 + \Omega_R^2} \sin^2(\sqrt{(\omega_d - \omega_q)^2 + \Omega_R^2} t_{burst}) e^{-t_{burst}/T_R} \quad (3.1)$$

Finally as derived in section 2.2.3, if the qubit is driven through the cavity, the Rabi frequency is fixed as  $\Omega_R = g\varepsilon_d/(\omega_q - \omega_c)$ . A high qubit-photon coupling strength  $g$  enables thus fast manipulation of the qubit but it can still be compensated by increasing the drive amplitude  $\varepsilon_d$ . This linear scaling of  $\Omega_R$  with  $\varepsilon_d$  constitutes an experimental sanity check.

**$T_1$  measurement:** Longitudinal relaxation is caused by transverse noise on the x or y axis. Resonant energy exchange can lead to transition from the qubit excited state  $|1\rangle$  to its ground state  $|0\rangle$ . The reverse transition is also possible but exponentially suppressed if  $k_B T \ll \hbar\omega_q$ . To characterize this relaxation, the qubit can be placed in its excited state  $|1\rangle$  with a  $\pi$  pulse whose duration has been determined through the Rabi measurement. We then wait a varying time  $\tau$  before measuring the cavity (see figure 3.17.b). We observe an exponential decay of the signal towards the value corresponding to the qubit ground state enabling to extract the associated characteristic time  $T_1$ . The exact  $\pi$  pulse duration is not crucial to know as the relaxation dynamic is the same no matter from where we start in the Bloch sphere. Starting from the excited state enables yet to maximize the output signal.

**$T_2^*$  measurement:** The transverse relaxation rate describes the loss of coherence of a superposition state. It is both related to transverse noise and longitudinal noise causing pure dephasing. This last is caused by longitudinal noise on the z axis and this non resonant phe-

nomenon makes the qubit frequency  $\omega_q$  fluctuate. One defines the transverse relaxation as:  $\Gamma_2 = \Gamma_1/2 + \Gamma_\varphi$  (see section 2.3.2). The associated characteristic time  $T_2^*$  can be measured by Ramsey interferometry [183] and is thus limited to  $T_2^* \leq 2T_1^2$ . For this, we start with a qubit in its ground state  $|\psi_0\rangle = |0\rangle$  to which we apply a  $\pi/2$  pulse to place it in a superposition state  $|\psi_1\rangle = (|0\rangle - |1\rangle)/\sqrt{2}$  in the equator plane of the Bloch sphere. We then wait a varying time  $\tau$  in which the qubit is subject to dephasing resulting in  $|\psi_2\rangle = (|0\rangle - e^{i\phi}|1\rangle)/\sqrt{2}$ . Finally, another  $\pi/2$  pulse is applied to project the qubit on the z axis leading to the state:  $|\psi_3\rangle = 1/2[(1 - e^{i\phi})|0\rangle - (1 + e^{i\phi})|1\rangle]$  (see figure 3.17.c). This measurement is commonly done at  $\omega_q + \delta\omega_q$  such that  $\phi = \delta\omega_q\tau$  is non zero, resulting in a damped oscillating signal from which  $T_2^*$  can be extracted. This measurement can also be done for various driving frequencies  $\omega_d$  around the qubit frequency  $\omega_q$  resulting in Ramsey fringes. The probability for the qubit to be in the excited state  $|1\rangle$  reads:

$$P_{0 \rightarrow 1}(\delta\omega_d, \tau) = |\langle 1|\psi_3\rangle|^2 = \cos^2\left(\frac{\delta\omega_d \tau}{2}\right) e^{-(\tau/T_2^*)^\alpha} \quad (3.2)$$

Where the parameter  $\alpha$  describes the type of decay-curve envelopes which hints to the origin of the noise causing the decay [111].

**Hahn-echo measurement:** The Hahn echo technique that has been developed in the field of Nuclear Magnetic Resonance enables to be less sensitive to low frequency noise than the Ramsey experiment. To do so, a  $\pi$  pulse is introduced in the middle of the varying waiting time  $\tau$  of the Ramsey sequence (see figure 3.17.d). This reverses the sign of dephasing acquired during the first half waiting time which is refocused during the second half waiting time:

$$\begin{aligned} |\psi_0\rangle &= |0\rangle \xrightarrow{\pi/2} |\psi_1\rangle = (|0\rangle - |1\rangle)/\sqrt{2} \xrightarrow{\tau/2} |\psi_2\rangle = (|0\rangle - e^{i\phi}|1\rangle)/\sqrt{2} \\ \xrightarrow{\pi} |\psi_3\rangle &= -(|1\rangle + e^{i\phi}|0\rangle)/\sqrt{2} \xrightarrow{\tau/2} |\psi_4\rangle = -(e^{i\phi'}|1\rangle + e^{i\phi}|0\rangle)/\sqrt{2} = -e^{i\phi}(|0\rangle + e^{i\delta\phi}|1\rangle)/\sqrt{2} \\ &\xrightarrow{\pi/2} |\psi_5\rangle = \frac{e^{i\phi}}{2} \left( (1 + e^{i\delta\phi})|0\rangle + (e^{i\delta\phi} - 1)|1\rangle \right) \end{aligned}$$

where  $\delta\phi = \phi - \phi' \ll \phi, \phi'$ . Finally, the probability for the qubit to be in its excited state is:

$$P_{0 \rightarrow 1}(\delta\phi) = |\langle 1|\psi_5\rangle|^2 = \sin^2\left(\frac{\delta\phi}{2}\right) e^{-(\tau/T_{2E})^\alpha} \quad (3.3)$$

This idea can be extended to any number  $N$  of  $\pi$  pulse in the waiting giving the Carr-Purcell-Meiboom-Gill (CPMG) pulse sequence which increases the decoherence time towards the  $2T_1$  limit.

---

<sup>2</sup> $T_2^* = 2T_1$  if there is no pure dephasing:  $\Gamma_\varphi = 0$

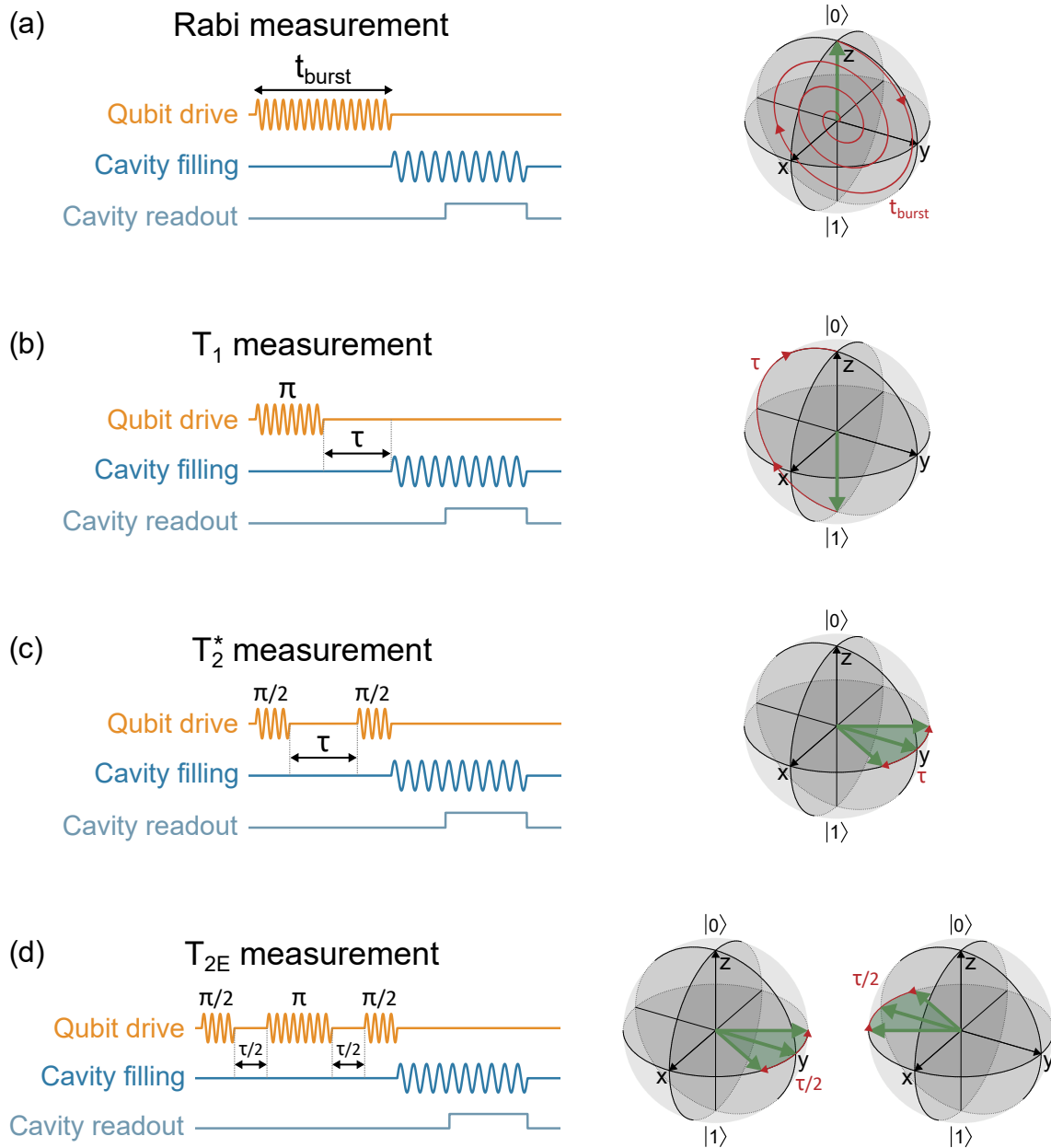


Figure 3.17: **Various pulse sequences for:** (a) Rabi measurement. (b)  $T_1$  measurement. (c)  $T_2^*$  measurement. (d)  $T_{2E}$  measurement. The evolution of the qubit state during the characteristic times is represented in the Bloch sphere.



## Chapter 4

# Towards new mesoscopic QED architectures

Two decades after its introduction, circuit QED is a leading architecture for quantum computing for the reasons that have been detailed in chapter 2. However, its implementation with spin qubits is less straightforward than with superconducting qubits. The need of DC lines complicates indeed a proper RF design required for a high Q cavity. It can be said that since the first coupling of a quantum dot circuit to a cavity [28], this challenge has been overcome with  $Q \sim 5000 - 10000$  [151, 171]. Furthermore, the associated spin-photon coupling strength is too weak ( $g_s \sim 1 - 2$  MHz [151, 152]) to reach the strong coupling regime. Nevertheless, it exists strategies to boost the spin-photon coupling based on the enhancement of the resonator impedance. In the hybrid spin-charge-photon qubit interfaces, the spin-photon coupling strength is indeed a fraction of the charge-photon coupling strength which scales with the square root of the resonator impedance. Such microwave cavities have enabled to reach the strong spin-photon coupling [30–32]. The first part of this chapter aims at presenting the implementation of high impedance resonators with a preliminary development using granular aluminum.

Even though circuit QED enables coupling between distant qubits, in the coplanar waveguide (CPW) based architecture the inter-qubit connectivity tends to be limited to nearest neighbors. A high inter-qubit connectivity is crucial for scale-up perspectives as it minimizes the number of required gates to facilitate the execution of complex quantum algorithms. The second part of this chapter presents a "2.5D" architecture enabling such a high connectivity largely inspired by a ring resonator developed by R. Vijay's group [213].

## 4.1 Increasing the spin-photon coupling with high impedance resonators

Chapter 2 gave a microscopic description of the charge-photon coupling and formula 2.8 highlighted the need of a strong photonic potential gradient between the two dots for reaching a finite value. However, the resonator itself also plays a major role in the final value of  $g_c$ . A CPW cavity sees its associated photonic potential varying from the central conductor to the ground plane by the zero-point fluctuation voltage  $V_{RMS}$ . In the double quantum dot region, the photonic potential varies then by a fraction of  $V_{RMS}$  fixed by the gate geometry but the zero-point fluctuation voltage itself depends on the resonator geometry as:

$$V_{RMS} = \omega_c \sqrt{\frac{\hbar Z_c}{\pi}} \quad (4.1)$$

This potential and therefore in the end the spin-photon coupling can be enhanced by increasing the resonator impedance  $Z_c$ . In the standard CPW architecture, the design sets  $Z_c$  to

50  $\Omega$  for a perfect impedance matching with the available instruments. The following part describes how to enhance the resonator impedance.

#### 4.1.1 Coplanar waveguide resonators

This section aims at introducing the useful concepts of CPW resonators within the framework of an increase of their impedance. A full description of CPW resonators can be found in reference [175, 177]. A CPW resonator is composed of a central track of length  $l = \lambda/2$  and of width  $w$  which is separated from the lateral ground planes by a gap of width  $s$  (see figure 4.1.a). In this work, one has focused so far on a necklace-type  $\lambda/2$  resonator consisting of an open-circuited transmission line capacitively coupled to a CPW transmission line at its two ends. We note that other designs are possible such as the hanger-type  $\lambda/2$  or  $\lambda/4$  resonator [214]. The CPW resonator dimensions defines the physical quantities of interest:

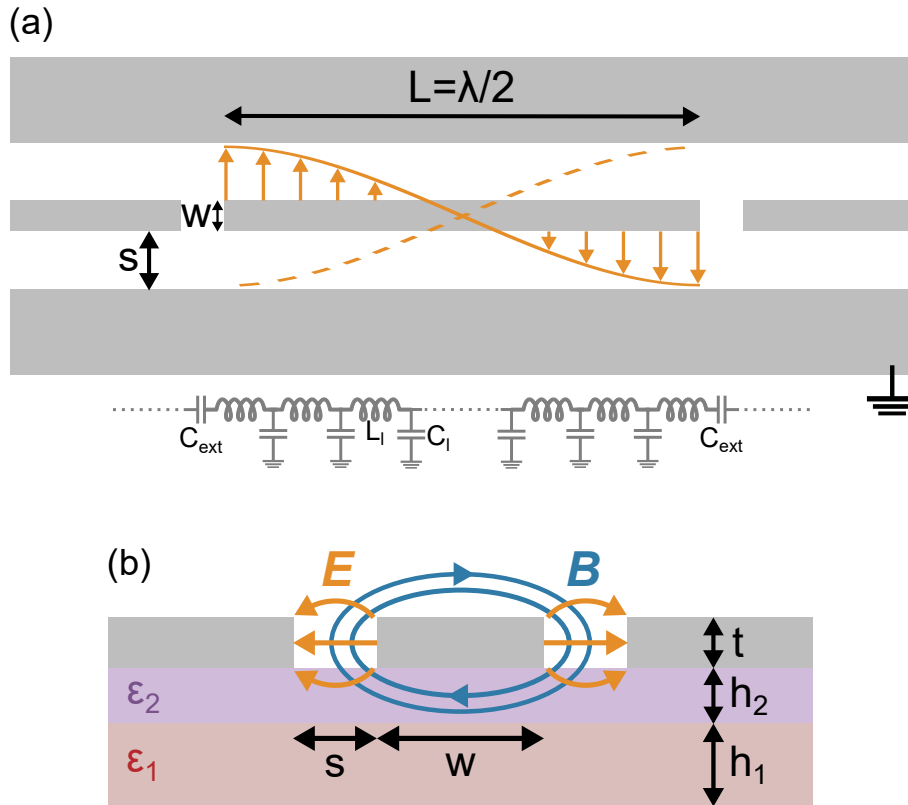


Figure 4.1: **Necklace-type half wavelength CPW resonator:** (a) Schematic layout with characteristic lengths. As the metallic film is superconducting, the equivalent lumped element circuit is a parallel LC circuit capacitively coupled to a transmission line. (b) Cross-section of the CPW resonator with schematic representations of the electric and magnetic field distributions.

the cavity resonance frequency  $f_c$  and the impedance  $Z_c$  [175]:

$$f_c = \frac{c}{\sqrt{\epsilon_{eff}} 2L} \quad (4.2)$$

$$Z_c = \sqrt{\frac{L_l}{C_l}} \quad (4.3)$$

where  $c$  is the speed of light in vacuum and  $\epsilon_{eff}$  is the effective permittivity of the CPW line defining the phase velocity as:  $v_{phi} = c/\sqrt{\epsilon_{eff}} = 1/\sqrt{L_l C_l}$ . The expression of  $\epsilon_{eff}$  which depends on variables depicted on figure 4.1.b can be obtained with formula 2.15 of reference [215].  $L_l$  and  $C_l$  are for themselves the inductance and capacitance per unit length of the resonator (see figure 4.1.a). Their expression can be found using conformal mapping theory:

$$L_l = \frac{\mu_0}{4} \frac{K(k'_0)}{K(k_0)} \quad (4.4)$$

$$C_l = 4\epsilon_0 \epsilon_{eff} \frac{K(k_0)}{K(k'_0)} \quad (4.5)$$

where the arguments of the complete elliptic integral of the first kind  $K^1$  are:  $k_0 = w/(w + 2s)$  and  $k'_0 = \sqrt{1 - k_0^2}$ . With those formula, one can see how the track and gap widths  $w$  and  $s$  affect the resonator impedance (see figure 4.2). For reasonable dimensions, one can reach  $Z_c = 180 \Omega$  which barely corresponds to a doubling of the charge-photon coupling strength.

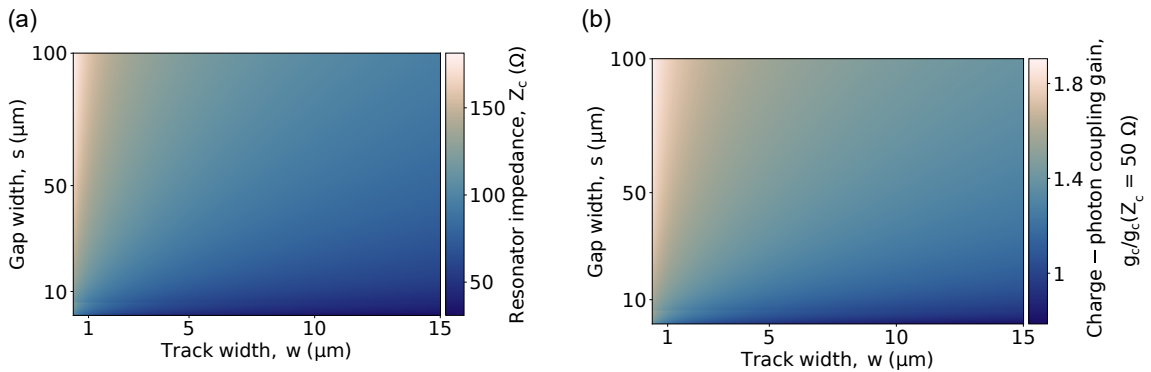


Figure 4.2: **Influence of the CPW dimensions:** (a) CPW resonator impedance  $Z_c$  ( $\Omega$ ) as a function of the track and gap width  $w$  and  $s$ . (b) Charge-photon coupling gain in comparison with a standard  $50 \Omega$  resonator.

---

<sup>1</sup> $K(k) = \int_0^{\pi/2} (1 - k^2 \sin^2(\theta))^{-1/2} d\theta$

The kinetic inductance contribution has however been neglected so far. It arises from the kinetic energy stored in the motion of the charge carriers. For a superconducting resonator, the kinetic inductance can be expressed as [216]:

$$L_k = \mu_0 \lambda_L \frac{L}{wt} \quad (4.6)$$

where  $\lambda_L$  is the London penetration depth evaluated to  $\sim 40$  nm for Nb [217]. In equation 4.3,  $L_l$  has thus to be replaced by  $L_l + L_k/L$ . Calculations shown in figure 4.2 considers a  $t = 100$  nm Nb thick film. In those conditions, considering the kinetic inductance modifies the resonator impedance by less than 2%. One can still decrease the film thickness for more significant change. This enables to reach  $Z_c = 200 \Omega$  for  $t = 15$  nm and corresponds to a factor two for the charge-photon coupling strength. These geometric changes have enabled to reach the strong spin-photon coupling regime with  $w = 0.6 \mu\text{m}$ ,  $s = 20 \mu\text{m}$  and  $t = 50$  nm [30] but another resource of leverage exists for more significant impedance enhancement.

#### 4.1.2 High impedance resonators

One has so far considered the use of Nb but it exists disordered superconductors which shows high kinetic inductance values which overwhelms the gain one obtains with geometrical changes. Among them one notably finds NbN [218–220], NbTiN [32, 221, 222], TiN [223] and Granular aluminium (grAl) [224, 225]. Array of Josephson junctions also results in high impedance resonators [172]. With those new materials, one can easily reach  $Z_c = 4 - 6 \text{ k}\Omega$  which corresponds to an increase of one order of magnitude of the charge-photon coupling. The ultra-strong coupling regime has been reached with a charge qubit coupled to a Josephson junction array resonator with a coupling strength  $g_c \sim 630 \text{ MHz}$  [82]. However, as opposed to disordered superconductors, this kind of resonator is not resilient to magnetic field making it not suitable for most spin qubit implementations. The highest reported spin-photon coupling has been obtained with a hole spin coupled to a NbN resonator and reaches:  $g_s \sim 330 \text{ MHz}$  [163]. This architecture has also enabled coherent coupling between distant spins [156].

These new materials have proved to enhance the spin-photon coupling nonetheless, this comes at a certain cost. First of all, a higher impedance results in a higher capacitive coupling between metallic structures. The microwave leakage of the cavity through the DC lines is then enhanced and the cavity quality factor decreased. To remedy this, on-chip low pass filters can be implemented with interdigitated or thin-film capacitors and spiral inductors or nanowires [34, 163, 171, 220]. Secondly, the nanofabrication of a high impedance resonator is much less straightforward than a standard Nb one. The film properties have to be well characterized to properly adapt the on chip transmission line dimensions to match the  $50 \Omega$

impedance of the RF measurement setup. Finally, with such high impedances, the resonator length gets smaller ( $L \sim 0.25 - 1$  mm) which lower the number of qubits one can couple to the same resonator and thus the inter-qubit connectivity.

As mentioned above, the challenge with such high impedance is to still reach a high quality factor  $Q = \omega_c/\kappa$  where  $\kappa$  is the total cavity decay rate (see section 2.3.1). It can be decomposed as  $\kappa = \kappa_{\text{int}} + \kappa_{\text{ext}}$  where  $\kappa_{\text{int}}$  is the internal loss rate and  $\kappa_{\text{ext}}$  is the external one. One can equivalently express the associated quality factors as:

$$\frac{1}{Q} = \frac{1}{Q_{\text{int}}} + \frac{1}{Q_{\text{ext}}} \quad (4.7)$$

In addition to microwave leakage, the internal losses can arise from resistive [226] and dielectric [222] losses. The external losses are for themselves linked to the coupling with the transmission line through the capacitance  $C_{\text{ext}}$  and reads:

$$\kappa_{\text{ext}} = \frac{4}{\pi} \omega_c^3 Z_c Z_0 C_{\text{ext}}^2 \quad (4.8)$$

The coupling between the resonator and the transmission line has been optimized for the standard 50  $\Omega$  CPW design [175] but has now to be adapted. One can define three distinct coupling regimes. The resonator can be overcoupled to the transmission line ( $\kappa_{\text{ext}} \gg \kappa_{\text{int}}$ ). In this regime, the cavity resonance frequency depends linearly on the capacitive coupling to the transmission line  $C_{\text{ext}}$  [175] and its quality factor is also set by  $C_{\text{ext}}$  as:  $Q \propto 1/C_{\text{ext}}^2 \ll Q_{\text{int}}$  resulting in a high signal to noise ratio desirable for readout. The photon lifetime is however not maximized as opposed to the undercoupled regime:  $\kappa_{\text{ext}} \ll \kappa_{\text{int}}$ . In this regime, the cavity quality factor saturates:  $Q = Q_{\text{int}}$  which is desirable for a quantum bus but the transmission is significantly reduced. In order to benefit from both advantages, we try to reach the critical coupling regime:  $\kappa_{\text{ext}} \sim \kappa_{\text{int}}$ .

Figure 4.1.a represents the necklace-type of coupling that one has considered so far. One introduces here the hanger-type one (see figure 4.3.a). In this configuration, the transmission line is continuous and one end of the resonator is brought close to it to enable driving the antinode of the  $\lambda/2$  resonator. This configuration enables to couple several resonators to the same transmission line which is desirable for parallel tests [219, 220, 222]. This results in a different transmission expression [227]:

$$T = \left( 1 + \frac{Q_{\text{int}}}{Q_{\text{ext}}} e^{i\phi} \frac{1}{1 + i2Q_{\text{int}}\delta x} \right)^{-1} \quad (4.9)$$

where  $\delta x = (f - f_c)/f_c$  and  $\phi$  is the impedance mismatch angle.

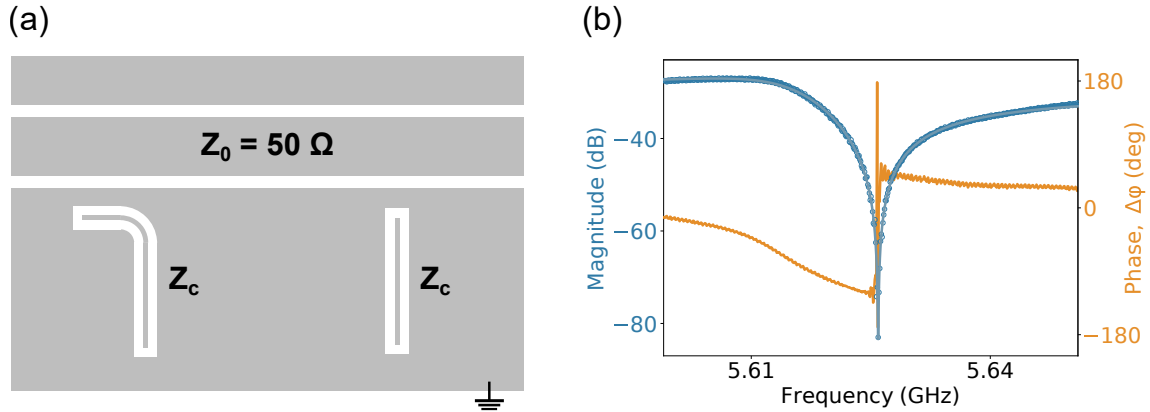


Figure 4.3: **Hanger-type of coupling:** (a)  $\lambda/2$  CPW resonators of impedance  $Z_c$  are capacitively coupled to a continuous transmission line of impedance  $Z_0 = 50 \Omega$ . (b) The transmission of the line reminds a notch filter behavior. One sees a deep at the resonator resonance frequency corresponding to energy stored in the resonator. By fitting the magnitude, one can extract:  $Q_{\text{int}} = (9.5 \pm 0.6) \times 10^4$  and  $Q_{\text{ext}} = 200 \pm 2$ . (sample 4 test 6)

### 4.1.3 Preliminary developments using granular aluminum

In the group, a granular aluminum evaporation recipe has been developed for the fabrication of magnetic field resilient superconducting circuits [212] in the context of a dark matter detection experiment. This has naturally guided our choice of material for the high impedance resonator.

#### Nanofabrication

Granular aluminum (grAl) belongs to the so-called disordered or dirty superconductors [228] whose crystalline defects or dopants introduction reduces the coherence length and quasi particle mean free path. In this particular case, it is question of uniform aluminum grains separated by Josephson contacts [229] which can be described by an effective Josephson junctions chain in the case of a resonator geometry [230]. The CPW resonators fabrication starts from a bare  $10 \text{ mm} \times 10 \text{ mm}$  chip . A 30 nm thick grAl film is deposited by evaporating aluminum in an  $\text{O}_2$  atmosphere. The film properties are very sensitive to the oxygen pressure inside the chamber which is set to  $P_E = 1.2 \times 10^{-5}$  mbar and the rate at which is evaporated the aluminum set to  $1.9 \text{ \AA/s}$  (see table 4.1). Those variables indeed defines the film resistivity  $\rho_{\text{grAl}}$  which has to be sufficiently high to bring a large kinetic inductance contribution but below the critical point where the film turns insulating:  $\rho_{\text{Al}} = 2.8 \mu\Omega.\text{cm} \ll \rho_{\text{grAl}} < \rho_{\text{crit}} \sim 10^4 \mu\Omega.\text{cm}$  [231]. In order to be on the safe side, we target  $\rho_{\text{grAl}} \sim 10^3 \mu\Omega.\text{cm}$  which is checked afterwards. The second step consists in patterning the transmission line and the CPW resonator. The film is first characterized at room temperature

see section 4.1.3 to adjust the aspect ratio for a  $50 \Omega$  transmission line patterned using e-beam lithography after a PMMA 500 resist spin-coating. The gap of the CPW is then defined by removing grAl with a physical Ar etching in a RIE chamber. In order to work with an easy nanofabrication recipe, reasonable aspect ratio have been considered for the CPW resonator. With a track width  $w = 2 \mu\text{m}$  and a gap width  $s = 40 \mu\text{m}$ , the whole exposure can be done using only the biggest aperture of the e-beam.

### Room temperature characterization

As mentioned previously, the grAl resistivity is very sensitive to the evaporation conditions. This results in a large variability from a sample to another. Once the grAl is deposited on the substrate, a room temperature characterization enables yet to measure the resistivity which can be linked to the kinetic inductance of the film through the Mattis-Bardenn theory. The van der Pauw measurement technique is used for that purpose.

The 30 nm thick  $10 \text{ mm} \times 10 \text{ mm}$  grAl film is characterized at the probe station with a four point measurement. For this, four ohmic contacts are placed on the four corners as close as possible to the boundary. A current  $I_{12}$  (typically  $10 \mu\text{A}$ ) is injected into contact 1 and taken out of contact 2. The voltage  $V_{34}$  is measured between contacts 3 and 4. From this, one can extract a resistance value  $R = V_{34}/I_{12}$  which can be more accurate by repeating this measurement for the other symmetrical configurations before averaging. The van der Pauw method enables to obtain the sheet resistance and the resistivity:

$$R_{\square} = \frac{\pi R}{\ln(2)} \quad (4.10)$$

$$\rho_{grAl} = R_{\square} t \quad (4.11)$$

Several grAl depositions reported in table 4.1 have been done resulting in a large variability of the measured sheet resistance and resistivity. The film properties are so sensitive to the evaporation conditions that even films deposited at the same time present a variability (samples 5 and 6). This can be explained by the  $\text{O}_2$  gradient in the chamber during the evaporation. Thermal annealing which has not been explored here enables to lower and stabilize the sheet resistance [232].

Sample	O <sub>2</sub> pressure (mbar)	Rate (Å/s)	R <sub>□</sub> (kΩ/□)	ρ <sub>grAl</sub> (μΩ.cm)
1	1.3 × 10 <sup>-5</sup> mbar	1.67	1.47	4.42 × 10 <sup>3</sup>
2	1.4 × 10 <sup>-5</sup> mbar	1.76	0.144	4.32 × 10 <sup>2</sup>
3	1.3 × 10 <sup>-5</sup> mbar	1.69	10.5	3.16 × 10 <sup>4</sup>
4	1 – 1.2 × 10 <sup>-5</sup> mbar	1.71	2.62	7.86 × 10 <sup>3</sup>
5a	1.2 × 10 <sup>-5</sup> mbar	1.70	2.86	8.58 × 10 <sup>3</sup>
5b	-	-	3.17	9.50 × 10 <sup>3</sup>
5c	-	-	2.68	8.04 × 10 <sup>3</sup>
6a	1.2 – 1.4 × 10 <sup>-5</sup> mbar	1.78	0.354	1.06 × 10 <sup>3</sup>
6b	-	-	0.372	1.12 × 10 <sup>3</sup>
6c	-	-	0.422	1.27 × 10 <sup>3</sup>

Table 4.1: Sheet resistance and resistivity of several grAl films evaporated in different conditions. The colored resistivity result in an isolating film according to [231].

### Low temperature characterization

The previous characterization can also be done as a function of the temperature. This highlights the superconducting transition from which the critical temperature T<sub>c</sub> (associated to a given resistivity) can be extracted. Such characterization has not been done but in the literature it has been shown that T<sub>c</sub> with respect to the resistivity presents a dome shape centered around ρ<sub>grAl</sub> ∼ 4 – 6 × 10<sup>2</sup> μΩ.cm with T<sub>c</sub> ∼ 2 – 3 K [231, 233, 234]. This value is larger than the critical temperature of pure aluminum (T<sub>c</sub> = 1.2 K). This critical temperature combined with the sheet resistance enables to estimate the sheet kinetic inductance [235]:

$$L_{k,\square} = L_k \frac{w}{L} = \frac{\hbar R_{\square}}{\pi \Delta_0} \quad (4.12)$$

where Δ<sub>0</sub> = 1.76k<sub>B</sub>T<sub>c</sub> is the superconducting gap whose factor 1.76 is known as the BCS ratio [236]. This ratio is supposed constant for all BCS superconductors but in the case of grAl, it starts to increase from ρ<sub>grAl</sub> ≈ 3 – 8 × 10<sup>2</sup> μΩ.cm up to ∼ 2.1 [231]. Finally, the resonator impedance can be determined:

$$Z_c = \sqrt{\frac{L_l + L_{k,\square}/w}{C_l}} \quad (4.13)$$

Most of RF tests have been done with grAl film that have been deposited in the same evaporation than sample 4 (see table 4.1). With such a resistivity, one can estimate Z<sub>c</sub> ∼ 3.6 kΩ which represents a factor ∼ 8.5 for the charge-photon coupling. This sets the resonator length to L = 400 μm for a fundamental mode at 5 GHz. The transmission line gap width is fixed to

$s_{\text{TL}} = 2 \mu\text{m}$  and the track width is then set to  $w_{\text{TL}} = 1100 \mu\text{m}$  which results in a  $Z_0 \approx 60 \Omega$  impedance. A perfect impedance matching ( $Z_0 = 50 \Omega$ ) would have implied  $w_{\text{TL}} \sim 2000 \mu\text{m}$  which was not suitable for the test design. The development test chip includes two transmission lines (see figure 4.4.a). A single CPW resonator is coupled to the first one for a reference. Eight resonators of different length  $L \in [200, 550] \mu\text{m}$  are coupled with different capacitive coupling to the second transmission line. The idea is to identify the eight resonances thanks to a previous measurement with the reference and to determine the proper coupling design. This characterization also enables to properly determine the associated kinetic inductance of which we only have a vague estimation with the characterization described above.

The first results are hard to interpret and a full understanding and design optimization would require further developments. Nevertheless, they have enabled to highlight the potential issues and the path to follow to remedy this. The RF transmission of the straight transmission line displays many deeps (see figure 4.4.c) which can not all match the predicted resonance frequencies (orange and red dots) even by adjusting the estimated impedance (here  $Z_c \sim 3.6 \text{ k}\Omega$ ). For better understanding, the curved transmission line which should only present a single deep has been measured. This has however also led to a RF transmission with many deeps. Two reasons could explain this issue. First, some of the modes are package mode that couple to the transmission line. During the cool-down, one can identify some of them that do not disperse with the temperature. Secondly, as the impedance is high, this could lead to parasitic coupling between different design elements resulting in a much more complex overall behavior. Chip 6c has been designed with only one transmission line and one resonator but presented two different deeps which can not be identified as a fundamental mode with its first harmonic.

Another interesting feature is to look at the resonances behavior as function of the cavity power and the magnetic field (see figure 4.5). Among the resonances, some show high dependence of their resonance frequency with the number of photons in the cavity (see figure 4.5.a). This witnesses a non-linear behavior of the resonator which can be explained by the highly inductive grAl film. Even though an accurate value for the kinetic inductance could not be determined, this qualitative data are a step in the right direction. Those high impedance resonators also have the good taste to be resilient to in-plane magnetic field  $B_{\parallel}$  up to several tesla [219, 221, 222, 225]. This is especially the case as the central track width  $w$  gets smaller as vortex nucleation takes less and less place. Figure 4.5.c does not show such a resilient behavior except for one resonance ( $f_c \sim 8 \text{ GHz}$  @0 mT) whose internal quality factor  $Q_{\text{int}}$  is tracked and displayed on figure 4.5.d. Usually, with such resonators  $Q_{\text{int}}$  remains constant

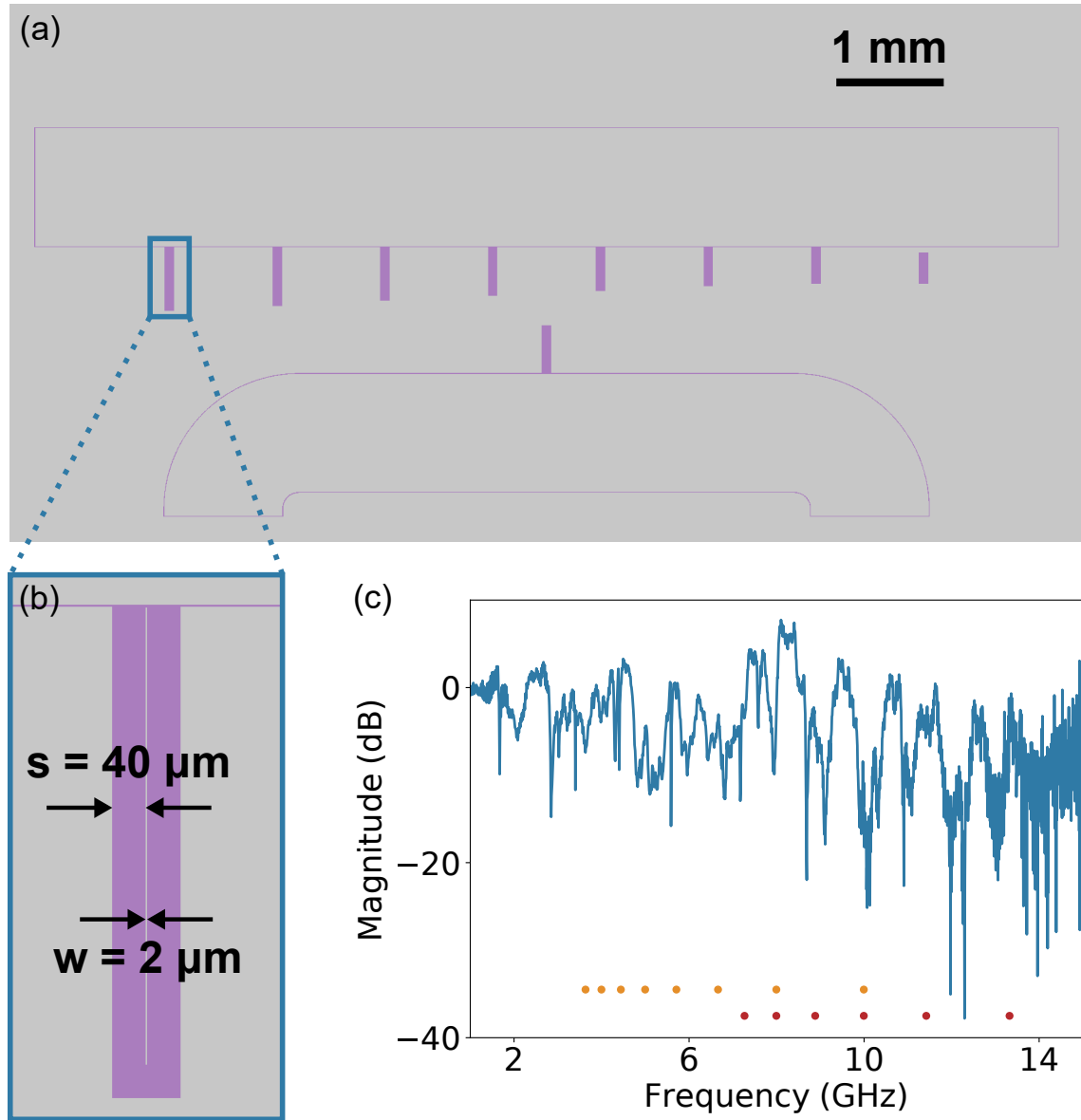


Figure 4.4: **GrAl test chip design:** (a) The chip includes two transmission lines: eight resonators are coupled to the first one and a single one is coupled to the other as a reference. (b) Zoom on the longest resonator which is the closest to the transmission line. The distance separating both central tracks varies from  $3 \mu\text{m}$  (on this picture) to  $100 \mu\text{m}$ . (c) Microwave transmission through the straight transmission line. The orange and red dots indicate where the fundamental mode and first harmonic of the eight resonators should figure by considering  $Z_c \sim 3.6 \text{ k}\Omega$ . The slope corresponding to the cable attenuation has been subtracted for more clarity. (sample 4 test 6)

with respect to the in-plane magnetic field except at a given magnetic field corresponding to a resonant coupling with the magnetic impurities which lower the internal quality factor. Here  $Q_{\text{int}}$  increases with  $B_{\parallel}$  up to decrease and stabilizes.

As a conclusion, the chosen design (see figure 4.4) complicates the data interpretation with many expected resonances (fundamental modes and harmonics). The fitting of various transmissions have highlighted that the chosen coupling distances correspond to an overcoupled regime:  $Q_{\text{ext}} \sim 10 - 200 \ll Q_{\text{int}} \sim 10^3 - 10^4$ . Finally, even though granular aluminum easily provides large kinetic inductance, the film properties are really different from one sample to another which makes a full mesoscopic-QED architecture development very challenging. In addition, it has been shown that grAl resonators are limited by the quasiparticles dynamic [237]. The choice of another material such as NbN seems more suitable for further developments. On another note, recent results have shown the potential of anti-squeezing for a dynamically enhanced qubit-photon interaction [238].

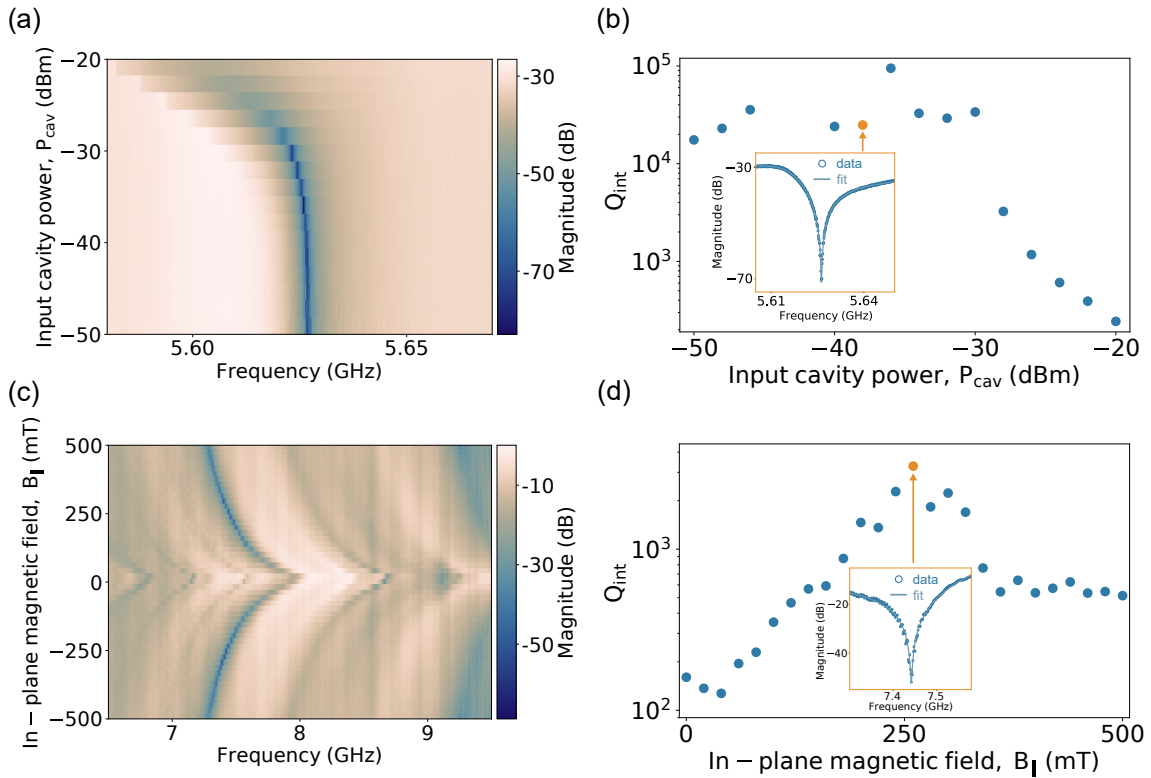


Figure 4.5: **GrAl resonators characterization:** (a) Power dependence of the resonance showing the strongest dispersion. (b) Tracking of the internal quality factor  $Q_{\text{int}}$  as a function of the cavity power.  $Q_{\text{int}}$  collapses above -30 dBm. The data and fitting curve of a given power (orange point) are also displayed. (c) In-plane magnetic field dependence of several resonances.  $Q_{\text{int}}$  rapidly falls down with one exception. The slope corresponding to the cable attenuation has been subtracted for more clarity. (d)  $Q_{\text{int}}$  tracking of the magnetic field resilient resonance ( $f_c \sim 8$  GHz @0 mT). The data and fitting curve of a given magnetic field (orange point) are also displayed. (sample 4 test 6)

## 4.2 Multiplexing with a "2.5D cavity"

### 4.2.1 Motivations

Chapter 2 has introduced circuit-QED as a scalable architecture towards quantum computation with the possibility of coupling distant qubits. However, most of quantum processors shows an inter-qubit connectivity limited to nearest neighbors because of spatial constraints on the chip layout (figure 4.6.a). This is also the case for the most advanced such as the the 72-qubit Sycamore device (Google) [27] or the 127-qubit Eagle device (IBM) [6]. This geometrical issue can somehow be circumvented by placing several qubits at the anti-nodes of the resonator playing the role of quantum bus [239] (figure 4.6.b). Unwanted cross-talk and variable coupling between qubits are the prices to pay with such a compact design. Reference [213] proposes to get rid of these issues by using a ring resonator as a cavity bus with qubits spatially separated around its circumference (figure 4.6.c). In this architecture, each of the 12 qubits has its own readout resonator for individual addressability. The inter-qubit coupling depends on their frequency and on their angular spacing in the ring. A regime can be found where the inter-qubit coupling only takes two values and has been confirmed experimentally.

This ring resonator architecture can be envisioned with any kind of quantum processor that rely on a microwave resonator as quantum bus. The ferromagnetic spin qubit (see section 1.3.2) can thus be seen at larger scale in such a coupling scheme. Furthermore, a 3D circuit-QED architecture would enable to decouple the RF part and the DC part of the current chip layout for a strong modularity. Next section presents how this ring resonator can be adapted to our spin-qubit architecture.

### 4.2.2 Designing a "2.5D cavity"

The ring resonator cavity bus [213] can not be used as it is with our spin qubit architecture. The needs of DC lines and of a vacuum tight sample holder strongly constraint the geometry. The will for compatibly with current setups such as the stapler or the  $^3\text{He}$  fridge have led us to replace the ring by a  $\lambda/2$  resonator for the first version that we call the "2.5D cavity" as it figures in between a 2D CPW and 3D architecture. The design provides four qubit slots but first of all only two of them will be used (see figure 4.7.a). Moreover, the  $^3\text{He}$  fridge only owns 12 DC lines whereas 14 are needed for controlling and measuring two double quantum dots. This is circumvented by making the gamma left and right gates of the two DQD share the same DC line ( $V_{\Gamma_{L,1}} = V_{\Gamma_{L,2}}$  &  $V_{\Gamma_{R,1}} = V_{\Gamma_{R,2}}$ ). Each slot includes a  $\lambda/4$  resonator and an RF line at its anti-node for individual driving and qubit readout. The  $\lambda/2$  resonator

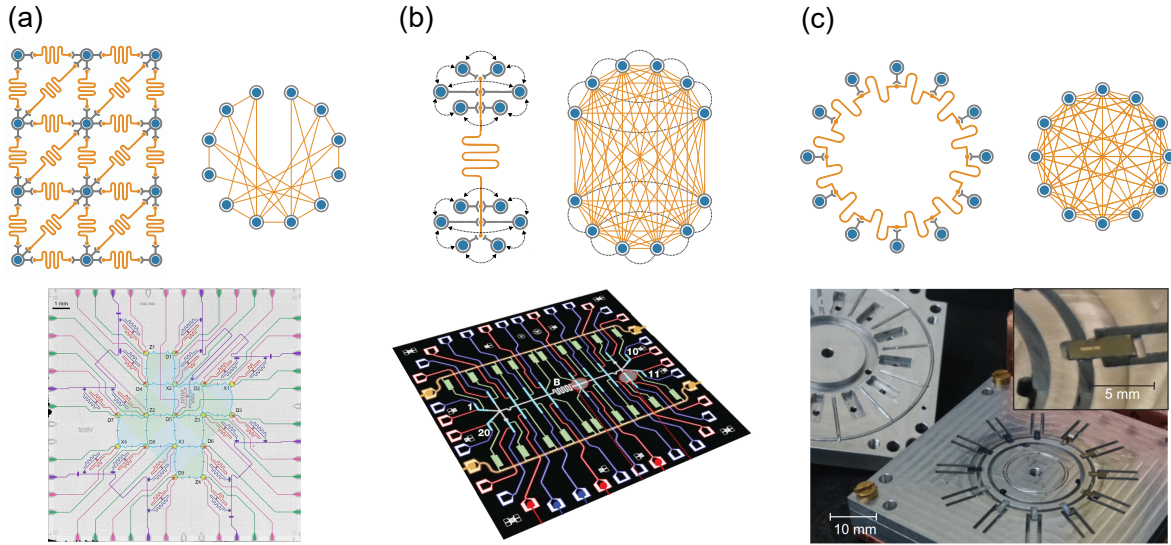


Figure 4.6: **12 qubits connectivity in various circuit-QED architectures with coupling scheme, connectivity graph and example of associated device:** (a) Coupling scheme limited to nearest neighbors largely used in quantum processors. The sample shown uses this architecture with 17 qubits [26]. (b) All-to-all connectivity enabled by coupling all qubits to the same resonator. The topology constraints results in parasitic couplings between neighbor qubits. This is represented by the black arrows/lines. This coupling scheme has been realized with 20 qubits [240]. (c) A novel coupling scheme based on a ring resonator enables high inter-qubit connectivity with negligible cross-talk. This 3D architecture is designed to host 12 qubits and enables to couple each of them to 9 others [213].

also includes two RF lines at its two ends to also enable driving and readout of all qubits. Concerning the chip itself, it has to be modified to enable the quantum dot circuit to couple to the cavity electric field. This is realized thanks to two antennas (see figure 4.7.b) which are arranged as in the transmon qubit design of [213]. Each of them is respectively connected to the source and drain electrode of the quantum dot circuit (see figure 4.7.c).

The design shown in figure 4.7 shows the general idea but before manufacturing such a device, the resonators lengths should be properly calibrated to result in adequate resonance frequencies. For this purpose, one uses Ansys HFSS: an EM finite-element simulation software. In the simulations, the device includes the metal copper parts<sup>2</sup>, four  $2\text{ mm} \times 5\text{ mm}$  silicon chips and two sapphire chips of the same dimensions used to maintain the  $\lambda/2$  resonator (see figure 4.8.a). Several notches are done in the metal parts for hosting the chips. The sample holder width constrains the maximal bus resonator length to  $L_{\lambda/2} = 16\text{ mm}$  which corresponds to a fundamental mode at 6.7 GHz. The corresponding electric field magnitude distribution is simulated and plotted on figure 4.8.b. The  $\lambda/4$  for themselves present a resonance fre-

<sup>2</sup>Using a superconducting metal would be more favorable but would leave the possibility for applying magnetic field.

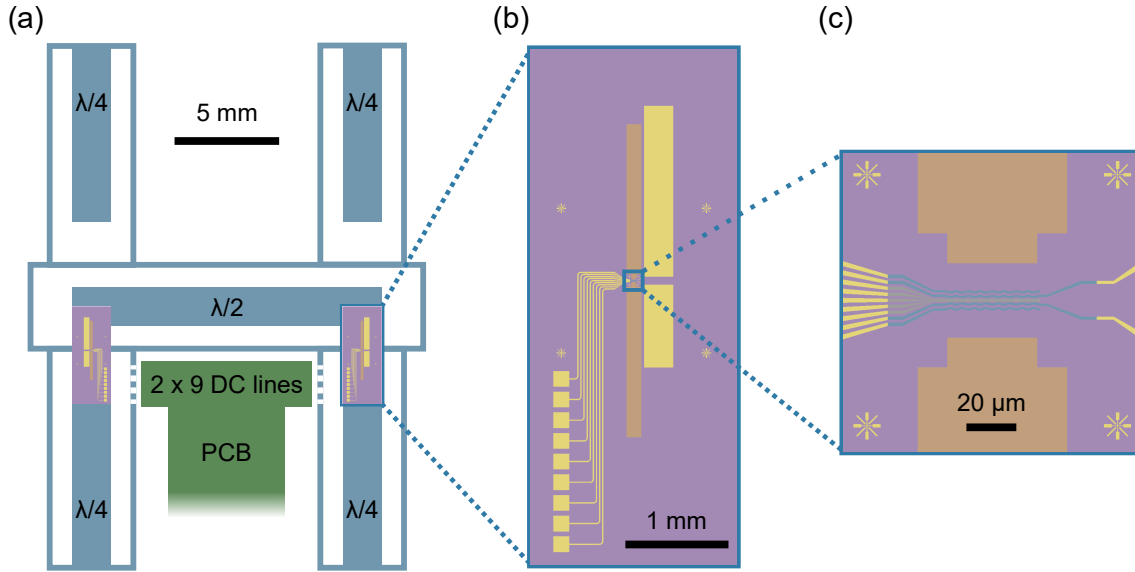


Figure 4.7: "2.5D cavity" design: (a) Overview of the adapted cavity bus architecture. The first version includes two qubits which can be coupled via the  $\lambda/2$  resonator. Additionally to the individual  $\lambda/4$  resonators, it can also be used for reading and driving the qubits. (b) The chip design is much more simple as the complex CPW architecture has been removed. Two antennas are nevertheless added to bring the cavity electric field in the vicinity of double quantum dot circuit. The trenches are still present to enable the carbon nanotube transfer. (c) Zoom on the carbon nanotube integration region. The DC signals are carried by the lines on the left and the RF ones by the ones on the right.

quency at 7.3 GHz with  $L_{\lambda/4} = 9$  mm. Afterwards, one introduces the two antennas in the simulations to optimize their geometry and position. From the electric field distribution, one can indeed integrate it between the two antennas and obtain an electric potential  $V$  which sets an upper bound for the photonic potential gradient between the two dots and thus the charge-photon coupling strength:

$$\hbar g_c \leq eV = e \int_{\text{antennas gap}} E_x dx \quad (4.14)$$

This electrostatic potential  $V$  has then to be as large as possible to ensure in the end a suitable spin-photon coupling. After some optimization, the  $\lambda/2$  and  $\lambda/4$  modes result in a potential between the antennas about  $1.1 \mu\text{V}$  and  $0.5 \mu\text{V}$ . This corresponds to an upper bound for the charge-photon coupling strength of 270 MHz and 120 MHz.

Once the design has been optimized, the mechanical drawings of the different parts can be initiated. The will of having a vacuum tight sample holder combined with very limited RF leaks or cross talks between the resonators makes the design really challenging. A perfect sealing of the sample holder cover indeed implies mechanical tolerance opening gaps for the

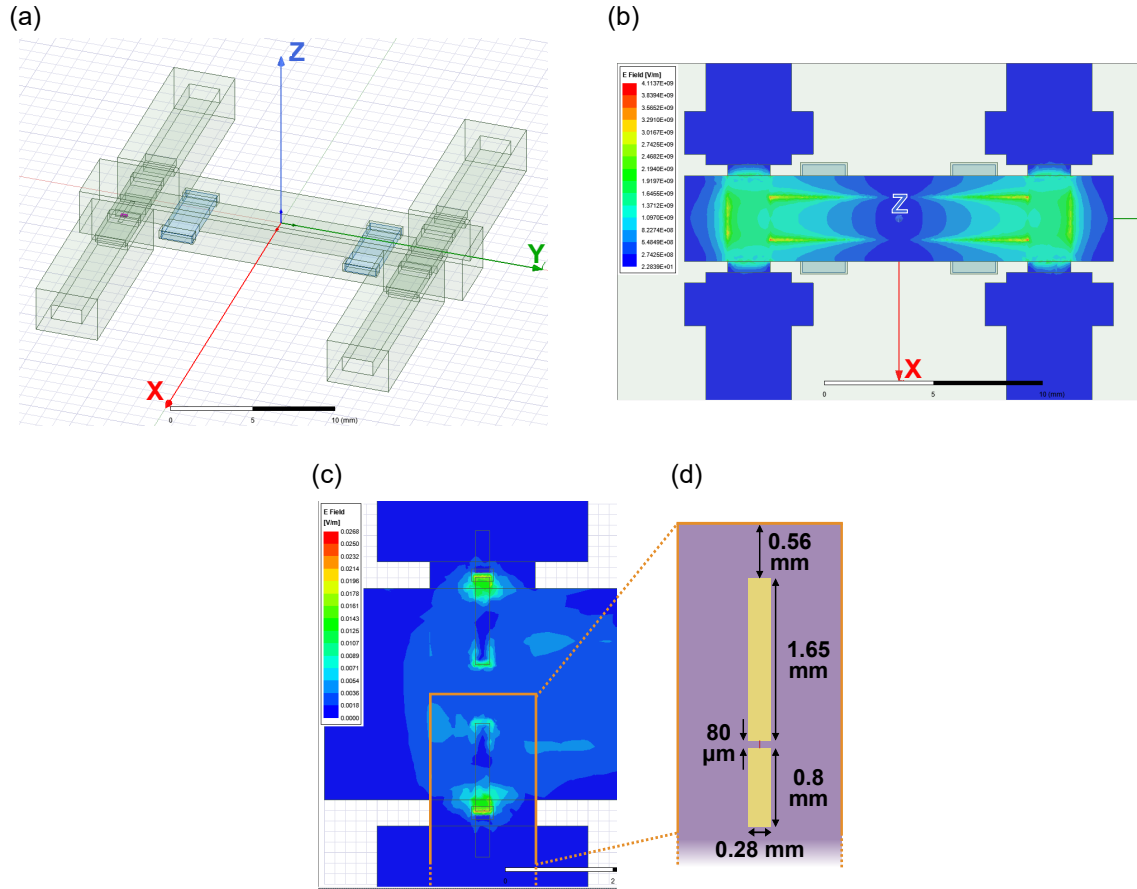


Figure 4.8: **Simulations for "2.5D cavity" design:** (a) Geometry considered for the simulations. The two sapphire chips (in blue) hold the  $\lambda/2$  resonator. (b) Electric field magnitude distribution of the fundamental mode of the  $\lambda/2$  resonator with four bare silicon chips. (c) Electric field magnitude distribution of the fundamental mode of the  $\lambda/2$  resonator with the introduction of two antennas on each chip. The field is mostly localized in between the antennas gap. (d) Antennas dimensions and positioning for a maximal charge-photon coupling. This is obtained by calculating the electric potential  $V$  for various configurations by integrating the electric field along the red segment in between the two antennas.

electric field to leak out. Before fabricating the sample holder, a sanity check is to import the CAO file in the Ansys HFSS simulation software and verify if the simulations give the same result than before. The resulting sample holder enabling the integration of two chips is shown in figure 4.9.

### 4.2.3 Experimental realization

After mounting this sample holder, the next step is to characterize its proper functioning. The semi-rigid cables central pin are first intentionally let too long. The transmission line is then overcoupled to the cavity. The central pins lengths are step by step reduced until reaching the

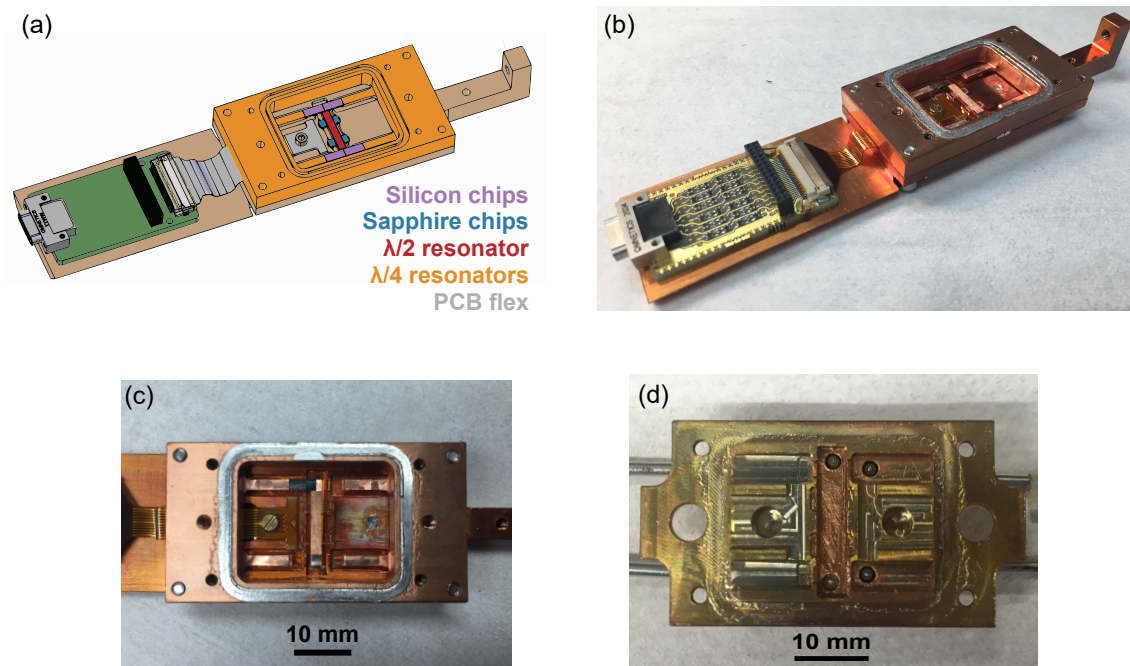


Figure 4.9: **Mechanical parts constituting the "2.5D cavity"**: (a) 3D drawing of the sample holder without the cover. Source: P. Morfin. (b) Assembled sample holder without the cover. (c) Zoom over the sample holder with one chip placed at the upper slot. (d) Bottom of the sample holder cover partly defining the resonators. Semi-rigid RF cables are placed in the holes located at the modes's anti-nodes.

critical coupling. We observe a shift of the resonance frequency combined with an increase of the quality factor  $Q$ . Those changes are less and less significant as we approach the critical coupling. In the absence of chips, at room temperature, the  $\lambda/2$  cavity bus resonates at 8.42 GHz with a corresponding quality factor  $Q = 715$  (see figure 4.10.b). Another advantage of using such a resonator is to provide a very controlled RF environment. Package modes are indeed suppressed as the whole volume defines the mode of interest (see figure 4.10.a). The introduction of chips in the sample holder reduces the resonance frequency as it increases the effective permittivity. However, it also considerably reduces the quality factor through dielectric losses and leakage (see figure 4.10.c). The RF leaks are even more problematic since the chip DC pads are wire-bounded to the PCB resulting in a very low quality factor:  $Q \approx 40$ . Finally, we also observe non negligible cross-talks between the four ports. Both chip and sample holder design have then to be reconsidered to envision readout via the cavity.

By removing the microwave cavity from the chip, we also naively ignored the issues faced in a mesoscopic-QED architecture. The chip has indeed been designed as if it only had to handle DC signals. The antennas and unfiltered DC lines are defined by a Ti/Au 5/45 nm thick film which emphasizes resistive losses and RF leakage. This last point has also been highlighted

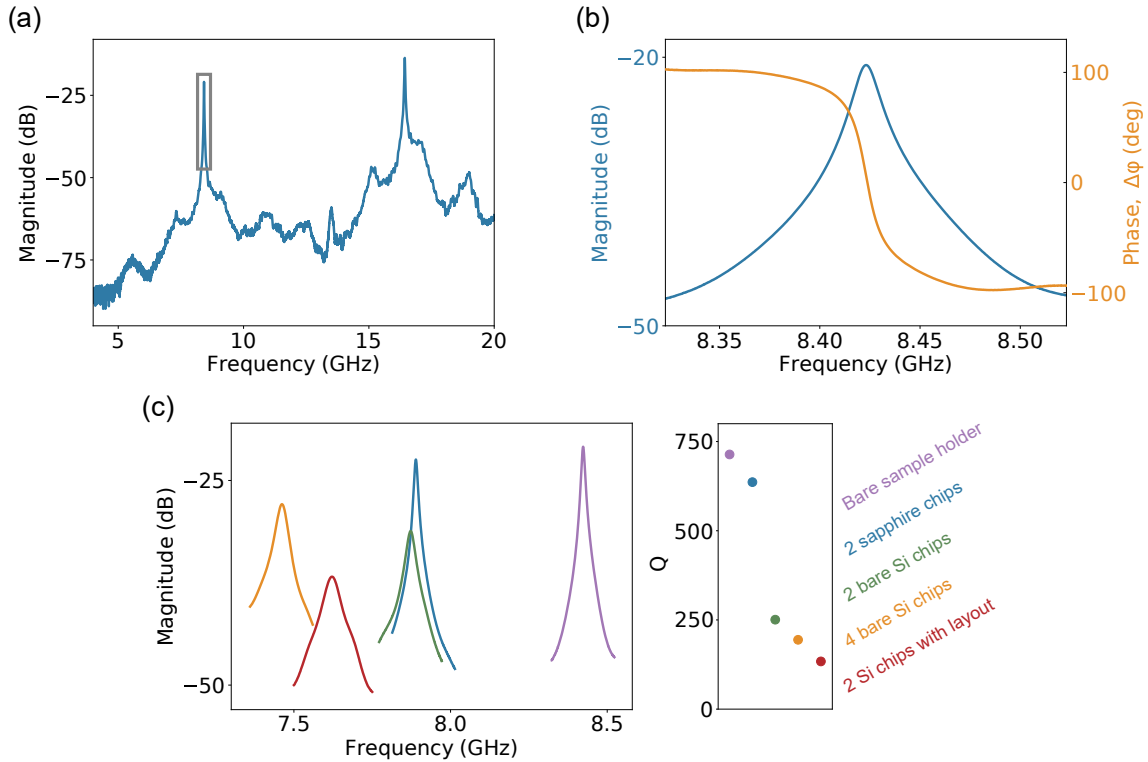


Figure 4.10: **Room temperature RF characterization:** (a) RF transmission of the bare  $\lambda/2$  resonator. The background is transmitted more than 30 dB below the cavity mode. (b) Zoom in the grey box showing magnitude and phase close the cavity resonance frequency. (c) Tracking of the transmission at resonance and associated quality factor with the introduction of chips in the sample holder.

by considering partial design of the chip in the Ansys HFSS simulations instead of the two antennas only (see figure 4.11.a). The chip layout has then been modified by introducing a ground plane and an interdigitated low-pass filter on each line, the whole in Nb (figure 4.11.b). The sample holder has also been modified to end up with the simplest version as possible to minimize RF leakage (figure 4.11.c). The two unused slots and the  $\lambda/4$  resonators have been removed. An RF line still provides fast driving on each slot but the readout is only possible via the  $\lambda/2$  cavity bus. Small issues have also been solved such as the PCB/chip height difference making the wire-bonding difficult or the introduction of intermediate parts onto which are soldered the semi-rigid cables making the central pin length adjustment more convenient.

Some tests have been carried out with these new considerations to underline a potential improvement. Chips have been fabricated with and without filters with aluminum evaporation for faster implementation. Without filters, the transmission does not clearly highlight the cavity resonance frequency with typical Lorentzian shape. With filters, the transmissions

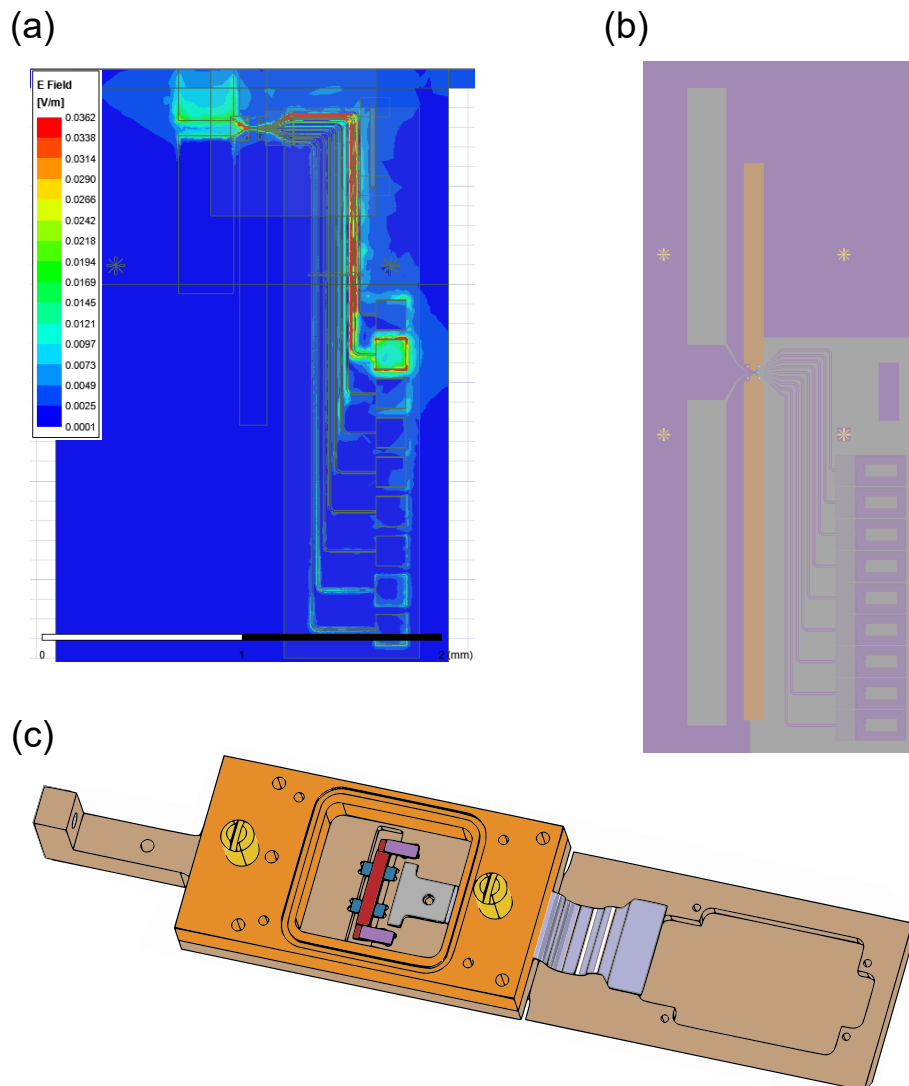


Figure 4.11: **Design modifications:** (a) Ansys HFSS simulation highlighting the cavity electric field leaking out via the DC line. (b) Novel chip layout implementing a ground plane and interdigitated low-pass filters on each DC line. (c) Simplified version of the sample holder.

reveals the  $\lambda/2$  resonator mode at 8.56 GHz with  $Q = 200$  (figure 4.12.a). This is still a very low quality factor for cavity readout perspectives and even more regarding coupling of distant qubits. Other approaches have been considered to maximize the quality factor such as replacing the  $\lambda/2$  copper blade by a silicon piece of same length and width covered by a 20 nm thick Nb film or acid treatment and polishing of the copper parts [241]. It did not show significant improvements which indicates RF leaks are the limiting factor. Despite this mitigate success, carbon nanotubes have been integrated several times on chips with design shown in figure 4.11.b. The cavity quality factor normally increases with a decrease of the

temperature as resistive losses subside. This expected dependence with the temperature is not observed in our case (see figure 4.12.b). On the contrary, the quality factor is reduced after being maximized around the aluminum critical temperature ( $T_c = 1.2$  K). This indicates the influence of parasitic modes interfering with the one of the cavity. In addition to those issues, the carbon nanotubes integrated in this "2.5D" architecture presented Schottky barriers at their interface with metal contacts. Double quantum dot could still be measured in transport by applying large gate voltages (see figure 4.12.c). An unambiguous charge-photon coupling has not been highlighted but a very tenuous signal matching the transport stability diagram has been observed (see figure 4.12.d).

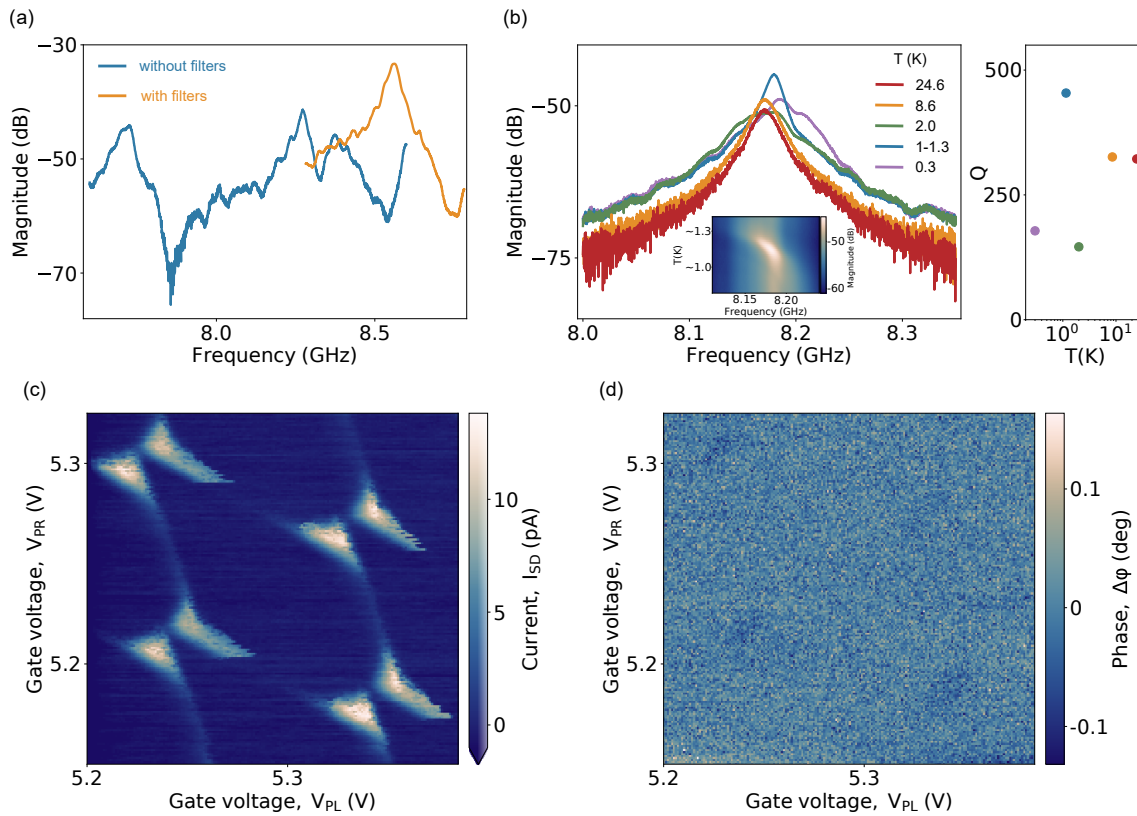


Figure 4.12: **Carbon nanotube embedded in a "2.5D cavity"**: (a) Preliminary tests with aluminum showing the filters's influence on the cavity quality factor. The transmission of the resonator is plotted for a design with and without filters on the DC pads. (b) Cavity transmission for various temperatures in the presence of a chip with novel layout integrating a carbon nanotube. The associated quality factors are displayed on the right as a function of the temperature. (c) Current through the double quantum dot circuit  $I_{SD}$  as a function of the gate voltages  $V_{PL}$  and  $V_{PR}$  at finite bias voltage  $V_{SD} = 2$  mV. The stability diagram shows bias triangles typical from the double quantum dot regime. (d) Corresponding stability diagram with cavity phase measurement. Four faint resonant lines at interdot transition location can be distinguished. The signal is however very weak. (device v3-a4)

As a conclusion, this novel "2.5D" architecture finally brings us back to the same issues faced with a standard fully on-chip design. The leakage of the cavity field through the DC lines for now limits the quality factor to low values. This has however also been the case for the standard architecture [28] which has evolved before enabling the important milestones of the recent years. Further developments towards a well controlled RF environment remain to be done to envision a similar destiny.



## Chapter 5

# Observation of microsecond lived quantum states in carbon-based circuits

The first two chapters of this thesis have shown the great potential of carbon nanotubes for hosting spin qubits in a circuit-QED architecture. On the one hand, carbon nanotubes can form well defined and tunable quantum dots [37], they can be suspended reducing the impact of stray charges and can be grown with pure  $^{12}\text{C}$  to offer a nuclear spin free environment for electronic spin qubits. On the other hand, the circuit-QED architecture which has been borrowed from superconducting qubits [4] is very appealing notably for upscaling spin qubits. An important milestone in that direction has moreover recently been reached with the realization of a two-qubit gate between distant spins [35]. Nevertheless, both carbon nanotubes qubits and spin qubits coupled to cavity photons have so far shown limited coherence times. In this chapter, we show that carbon nanotube based quantum device finally hold their promise, the whole coupled to a microwave cavity, with coherence times of the order of  $1 \mu\text{s}$ . This is two orders of magnitude larger than what has been measured so far in any carbon quantum circuit [42, 242] and one order of magnitude larger than Si based quantum dots in comparable environment [30, 31, 163].

The first part recalls the ferromagnetic spin qubit principal and geometry before showing measurements witnessing signatures of its physical implementation. The second part presents the dynamics of our system through time domain measurements. Finally, the last part discusses the specific dynamics attributed to a spectrum implying multiple levels.

## 5.1 Shaping and highlighting the ferromagnetic spin qubit

### 5.1.1 Working principle

The implementation of a spin qubit in a cQED architecture imposes a spin-charge hybridization to enable a spin-photon coupling. This results in a spin-orbit qubit which can be realized in different ways (see section 1.3.3). In the ferromagnetic spin qubit implementation [7], a single-wall suspended carbon nanotube is connected to ferromagnetic electrodes with non-collinear magnetizations and coupled electrostatically to five gate electrodes (see figure 5.1.a). In such an architecture, a single electron can be trapped in a double quantum dot comprising then a large synthetic spin-orbit coupling. Additionally, one of the gates is directly connected to the central track of a coplanar waveguide (CPW) resonator in order to induce large charge/spin-photon coupling [151]. The DC potentials of the middle and outside gates ( $V_t$  and  $V_{\Gamma_{L/R}}$ ) respectively set the interdot tunnel rate  $t$  and the one between the dot and its neighboring lead  $\Gamma_{L/R}$ . The plunger gates voltages  $V_{P_L}$  and  $V_{P_R}$  set the detuning  $\epsilon_\delta$  defining different qubit sweet spots.

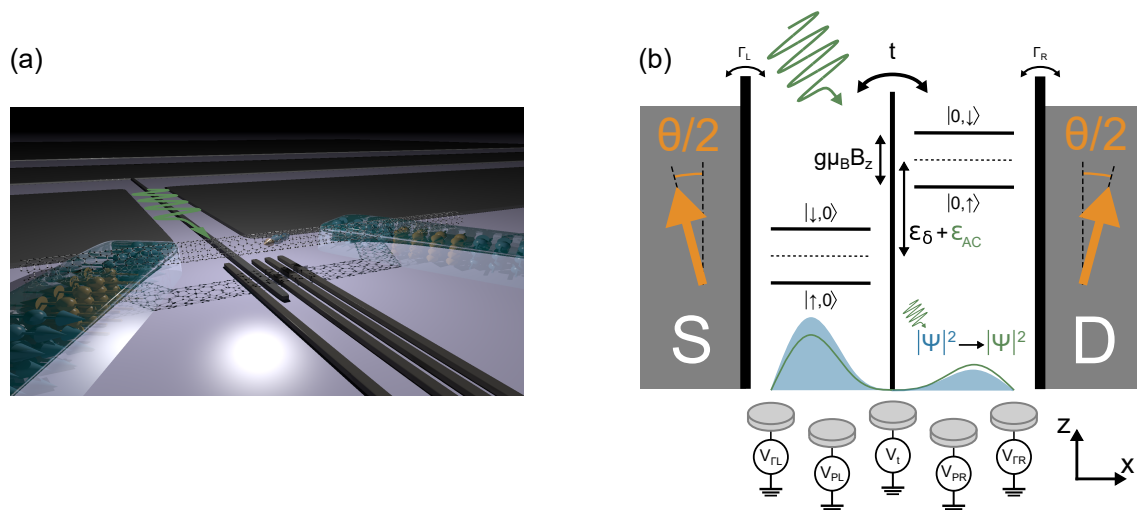


Figure 5.1: **Ferromagnetic spin qubit implementation:** (a) 3D representation of the mesoscopic-QED architecture. (b) Schematics of the spin-polarized double quantum dot electronic states enabling spin-photon coupling. Here  $\theta = \pi/6$ .

### 5.1.2 Device fabrication

The device fabrication has been done in collaboration with G. Abulizi and J. Becdelieuvre working as clean room engineers at C12. They took care of the first half of the nanofabrication steps to provide a  $200 \mu\text{m}$  thick  $2''$  diameter Si wafer containing  $9 \times 10 \text{ mm} \times 10 \text{ mm}$  chips, being 18 potential devices as shown as in figure 5.2. This wafer has then been diced to proceed to the second half of the nanofabrication on individual  $10 \text{ mm} \times 10 \text{ mm}$  chip. The different steps are presented in details in section 3.1 and a full recipe is given in appendix B.1. Figure 5.2 shows optical and SEM images for a typical final layout. The results presented in this chapter have been obtained using chip W11A. The coplanar waveguide cavity visible in figure 5.2.a is made out of 100 nm layer of Nb. The fundamental resonance frequency at 300 mK is  $f_c = 6.975 \text{ GHz}$  and its quality factor is  $Q = 4853$ . The DC lines end up in the region where the carbon nanotube is thereafter transferred (see figure 5.2.c). The zigzag ferromagnetic electrodes are made with a Ti(185nm)/Ni<sub>80</sub>Pd<sub>20</sub>(35nm)/Pd(4nm) stack whereas the gates are made with a Ti(5nm)/Pd(50nm) one. The latter choice of gate electrodes with a conducting surface ensures that we can check electrically on the final device that the nanotube is indeed suspended and well isolated from the gates. Trenches which sit in between the microwave cavity and the DC lines (see figure 5.2.a&b) are etched for the integration of the nanotubes afterwards. The later are indeed grown on a dedicated chip using a CH<sub>4</sub> based Chemical Vapor Deposition (CVD) process (see section 3.2.1) and transferred in a vacuum chamber ( $P_E \leq 10^{-6} \text{ mbar}$ ) thanks to a nanosacle alignment (see section 3.2.2).

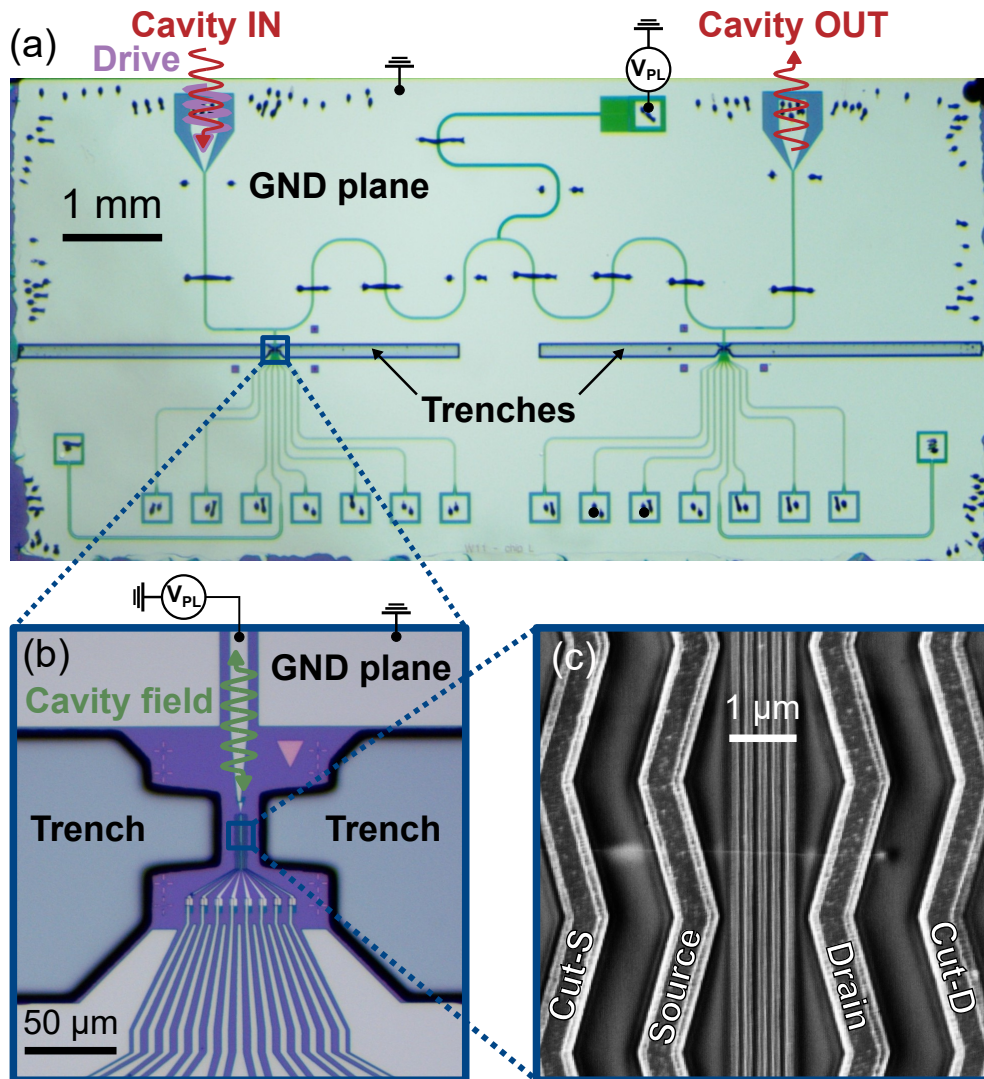


Figure 5.2: **Device layout:** (a) Optical image of the  $10\text{ mm} \times 5\text{ mm}$  chip. Two double quantum dot circuits are coupled to the same microwave cavity. Here only one of the two is used. (b) Optical image centered on the region where is transferred the carbon nanotube. (c) SEM image of a typical device with a suspended carbon nanotube transferred onto the ferromagnetic electrodes and over the gate.

Once transferred, the carbon nanotube can already be characterized at room temperature inside the vacuum chamber. First, the contact resistance is a good indication whether or not Schottky barriers at the CNT/electrode interface prevent low temperature transport measurements at low bias voltage. The contact resistance typically ranges from 0.5 to 2 M $\Omega$ . The particular device studied here has a room temperature resistance  $R_{RT} \approx 10\text{ M}\Omega$  which should not have been measured according to the selection criteria. Furthermore, a gate dependence is also performed inside the vacuum chamber to prioritize narrow gap carbon nanotubes for reaching the single electron regime. The current measurement as a function

of the gate voltages did not show any dependence suggesting a metallic tube. Despite these non ideal features, this device was transferred in the  $^3\text{He}$  fridge for further characterization at low temperature. As in the previous chapter, all the measurements presented here have been done at 300 mK.

### 5.1.3 Tuning the double quantum dot

The main features of our device can first be determined via DC transport and continuous wave spectroscopy. In the first instance, one should tune the device in the double quantum dot regime. For this purpose, the current through the nanotube  $I_{\text{SD}}$  can be measured at finite bias ( $V_{\text{SD}} = 10$  mV) as a function of the two plunger gate voltages ( $V_{\text{P}_L}$  and  $V_{\text{P}_R}$ ) for fixed tunnel gate voltages (here  $V_t = V_{\Gamma_{L/R}} = -0.4$  V). This results in stability diagram whose pattern gives insights on the coupling between the two dots but also on the device disorder. Further characterization is done by looking at the phase contrast of the microwave signal at the resonance frequency of the cavity 6.975 GHz. If the double quantum dot is well tuned, it should highlight resonant lines where interdot transitions occur delimiting the two adjacent associated charge states. We are looking for regularly spaced and highly contrasted resonant lines testifying a well defined double quantum dot coupled to the microwave cavity. Figures 5.3.a&b show the stability diagram in the region we focus on in this chapter and figure 5.3.c the interdot transition studied with associated working point (red dot). In such a continuous wave measurement, it is well established that the phase signal is compound from all transitions starting from the groundstate [170].

### 5.1.4 Two-tone spectroscopy

In order to highlight individually the different transitions implied in the phase measurement (figure 5.3.c), we apply a second tone at a varying frequency to address and identify them all. As the  $^3\text{He}$  fridge only includes one input RF line, the second tone is mixed with the one at the cavity resonance frequency (see figure 3.12). This driving tone is thus applied via the cavity which reduces the drive amplitude as opposed to the use of a fast line but ensures a proper cQED architecture. At the zero detuning working point, a resonance is found at  $f_q = 9.0987$  GHz with a full linewidth at half maximum of  $2\gamma = 2\pi \times 589$  kHz which corresponds to a decay rate about  $2\pi \times 295$  kHz (see figure 5.4.a). Looking at the dispersion of the transition as a function of external variables enables a better understanding of the system. The power broadening and the AC-Stark shift constitute sanity check measurements attesting of a transition coupled to the cavity and discriminate thus possible artifacts. It is also interesting to follow the transition with the detuning  $\epsilon_\delta$  as illustrated in figure 5.4.b. A proper implementation of the ferromagnetic spin qubit predicts a dispersion for the 01

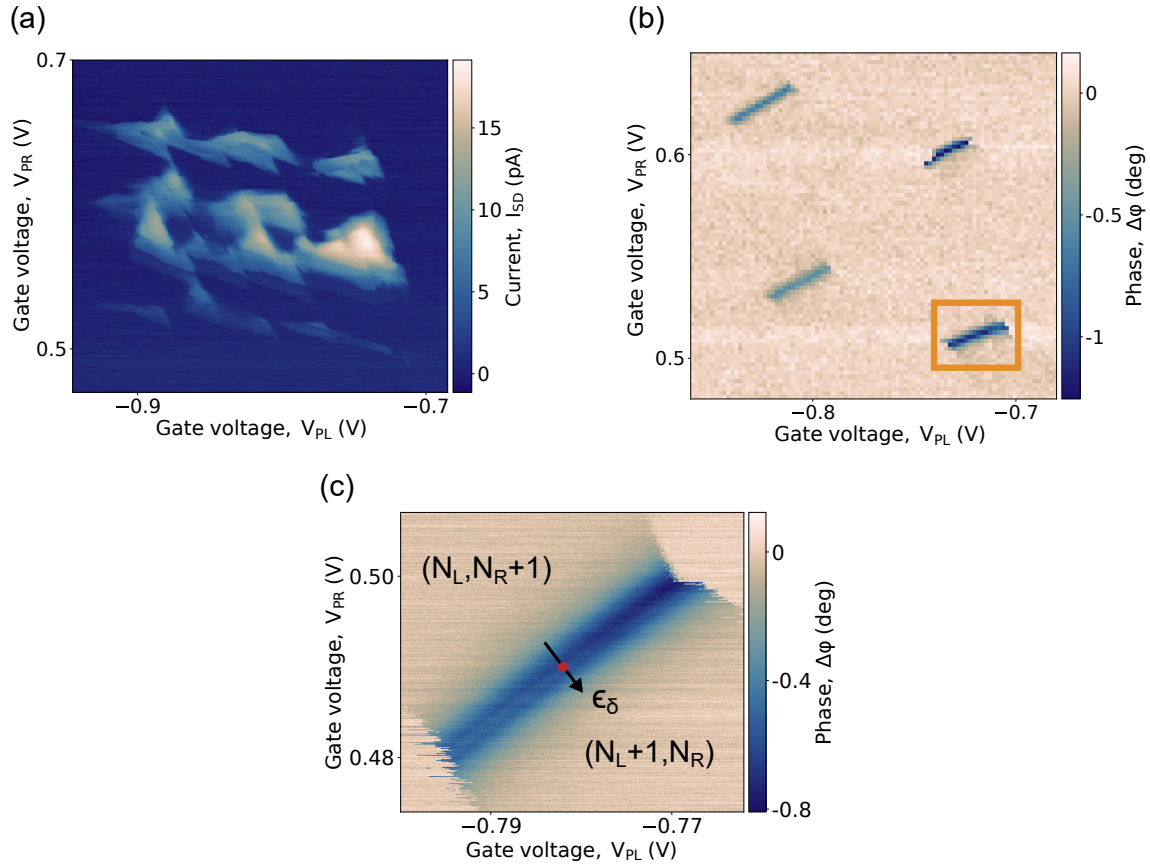


Figure 5.3: **Stability diagram:** (a) Current  $I_{SD}$  as a function of the two plunger gates voltages  $V_{PL}$  and  $V_{PR}$  at a fixed bias voltage  $V_{SD} = 10$  mV in the region where the system has been operated. (b) Continuous wave spectroscopy showing four oblique resonant lines corresponding to interdot transitions. The one of interest is framed in orange. (c) Zoom on the interdot transition implied in the further measurements. The latter have been performed in the center of the resonant line (red dot).

transition with a minimum at zero detuning and a saturation at large detuning. A weak dependence of this type is qualitatively observed in figure 5.4. Finally, as it involves the spin of the electron, the 01 transition is logically affected by an external magnetic field. Such a dependence has not been observed for reasons that will be discussed later. However, as shown as in figure 5.4.c, a characteristic hysteretic signal in the current is observed validating spin injection [151] and therefore the presence a priori of interface exchange fields. These continuous wave spectroscopy measurements provides first intuitions on the system but going to the time domain is crucial to further understand the spectrum and its dynamics. The following has been done at the center of the resonant line (red dot) without any external magnetic field.

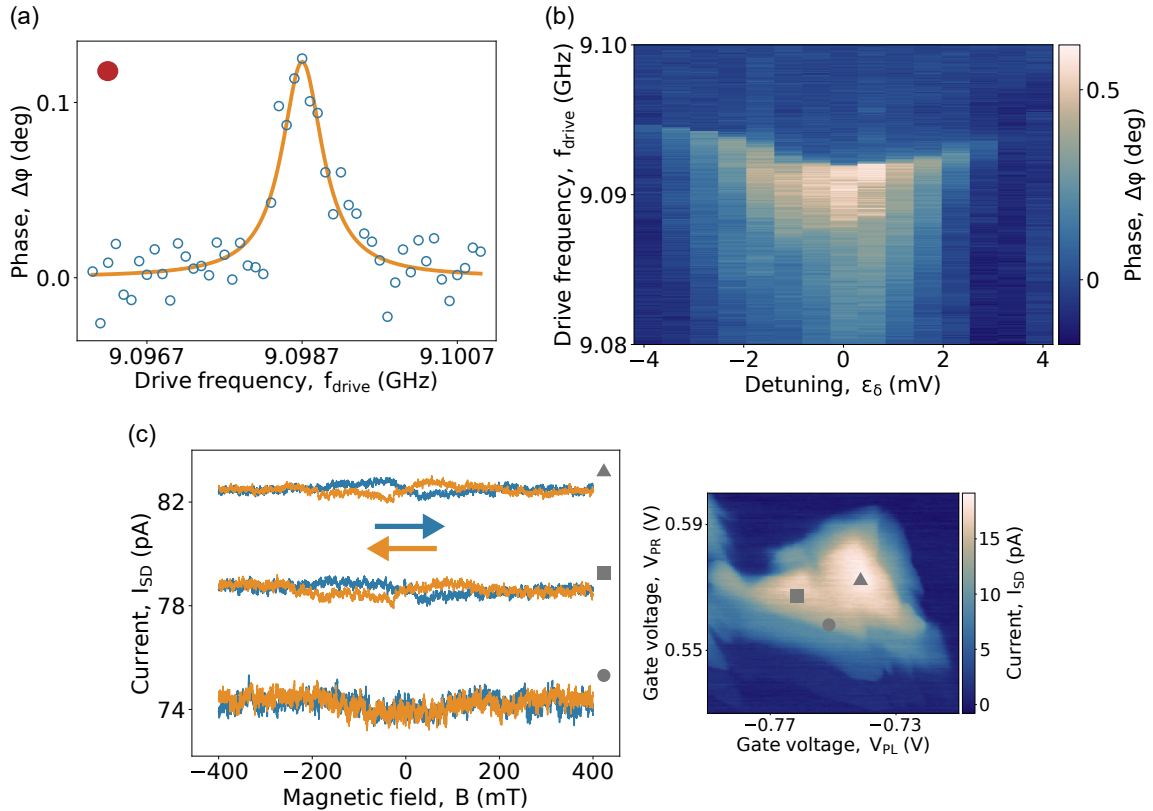


Figure 5.4: **Transition characteristics:** (a) Two-tone spectroscopy where the phase contrast is measured as a function of the drive frequency  $f_{\text{drive}}$  (at the red dot working point). The full width at half maximum (FWHM) of the transition is 589 kHz. (b) Two-tone spectroscopy as a function of the detuning  $\epsilon_\delta$ . The dispersion with a minimum at zero detuning and a saturation at large detuning is in accordance with the 01 transition of the ferromagnetic spin qubit. (c) Tunneling Magneto-Resistance (TMR) measurements: the current  $I_{\text{SD}}$  through the double quantum dot is measured while sweeping the external magnetic field with a bias voltage  $V_{\text{SD}} = 10\text{mV}$ . This is done at three different working points in the stability diagram represented by a circle, a square and a triangle.

## 5.2 Quantum manipulation of the system

### 5.2.1 Rabi manipulation

As opposed to continuous wave spectroscopy, the system is driven for a given time without photon in the cavity which is pulsed right after to readout the resulting system state. The first time domain experiments to perform are Rabi manipulations. This enables to determine how fast we can manipulate the system and sets thus the  $\pi$  pulse duration, that is the time required to bring the system from its ground to excited state. For this purpose, the system is driven at a frequency  $f_{\text{drive}}$  close to the resonance found in figure 5.4.a for a varying time  $t_{\text{burst}}$  up to  $2\ \mu\text{s}$ . The cavity is filled during  $1\ \mu\text{s}$  and readout during the last 600 ns (see

figure 5.5.a). The corresponding measurements is shown in figure 5.5.c, with the resulting Fourier spectrum in figure 5.5.d . We observe fringes signaling quantum oscillations of the state of our device. These fringes resemble the conventional Rabi chevrons observed in many qubit experiments and extend up to  $2 \mu\text{s}$ , giving hints that coherence times exceed the state of the art for this kind of circuit. However, there are two main differences here. First,

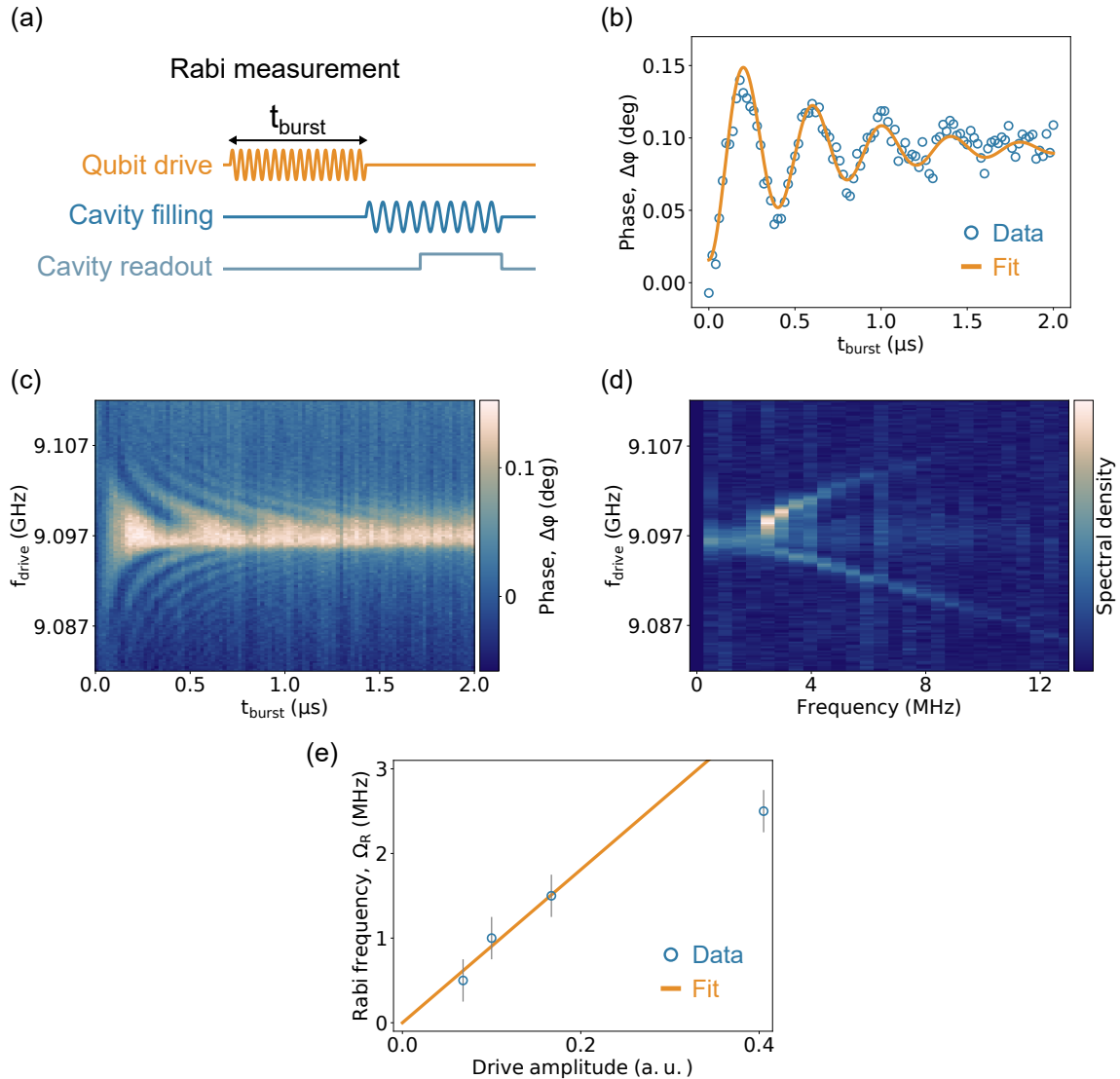


Figure 5.5: **Rabi measurement:** (a) Rabi pulse sequence. The cavity is filled during  $1 \mu\text{s}$  and readout the last 600 ns. (b) Rabi oscillations at  $f_{\text{drive}} = 9.0984 \text{ GHz}$  observed in the microwave phase as a function of time  $t_{\text{burst}}$  fitted with an exponentially decaying cosine. (c) Rabi chevron pattern as a function of drive frequency  $f_{\text{drive}}$  and time  $t_{\text{burst}}$ . (d) Fourier transform of the measured Rabi chevrons. (e) Drive amplitude dependence of the Rabi frequency  $\Omega_R$ . The linear fit excludes the point of highest drive amplitude (used for the measurements).

the Rabi chevrons are not symmetric on both sides of the transition frequency: oscillations for  $f_{\text{drive}} > f_{\bar{q}} \sim 9.097$  GHz are slightly slower than those for  $f_{\text{drive}} < f_{\bar{q}}$ . Second, there is a horizontal stripe of zero Rabi contrast very close to the resonance. Nevertheless, the cut at  $f_{\text{drive}} = 9.0984$  GHz displays well defined damped oscillations (see figure 5.5.b) which we fit with an exponentially decaying cosine. We extract a Rabi frequency  $\Omega_{\text{R}} = 2.47$  MHz and a Rabi decay time  $T_{\text{R}} = 0.63$   $\mu\text{s}$ . Finally, as expected, the Rabi chevrons oscillates faster as the drive amplitude increases. It scales linearly up to a certain drive amplitude (see figure 5.5.e).

These Rabi oscillations are a first step towards single qubit gates but also allow us to get a clearer picture of the kind of spectrum at stake here. The Rabi chevrons are indeed very discriminating between two- and multi-level dynamics [212]. Our non standard Rabi chevrons are most likely hiding a more complex dynamics than just a two-level system encoding a qubit. The ferromagnetic spin qubit implementation naturally involves four states through the spin-orbit hybridization. The specific multilevel dynamic behind this will be discussed in details in the next section. Despite this additional complexity, we adopt the terminology qubit for our system although more than two levels are involved. This qubit is then characterized here as a standard one by considering the  $\pi$  pulse associated to the cut at  $f_{\text{drive}} = 9.0984$  GHz.

### 5.2.2 Qubit characterization

A qubit is affected by both transverse and longitudinal noise. The relaxation processes are then characterized by two distinct lifetimes: the relaxation time  $T_1$  and the coherence time  $T_2^*$  [211]. Determining those two characteristic times enables to understand what is limiting the qubit coherence, opening the path to further potential improvements. The previous Rabi measurement is crucial for these characterizations as they require the  $\pi$  and  $\pi/2$  pulse durations which are respectively 200 ns and 100 ns for the cut at  $f_{\text{drive}} = 9.0984$  GHz (figure 5.5.b).

We first characterize the relaxation time  $T_1$  as it helps to properly calibrate the time domain measurements. It indeed sets the time required for the qubit to relax in its ground state after each pulse sequence. For the  $T_1$  measurement, a  $\pi$  pulse is applied to bring the qubit in its excited state before waiting a varying time  $\tau$  up to 5  $\mu\text{s}$  after which the qubit state is readout via the cavity (see figure 5.6.a). As expected, we obtain an exponential decay that we can fit and gives  $T_1 = 1.12$   $\mu\text{s}$  (see figure 5.6.b).

As for the coherence time  $T_2^*$ , it is determined using Ramsey interferometry. The qubit is brought in the equatorial plane of the Bloch sphere with a  $\pi/2$  pulse before a free evolution

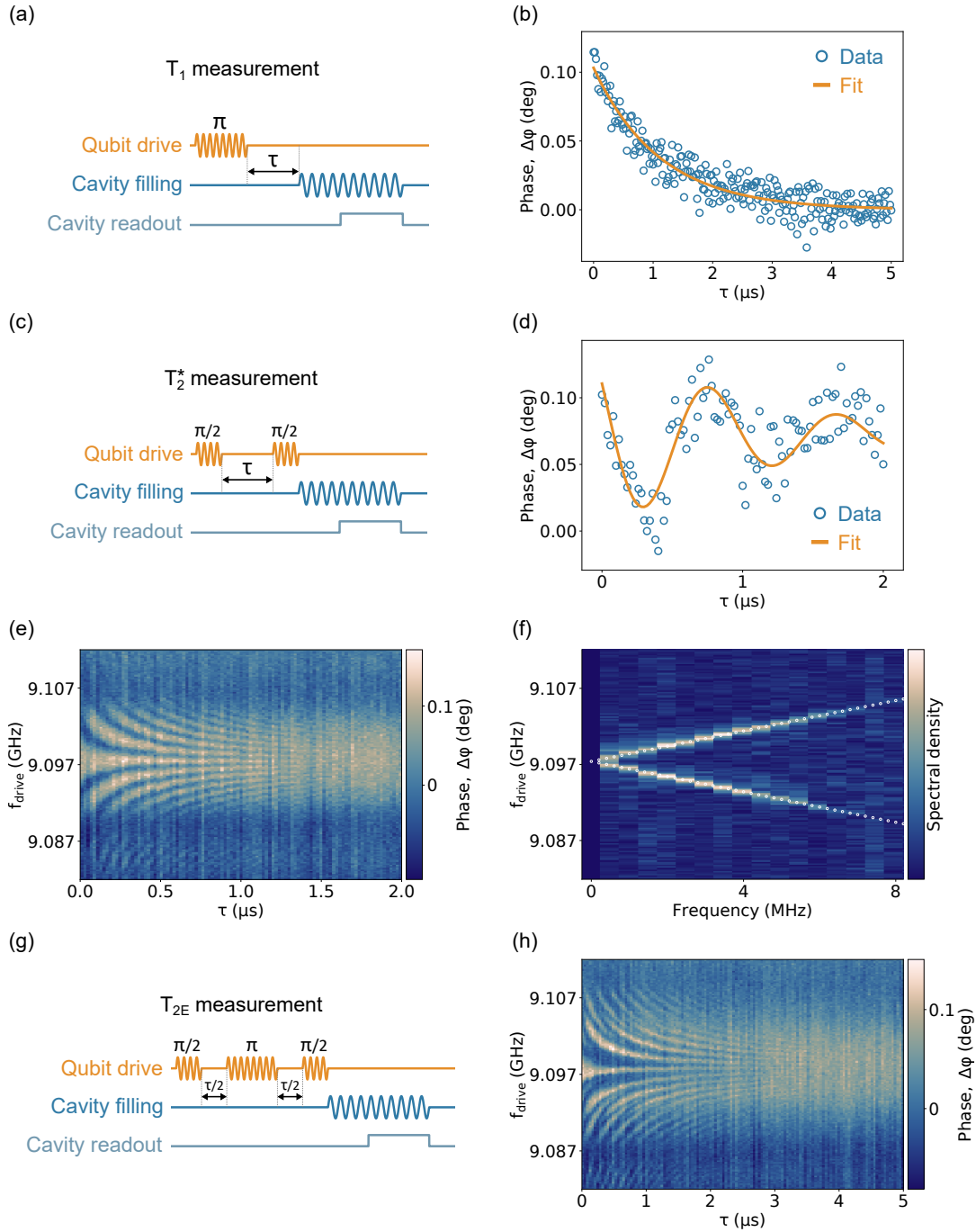


Figure 5.6: **Qubit characterization:** (a) Pulse sequence for  $T_1$  measurement. (b) Relaxation curve of the qubit yielding  $T_1 = 1.12 \mu\text{s}$ . (c) Pulse sequence for  $T_2^*$  measurement. (d) Cut of Ramsey fringes as a function of time  $\tau$  at  $f_{\text{drive}} = 9.0986 \text{ GHz}$ . The fit to an exponentially decaying sinusoidal function yields  $T_2^* = 1.1 \mu\text{s}$ . (e) Ramsey fringes as a function of drive frequency  $f_{\text{drive}}$  and time  $\tau$ . (f) Fourier transform of the Ramsey fringe. (g) Pulse sequence for  $T_{2E}$  measurement. (h) Hahn echo pattern as a function of drive frequency  $f_{\text{drive}}$  and time  $\tau$ .

during a varying time  $\tau$  up to  $2 \mu\text{s}$ . Another  $\pi/2$  pulse is applied to project the qubit state back on to the z-axis before the readout (see figure 5.6.c). This yields Ramsey fringes where the phase contrast is plotted as a function of the drive frequency  $f_{\text{drive}}$  and the time  $\tau$  (see figure 5.6.e). Despite the multi-level dynamics, it displays similar features than the one expected for a qubit. A cut at  $f_{\text{drive}} = 9.0986 \text{ GHz}$  is fitted with an exponentially decaying sinusoidal function resulting in  $T_2^* = 1.1 \mu\text{s}$  (see figure 5.6.d). A Ramsey interferometry experiment presents indeed fringes oscillating at a frequency  $|f_{\text{drive}} - f_{\text{q}}|$ . This is confirmed by the Fourier transform in figure 5.6.f where the expected frequencies are shown with white dashed lines. The extracted coherence time, being the highest for a state in a quantum dot in a cavity, yields a pure dephasing time  $T_\varphi = 2.16 \mu\text{s}$ .

In order to characterize further the dephasing mechanisms of our qubit, it is instructive to perform Hahn echoes for which one intercalates a  $\pi$  pulse in between the two  $\pi/2$  pulses for the same total duration (see figure 5.6.g). This additional  $\pi$  pulse enables refocalisation which partly eliminates low frequency noise. This measurement is shown in figure 5.6.h and enables to extend the coherence time to  $T_{2\text{E}} = 1.7 \mu\text{s}$ . The  $T_2$  time is thus not far from the  $2T_1$  limit.

### 5.2.3 Decoherence budget

Now that the qubit lifetimes have been determined, it is interesting to estimate what is limiting its coherence. The ferromagnetic spin qubit relies on a very hybrid implementation involving then many physical processes. We can review them to make the qubit decoherence "budget". As the system is coupled to a microwave cavity, a spontaneous emission of photons can be enhanced and limit the qubit coherence. This is known as the Purcell effect which is characterized by the Purcell rate:  $\gamma_{\text{Purcell}} = \kappa g^2 / (f_c - f_q)$ , where the cavity linewidth is  $\kappa = 1.44 \text{ MHz}$  and the coupling strength of our transition is estimated to  $g \approx 2.5 \text{ MHz}$ . This yields  $\gamma_{\text{Purcell}} = 1.7 \times 10^{-6} \text{ MHz}$  which is 6 orders of magnitude below the rates we measure. Regarding processes involving the cavity, this is the dominant one as the used pulse sequences prevent from measurement induced dephasing and the cavity occupation is about 0.48 at 300 mK.

The hybridization of the spin with the charge consequently brings in charge noise. Its influence in a double quantum dot circuit can be inferred to the slope of the transition with respect to the detuning  $\epsilon_\delta$ . From figure 5.4.b, we find a very weak dispersion of  $4 \times 10^{-3} \text{ MHz}/\mu\text{eV}$ . With similar devices, the typical charge noise root mean squared is  $\sqrt{\langle \sigma_{\epsilon_\delta}^2 \rangle} \approx 10 \mu\text{eV}$  leading to  $\Gamma_{\varphi, \text{charge}} \approx 4 \times 10^{-2} \text{ MHz}$  which is 2 orders of magnitude below the rates we measure. Despite the spin is well isolated from its environment, nuclear spin bath still mediates spin

dephasing through hyperfine interaction. With isotopically purified  $^{12}\text{C}$  one could completely get rid of this nuclear spin bath but here it still leads to finite dephasing estimated around  $\Gamma_{\varphi,\text{hf}} \approx 4 \times 10^{-2}$  MHz [43].

Finally, cotunneling processes also affect the charge states coherence [243] and their influence can be estimated from transport measurements. Assuming ballistic transport, the transmission  $T$  of the tunnel barriers can be deduced from the room temperature resistance:  $1/R_{\text{RT}} \approx T \times 2e^2/h$ . From  $R_{\text{RT}} \approx 10 \text{ M}\Omega$ , we get  $T \approx 1.3 \times 10^{-3}$ . This implies that the tunneling rates to the leads  $\Gamma_{\text{L/R}}$  are in the range of  $\Gamma_{\text{L/R}} \approx T \times \delta E \approx 1.3 \text{ GHz}$ , where we have assumed the mean level spacing  $\delta E$  to be in the THz range, which is a standard value for our devices. Both the decoherence and relaxation rates arising from cotunneling scale like  $\Gamma_{\text{L/R}}^2/E_{\text{C}_{\text{L/R}}}$ , where  $E_{\text{C}_{\text{L/R}}}$  is the on-site charging energy. The latter can be determined from the transport triangles (see Appendix A) and reads:  $E_{\text{C}_{\text{L/R}}} \approx 20 \text{ meV}$ . With this rough estimation, we finally arrive at  $\Gamma_{\text{L/R}}^2/E_{\text{C}_{\text{L/R}}} \approx 0.35 \text{ MHz}$  which is of the right order of magnitude to possibly explain both the relaxation and the dephasing of our qubit.

### 5.3 Multi-level quantum dynamics

As mentioned previously, the non standard Rabi chevrons (figure 5.5.c) of our system most likely entail a multi-level quantum dynamics which is possible for specific spectra of the ferromagnetic spin qubit hosted in a CNT. This section aims at discussing the possible regimes and their consequences.

#### 5.3.1 Four-level spectrum

The ferromagnetic spin qubit Hamiltonian has been introduced in section 1.3.2 (equation 1.22). Here we start with the one describing the general case of a spin-orbit qubit. In the  $\{|\uparrow, 0\rangle, |\downarrow, 0\rangle, |0, \uparrow\rangle, |0, \downarrow\rangle\}$  basis, the Hamiltonian reads:

$$H_{SO \text{ qubit}} = \frac{1}{2} \begin{pmatrix} -\epsilon_\delta - g\mu_B B_z & -g\mu_B B_x & 2t & 0 \\ -g\mu_B B_x & -\epsilon_\delta + g\mu_B B_z & 0 & 2t \\ 2t & 0 & \epsilon_\delta - g\mu_B B_z & g\mu_B B_x \\ 0 & 2t & g\mu_B B_x & \epsilon_\delta + g\mu_B B_z \end{pmatrix} \quad (5.1)$$

where  $B_z$  is the symmetric part of the total magnetic field  $B_{\text{tot}}$  that lifts the spin degeneracy and  $B_x$  is its anti-symmetric part responsible for the spin-charge hybridization.  $g$  is the electron  $g$ -factor and  $\mu_B$  the Bohr magneton. Finally the detuning  $\epsilon_\delta$  and the interdot tunnel rate  $t$  set the charge qubit.

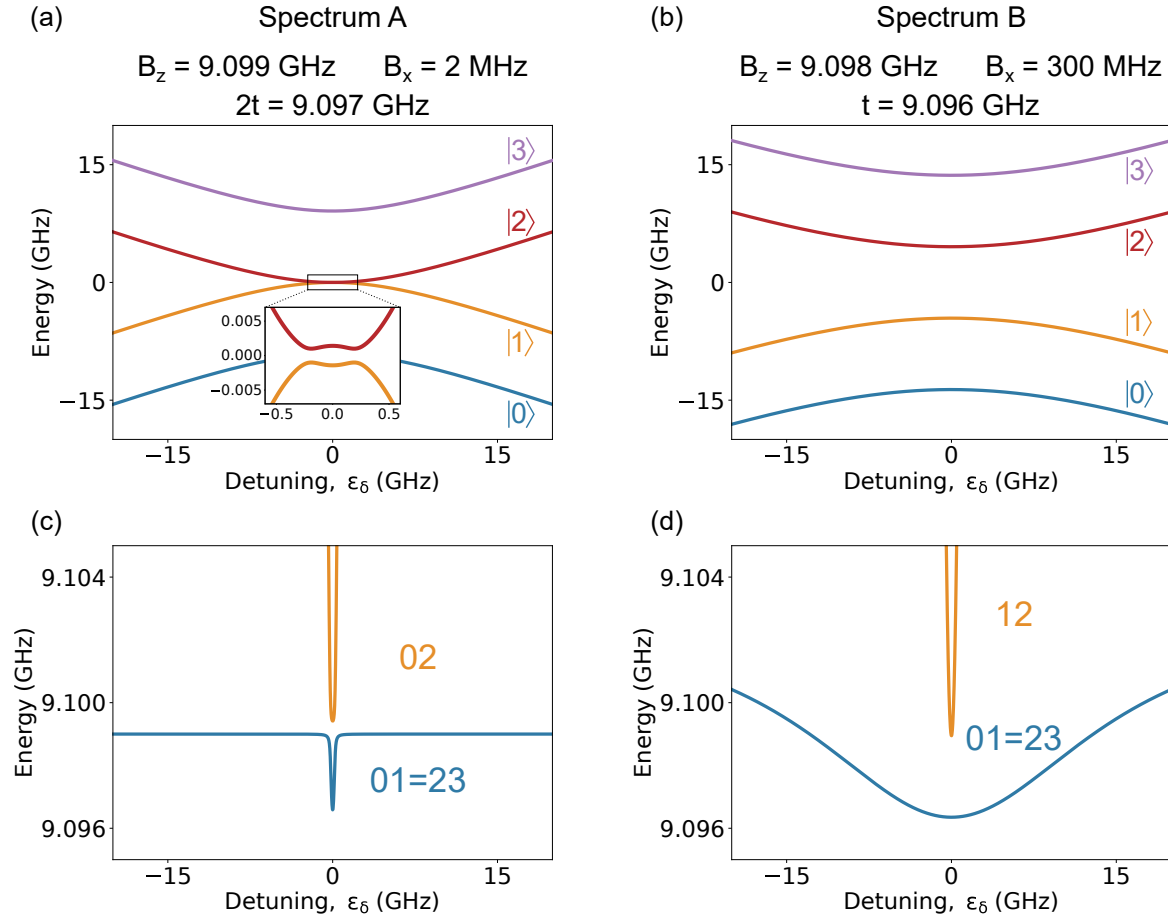


Figure 5.7: **Spectrum and transition frequencies of the ferromagnetic spin qubit in the multi-level dynamics limit:** (a) and (c) For configuration A. (b) and (d) For configuration B.

By playing on the different parameters, one can find specific spectra which can not be operated as a two-level system anymore. We consider here two distinct possibilities. The first spectrum (labeled A) considers the two first excited states  $|1\rangle$  and  $|2\rangle$  very close to each other close to  $\epsilon_\delta \sim 0$ . In those conditions, it is then inevitable to address both the 01 and the 02 transitions. Furthermore, once the first and second excited states  $|1\rangle$  and  $|2\rangle$  start to be populated, due to the symmetry of the spectrum ( $f_{01} = f_{23}$ ) the applied driving frequency also enables to reach the third excited state  $|3\rangle$ . Such a spectrum is obtained by considering  $2t \sim g\mu_B B_z$  combined with a very weak spin-charge hybridization:  $2t = 9.097$  GHz,  $g\mu_B B_z = 9.099$  GHz and  $g\mu_B B_x = 2$  MHz (see figure 5.7.a). The second spectrum (labeled B) is considered quasi-harmonic:  $f_{01} \sim f_{12}$ . Once again, as  $f_{01} = f_{23}$ , we are able to reach the third excited states  $|3\rangle$ . Figure 5.7.b depicts such a spectrum considering:  $t = 9.096$  GHz,  $g\mu_B B_z = 9.098$  GHz and  $g\mu_B B_x = 300$  MHz. The corresponding transitions of spectra A and B are shown in figure 5.7.c&d.

As the ferromagnetic spin qubit transitions involve spin, one should a priori see a linear change of their frequency when varying the external magnetic field  $B_{\text{ext}}$ . As mentioned previously, such a feature has not been experimentally observed. Spectrum A brings an answer to this flat dispersion. The very small spin-charge hybridization ( $B_x \ll B_z$ ) makes the operated working point ( $\epsilon_\delta = 0$  and  $B_{\text{ext}} = 0$ ) a very local sweet spot where the spin and charge states hybridize. Applying few tens of mT immediately sets the system out of this sweet spot. One transition is then almost "charge-like" and not affected by  $B_{\text{ext}}$  whereas the "spin-like" one does not couple to the cavity electric field. Configuration A raises somehow questions on other aspects. The anti-symmetric component of the magnetic field is very small compared to the symmetric one:  $B_x \approx 0.0002 B_z$ . Those fields arising from the interface exchange fields of the ferromagnetic contacts are in principle linked through the chosen geometry:  $\theta = \pi/6$  imposes  $B_x = \tan(\theta/2)B_z \approx 0.27 B_z$  which is far from being the case here. Moreover in configuration A, it is not possible to obtain a spectrum which matches both experimental measurements of Rabi chevrons and two-tone spectroscopy as a function of the detuning  $\epsilon_\delta$ . Obtaining  $f_{01}$  close enough to  $f_{02}$  to satisfy the multi-level dynamics indeed implies the 01 dispersion to be flat except very locally close to  $\epsilon_\delta \sim 0$  (see figure 5.7.c). This is not what is experimentally observed as  $f_{01}$  varies all along the width of the resonant line (see figure 5.4.b).

Considering spectrum B enables to answer the previous issues. Even though the aspect ratio between  $B_x$  and  $B_z$  is not fully satisfying, it is much more reasonable ( $B_x \approx 0.033 B_z$ ). This time the transitions are both expected to disperse linearly with  $B_{\text{ext}}$ . One can nevertheless invoke the possibility of having the external magnetic field along  $B_x$  instead of  $B_z$  depending on the ferromagnetic contacts magnetization. Such a configuration results in a very weak dispersion. To this can be added the re-normalization of the Landé g-factor in carbon nanotubes which can be drastically reduced ( $\tilde{g}\mu_B = 176 \text{ MHz/T}$  [152] and  $300 \text{ MHz/T}$  [151]). The main issue of spectrum B concerns the coupling strength associated to the different transitions. First, one should consider the working point not to be strictly at zero detuning ( $\epsilon_\delta \neq 0$ ) in order to have  $g_{12} \neq 0$  required for the multi-level dynamics. Second, the coupling strength associated to transitions 02 and 13 is predicted to overcome all the other ones being for themselves comparable. With these considerations, it is not possible to faithfully reproduce the measured Rabi Chevrons. Nevertheless, by relaxing the latter constraint, our peculiar Rabi chevrons can almost be reproduced (see figure 5.8). The evolution of the four populations under a drive of finite time has been calculated by Q. Schaeverbeke working at C12 as theoretician. This simulation takes into account the initial populations, the different transitions with respective coupling strengths and the characteristic lifetimes (see details in caption of figure 5.8).

### 5.3.2 Eight-level spectrum

As spectra A and B do not rigorously explain the whole experimental data set, one can consider a more complex model by introducing a variable ignored so far. As explained in section 1.1.1, carbon nanotubes present a valley degree of freedom. Local disorder inside the CNT induces valley mixing which is described by the phenomenological term  $\Delta_{KK'}$ . As a consequence, each level of the ferromagnetic spin qubit spectrum splits into two levels (K and K') separated by  $\Delta_{KK'}$  resulting in an eight-level energy spectrum. For specific regimes, such as  $2\Delta_{KK'} \sim g\mu_B B_z$ , it is possible to reach a quasi harmonic spectrum whose dynamics implies more than two levels. Manipulating and reading valley transitions can be done by considering specific magnetic fields for each valley:  $B_{z,K}, B_{z,K'}, B_{x,K}$  and  $B_{x,K'}$ . A small asymmetry can furthermore be considered depending on the left and right dot [151]. With those new considerations, it is possible to return to a situation equivalent to spectrum B with spin and valley transitions making them very weakly sensitive to both the detuning  $\epsilon_\delta$  and the tunnel rate  $t$ . As the external magnetic field is applied perpendicularly to the CNT, valley transitions are not supposed to be affected when varying  $B_{\text{ext}}$ .

As it is, the possible multi-level dynamics arising from the ferromagnetic spin qubit do not strictly explain the whole data set. By relaxing some constraints on the model such as the predicted couplings, it is possible to reproduce the measured Rabi Chevrons with relatively good agreement. Finally, we can also note that our system was not operated in the single electron regime which is likely to complicate the model.

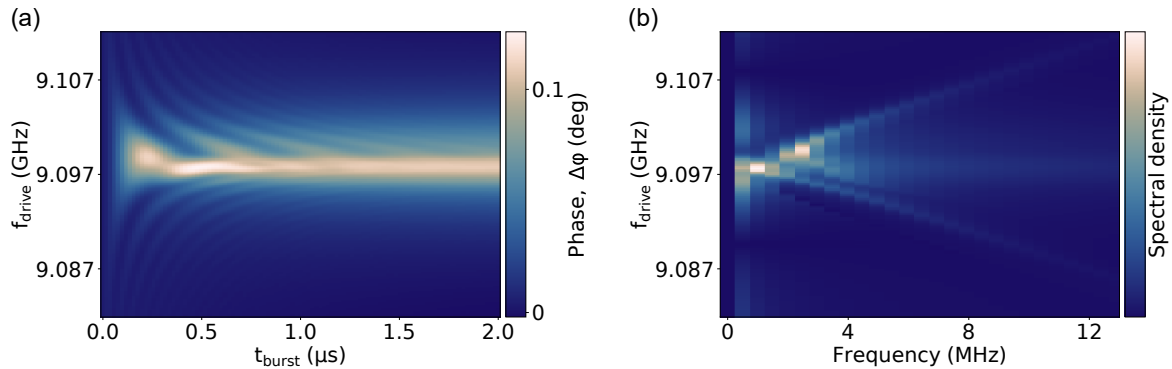


Figure 5.8: **Simulating the dynamics of a quasi-harmonic 4-level system:** (a) Rabi chevrons simulation as a function of the time  $t_{\text{burst}}$  and the drive frequency  $f_{\text{drive}}$  (b) Associated Fourier transform. Parameters:  $p_1 = p_2 = 0.153$ ,  $p_3 = 0.036$ ,  $f_{01} = 9.0982$  GHz,  $f_{12} = 9.0965$  GHz,  $f_{23} = 9.0988$  GHz,  $g_{01} = 2.4$  MHz,  $g_{02} = g_{13} = 1.4$  MHz,  $g_{03} = 0.5$  MHz,  $g_{12} = 1.8$  MHz,  $g_{23} = 2$  MHz,  $\Gamma_1 = 100$  kHz and  $\Gamma_\varphi = 200$  kHz.



# Conclusion and perspectives

This thesis work focused on the realization of the ferromagnetic spin qubit [7]. Its implementation requires three major ingredients: a carbon nanotube, a double quantum dot circuit and a circuit QED architecture. This result in a very hybrid system with plenty of technical challenges to overcome. Among those ones, we notably find the nanotube integration and the implementation of the spin-photon coupling. Chapter 3 described the growth and selection of carbon nanotubes on a dedicated cantilever chip enabling an integration inside a vacuum chamber for a resulting ultraclean device [189]. Concerning the spin-photon coupling, as explained in chapter 1, reaching a finite value requires a spin-charge hybridization which is here achieved with non collinear ferromagnetic contacts. The spin-photon coupling is then a fraction of the charge-photon coupling which can be itself enhanced by increasing the resonator impedance. Chapter 4 developed this idea which can be implemented with disordered superconductors. Preliminary measurements have been performed using granular aluminum. The architecture can also be improved anticipating the integration of several qubits and the need of a high inter-qubit connectivity. Chapter 4 presented the development of a "2.5D" cavity also providing strong modularity and separate nanofabrication optimization. Finally, chapter 5 reported the observation of microsecond lived quantum states in a carbon-based circuit. The non standard Rabi chevrons measured have been related to specific spectra of the system resulting in a multi-level quantum dynamics.

As the studied system includes diverse components, the perspectives are multiple. The last results obtained that are shown in chapter 5 helps in listing what can be improved. The first feature to work on is the increase of the spin-photon coupling strength as it plays a major role in reaching high one and two qubit gate fidelities but even before this, it is also crucial for the readout. Academic groups working with similar systems have all switched to high impedance resonator obtained with disordered supraconductors and more specifically NbN. Chapter 4 presented some developments in that direction using granular aluminum for rapid tests which unfortunately did not led to any robust design.

The multi-level quantum dynamics presented in chapter 5 is still not completely understood using the ferromagnetic spin qubit model. Further investigations are still ongoing in that direction. Reproducing a similar experiment would then be instructive to further understand the implemented spectrum and strictly manipulate a two-level system. In parallel, for better control of the artificial spin-orbit coupling, it is instructive to use as the other groups a micromagnet. Such an architecture adapted to the nanotube integration is being developed at C12 and could constitute a shortcut towards the realization of the two qubit gate. However, a full electrical control of the ferromagnetic spin qubit frequency without any external magnetic field would be extremely valuable for scale-up perspectives.

Better control and understanding of the system would be possible with a double quantum dot filled with a single electron. Reaching the so-called single electron regime requires an accurate selection for identifying narrow gap single-wall carbon nanotubes without defects. Along this thesis the selection before transfer has been done almost exclusively through scanning electron microscope observations. This incomplete nanotube characterization is being consolidated at C12 with notably Raman spectroscopy, Rayleigh measurements in an optical setup and the development of electrical measurement directly on the cantilever chip after the growth.

# Appendix A

## Charging energies extraction for detuning axis energy conversion

### A.1 Charging energies

The goal of this appendix is to convert the detuning axis  $\epsilon_\delta$  into an absolute energy axis. This can further be used to fit system parameters such as the interdot tunnel rate  $t$  or the charge-photon coupling  $g_c$ . These values can also directly be obtained in the case of the strong coupling regime by looking at the dispersive shift as a function of the temperature (see appendix 4 of [163]). Here we use DC transport measurement in the non-linear regime (see figure A.1.b) to determine the charging energies [62]. The double quantum dot equivalent electrical circuit is presented in section 1.2.1 (see figure 1.4.a) and the parameters are linked together through the following equations:

$$\Delta V_{gL} = \frac{|e|}{C_{gL}} \quad (\text{A.1})$$

$$\Delta V_{gR} = \frac{|e|}{C_{gR}} \quad (\text{A.2})$$

$$\Delta V_{gL}^m = \frac{|e|C_m}{C_{gL}C_{\Sigma R}} = \Delta V_{gL} \frac{C_m}{C_{\Sigma R}} \quad (\text{A.3})$$

$$\Delta V_{gR}^m = \frac{|e|C_m}{C_{gR}C_{\Sigma L}} = \Delta V_{gR} \frac{C_m}{C_{\Sigma L}} \quad (\text{A.4})$$

$$\alpha_L \delta V_{gL} = \frac{C_{gL}}{C_{\Sigma L}} |e| \delta V_{gL} = |eV_{SD}| \quad (\text{A.5})$$

$$\alpha_R \delta V_{gR} = \frac{C_{gR}}{C_{\Sigma R}} |e| \delta V_{gR} = |eV_{SD}| \quad (\text{A.6})$$

From figure A.1.b&d, we get:

$\Delta V_{gL}$	$\Delta V_{gR}$	$\Delta V_{gL}^m$	$\Delta V_{gR}^m$	$\delta V_{gL}$	$\delta V_{gR}$
85 mV	80 mV	12 mV	17 mV	27 mV	31 mV

which gives:

$C_{gL}$	$C_{gR}$	$C_m$	$C_{\Sigma L}$	$C_{\Sigma R}$
1.89 aF	2.00 aF	1.41 aF	7.32 aF	8.98 aF

And according to equations 1.4, 1.5 and 1.6 the following charging energies:

$E_{CL}$	$E_{CR}$	$E_{Cm}$
22.56 meV	18.41 meV	3.55 meV

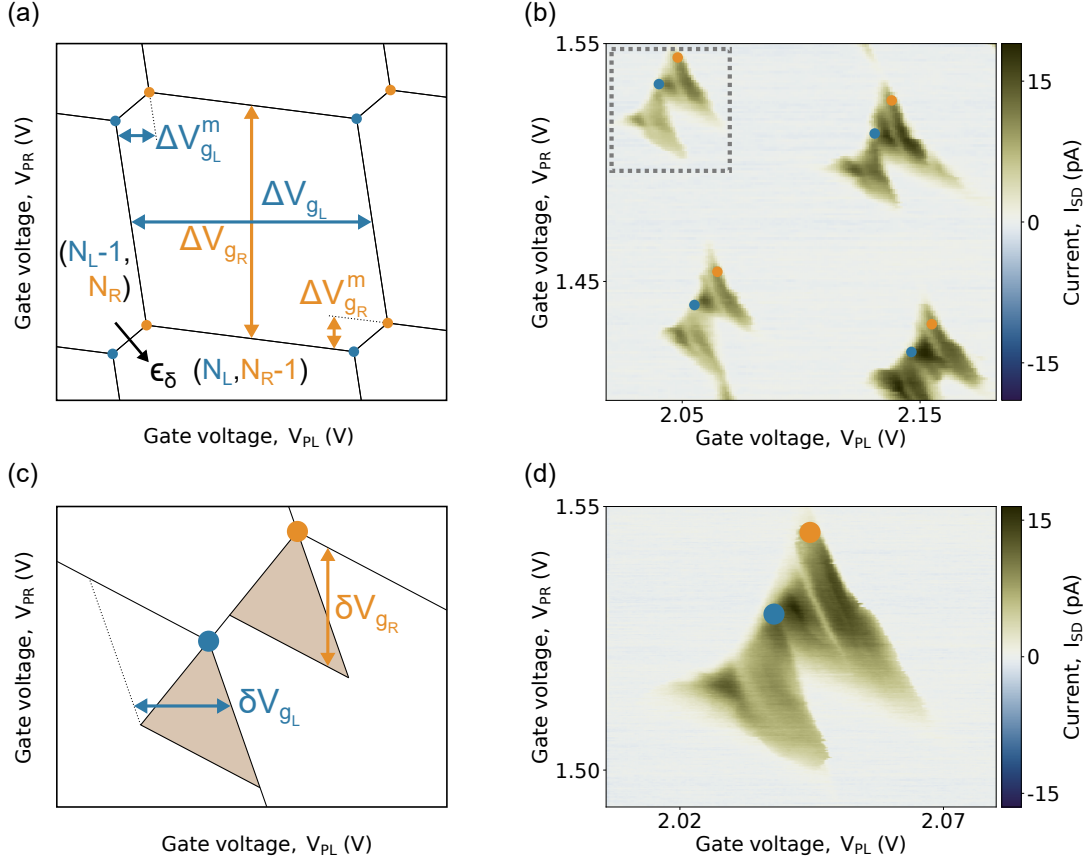


Figure A.1: **Charging energies identification:** (a) Representation of several quantities used to determine the charging energies in the  $V_{PL} - V_{PR}$  plane. (b) Current  $I_{SD}$  as a function of the plunger gate voltages  $V_{PL}$  and  $V_{PR}$  a finite bias:  $V_{SD} = 7$  mV. This enables to determine the quantities plotted in (a). (c) Schematic of a bias triangle in the  $V_{PL} - V_{PR}$  plane with associated quantities. (d) Zoom on plot (b) (grey rectangle) showing two bias triangles overlapping each other still enabling to determine the quantities plotted in (c).

## A.2 Detuning energy axis

The detuning energy has been defined as:  $\epsilon_\delta = \epsilon_R - \epsilon_L$ , with  $\epsilon_{L/R}$  the energy of the left/right dot. Those energies can be determined with the electrical model as any  $(N_L, N_R)$  charge configuration in the double quantum dot has the following energy [62]:

$$U(N_L, N_R) = \frac{1}{-|e|} \left( C_{g_L} V_{g_L} (N_L E_{C_L} + N_R E_{C_m}) + C_{g_R} V_{g_R} (N_L E_{C_m} + N_R E_{C_R}) \right) + f(V_{g_L}, V_{g_R}) + U_{offset} \quad (\text{A.7})$$

The detuning energy is then defined as:  $\epsilon_\delta = U(N_L - 1, N_R) - U(N_L, N_R - 1)$  and reads:

$$\epsilon_\delta = \frac{C_{g_L} (E_{C_L} - E_{C_m})}{|e|} V_{g_L} - \frac{C_{g_R} (E_{C_R} - E_{C_m})}{|e|} V_{g_R} \quad (\text{A.8})$$



# Appendix B

## Detailed fabrication recipes

### B.1 Ferromagnetic spin qubit chip nanofabrication

#### B.1.1 Dicing preparation

The nanofabriaction starts with a 4" undoped silicon wafer which is  $500\mu\text{m}$  thick and covered by  $500\text{nm}$  of  $\text{SiO}_2$ . It is then diced into  $9.9\text{mm} \times 9.9\text{mm}$  square chips with beforehand a protecting resist deposition:

- Fill a pipette with AZ514 resist<sup>1</sup> and wait **10mn** to get it to ambient temperature.
- Launch the pumping of the wafer and remove the possible dirt with the nitrogen blower.
- Cover the wafer with AZ514 resist and launch the 4000-4000-30 program (4000 turns/s<sup>2</sup>, 4000 turns, 30 sec).
- **2 mn**: bake the wafer at **110°C**. The wafer is now protected for dicing.

#### B.1.2 First cleaning

After the dicing, the wafer is divided into square chips on which we can fabricate two devices. The first step consists in cleaning one of those square chip:

- **3 mn**: IPA at **20°C** + sonic-bath (force 9) to get rid of silicon pieces without removing the resist.
- **20 mn**: Acetone at **50°C**.

---

<sup>1</sup>this optical resist have been introduced as the PMMA was often removed during the dicing

- **30 sec:** Vigorous shaking in acetone.
- **5 mn:** Acetone at **50°C** + sonic-bath (force 9). Use another beaker for this step.
- **30 sec:** Vigorous shaking in IPA then dry with nitrogen gun.
- Check under the microscope the aspect of the chip. Using "dark field" mode helps to identify potential defects. The chip has to be almost perfect. If not, repeat the cleaning process or take another chip if it is still not successful.

### B.1.3 Gold precontacts and alignment crosses

#### PMMA 500 spin coating

- **3 mn:** bake the chip at **185°C** to evaporate adsorbates (such as H<sub>2</sub>O).
- Launch the pumping of the chip and remove the possible dirt with the nitrogen blower.
- Deposit 3-4 drops of PMMA 500 and launch the program qelec-jpc (4sec, 1000turns/s<sup>2</sup>, 500 turns/s, followed by 60 sec, 4000turns/s<sup>2</sup>, 4000 turns/s).
- **3 mn:** bake the chip at **185°C**.
- Check under the microscope the resist profile. There should be no bubbles or dirt on the surface. If not, put the chip 5mn in acetone at **50°C**, rinse it in IPA for 30 sec and dry before starting again the spin coating.

#### Two-current e-beam lithography

SEM parameters:

- Aperture: 7.5 $\mu$ m and 120 $\mu$ m
- Acceleration voltage : 20kV

Procedure:

- Set the aperture to 7.5 $\mu$ m and the zoom to 1000.
- After reset UV, localize the bottom left hand corner of the chip and perform a 2 points alignment.
- Make a contamination dot at the center of the chip with a 100k zoom. Adjust the focus and center it before saving the column parameters for the 7.5 $\mu$ m aperture.

- Launch the manual WF alignment procedure at  $5\mu\text{m}$  and then at  $1\mu\text{m}$  and save it.
- Call the  $120\mu\text{m}$  aperture column parameter and set the focus to the value used for the  $7.5\mu\text{m}$  aperture.
- DO NOT TOUCH THE JOYSTICK. Set roughly the beam shift to -22% and 10%. Set the zoom to  $\sim 50\text{k}$  to locate the contamination dot. Refine the focus and center it by adjusting the beam shift before saving the column parameters for the  $120\mu\text{m}$  aperture.
- Launch the manual WF alignment procedure at  $5\mu\text{m}$  and then at  $1\mu\text{m}$  and save it.
- Measure the currents for the  $7.5\mu\text{m}$  and  $120\mu\text{m}$  apertures.
- Scan the following position list.

Position list:

- Call of the  $7.5\mu\text{m}$  aperture column parameters
- Call of the WF parameters for the  $7.5\mu\text{m}$  aperture
- Exposition of the layers with precontacts and small alignment crosses (for the layer 63):
  - Dose:  $360\ \mu\text{C}/\text{cm}^2$
  - Area step size:  $U=V=20\text{nm}$
- Call of the  $120\mu\text{m}$  aperture column parameters
- Call of the WF parameters for the  $120\mu\text{m}$  aperture
- Exposition of the layers with chip name and big alignment crosses:
  - Dose:  $360\ \mu\text{C}/\text{cm}^2$
  - Area step size:  $U=V=150\text{nm}$
- Beam shutdown

**Reveal MIBK/IPA**

- **1 mn:** Reveal in MIBK/IPA solution (1:MIBK, 3:IPA)
- **30 sec:** Rinse in IPA then dry.

- Check under the microscope if the lithography went well. Save pictures to have the chip background afterwards.

### Evaporation

- **5 mn**: "Clean" program ( $\text{CHF}_3$  &  $\text{O}_2$ ) and **1 mn**: "stripping" program ( $\text{O}_2$ ) without the chip in the RIE to clean the chamber.
- **10 sec**: "Stripping" program with the chip inside. Load it in the evaporator load-lock directly after.
- 5nm of Ti at  $2\text{\AA}/\text{s}$
- 45nm of Au at  $5\text{\AA}/\text{s}$

### Lift-off

- **20 mn**: Acetone at **50°C**.
- Pipetting until there is no visible remaining metal on the chip.
- **5 mn**: Acetone at **50°C** + ultrasonic (force 9). Use another beaker for this step.
- **30 sec**: Vigorous shake in acetone.
- **30 sec**: Vigorous shake in IPA then dry.
- Check under the microscope and save pictures.
- **5 mn**: "Clean" program and **3 mn**: "stripping" program without the chip in the RIE to clean the chamber.
- **5 mn**: "stripping" program with the chip inside. Go for next step immediately after.

## B.1.4 Niobium mesoscopic QED architecture

### Evaporation

- Load the chip in the evaporator load-lock.
- Launch the cool-down of the evaporator cryo-panels by filling them with liquid nitrogen and wait  $\sim 30\text{mn}$  before starting the evaporation.

- 100nm of Nb at  $10\text{\AA}/\text{s}$  (with the gun focused on one specific location of the Nb metal piece).

### PMMA 500 spin coating

#### 120 $\mu\text{m}$ aperture e-beam lithography

SEM parameters:

- Aperture: 120 $\mu\text{m}$
- Acceleration voltage : 20kV

Procedure:

- Set the aperture to 7.5 $\mu\text{m}$  and the zoom to 1000.
- After reset UV, localize the bottom left hand corner of the chip and perform a 2 points alignment.
- Use a  $\sim 8\text{k}$  zoom to perform a 3 points alignment with the large alignment crosses.
- Make a contamination dot at the center of the chip with a 100k zoom. Adjust the focus and center it before saving the column parameters for the 7.5 $\mu\text{m}$  aperture.
- Call the 120 $\mu\text{m}$  aperture column parameter and set the focus to the value used for the 7.5 $\mu\text{m}$  aperture.
- DO NOT TOUCH THE JOYSTICK. Set roughly the beam shift to -22% and 10%. Set the zoom to  $\sim 50\text{k}$  to locate the contamination dot. Refine the focus and center it by adjusting the beam shift before saving the column parameters for the 120 $\mu\text{m}$  aperture.
- Launch the manual WF alignment procedure at 5 $\mu\text{m}$  and then at 1 $\mu\text{m}$  and save it.
- Measure the current for the 120 $\mu\text{m}$  aperture.
- Scan the following position list.

Position list:

- Call of the 120 $\mu\text{m}$  aperture column parameters.
- Call of the WF parameters for the 120 $\mu\text{m}$  aperture.

- Exposition of the layer corresponding to the region where Nb will be etched:
  - Dose:  $320 \mu\text{C}/\text{cm}^2$
  - Area step size:  $U=V=150\text{nm}$
- Beam shutdown.

## Reveal MIBK/IPA

### Niobium etching

- **5 mn**: "Clean" program.
- **5 mn**: Purge  $\text{SF}_6$  line with "test" program.
- **1 mn**: "Nb" program ( $\text{SF}_6$ ) without the chip in the RIE.
- Load the chip in the RIE and launch the "Nb" program. The etching progress is monitored with reflectometry measurement. The reflectivity slowly increases up to decreases abruptly and reaches a minimum. At this point, the Nb has been etched away.
- **20 sec**: Overetch after reaching this minimum of reflectivity.

### Cleaning

- **20 mn**: Acetone at  $50^\circ\text{C}$ .
- **30 sec**: Vigorous shaking in acetone .
- **3 mn**: Acetone at  $50^\circ\text{C}$  + sonic-bath (force 9). Use another beaker for this step.
- **30 sec**: Vigorous shaking in IPA then dry.
- **5 mn**: "Clean" program ( $\text{CHF}_3$  &  $\text{O}_2$ ) and **3 mn**: "stripping" program ( $\text{O}_2$ ) without the chip in the RIE to clean the chamber.
- **3 mn**: "Stripping" program with the chip inside.
- Check under the microscope and save pictures.

### B.1.5 Gate electrodes

#### PMMA 150 spin coating

- **3 mn:** bake the chip at **185°C**
- Launch the pumping of the chip and remove the possible dirt with the nitrogen blower.
- Deposit 3-4 drops of PMMA 150 and launch the program qelec-jpc (4sec, 1000turns/s<sup>2</sup>, 500 turns/s, followed by 60 sec, 4000turns/s<sup>2</sup>, 4000 turns/s).
- **3 mn:** bake the chip at **185°C**.
- Check under the microscope the resist profile. There should be no bubbles or dirt on the surface. If not, put the chip 5mn in acetone at **185°C**, rinse it in IPA for 30 sec and dry before starting again the spin coating.

#### 7.5 $\mu$ m aperture e-beam lithography

SEM parameters:

- Aperture: 7.5 $\mu$ m
- Acceleration voltage : 20kV

Procedure:

- Set the aperture to 7.5 $\mu$ m and the zoom to 1000.
- After reset UV, localize the bottom left hand corner of the chip and perform a 2 points alignment.
- Use a  $\sim$  8k zoom to perform a 3 points alignment with the large alignment crosses.
- Make a contamination dot at the center of the chip with a 100k zoom. Adjust the focus and center it before saving the column parameters for the 7.5 $\mu$ m aperture.
- Launch the manual WF alignment procedure at 5 $\mu$ m and then at 1 $\mu$ m and save it.
- Measure the current for the 7.5 $\mu$ m aperture.
- For each of the 100 $\mu$ m  $\times$  100 $\mu$ m area containing gates:
  - Make a contamination dot in the trench close to the 100 $\mu$ m  $\times$  100 $\mu$ m zone to

locally refine the focus (optional).

- Exposition of the layer 63 (alignment macro).
- Exposition of the layer associated to the gates:
  - \* Dose  $260 \mu\text{C}/\text{cm}^2$  (the dose is sensitive so frequent dose tests are useful).
  - \* Area step size:  $U=V=20\text{nm}$

### Reveal IPA/H<sub>2</sub>O

- **40 mn:** Put the IPA/H<sub>2</sub>O developer solution (3:IPA, 1H<sub>2</sub>O) in the cold bath so that it reaches **6°C**.
- **1 mn 30 sec:** Reveal in the developer solution.
- **30 sec:** Rinse in IPA.
- Check under the microscope if the lithography went well. Only the biggest part is visible. Save pictures.

### Evaporation

- **5 mn:** "Clean" program (CHF<sub>3</sub> & O<sub>2</sub>) and **1 mn:** "stripping" program (O<sub>2</sub>) without the chip in the RIE to clean the chamber.
- **10 sec:** "Stripping" program with the chip inside. Load it in the evaporator load-lock directly after.
- 35nm of Ti at 2Å/s
- 20nm of Pd at 5Å/s

### Lift-off

- **40 mn:** Acetone at **50°C**.
- Pipetting until there is no visible remaining metal on the chip.
- **3 mn:** Acetone at **50°C** + ultrasonic (force 9). Use another beaker for this step.
- **30 sec:** Vigorous shake in acetone.
- **30 sec:** Vigorous shake in IPA then dry.

- **5 mn:** "Clean" program and **3 mn:** "stripping" program without the chip in the RIE to clean the chamber.
- **5 mn:** "stripping" program with the chip inside.
- Check under the microscope and save pictures.

### B.1.6 Contact electrodes

#### PMMA 500 spin coating

#### 7.5 $\mu$ m aperture e-beam lithography

Same procedure than for the gates electrodes except:

- Exposition of the layer corresponding to the contacts
- Dose 320  $\mu\text{C}/\text{cm}^2$

#### Reveal MIBK/IPA

#### Evaporation

- **5 mn:** "Clean" program ( $\text{CHF}_3$  &  $\text{O}_2$ ) and **1 mn:** "stripping" program ( $\text{O}_2$ ) without the chip in the RIE to clean the chamber.
- **10 sec:** "Stripping" program with the chip inside. Load it in the evaporator load-lock directly after.
- 185nm of Ti at 3.5 $\text{\AA}/\text{s}$
- Wait 15 mn
- 35nm of PdNi at 2 $\text{\AA}/\text{s}$
- 4nm of Pd at 2 $\text{\AA}/\text{s}$

#### Lift-off

- **20 mn:** Acetone at **50°C**.
- Pipetting until there is no visible remaining metal on the chip.
- **3 mn:** Acetone at **50°C** + ultrasonic (force 9). Use another beaker for this step.

- **30 sec:** Vigorous shake in acetone.
- **30 sec:** Vigorous shake in IPA then dry.
- **5 mn:** "Clean" program and **3 mn:** "stripping" program without the chip in the RIE to clean the chamber.
- **3 mn:** "stripping" program with the chip inside.
- Quickly check under the microscope. If it seems fine, do an SEM observation and save pictures.

### B.1.7 Trenches

#### PMMA 3000 spin coating

- **3 mn:** bake the chip at **185°C**
- Launch the pumping of the chip and remove the possible dirt with the nitrogen blower.
- Deposit 3-4 drops of PMMA 3000 and launch the program qelec-jpc (4sec, 1000turns/s<sup>2</sup>, 500 turns/s, followed by 60 sec, 4000turns/s<sup>2</sup>, 4000 turns/s).
- **3 mn:** bake the chip at **185°C**.
- **WARNING:** at this stage there is only  $\approx 1.5\mu\text{m}$  of resist. One has to go for **another layer**
- Deposit 3-4 drops of PMMA 3000 and launch the program qelec-jpc (4sec, 1000turns/s<sup>2</sup>, 500 turns/s, followed by 60 sec, 4000turns/s<sup>2</sup>, 4000 turns/s).
- **3 mn:** bake the chip at **185°C**.
- Check under the microscope the resist profile. There should be no bubbles or dirt on the surface. If not, put the chip 5mn in acetone at **185°C**, rinse it in IPA for 30 sec and dry before starting again the spin coating.

#### 120 $\mu\text{m}$ aperture e-beam lithography: step 1/2

This first step aims at removing the resist covering big alignment crosses to be able to perform a 3 points alignment in the next step. SEM parameters:

- Aperture: 120 $\mu\text{m}$

- Acceleration voltage : 20kV

Procedure:

- Set the aperture to  $7.5\mu\text{m}$  and the zoom to 1000.
- After reset UV, localize the bottom left hand corner of the chip and perform a 2 points alignment.
- As the resist is too thick, we can neither see the alignment crosses nor do a contamination dot. We have to go blindly.
- Call the  $120\mu\text{m}$  aperture column parameter with saved parameters of a previous lithography.
- Call of the WF parameters for the  $120\mu\text{m}$  aperture with saved parameters of a previous lithography.
- Measure the current for the  $120\mu\text{m}$  aperture.
- Scan the following position list.

Position list:

- Exposition of the layer corresponding to  $100\mu\text{m} \times 100\mu\text{m}$  squares centered on the big alignment crosses.
  - Dose:  $390 \mu\text{C}/\text{cm}^2$  (over-exposition)
  - Area step size:  $U=V=150\text{nm}$
- Beam shutdown.

### Reveal MIBK/IPA

#### **$120\mu\text{m}$ aperture e-beam lithography: step 2/2**

SEM parameters:

- Aperture:  $120\mu\text{m}$
- Acceleration voltage : 20kV

Procedure:

- Set the aperture to  $7.5\mu\text{m}$  and the zoom to 1000.
- After reset UV, localize the bottom left hand corner of the chip and perform a 2 points alignment.
- Perform a 3 points alignment.
- Call the  $120\mu\text{m}$  aperture column parameter with saved parameters of a previous lithography.
- Call of the WF parameters for the  $120\mu\text{m}$  aperture with saved parameters of a previous lithography.
- Measure the current for the  $120\mu\text{m}$  aperture.
- Scan the following position list.

Position list:

- Exposition of the layer corresponding to the trenches.
  - Dose:  $390\ \mu\text{C}/\text{cm}^2$  (over-exposition)
  - Area step size:  $U=V=150\text{nm}$
- Beam shutdown.

### SiO<sub>2</sub> and Si etching

- **5 mn**: "Clean" program.
- **1 mn**: Purge CHF<sub>3</sub> line with "test" program.
- **2 mn**: "DavidSiO<sub>2</sub>" program (CHF<sub>3</sub>) without the chip in the RIE.
- **1 mn**: Load the chip in the RIE. Purge CHF<sub>3</sub> line with "test" program.
- **~28 mn (without breaks)**: Launch "DavidSiO<sub>2</sub>-4cycles" program (CHF<sub>3</sub>). 5 mn breaks are implemented every 10 mn to reduce heating. The etching process is monitored with reflectometry measurement. The reflectivity oscillates up to be constant at the summit of an oscillation meaning that the SiO<sub>2</sub> has been etched away.
- **2 mn**: Overetch after reaching this constant value of reflectivity .

- **1 mn**: Purge O<sub>2</sub>&SF<sub>6</sub> lines with "test" program.
- **6 mn 30 sec**: Launch the "Si100W – O<sub>2</sub> – 80mT" program (O<sub>2</sub>&SF<sub>6</sub>). The reflectivity can be monitored on the resist (it oscillates) to make sure it is still protecting the device.
- Measure the depth of the trench with the "Dektack". It should be  $\sim 15\mu\text{m}$  (optional).

### Cleaning

- **3 mn**: IPA at **20°C** + ultra-sonic (force 3). Check under the microscope if the SiO<sub>2</sub> on the trenches edges has been removed. If not, repeat this step.
- **10 mn**: Acetone at **50°C**.
- **2 mn**: Acetone at **50°C** in a new beaker.
- **2 mn**: Acetone at **50°C** in a new beaker.
- **30 sec**: Vigorous shaking in acetone.
- **30 sec**: Vigorous shaking in IPA then dry with nitrogen gun.

### B.1.8 Dicing

As the chip contains two devices and the sample holder is designed to host only one, the chip has to be diced.

### PMMA 500 spin coating

#### Scribing machine

- Glue the chip on a piece of clean room tape.
- Launch the pumping of the chip.
- Adjust the settings such that the diamond tip can pass on the 2 devices frontier.
- Pass across the chip  $\sim 20$  times.
- Press along this line with the razor blade to cut the chip.

### B.1.9 Last cleaning

- **3 mn**: IPA at **20°C** + sonic-bath (force 3) to get rid of silicon pieces without removing the resist.

- **30 mn**: Acetone at **50°C**.
- **30 sec**: Vigorous chaking in acetone.
- **30 sec**: Vigorous chaking in IPA.
- **5 mn**: "Clean" program and **3 mn**: "stripping" program without the chip in the RIE to clean the chamber.
- **3 mn**: "stripping" program with the chip inside.
- **3 mn**: "Ar-plasma" program. This aims at removing oxide on contacts so the tube should be transferred rapidly after.

## B.2 CNT fabrication

The recipe used at the beginning of this work can be found in appendixes A and C of [188]. The C12 team rapidly took care of the CNT growth with several different developments. Here is detailed the recipe used for results presented in chapter 5. It corresponds to deposition 235 on cad 040 from lot 003 with catalyst solution 022.

### B.2.1 Catalyst recipe

- **10 mn**: Clean the catalyst bottle with acetone in the ultrasonic bath.
- **10 mn**: Clean the catalyst bottle with IPA in the ultrasonic bath.
- With a buret, take 60 mL of IPA.
- Clean 3 plastic beakers and 3 spatula with IPA.
- Weight 78 mg of  $\text{Fe}(\text{NO}_3)_3 - \text{H}_2\text{O}$  with 1 spatula in 1 plastic beaker. Put it in the catalyst bottle. Rinse the plastic beaker with some of the 60 mL of IPA into the catalyst bottle.
- Redo this step with 15.8 mg of  $\text{MoO}_2$  and then with 64 mg of  $\text{Al}_2\text{O}_3$ .
- Put the remaining of the 60 mL of IPA into the catalyst bottle.

### B.2.2 Catalyst deposition

- **10 sec**: Vigorously agitate the catalyst solution bottle manually.

- **1 hour:** Put the catalyst solution in the ultrasonic bath.
- **10 sec:** Vigorously agitate the catalyst solution bottle manually.
- **45 mn:** Let the catalyst solution for sedimentation.
- Prepare a beaker with IPA solution. One should have a dedicated one for this.
- Opens very gently the catalyst solution bottle such that it is not stirred.
- With a pipette, take a some of the catalyst solution from the surface.
- Hold a cantilever chip with tweezers on a clean room paper.
- Put 3 drops of the catalyst solution on the cantilever chip.
- **3 sec:** Wait.
- **3 sec:** Rinse the cantilever chip in IPA.
- **10 sec:** Dry the cantilever chip with the N<sub>2</sub> gun.
- Check under the microscope the catalyst density. Using "dark field" mode should help.

### B.2.3 Growth recipe

- After checking the regulators are set to 10 bars, open the CH<sub>4</sub> and H<sub>2</sub> bottles by a quarter turn . These bottles are stored outside.
- Write down the bottles pressure.
- In the furnace room, after checking the regulators are set to 1 bar, open the Ar bottle and write down the bottle pressure.
- Make sure that the tube is well positioned.
- Open the 3 valves connected to Ar, CH<sub>4</sub> and H<sub>2</sub>
- Open the main valve.
- Start the furnace and the pump before opening the CVD software.
- Set an Ar flow to 1000 sccm ("Argon Flow" recipe in the software).
- Clean the quartz boat sample holder and the small plastic platform with IPA.

- Place the cantilever chips on the quartz boat sample holder with clean tweezers and gently introduce it at the quartz tube outlet before closing it.
- **1 mn 30 sec:** Wait. Then stop the Ar flow.
- Pump (check details)
- Load the production recipe and start it before closing and locking the furnace gently.

Step	Description	Time (mn)	Temperature (°C)	Ar (%vol.)	H <sub>2</sub> (%vol.)	CH <sub>4</sub> (%vol.)	Cumul flow rate (sccm)
1	Heating	-	↗ 900°C	100	0	0	1000
2	Reduction	8	900°C	0	100	0	390
3	Growth	6	900°C	0	34	66	1157
4	Cool down	-	↘ 280°C	72	28	0	1390
5	Cool down	-	↘ RT	100	0	0	1000

- After the growth step, gently open the furnace.
- After step 5, close the 3 blue valves and the main one before taking the cantilever chips out of the quartz boat sample holder.
- Close the Ar, CH<sub>4</sub> and H<sub>2</sub> gas bottles.

# Bibliography

- [1] Feynman RP. Simulating physics with computers. *International Journal of Theoretical Physics*. 1982;21(6-7):467-88. Available from: <https://doi.org/10.1007/BF02650179>.
- [2] Shor PW. Polynomial-time algorithms for prime factorization and discrete logarithms on a quantum computer. *SIAM Journal on Computing*. 1997;26(5):1484-509. Available from: <https://doi.org/10.1137/S0097539795293172>.
- [3] Shor PW. Scheme for reducing decoherence in quantum computer memory. *Phys Rev A*. 1995 Oct;52:R2493-6. Available from: <https://doi.org/10.1103/PhysRevA.52.R2493>.
- [4] Wallraff A, Schuster DI, Blais A, Frunzio L, Huang RS, Majer J, et al. Strong coupling of a single photon to a superconducting qubit using circuit quantum electrodynamics. *Nature*. 2004;431(7005):162-7. Available from: <https://doi.org/10.1038/nature02851>.
- [5] Arute F, Arya K, Babbush R, Bacon D, Bardin JC, Barends R, et al. Quantum supremacy using a programmable superconducting processor. *Nature*. 2019;574(7779):505-10. Available from: <https://doi.org/10.1038/s41586-019-1666-5>.
- [6] Kim Y, Eddins A, Anand S, Wei KX, van den Berg E, Rosenblatt S, et al. Evidence for the utility of quantum computing before fault tolerance. *Nature*. 2023;618(7965):500-5. Available from: <https://doi.org/10.1038/s41586-023-06096-3>.
- [7] Cottet A, Kontos T. Spin Quantum Bit with Ferromagnetic Contacts for Circuit QED. *Phys Rev Lett*. 2010 Oct;105:160502. Available from: <https://link.aps.org/doi/10.1103/PhysRevLett.105.160502>.
- [8] DiVincenzo DP. The physical implementation of quantum computation. *Fortschritte*

- der Physik. 2000;48(9-11):771-83. Available from: [https://doi.org/10.1002/1521-3978\(200009\)48:9/11<771::AID-PROP771>3.0.CO;2-E](https://doi.org/10.1002/1521-3978(200009)48:9/11<771::AID-PROP771>3.0.CO;2-E).
- [9] van Wees BJ, van Houten H, Beenakker CWJ, Williamson JG, Kouwenhoven LP, van der Marel D, et al. Quantized conductance of point contacts in a two-dimensional electron gas. *Phys Rev Lett*. 1988 Feb;60:848-50. Available from: <https://link.aps.org/doi/10.1103/PhysRevLett.60.848>.
- [10] Wharam DA, Thornton TJ, Newbury R, Pepper M, Ahmed H, Frost JEF, et al. One-dimensional transport and the quantisation of the ballistic resistance. *Journal of Physics C: Solid State Physics*. 1988 mar;21(8):L209. Available from: <https://dx.doi.org/10.1088/0022-3719/21/8/002>.
- [11] Kouwenhoven LP, Marcus CM, Mceuen PL, Tarucha S, Westervelt RM, Wingreen NS. Electron transport in quantum dots. *Superlattices and Microstructures*. 1997;10(2):197-201. Available from: [https://doi.org/10.1007/978-94-015-8839-3\\_4](https://doi.org/10.1007/978-94-015-8839-3_4).
- [12] Loss D, DiVincenzo DP. Quantum computation with quantum dots. *Phys Rev A*. 1998 Jan;57:120-6. Available from: <https://link.aps.org/doi/10.1103/PhysRevA.57.120>.
- [13] Nowack KC, Koppens FHL, Nazarov YV, Vandersypen LMK. Coherent Control of a Single Electron Spin with Electric Fields. *Science*. 2007;318(5855):1430-3. Available from: <https://www.science.org/doi/abs/10.1126/science.1148092>.
- [14] Pioro-Ladrière M, Obata T, Tokura Y, Shin YS, Kubo T, Yoshida K, et al. Electrically driven single-electron spin resonance in a slanting Zeeman field. *Nature Physics*. 2008;4(10):776-9. Available from: <https://doi.org/10.1038/nphys1053>.
- [15] Yoneda J, Takeda K, Otsuka T, Nakajima T, Delbecq MR, Allison G, et al. A quantum-dot spin qubit with coherence limited by charge noise and fidelity higher than 99.9%. *Nature Nanotechnology*. 2018. Available from: <https://doi.org/10.1038/s41565-017-0014-x>.
- [16] Yang CH, Chan KW, Harper R, Huang W, Evans T, Hwang JCC, et al. Silicon qubit fidelities approaching incoherent noise limits via pulse engineering. *Nature Electronics*. 2019;2(4):151-8. Available from: <https://doi.org/10.1038/s41928-019-0234-1>.
- [17] Hendrickx NW, Lawrie WIL, Russ M, van Riggelen F, de Snoo SL, Schouten RN, et al. A four-qubit germanium quantum processor. *Nature*. 2021;591(7851):580-5. Available

- from: <https://doi.org/10.1038/s41586-021-03332-6>.
- [18] Philips SGJ, Mądzik MT, Amitonov SV, de Snoo SL, Russ M, Kalthor N, et al. Universal control of a six-qubit quantum processor in silicon. *Nature*. 2022;609(7929):919-24. Available from: <https://doi.org/10.1038/s41586-022-05117-x>.
- [19] Tormo-Queralt R, Møller CB, Czaplewski DA, Gruber G, Cagetti M, Forstner S, et al. Novel Nanotube Multiquantum Dot Devices. *Nano Letters*. 2022;22(21):8541-9. Available from: <https://doi.org/10.1021/acs.nanolett.2c03034>.
- [20] Waissman J, Honig M, Pecker S, Benyamini A, Hamo A, Ilani S. Realization of pristine and locally tunable one-dimensional electron systems in carbon nanotubes. *Nature Nanotechnology*. 2013;8(8):569-74. Available from: <https://doi.org/10.1038/nnano.2013.143>.
- [21] Nakamura Y, Pashkin Ys, Tsai Js. Coherent control of macroscopic quantum states in a single-Cooper-pair box. *Nature*. 1999;398(April):786-8. Available from: <https://doi.org/10.1038/19718>.
- [22] Vion D, Aassime A, Cottet A, Joyez P, Pothier H, Urbina C, et al. Manipulating the Quantum State of an Electrical Circuit. *Science*. 2002;296(5569):886-9. Available from: <https://www.science.org/doi/abs/10.1126/science.1069372>.
- [23] Raimond JM, Brune M, Haroche S. Manipulating quantum entanglement with atoms and photons in a cavity. *Rev Mod Phys*. 2001 Aug;73:565-82. Available from: <https://link.aps.org/doi/10.1103/RevModPhys.73.565>.
- [24] Majer J, Chow JM, Gambetta JM, Koch J, Johnson BR, Schreier JA, et al. Coupling superconducting qubits via a cavity bus. *Nature*. 2007;449(7161):443-7. Available from: <https://doi.org/10.1038/nature06184>.
- [25] Sillanpää MA, Park JI, Simmonds RW. Coherent quantum state storage and transfer between two phase qubits via a resonant cavity. *Nature*. 2007;449(7161):438-42. Available from: <https://doi.org/10.1038/nature06124>.
- [26] Krinner S, Lacroix N, Remm A, Di Paolo A, Genois E, Leroux C, et al. Realizing repeated quantum error correction in a distance-three surface code. *Nature*. 2022;605(7911):669-74. Available from: <https://doi.org/10.1038/s41586-022-04566-8>.

- [27] Acharya R, Aleiner I, Allen R, Andersen TI, Ansmann M, Arute F, et al. Suppressing quantum errors by scaling a surface code logical qubit. *Nature*. 2023;614(7949):676-81. Available from: <https://doi.org/10.1038/s41586-022-05434-1>.
- [28] Delbecq MR, Schmitt V, Parmentier FD, Roch N, Viennot JJ, Fève G, et al. Coupling a Quantum Dot, Fermionic Leads, and a Microwave Cavity on a Chip. *Phys Rev Lett*. 2011 Dec;107:256804. Available from: <https://link.aps.org/doi/10.1103/PhysRevLett.107.256804>.
- [29] Frey T, Leek PJ, Beck M, Blais A, Ihn T, Ensslin K, et al. Dipole Coupling of a Double Quantum Dot to a Microwave Resonator. *Phys Rev Lett*. 2012 Jan;108:046807. Available from: <https://link.aps.org/doi/10.1103/PhysRevLett.108.046807>.
- [30] Mi X, Benito M, Putz S, Zajac DM, Taylor JM, Burkard G, et al. A coherent spin-photon interface in silicon. *Nature*. 2018;555(7698):599-603. Available from: <https://doi.org/10.1038/nature25769>.
- [31] Samkharadze N, Zheng G, Kalhor N, Brousse D, Sammak A, Mendes UC, et al. Strong spin-photon coupling in silicon. *Science*. 2018;359(6380):1123-7. Available from: <https://www.science.org/doi/abs/10.1126/science.aar4054>.
- [32] Landig AJ, Koski JV, Scarlino P, Mendes UC, Blais A, Reichl C, et al. Coherent spin-photon coupling using a resonant exchange qubit. *Nature*. 2018;560(7717):179-84. Available from: <http://dx.doi.org/10.1038/s41586-018-0365-y>.
- [33] Borjans F, Croot XG, Mi X, Gullans MJ, Petta JR. Resonant microwave-mediated interactions between distant electron spins. *Nature*. 2019 may. Available from: <https://doi.org/10.1038/s41586-019-1867-y>.
- [34] Harvey-Collard P, Zheng G, Dijkema J, Samkharadze N, Sammak A, Scappucci G, et al. On-Chip Microwave Filters for High-Impedance Resonators with Gate-Defined Quantum Dots. *Phys Rev Appl*. 2020 Sep;14:034025. Available from: <https://link.aps.org/doi/10.1103/PhysRevApplied.14.034025>.
- [35] Dijkema J, Xue X, Harvey-Collard P, Rimbach-Russ M, de Snoo SL, Zheng G, et al. Two-qubit logic between distant spins in silicon. 2023:1-17. Available from: <https://doi.org/10.48550/arXiv.2310.16805>.
- [36] Loss D, DiVincenzo DP. Quantum computation with quantum dots. *Phys Rev A*. 1998 Jan;57:120-6. Available from: <https://link.aps.org/doi/10.1103/PhysRevA.>

- 57.120.
- [37] Laird EA, Kuemmeth F, Steele GA, Grove-Rasmussen K, Nygård J, Flensberg K, et al. Quantum transport in carbon nanotubes. *Rev Mod Phys*. 2015 Jul;87:703-64. Available from: <https://link.aps.org/doi/10.1103/RevModPhys.87.703>.
- [38] Kuemmeth F, Ilani S, Ralph DC, McEuen PL. Coupling of spin and orbital motion of electrons in carbon nanotubes. *Nature*. 2008;452(7186):448-52. Available from: <https://doi.org/10.1038/nature06822>.
- [39] Steele GA, Pei F, Laird EA, Jol JM, Meerwaldt HB, Kouwenhoven LP. Large spin-orbit coupling in carbon nanotubes. *Nature Communications*. 2013;4:1-7. Available from: <https://doi.org/10.1038/ncomms2584>.
- [40] Churchill HOH, Kuemmeth F, Harlow JW, Bestwick AJ, Rashba EI, Flensberg K, et al. Relaxation and Dephasing in a Two-Electron  $^{13}\text{C}$  Nanotube Double Quantum Dot. *Phys Rev Lett*. 2009 Apr;102:166802. Available from: <https://link.aps.org/doi/10.1103/PhysRevLett.102.166802>.
- [41] Jespersen TS, Grove-Rasmussen K, Paaske J, Muraki K, Fujisawa T, Nygård J, et al. Gate-dependent spin-orbit coupling in multielectron carbon nanotubes. *Nature Physics*. 2011;7(4):348-53. Available from: <https://doi.org/10.1038/nphys1880>.
- [42] Laird EA, Pei F, Kouwenhoven LP. A valley-spin qubit in a carbon nanotube. *Nature Nanotechnology*. 2013;8(8):565-8. Available from: <https://doi.org/10.1038/nnano.2013.140>.
- [43] Delbecq M. Spin quantum dynamics in hybrid circuits [Habilitation à diriger des recherches]. Sorbonne Université; 2020. Available from: <https://theses.hal.science/tel-02963713>.
- [44] Iijima S. Helical microtubules of graphitic carbon. *Nature*. 1991;368:444-6. Available from: <https://doi.org/10.1038/354056a0>.
- [45] Bockrath M, Cobden DH, McEuen PL, Chopra NG, Zettl A, Thess A, et al. Single-Electron Transport in Ropes of Carbon Nanotubes. *Science*. 1997;275(5308):1922-5. Available from: <https://www.science.org/doi/abs/10.1126/science.275.5308.1922>.
- [46] Tans SJ, Zhang L, Wang N, Zhang XX, Wen GH, Li GD, et al. Individual single-wall

- carbon nanotubes as quantum wires. *Nature*. 1997;386(APRIL):474-7. Available from: <https://doi.org/10.1038/386474a0>.
- [47] Sander J Tans, Alwin R M Verschueren, Cees Dekker. Room-temperature transistor based on a single carbon nanotube. *Nature*. 1998;393(1989):49-52. Available from: <https://doi.org/10.1038/29954>.
- [48] Bachtold A, Hadley P, Nakanishi T, Dekker C. Logic Circuits with Carbon Nanotube Transistors. *Science*. 2001;294(5545):1317-20. Available from: <https://www.science.org/doi/abs/10.1126/science.1065824>.
- [49] Cottet A, Kontos T, Belzig W, Schönenberger C, Bruder C. Controlling spin in an electronic interferometer with spin-active interfaces. *Europhysics Letters*. 2006;74(2):320-6. Available from: <https://doi.org/10.1209/epl/i2006-10006-0>.
- [50] Kuemmeth F, Churchill HOH, Herring PK, Marcus CM. Carbon nanotubes for coherent spintronics. *Materials Today*. 2010;13(3):18-26. Available from: [http://dx.doi.org/10.1016/S1369-7021\(10\)70030-4](http://dx.doi.org/10.1016/S1369-7021(10)70030-4).
- [51] Cao J, Wang Q, Dai H. Electron transport in very clean, as-grown suspended carbon nanotubes. *Nature Materials*. 2005;4(10):745-9. Available from: <https://doi.org/10.1038/nmat1478>.
- [52] Wen Y, Ares N, Schupp FJ, Pei T, Briggs GAD, Laird EA, et al. A coherent nanomechanical oscillator driven by single-electron tunnelling. *Nature physics*. 2019;16:75-82. Available from: <https://doi.org/10.1038/s41567-019-0683-5>.
- [53] Kouwenhoven LP, Schön G, Sohn LL. Introduction to Mesoscopic Electron Transport. 1997. Available from: [https://doi.org/10.1007/978-94-015-8839-3\\_1](https://doi.org/10.1007/978-94-015-8839-3_1).
- [54] Hanson R, Kouwenhoven LP, Petta JR, Tarucha S, Vandersypen LMK. Spins in few-electron quantum dots. *Rev Mod Phys*. 2007 Oct;79:1217-65. Available from: <https://link.aps.org/doi/10.1103/RevModPhys.79.1217>.
- [55] Kouwenhoven LP, Van Der Vaart NC, Johnson AT, Kool W, Harmans CJPM, Williamson JG, et al. Single electron charging effects in semiconductor quantum dots. *Z Phys B Condensed Matter*. 1991;85:36-373. Available from: <https://doi.org/10.1007/BF01307632>.
- [56] Buitelaar MR, Bachtold A, Nussbaumer T, Iqbal M, Schönenberger C. Multiwall Car-

- bon Nanotubes as Quantum Dots. *Phys Rev Lett*. 2002 Mar;88:156801. Available from: <https://link.aps.org/doi/10.1103/PhysRevLett.88.156801>.
- [57] Sapmaz S, Jarillo-Herrero P, Kong J, Dekker C, Kouwenhoven LP, van der Zant HSJ. Electronic excitation spectrum of metallic carbon nanotubes. *Phys Rev B*. 2005 Apr;71:153402. Available from: <https://link.aps.org/doi/10.1103/PhysRevB.71.153402>.
- [58] Liang W, Bockrath M, Bozovic D, Hafner JH, Tinkham M, Park H. Fabry-Perot interference in a nanotube electron waveguide. *Nature*. 2001;635(1970):665-9. Available from: <https://doi.org/10.1038/35079517>.
- [59] Yang CH, Leon RCC, Hwang JCC, Saraiva A, Tantt T, Huang W, et al. Operation of a silicon quantum processor unit cell above one kelvin. *Nature*. 2020;580(7803):350-4. Available from: <https://doi.org/10.1038/s41586-020-2171-6>.
- [60] Buitelaar MR, Nussbaumer T, Schönenberger C. Quantum Dot in the Kondo Regime Coupled to Superconductors. *Phys Rev Lett*. 2002 Dec;89:256801. Available from: <https://link.aps.org/doi/10.1103/PhysRevLett.89.256801>.
- [61] Desjardins MM, Viennot JJ, Dartiailh MC, Bruhat LE, Delbecq MR, Lee M, et al. Observation of the frozen charge of a Kondo resonance. *Nature*. 2017;545(7652):71-4. Available from: <https://doi.org/10.1038/nature21704>.
- [62] van der Wiel WG, De Franceschi S, Elzerman JM, Fujisawa T, Tarucha S, Kouwenhoven LP. Electron transport through double quantum dots. *Rev Mod Phys*. 2002 Dec;75:1-22. Available from: <https://link.aps.org/doi/10.1103/RevModPhys.75.1>.
- [63] Gaudreau L, Granger G, Kam A, Aers GC, Studenikin SA, Zawadzki P, et al. Coherent control of three-spin states in a triple quantum dot. *Nature Physics*. 2012;8(1):54-8. Available from: <https://doi.org/10.1038/nphys2149>.
- [64] Thalineau R, Hermelin S, Wieck AD, Bäuerle C, Saminadayar L, Meunier T. A few-electron quadruple quantum dot in a closed loop. *Applied Physics Letters*. 2012 09;101(10):103102. Available from: <https://doi.org/10.1063/1.4749811>.
- [65] Ito T, Otsuka T, Nakajima T, Delbecq MR, Amaha S, Yoneda J, et al. Four single-spin Rabi oscillations in a quadruple quantum dot. *Applied Physics Letters*. 2018 08;113(9):093102. Available from: <https://doi.org/10.1063/1.5040280>.

- [66] Kiczynski M, Gorman SK, Geng H, Donnelly MB, Chung Y, He Y, et al. Engineering topological states in atom-based semiconductor quantum dots. *Nature*. 2022;606(7915):694-9. Available from: <https://doi.org/10.1038/s41586-022-04706-0>.
- [67] van der Vaart NC, Godijn SF, Nazarov YV, Harmans CJPM, Mooij JE, Molenkamp LW, et al. Resonant Tunneling Through Two Discrete Energy States. *Phys Rev Lett*. 1995 Jun;74:4702-5. Available from: <https://link.aps.org/doi/10.1103/PhysRevLett.74.4702>.
- [68] Fujisawa T, Tarucha S. Resonant tunneling properties of single electron transistors with a novel double-gate geometry. *Applied Physics Letters*. 1996 01;68(4):526-8. Available from: <https://doi.org/10.1063/1.116388>.
- [69] Mason N, Biercuk MJ, Marcus CM. Local Gate Control of a Carbon Nanotube Double Quantum Dot. *Science*. 2004;303(5658):655-8. Available from: <https://www.science.org/doi/abs/10.1126/science.1093605>.
- [70] Biercuk MJ, Garaj S, Mason N, Chow JM, Marcus CM. Gate-Defined Quantum Dots on Carbon Nanotubes. *Nano Letters*. 2005;5(7):1267-71. PMID: 16178222. Available from: <https://doi.org/10.1021/nl050364v>.
- [71] Pothier H, Lafarge P, Urbina C, Esteve D, Devoret MH. Single-Electron Pump Based on Charging Effects. *Europhysics Letters*. 1992 jan;17(3):249. Available from: <https://dx.doi.org/10.1209/0295-5075/17/3/011>.
- [72] Botzem T, Shulman MD, Foletti S, Harvey SP, Dial OE, Bethke P, et al. Tuning Methods for Semiconductor Spin Qubits. *Phys Rev Appl*. 2018 Nov;10:054026. Available from: <https://link.aps.org/doi/10.1103/PhysRevApplied.10.054026>.
- [73] Baart TA, Eendebak PT, Reichl C, Wegscheider W, Vandersypen LMK. Computer-automated tuning of semiconductor double quantum dots into the single-electron regime. *Applied Physics Letters*. 2016 05;108(21):213104. Available from: <https://doi.org/10.1063/1.4952624>.
- [74] Mills AR, Feldman MM, Monical C, Lewis PJ, Larson KW, Mounce AM, et al. Computer-automated tuning procedures for semiconductor quantum dot arrays. *Applied Physics Letters*. 2019 09;115(11):113501. Available from: <https://doi.org/10.1063/1.5121444>.

- [75] Wang W, Rooney JD, Jiang H. Automated Characterization of a Double Quantum Dot using the Hubbard Model. 2023. Available from: <http://arxiv.org/abs/2309.03400>.
- [76] Moon H, Lennon DT, Kirkpatrick J, Esbroeck NMV, Camenzind LC, Yu L, et al. Machine learning enables completely automatic tuning of a quantum device faster than human experts. *Nature Communications*; (2020):24-9. Available from: <https://doi.org/10.1038/s41467-020-17835-9>.
- [77] Lennon DT, Moon H, Camenzind LC, Yu L, Zumbühl DM, Briggs GAD, et al. Efficiently measuring a quantum device using machine learning. *npj Quantum Information*. 2019;1-8. Available from: <https://doi.org/10.1038/s41534-019-0193-4>.
- [78] Hayashi T, Fujisawa T, Cheong HD, Jeong YH, Hirayama Y. Coherent Manipulation of Electronic States in a Double Quantum Dot. *Phys Rev Lett*. 2003 Nov;91:226804. Available from: <https://link.aps.org/doi/10.1103/PhysRevLett.91.226804>.
- [79] Elzerman JM, Hanson R, Greidanus JS, Willems van Beveren LH, De Franceschi S, Vandersypen LMK, et al. Few-electron quantum dot circuit with integrated charge read out. *Phys Rev B*. 2003 Apr;67:161308. Available from: <https://link.aps.org/doi/10.1103/PhysRevB.67.161308>.
- [80] Petersen G, Hoffmann EA, Schuh D, Wegscheider W, Giedke G, Ludwig S. Large Nuclear Spin Polarization in Gate-Defined Quantum Dots Using a Single-Domain Nanomagnet. *Phys Rev Lett*. 2013 Apr;110:177602. Available from: <https://link.aps.org/doi/10.1103/PhysRevLett.110.177602>.
- [81] Viennot JJ, Delbecq MR, Dartiailh MC, Cottet A, Kontos T. Out-of-equilibrium charge dynamics in a hybrid circuit quantum electrodynamics architecture. *Phys Rev B*. 2014 Apr;89:165404. Available from: <https://link.aps.org/doi/10.1103/PhysRevB.89.165404>.
- [82] Scarlino P, Ungerer JH, van Woerkom DJ, Mancini M, Stano P, Müller C, et al. In situ Tuning of the Electric-Dipole Strength of a Double-Dot Charge Qubit: Charge-Noise Protection and Ultrastrong Coupling. *Phys Rev X*. 2022 Jul;12:031004. Available from: <https://link.aps.org/doi/10.1103/PhysRevX.12.031004>.
- [83] Kuhlmann AV, Houel J, Ludwig A, Greuter L, Reuter D, Wieck AD, et al. Charge noise and spin noise in a semiconductor quantum device. *Nature Physics*. 2013;9(9):570-5. Available from: <https://doi.org/10.1038/nphys2688>.

- [84] Petersson KD, Petta JR, Lu H, Gossard AC. Quantum Coherence in a One-Electron Semiconductor Charge Qubit. *Phys Rev Lett*. 2010 Dec;105:246804. Available from: <https://link.aps.org/doi/10.1103/PhysRevLett.105.246804>.
- [85] Penfold-Fitch ZV, Sfigakis F, Buitelaar MR. Microwave Spectroscopy of a Carbon Nanotube Charge Qubit. *Phys Rev Appl*. 2017 May;7:054017. Available from: <https://link.aps.org/doi/10.1103/PhysRevApplied.7.054017>.
- [86] Tyryshkin AM, Tojo S, Morton JJJ, Riemann H, Abrosimov NV, Becker P, et al. Electron spin coherence exceeding seconds in high-purity silicon. *Nature Materials*. 2012;11(2):143-7. Available from: <https://doi.org/10.1038/nmat3182>.
- [87] Saeedi K, Simmons S, Salvail JZ, Dluhy P, Riemann H, Abrosimov NV, et al. Room-Temperature Quantum Bit Storage Exceeding 39 Minutes Using Ionized Donors in Silicon-28. *Science*. 2013;342(6160):830-3. Available from: <https://www.science.org/doi/abs/10.1126/science.1239584>.
- [88] Eizerman JM, Hanson R, Van Beveren LHW, Witkamp B, Vandersypen LMK, Kouwenhoven LP. Single-shot read-out of an individual electron spin in a quantum dot. *Nature*. 2004;430(6998):431-5. Available from: <https://doi.org/10.1038/nature02693>.
- [89] Mills AR, Guinn CR, Gullans MJ, Sigillito AJ, Feldman MM, Nielsen E, et al. Two-qubit silicon quantum processor with operation fidelity exceeding 99%. *Science Advances*. 2022;8(14):eabn5130. Available from: <https://www.science.org/doi/abs/10.1126/sciadv.abn5130>.
- [90] Xue X, Watson TF, Helsen J, Ward DR, Savage DE, Lagally MG, et al. Benchmarking Gate Fidelities in a Si/SiGe Two-Qubit Device. *Phys Rev X*. 2019 Apr;9:021011. Available from: <https://link.aps.org/doi/10.1103/PhysRevX.9.021011>.
- [91] Yoneda J, Takeda K, Noiri A, Nakajima T, Li S, Kamioka J, et al. Quantum non-demolition readout of an electron spin in silicon. *Nature Communications*. 2020;11(1):1-7. Available from: <https://doi.org/10.1038/s41467-020-14818-8>.
- [92] Koppens FHL, Buizert C, Tielrooij KJ, Vink IT, Nowack KC, Meunier T, et al. Driven coherent oscillations of a single electron spin in a quantum dot. *Nature*. 2006;442(7104):766-71. Available from: <https://doi.org/10.1038/nature05065>.
- [93] Koppens FHL, Nowack KC, Vandersypen LMK. Spin Echo of a Single Electron Spin in a Quantum Dot. *Phys Rev Lett*. 2008 Jun;100:236802. Available from: <https://link.aps.org/doi/10.1103/PhysRevLett.100.236802>.

- [//link.aps.org/doi/10.1103/PhysRevLett.100.236802](https://link.aps.org/doi/10.1103/PhysRevLett.100.236802).
- [94] Veldhorst M, Yang CH, Hwang JCC, Huang W, Dehollain JP, Muhonen JT, et al. A two-qubit logic gate in silicon. *Nature*. 2015;526(7573):410-4. Available from: <https://doi.org/10.1038/nature15263>.
- [95] Forster F, Mühlbacher M, Schuh D, Wegscheider W, Ludwig S. Electric-dipole-induced spin resonance in a lateral double quantum dot incorporating two single-domain nanomagnets. *Phys Rev B*. 2015 May;91:195417. Available from: <https://link.aps.org/doi/10.1103/PhysRevB.91.195417>.
- [96] Nadj-Perge S, Frolov SM, Bakkers EPAM, Kouwenhoven LP. Spin-orbit qubit in a semiconductor nanowire. *Nature*. 2010;468(7327):1084-7. Available from: <https://doi.org/10.1038/nature09682>.
- [97] Maurand R, Jehl X, Kotekar-Patil D, Corna A, Bohuslavskyi H, Laviéville R, et al. A CMOS silicon spin qubit. *Nature Communications*. 2016;7:3-8. Available from: <https://doi.org/10.1038/ncomms13575>.
- [98] Watzinger H, Kukučka J, Vukušić L, Gao F, Wang T, Schäffler F, et al. A germanium hole spin qubit. *Nature Communications*. 2018;9(1):2-7. Available from: <https://doi.org/10.1038/s41467-018-06418-4>.
- [99] Piot N, Brun B, Schmitt V, Zihlmann S, Michal VP, Apra A, et al. A single hole spin with enhanced coherence in natural silicon. *Nature Nanotechnology*. 2022;17(10):1072-7. Available from: <https://doi.org/10.1038/s41565-022-01196-z>.
- [100] Yoneda J, Otsuka T, Nakajima T, Takakura T, Obata T, Pioro-Ladrière M, et al. Fast Electrical Control of Single Electron Spins in Quantum Dots with Vanishing Influence from Nuclear Spins. *Phys Rev Lett*. 2014 Dec;113:267601. Available from: <https://link.aps.org/doi/10.1103/PhysRevLett.113.267601>.
- [101] Zajac DM, Sigillito AJ, Russ M, Borjans F, Taylor JM, Burkard G, et al. Resonantly driven CNOT gate for electron spins. *Science*. 2018;359(6374):439-42. Available from: <https://www.science.org/doi/abs/10.1126/science.aao5965>.
- [102] Petta JR, Johnson AC, Taylor JM, Laird EA, Yacoby A, Lukin MD, et al. Coherent Manipulation of Coupled Electron Spins in Semiconductor Quantum Dots. *Science*. 2005;309(5744):2180-4. Available from: <https://www.science.org/doi/abs/10.1126/science.1116955>.

- [103] Nowack KC, Shafiei M, Laforest M, Prawiroatmodjo GEDK, Schreiber LR, Reichl C, et al. Single-Shot Correlations and Two-Qubit Gate of Solid-State Spins. *Science*. 2011;333(6047):1269-72. Available from: <https://www.science.org/doi/abs/10.1126/science.1209524>.
- [104] Bertrand B, Hermelin S, Takada S, Yamamoto M, Tarucha S, Ludwig A, et al. Fast spin information transfer between distant quantum dots using individual electrons. *Nature Nanotechnology*. 2016;11(8):672-6. Available from: <https://doi.org/10.1038/nnano.2016.82>.
- [105] Jadot B, Mortemousque PA, Chanrion E, Thiney V, Ludwig A, Wieck AD, et al. Distant spin entanglement via fast and coherent electron shuttling. *Nature Nanotechnology*. 2021;16(5):570-5. Available from: <https://doi.org/10.1038/s41565-021-00846-y>.
- [106] Baart TA, Fujita T, Reichl C, Wegscheider W, Vandersypen LMK. Coherent spin-exchange via a quantum mediator. *Nature Nanotechnology*. 2016;12(1):26-30. Available from: <https://doi.org/10.1038/nnano.2016.188>.
- [107] Mills AR, Zajac DM, Gullans MJ, Schupp FJ, Hazard TM, Petta JR. Shuttling a single charge across a one-dimensional array of silicon quantum dots. *Nature Communications*. 2019;10(1). Available from: <https://doi.org/10.1038/s41467-019-08970-z>.
- [108] Yoneda J, Huang W, Feng M, Yang CH, Chan KW, Tanttü T, et al. Coherent spin qubit transport in silicon. *Nature Communications*. 2021;12(1):1-9. Available from: <https://doi.org/10.1038/s41467-021-24371-7>.
- [109] Qiao H, Kandel YP, Fallahi S, Gardner GC, Manfra MJ, Hu X, et al. Long-Distance Superexchange between Semiconductor Quantum-Dot Electron Spins. *Phys Rev Lett*. 2021 Jan;126:017701. Available from: <https://link.aps.org/doi/10.1103/PhysRevLett.126.017701>.
- [110] Shulman MD, Dial OE, Harvey SP, Bluhm H, Umansky V, Yacoby A. Demonstration of Entanglement of Electrostatically Coupled Singlet-Triplet Qubits. *Science*. 2012;336(6078):202-5. Available from: <https://www.science.org/doi/abs/10.1126/science.1217692>.
- [111] Stano P, Loss D. Review of performance metrics of spin qubits in gated semiconducting nanostructures. *Nature Reviews Physics*. 2022;4(10):672-88. Available from: <https://doi.org/10.1038/s42254-022-00484-w>.

- [112] Veldhorst M, Hwang JCC, Yang CH, Leenstra AW, De Ronde B, Dehollain JP, et al. An addressable quantum dot qubit with fault-tolerant control-fidelity. *Nature Nanotechnology*. 2014;9(12):981-5. Available from: <https://doi.org/10.1038/nnano.2014.216>.
- [113] Chan KW, Sahasrabudhe H, Huang W, Wang Y, Yang HC, Veldhorst M, et al. Exchange Coupling in a Linear Chain of Three Quantum-Dot Spin Qubits in Silicon. *Nano Letters*. 2021;21(3):1517-22. PMID: 33481612. Available from: <https://doi.org/10.1021/acs.nanolett.0c04771>.
- [114] Noiri A, Takeda K, Nakajima T, Kobayashi T, Sammak A, Scappucci G, et al. Fast universal quantum gate above the fault-tolerance threshold in silicon. *Nature*. 2022;601(7893):338-42. Available from: <https://doi.org/10.1038/s41586-021-04182-y>.
- [115] Lawrie WIL, Russ M, van Riggelen F, Hendrickx NW, de Snoo SL, Sammak A, et al. Simultaneous single-qubit driving of semiconductor spin qubits at the fault-tolerant threshold. *Nature Communications*. 2023:1-7. Available from: <https://doi.org/10.1038/s41467-023-39334-3>.
- [116] Kane BE. A silicon-based nuclear spin quantum computer. *Nature*. 1998;393(6681):133-7. Available from: <https://doi.org/10.1038/30156>.
- [117] Muhonen JT, Dehollain JP, Laucht A, Hudson FE, Kalra R, Sekiguchi T, et al. Storing quantum information for 30 seconds in a nanoelectronic device. *Nature Nanotechnology*. 2014;9(12):986-91. Available from: <https://doi.org/10.1038/nnano.2014.211>.
- [118] Morello A, Pla JJ, Zwanenburg FA, Chan KW, Tan KY, Huebl H, et al. Single-shot readout of an electron spin in silicon. *Nature*. 2010;467(7316):687-91. Available from: <https://doi.org/10.1038/nature09392>.
- [119] Fuechsle M, Miwa JA, Lee S. A Single-Atom Transistor. *Nature Nanotechnology*. 2012. Available from: <https://doi.org/10.1038/nnano.2012.21>.
- [120] Pla JJ, Tan KY, Dehollain JP, Lim WH, Morton JJJ, Zwanenburg FA, et al. High-fidelity readout and control of a nuclear spin qubit in silicon. *Nature*. 2013;496(7445):334-8. Available from: <https://doi.org/10.1038/nature12011>.
- [121] Laucht A, Kalra R, Simmons S, Dehollain JP, Muhonen JT, Mohiyaddin FA, et al. A dressed spin qubit in silicon. *Nature Nanotechnology*. 2017;12(1):61-6. Available from: <https://doi.org/10.1038/nnano.2016.178>.

- [122] Mądzik MT, Asaad S, Youssry A, Joecker B, Rudinger KM, Nielsen E, et al. Precision tomography of a three-qubit donor quantum processor in silicon. *Nature*. 2022 jun. Available from: <https://doi.org/10.1038/s41586-021-04292-7>.
- [123] Levy J. Universal Quantum Computation with Spin-1/2 Pairs and Heisenberg Exchange. *Phys Rev Lett*. 2002 Sep;89:147902. Available from: <https://link.aps.org/doi/10.1103/PhysRevLett.89.147902>.
- [124] Laird EA, Barthel C, Rashba EI, Marcus CM, Hanson MP, Gossard AC. Hyperfine-Mediated Gate-Driven Electron Spin Resonance. *Phys Rev Lett*. 2007 Dec;99:246601. Available from: <https://link.aps.org/doi/10.1103/PhysRevLett.99.246601>.
- [125] Wu X, Ward DR, Prance JR, Kim D, Gamble JK, Mohr RT, et al. Two-axis control of a singlet–triplet qubit with an integrated micromagnet. *Proceedings of the National Academy of Sciences*. 2014;111(33):11938-42. Available from: <https://www.pnas.org/doi/abs/10.1073/pnas.1412230111>.
- [126] Lai NS, Lim WH, Yang CH, Zwanenburg FA, Coish WA, Qassemi F, et al. Pauli spin blockade in a highly tunable silicon double quantum dot. *Scientific Reports*. 2011;1. Available from: <https://doi.org/10.1038/srep00110>.
- [127] Noiri A, Takeda K, Yoneda J, Nakajima T, Kodera T, Tarucha S. Radio-Frequency-Detected Fast Charge Sensing in Undoped Silicon Quantum Dots. *Nano Letters*. 2020;20(2):947-52. PMID: 31944116. Available from: <https://doi.org/10.1021/acs.nanolett.9b03847>.
- [128] Takeda K, Noiri A, Yoneda J, Nakajima T, Tarucha S. Resonantly Driven Singlet-Triplet Spin Qubit in Silicon. *Phys Rev Lett*. 2020 Mar;124:117701. Available from: <https://link.aps.org/doi/10.1103/PhysRevLett.124.117701>.
- [129] Cerfontaine P, Botzem T, Ritzmann J, Humpohl SS, Ludwig A, Schuh D, et al. Closed-loop control of a GaAs-based singlet-triplet spin qubit with 99.5 % Fidelity. *Nature Communications*. 2020;11(1):1-7. Available from: <https://doi.org/10.1038/s41467-020-17865-3>.
- [130] Nichol JM, Orona LA, Harvey SP, Fallahi S, Gardner GC, Manfra MJ, et al. High-fidelity entangling gate for double-quantum-dot spin qubits. *npj Quantum Information*. 2017;3(1):1-4. Available from: <https://doi.org/10.1038/s41534-016-0003-1>.
- [131] Bacon D, Kempe J, Lidar DA, Whaley KB. Universal Fault-Tolerant Quantum Compu-

- tation on Decoherence-Free Subspaces. *Phys Rev Lett.* 2000 Aug;85:1758-61. Available from: <https://link.aps.org/doi/10.1103/PhysRevLett.85.1758>.
- [132] Laird EA, Taylor JM, DiVincenzo DP, Marcus CM, Hanson MP, Gossard AC. Coherent spin manipulation in an exchange-only qubit. *Phys Rev B.* 2010 Aug;82:075403. Available from: <https://link.aps.org/doi/10.1103/PhysRevB.82.075403>.
- [133] Thorgrimsson B, Kim D, Yang YC, Smith LW, Simmons CB, Ward DR, et al. Extending the coherence of a quantum dot hybrid qubit. *npj Quantum Information.* 2017;3(1). Available from: <https://doi.org/10.1038/s41534-017-0034-2>.
- [134] Blumoff JZ, Pan AS, Keating TE, Andrews RW, Barnes DW, Brecht TL, et al. Fast and High-Fidelity State Preparation and Measurement in Triple-Quantum-Dot Spin Qubits. *PRX Quantum.* 2022 Mar;3:010352. Available from: <https://link.aps.org/doi/10.1103/PRXQuantum.3.010352>.
- [135] Martins F, Malinowski FK, Nissen PD, Barnes E, Fallahi S, Gardner GC, et al. Noise Suppression Using Symmetric Exchange Gates in Spin Qubits. *Phys Rev Lett.* 2016 Mar;116:116801. Available from: <https://link.aps.org/doi/10.1103/PhysRevLett.116.116801>.
- [136] Reed MD, Maune BM, Andrews RW, Borselli MG, Eng K, Jura MP, et al. Reduced Sensitivity to Charge Noise in Semiconductor Spin Qubits via Symmetric Operation. *Phys Rev Lett.* 2016 Mar;116:110402. Available from: <https://link.aps.org/doi/10.1103/PhysRevLett.116.110402>.
- [137] Andrews RW, Jones C, Reed MD, Jones AM, Ha SD, Jura MP, et al. Quantifying error and leakage in an encoded Si/SiGe triple-dot qubit. *Nature Nanotechnology.* 2019;14(8):747-50. Available from: <https://doi.org/10.1038/s41565-019-0500-4>.
- [138] Ha W, Ha SD, Choi MD, Tang Y, Schmitz AE, Levendorf MP, et al. A Flexible Design Platform for Si/SiGe Exchange-Only Qubits with Low Disorder. *Nano Letters.* 2022;22(3):1443-8. PMID: 34806894. Available from: <https://doi.org/10.1021/acs.nanolett.1c03026>.
- [139] Weinstein AJ, Reed MD, Jones AM, Andrews RW, Barnes D, Blumoff JZ, et al. Universal logic with encoded spin qubits in silicon. *Nature.* 2023;615(March 2022). Available from: <https://doi.org/10.1038/s41586-023-05777-3>.
- [140] Medford J, Beil J, Taylor JM, Rashba EI, Lu H, Gossard AC, et al. Quantum-Dot-

- Based Resonant Exchange Qubit. *Phys Rev Lett*. 2013 Jul;111:050501. Available from: <https://link.aps.org/doi/10.1103/PhysRevLett.111.050501>.
- [141] Blais A, Huang RS, Wallraff A, Girvin SM, Schoelkopf RJ. Cavity quantum electrodynamics for superconducting electrical circuits: An architecture for quantum computation. *Phys Rev A*. 2004 Jun;69:062320. Available from: <https://link.aps.org/doi/10.1103/PhysRevA.69.062320>.
- [142] Lescanne R, Villiers M, Peronnin T, Sarlette A, Delbecq M, Huard B, et al. Exponential suppression of bit-flips in a qubit encoded in an oscillator. *Nature Physics*. 2020;16(5):509-13. Available from: <https://doi.org/10.1038/s41567-020-0824-x>.
- [143] Kubo Y, Ong FR, Bertet P, Vion D, Jacques V, Zheng D, et al. Strong Coupling of a Spin Ensemble to a Superconducting Resonator. *Phys Rev Lett*. 2010 Sep;105:140502. Available from: <https://link.aps.org/doi/10.1103/PhysRevLett.105.140502>.
- [144] Wang Z, Balembois L, Rančić M, Billaud E, Le Dantec M, Ferrier A, et al. Single-electron spin resonance detection by microwave photon counting. *Nature*. 2023;619(7969):276-81. Available from: <https://doi.org/10.1038/s41586-023-06097-2>.
- [145] Cottet A, Kontos T, Sahoo S, Man HT, Choi MS, Belzig W, et al. Nanospintronics with carbon nanotubes. *Semiconductor Science and Technology*. 2006 oct;21(11):S78. Available from: <https://dx.doi.org/10.1088/0268-1242/21/11/S11>.
- [146] Bruhat LE, Cubaynes T, Viennot JJ, Dartiailh MC, Desjardins MM, Cottet A, et al. Circuit QED with a quantum-dot charge qubit dressed by Cooper pairs. *Phys Rev B*. 2018 Oct;98:155313. Available from: <https://link.aps.org/doi/10.1103/PhysRevB.98.155313>.
- [147] Sahoo S, Kontos T, Furer J, Hoffmann C, Gräber M, Cottet A, et al. Electric field control of spin transport. *Nature Physics*. 2005;1(2):99-102. Available from: <https://doi.org/10.1038/nphys149>.
- [148] Feuillet-Palma C, Delattre T, Morfin P, Berroir JM, Fève G, Glattli DC, et al. Conserved spin and orbital phase along carbon nanotubes connected with multiple ferromagnetic contacts. *Phys Rev B*. 2010 Mar;81:115414. Available from: <https://link.aps.org/doi/10.1103/PhysRevB.81.115414>.
- [149] Hauptmann JR, Paaske J, Lindelof PE. Electric-field-controlled spin reversal in a

- quantum dot with ferromagnetic contacts. *Nature Physics*. 2008;4(5):373-6. Available from: <https://doi.org/10.1038/nphys931>.
- [150] Bordoloi A, Zannier V, Sorba L, Schönenberger C, Baumgartner A. A double quantum dot spin valve. *Communications Physics*. 2020;3(1):1-7. Available from: <https://doi.org/10.1038/s42005-020-00405-2>.
- [151] Viennot JJ, Dartiailh MC, Cottet A, Kontos T. Coherent coupling of a single spin to microwave cavity photons. *Science*. 2015;349(6246):408-11. Available from: <https://www.science.org/doi/abs/10.1126/science.aaa3786>.
- [152] Cubaynes T, Delbecq MR, Dartiailh MC, Assouly R, Desjardins MM, Contamin LC, et al. Highly coherent spin states in carbon nanotubes coupled to cavity photons. *npj Quantum Information*. 2019 dec;5(1). Available from: <https://doi.org/10.1038/s41534-019-0169-4>.
- [153] Pioro-Ladrière M, Tokura Y, Obata T, Kubo T, Tarucha S. Micromagnets for coherent control of spin-charge qubit in lateral quantum dots. *Applied Physics Letters*. 2007 01;90(2):024105. Available from: <https://doi.org/10.1063/1.2430906>.
- [154] Yoneda J, Otsuka T, Takakura T, Pioro-Ladrière M, Brunner R, Lu H, et al. Robust micromagnet design for fast electrical manipulations of single spins in quantum dots. *Applied Physics Express*. 2015 jul;8(8):084401. Available from: <https://dx.doi.org/10.7567/APEX.8.084401>.
- [155] Legrand W, Lopes S, Schaefferbeke Q, Moutaigne F, Desjardins MM. Optimal design of nanomagnets for on-chip field gradients. *Phys Rev Appl*. 2023 Oct;20:044062. Available from: <https://link.aps.org/doi/10.1103/PhysRevApplied.20.044062>.
- [156] Harvey-Collard P, Dijkema J, Zheng G, Sammak A, Scappucci G, Vandersypen LMK. Coherent Spin-Spin Coupling Mediated by Virtual Microwave Photons. *Phys Rev X*. 2022 May;12:021026. Available from: <https://link.aps.org/doi/10.1103/PhysRevX.12.021026>.
- [157] Desjardins MM, Contamin LC, Delbecq MR, Dartiailh MC, Bruhat LE. Synthetic spin orbit interaction for Majorana devices. *Nature Materials*. 2019:1-60. Available from: <https://doi.org/10.1038/s41563-019-0457-6>.
- [158] Contamin LC, Jarjat L, Legrand W, Cottet A, Kontos T, Delbecq MR. Zero energy states clustering in an elemental nanowire coupled to a superconductor. *Nature*

- ture Communications. 2022;13(1):1-7. Available from: <https://doi.org/10.1038/s41467-022-33960-z>.
- [159] Haugen H, Huertas-Hernando D, Brataas A. Spin transport in proximity-induced ferromagnetic graphene. *Phys Rev B*. 2008 Mar;77:115406. Available from: <https://link.aps.org/doi/10.1103/PhysRevB.77.115406>.
- [160] Nadj-Perge S, Pribiag VS, van den Berg JWG, Zuo K, Plissard SR, Bakkers EPAM, et al. Spectroscopy of Spin-Orbit Quantum Bits in Indium Antimonide Nanowires. *Phys Rev Lett*. 2012 Apr;108:166801. Available from: <https://link.aps.org/doi/10.1103/PhysRevLett.108.166801>.
- [161] Camenzind LC, Geyer S, Fuhrer A, Warburton RJ, Zumbühl DM, Kuhlmann AV. A hole spin qubit in a fin field-effect transistor above 4 kelvin. *Nature Electronics*. 2022;5(3):178-83. Available from: <https://doi.org/10.1038/s41928-022-00722-0>.
- [162] Petersson KD, McFaul LW, Schroer MD, Jung M, Taylor JM, Houck AA, et al. Circuit quantum electrodynamics with a spin qubit. *Nature*. 2012;490(7420):380-3. Available from: <https://doi.org/10.1038/nature11559>.
- [163] Yu CX, Zihlmann S, Abadillo-Uriel JC, Michal VP, Rambal N, Niebojewski H, et al. Strong coupling between a photon and a hole spin in silicon. 2022 jun. Available from: <https://doi.org/10.1038/s41565-023-01332-3>.
- [164] Russ M, Ginzl F, Burkard G. Coupling of three-spin qubits to their electric environment. *Phys Rev B*. 2016 Oct;94:165411. Available from: <https://link.aps.org/doi/10.1103/PhysRevB.94.165411>.
- [165] Ungerer JH, Pally A, Kononov A, Lehmann S, Ridderbos J, Thelander C, et al. Strong coupling between a microwave photon and a singlet-triplet qubit. in *Preparation*. 2023;1:1-10. Available from: <https://arxiv.org/abs/2303.16825>.
- [166] Goy P, Raimond JM, Gross M, Haroche S. Observation of Cavity-Enhanced Single-Atom Spontaneous Emission. *Phys Rev Lett*. 1983 Jun;50:1903-6. Available from: <https://link.aps.org/doi/10.1103/PhysRevLett.50.1903>.
- [167] Boulant N, Ithier G, Meeson P, Nguyen F, Vion D, Esteve D, et al. Quantum nondemolition readout using a Josephson bifurcation amplifier. *Phys Rev B*. 2007 Jul;76:014525. Available from: <https://link.aps.org/doi/10.1103/PhysRevB.76.014525>.

- [168] Lupaşcu A, Saito S, Picot T, de Groot PC, Harmans CJPM, Mooij JE. Quantum non-demolition measurement of a superconducting two-level system. *Nature Physics*. 2007 Jan;3(2):119–123. Available from: <http://dx.doi.org/10.1038/nphys509>.
- [169] Childress L, Sørensen AS, Lukin MD. Mesoscopic cavity quantum electrodynamics with quantum dots. *Phys Rev A*. 2004 Apr;69:042302. Available from: <https://link.aps.org/doi/10.1103/PhysRevA.69.042302>.
- [170] Cottet A, Dartiailh MC, Desjardins MM, Cubaynes T, Contamin LC, Delbecq M, et al. Cavity QED with hybrid nanocircuits: from atomic-like physics to condensed matter phenomena. *Journal of Physics: Condensed Matter*. 2017 sep;29(43):433002. Available from: <https://dx.doi.org/10.1088/1361-648X/aa7b4d>.
- [171] Mi X, Cady JV, Zajac DM, Deelman PW, Petta JR. Strong coupling of a single electron in silicon to a microwave photon. *Science*. 2017;355(6321):156-8. Available from: <https://www.science.org/doi/abs/10.1126/science.aal2469>.
- [172] Stockklauser A, Scarlino P, Koski JV, Gasparinetti S, Andersen CK, Reichl C, et al. Strong Coupling Cavity QED with Gate-Defined Double Quantum Dots Enabled by a High Impedance Resonator. *Phys Rev X*. 2017 Mar;7:011030. Available from: <https://link.aps.org/doi/10.1103/PhysRevX.7.011030>.
- [173] Delbecq MR, Bruhat LE, Viennot JJ, Datta S, Cottet A, Kontos T. Photon-mediated interaction between distant quantum dot circuits. *Nature Communications*. 2013;4:1-8. Available from: <https://doi.org/10.1038/ncomms2407>.
- [174] Deng GW, Wei D, Li SX, Johansson JR, Kong WC, Li HO, et al. Coupling Two Distant Double Quantum Dots with a Microwave Resonator. *Nano Letters*. 2015;15(10):6620-5. PMID: 26327140. Available from: <https://doi.org/10.1021/acs.nanolett.5b02400>.
- [175] Göppl M, Fregner A, Baur M, Bianchetti R, Filipp S, Fink JM, et al. Coplanar waveguide resonators for circuit quantum electrodynamics. *Journal of Applied Physics*. 2008 12;104(11):113904. Available from: <https://doi.org/10.1063/1.3010859>.
- [176] Pozar DM. *Microwave engineering* - 4th ed. Hoboken, NJ: Wiley; 2011.
- [177] Delbecq M. Coupling quantum dot circuits to microwave cavities [Theses]. Université Pierre et Marie Curie - Paris VI; 2012. Available from: <https://theses.hal.science/tel-00828147>.

- [178] Viennot J. Charge and spin dynamics in a hybrid circuit quantum electrodynamics architecture [Theses]. Ecole Normale Supérieure de Paris - ENS Paris; 2014. Available from: <https://theses.hal.science/tel-01062841>.
- [179] Haroche S. Nobel Lecture: Controlling photons in a box and exploring the quantum to classical boundary. *Rev Mod Phys.* 2013 Jul;85:1083-102. Available from: <https://link.aps.org/doi/10.1103/RevModPhys.85.1083>.
- [180] Cottet A, Kontos T, Douçot B. Electron-photon coupling in mesoscopic quantum electrodynamics. *Phys Rev B.* 2015 May;91:205417. Available from: <https://link.aps.org/doi/10.1103/PhysRevB.91.205417>.
- [181] Blais A, Grimsmo AL, Girvin SM, Wallraff A. Circuit quantum electrodynamics. *Rev Mod Phys.* 2021 May;93:025005. Available from: <https://link.aps.org/doi/10.1103/RevModPhys.93.025005>.
- [182] Richer S, DiVincenzo D. Circuit design implementing longitudinal coupling: A scalable scheme for superconducting qubits. *Phys Rev B.* 2016 Apr;93:134501. Available from: <https://link.aps.org/doi/10.1103/PhysRevB.93.134501>.
- [183] Haroche S, Raimond JM. *Exploring the Quantum: Atoms, Cavities, and Photons.* Oxford: Oxford Univ. Press; 2006. Available from: <https://cds.cern.ch/record/993568>.
- [184] Schuster DI, Wallraff A, Blais A, Frunzio L, Huang RS, Majer J, et al. ac Stark Shift and Dephasing of a Superconducting Qubit Strongly Coupled to a Cavity Field. *Phys Rev Lett.* 2005 Mar;94:123602. Available from: <https://link.aps.org/doi/10.1103/PhysRevLett.94.123602>.
- [185] Clerk AA, Devoret MH, Girvin SM, Marquardt F, Schoelkopf RJ. Introduction to quantum noise, measurement, and amplification. *Rev Mod Phys.* 2010 Apr;82:1155-208. Available from: <https://link.aps.org/doi/10.1103/RevModPhys.82.1155>.
- [186] Chen QM, Partanen M, Fesquet F, Honasoge KE, Kronowetter F, Nojiri Y, et al. Scattering coefficients of superconducting microwave resonators. II. System-bath approach. *Phys Rev B.* 2022 Dec;106:214506. Available from: <https://link.aps.org/doi/10.1103/PhysRevB.106.214506>.
- [187] Blum K. *Density matrix theory and applications*; 3rd ed. Springer series on atomic, optical, and plasma physics. Berlin: Springer; 2012. Available from: <https://doi>.

- [org/10.1007/978-3-642-20561-3](https://doi.org/10.1007/978-3-642-20561-3).
- [188] Cubaynes T. Shaping the spectrum of carbon nanotube quantum dots with superconductivity and ferromagnetism for mesoscopic quantum electrodynamics [Theses]. Sorbonne Université; 2018. Available from: <https://theses.hal.science/tel-02448439>.
- [189] Cubaynes T, Contamin LC, Dartiailh MC, Desjardins MM, Cottet A, Delbecq MR, et al. Nanoassembly technique of carbon nanotubes for hybrid circuit-QED. *Applied Physics Letters*. 2020 09;117(11):114001. Available from: <https://doi.org/10.1063/5.0021838>.
- [190] Holman N, Dodson JP, Edge LF, Coppersmith SN, Friesen M, McDermott R, et al. Microwave engineering for semiconductor quantum dots in a cQED architecture. *Applied Physics Letters*. 2020 08;117(8):083502. Available from: <https://doi.org/10.1063/5.0016248>.
- [191] Chauleau JY, McMorran BJ, Belkhou R, Bergeard N, Mentş TO, Niño MA, et al. Magnetization textures in NiPd nanostructures. *Phys Rev B*. 2011 Sep;84:094416. Available from: <https://link.aps.org/doi/10.1103/PhysRevB.84.094416>.
- [192] Charlier JC, Blase X, Roche S. Electronic and transport properties of nanotubes. *Rev Mod Phys*. 2007 May;79:677-732. Available from: <https://link.aps.org/doi/10.1103/RevModPhys.79.677>.
- [193] Chen Z, Appenzeller J, Knoch J, Lin Ym, Avouris P. The Role of MetalNanotube Contact in the Performance of Carbon Nanotube Field-Effect Transistors. *Nano Letters*. 2005;5(7):1497-502. PMID: 16178264. Available from: <https://doi.org/10.1021/nl10508624>.
- [194] A J, J G, Q W, M L, H D. Ballistic Carbon Nanotube field-effect transistors. *Nature*. 2003;424(August):654. Available from: <https://doi.org/10.1038/nature01797>.
- [195] Shan B, Cho K. First Principles Study of Work Functions of Single Wall Carbon Nanotubes. *Phys Rev Lett*. 2005 Jun;94:236602. Available from: <https://link.aps.org/doi/10.1103/PhysRevLett.94.236602>.
- [196] Endo M, Takeuchi K, Igarashi S, Kobori K, Shiraishi M, Kroto HW. The production and structure of pyrolytic carbon nanotubes (PCNTs). *Journal of Physics and Chem-*

- istry of Solids. 1993;54(12):1841-8. Available from: <https://www.sciencedirect.com/science/article/pii/0022369793902975>.
- [197] Endo M, Takeuchi K, Kobori K, Takahashi K, Kroto HW, Sarkar A. Pyrolytic carbon nanotubes from vapor-grown carbon fibers. *Carbon*. 1995;33(7):873-81. Nanotubes. Available from: <https://www.sciencedirect.com/science/article/pii/0008622395000167>.
- [198] Furer J. Growth of single-wall carbon nanotubes by chemical vapor deposition for electrical devices. University\_of\_Basel; 2006. Available from: [https://nanoelectronics.unibas.ch/wordpress/wp-content/uploads/theses/2005\\_Thesis\\_Juerg\\_Furer.pdf](https://nanoelectronics.unibas.ch/wordpress/wp-content/uploads/theses/2005_Thesis_Juerg_Furer.pdf).
- [199] Churchill HOH, Kuemmeth F, Harlow JW, Bestwick AJ, Rashba EI, Flensberg K, et al. Relaxation and Dephasing in a Two-Electron  $^{13}\text{C}$  Nanotube Double Quantum Dot. *Phys Rev Lett*. 2009 Apr;102:166802. Available from: <https://link.aps.org/doi/10.1103/PhysRevLett.102.166802>.
- [200] Wu CC, Liu CH, Zhong Z. One-Step Direct Transfer of Pristine Single-Walled Carbon Nanotubes for Functional Nanoelectronics. *Nano Letters*. 2010;10(3):1032-6. PMID: 20108926. Available from: <https://doi.org/10.1021/nl904260k>.
- [201] Pei F, Laird EA, Steele GA, Kouwenhoven LP. Valley-spin blockade and spin resonance in carbon nanotubes. *Nature Nanotechnology*. 2012;7(10):630-4. Available from: <https://doi.org/10.1038/nnano.2012.160>.
- [202] Gramich J, Baumgartner A, Muoth M, Hierold C, Schönenberger C. Fork stamping of pristine carbon nanotubes onto ferromagnetic contacts for spin-valve devices: Stamping CNTs onto ferromagnetic contacts. *physica status solidi (b)*. 2015 Jul;252(11):2496-2502. Available from: <http://dx.doi.org/10.1002/pssb.201552213>.
- [203] Blien S, Steger P, Albang A, Paradiso N, Hüttel AK. Quartz Tuning-Fork Based Carbon Nanotube Transfer into Quantum Device Geometries. *physica status solidi (b)*. 2018;255(12):1800118. Available from: <https://onlinelibrary.wiley.com/doi/abs/10.1002/pssb.201800118>.
- [204] Viennot JJ, Palomo J, Kontos T. Stamping single wall nanotubes for circuit quantum electrodynamics. *Applied Physics Letters*. 2014 03;104(11):113108. Available from: <https://doi.org/10.1063/1.4868868>.

- [205] Collins PG, Hersam M, Arnold M, Martel R, Avouris P. Current saturation and electrical breakdown in multiwalled carbon nanotubes. *Physical Review Letters*. 2001;86(14):3128-31. Available from: <https://doi.org/10.1103/PhysRevLett.86.3128>.
- [206] Collins PG, Arnold MS, Avouris P. Engineering Carbon Nanotubes and Nanotube Circuits Using Electrical Breakdown. *Science*. 2001;292(5517):706-9. Available from: <https://www.science.org/doi/abs/10.1126/science.1058782>.
- [207] Villiers M. Dynamically Enhancing Qubit-Photon Interactions with Anti-Squeezing [Theses]. Sorbonne Université; 2023. Available from: <https://hal.science/tel-04209718>.
- [208] Paik H, Schuster DI, Bishop LS, Kirchmair G, Catelani G, Sears AP, et al. Observation of High Coherence in Josephson Junction Qubits Measured in a Three-Dimensional Circuit QED Architecture. *Phys Rev Lett*. 2011 Dec;107:240501. Available from: <https://link.aps.org/doi/10.1103/PhysRevLett.107.240501>.
- [209] Desjardins M. Exploring quantum circuits with a cQed architecture : application to compressibility measurements [Theses]. PSL Research University; 2016. Available from: <https://theses.hal.science/tel-01745379>.
- [210] Althuon T, Cubaynes T, Auer A, Sürgers C, Wernsdorfer W. Nano-assembled open quantum dot nanotube devices. *Communications Materials*. 2024;5(1):1-7. Available from: <https://doi.org/10.1038/s43246-023-00439-3>.
- [211] Krantz P, Kjaergaard M, Yan F, Orlando TP, Gustavsson S, Oliver WD. A quantum engineer's guide to superconducting qubits. *Applied Physics Reviews*. 2019 06;6(2):021318. Available from: <https://doi.org/10.1063/1.5089550>.
- [212] Théry A, Neukelmance B, Hue B, Legrand W, Jarjat L, Craquelin J, et al. Observation of quantum oscillations in the extreme weak anharmonic limit. *Phys Rev B*. 2024 Feb;109:064505. Available from: <https://link.aps.org/doi/10.1103/PhysRevB.109.064505>.
- [213] Hazra S, Bhattacharjee A, Chand M, Salunkhe KV, Gopalakrishnan S, Patankar MP, et al. Ring-Resonator-Based Coupling Architecture for Enhanced Connectivity in a Superconducting Multiqubit Network. *Phys Rev Appl*. 2021 Aug;16:024018. Available from: <https://link.aps.org/doi/10.1103/PhysRevApplied.16.024018>.

- [214] Chen QM, Pfeiffer M, Partanen M, Fesquet F, Honasoge KE, Kronowetter F, et al. Scattering coefficients of superconducting microwave resonators. I. Transfer matrix approach. *Phys Rev B*. 2022 Dec;106:214505. Available from: <https://link.aps.org/doi/10.1103/PhysRevB.106.214505>.
- [215] Simons RN. Coplanar Waveguide Applications. vol. 7; 2001. Available from: <https://gctjaipur.files.wordpress.com/2015/08/coplanar-waveguide-circuits-components-and-systems.pdf>.
- [216] Annunziata AJ, Santavicca DF, Frunzio L, Catelani G, Rooks MJ, Frydman A, et al. Tunable superconducting nanoinductors. *Nanotechnology*. 2010 oct;21(44):445202. Available from: <https://dx.doi.org/10.1088/0957-4484/21/44/445202>.
- [217] Maxfield BW, McLean WL. Superconducting Penetration Depth of Niobium. *Phys Rev*. 1965 Aug;139:A1515-22. Available from: <https://link.aps.org/doi/10.1103/PhysRev.139.A1515>.
- [218] Niepce D, Burnett J, Bylander J. High Kinetic Inductance NbN Nanowire Superinductors. *Phys Rev Appl*. 2019 Apr;11:044014. Available from: <https://link.aps.org/doi/10.1103/PhysRevApplied.11.044014>.
- [219] Yu CX, Zihlmann S, Troncoso Fernández-Bada G, Thomassin JL, Gustavo F, Dumur et al. Magnetic field resilient high kinetic inductance superconducting niobium nitride coplanar waveguide resonators. *Applied Physics Letters*. 2021 02;118(5):054001. Available from: <https://doi.org/10.1063/5.0039945>.
- [220] Zhang X, Zhu Z, Ong NP, Petta JR. Developing high-impedance superconducting resonators and on-chip filters for semiconductor quantum dot circuit quantum electrodynamics. 2023:1-5. Available from: <http://arxiv.org/abs/2306.16499>.
- [221] Samkharadze N, Bruno A, Scarlino P, Zheng G, DiVincenzo DP, DiCarlo L, et al. High-Kinetic-Inductance Superconducting Nanowire Resonators for Circuit QED in a Magnetic Field. *Phys Rev Appl*. 2016 Apr;5:044004. Available from: <https://link.aps.org/doi/10.1103/PhysRevApplied.5.044004>.
- [222] Ungerer JH, Sarmah D, Kononov A, Ridderbos J, Haller R, Cheung LY, et al. Performance of high impedance resonators in dirty dielectric environments. 2023;5:1-10. Available from: <http://arxiv.org/abs/2302.06303>.
- [223] Shearrow A, Koolstra G, Whiteley SJ, Earnest N, Barry PS, Heremans FJ, et al. Atomic

- layer deposition of titanium nitride for quantum circuits. *Applied Physics Letters*. 2018 11;113(21):212601. Available from: <https://doi.org/10.1063/1.5053461>.
- [224] Grünhaupt L, Spiecker M, Gusenkova D, Maleeva N, Skacel ST, Takmakov I, et al. Granular aluminium as a superconducting material for high-impedance quantum circuits. *Nature Materials*. 2019;18(8):816-9. Available from: <https://doi.org/10.1038/s41563-019-0350-3>.
- [225] Borisov K, Rieger D, Winkel P, Henriques F, Valenti F, Ionita A, et al. Superconducting granular aluminum resonators resilient to magnetic fields up to 1 Tesla. *Applied Physics Letters*. 2020 09;117(12):120502. Available from: <https://doi.org/10.1063/5.0018012>.
- [226] Zheng G. Circuit Quantum Electrodynamics with Single Electron Spins in Silicon; 2021. Available from: <https://doi.org/10.4233/uuid:ee9e2137-630b-454b-8f37-228f068bcc89>.
- [227] Megrant A, Neill C, Barends R, Chiaro B, Chen Y, Feigl L, et al. Planar superconducting resonators with internal quality factors above one million. *Applied Physics Letters*. 2012 03;100(11):113510. Available from: <https://doi.org/10.1063/1.3693409>.
- [228] Anderson PW. Theory of dirty superconductors. *Journal of Physics and Chemistry of Solids*. 1959;11(1):26-30. Available from: <https://www.sciencedirect.com/science/article/pii/0022369759900368>.
- [229] Parmenter RH. Isospin Formulation of the Theory of a Granular Superconductor. *Phys Rev*. 1967 Feb;154:353-68. Available from: <https://link.aps.org/doi/10.1103/PhysRev.154.353>.
- [230] Maleeva N, Grünhaupt L, Klein T, Levy-Bertrand F, Dupré O, Calvo M, et al. Circuit quantum electrodynamics of granular aluminum resonators. *Nature Communications*. 2018;9(1):1-7. Available from: <https://doi.org/10.1038/s41467-018-06386-9>.
- [231] Levy-Bertrand F, Klein T, Grenet T, Dupré O, Benoît A, Bideaud A, et al. Electrodynamics of granular aluminum from superconductor to insulator: Observation of collective superconducting modes. *Phys Rev B*. 2019 Mar;99:094506. Available from: <https://link.aps.org/doi/10.1103/PhysRevB.99.094506>.
- [232] Rotzinger H, Skacel ST, Pfirrmann M, Voss JN, Münzberg J, Probst S, et al. Aluminium-oxide wires for superconducting high kinetic inductance circuits. *Super-*

- conductor Science and Technology. 2016 nov;30(2):025002. Available from: <https://dx.doi.org/10.1088/0953-2048/30/2/025002>.
- [233] Bachar N, Lerer S, Levy A, Hacoheh-Gourgy S, Almog B, Saadaoui H, et al. Mott transition in granular aluminum. *Phys Rev B*. 2015 Jan;91:041123. Available from: <https://link.aps.org/doi/10.1103/PhysRevB.91.041123>.
- [234] Pracht US, Bachar N, Benfatto L, Deutscher G, Farber E, Dressel M, et al. Enhanced Cooper pairing versus suppressed phase coherence shaping the superconducting dome in coupled aluminum nanograins. *Phys Rev B*. 2016 Mar;93:100503. Available from: <https://link.aps.org/doi/10.1103/PhysRevB.93.100503>.
- [235] Winkel P, Borisov K, Grünhaupt L, Rieger D, Spiecker M, Valenti F, et al. Implementation of a Transmon Qubit Using Superconducting Granular Aluminum. *Phys Rev X*. 2020 Aug;10:031032. Available from: <https://link.aps.org/doi/10.1103/PhysRevX.10.031032>.
- [236] Bardeen J, Cooper LN, Schrieffer JR. Theory of Superconductivity. *Phys Rev*. 1957 Dec;108:1175-204. Available from: <https://link.aps.org/doi/10.1103/PhysRev.108.1175>.
- [237] Grünhaupt L, Maleeva N, Skacel ST, Calvo M, Levy-Bertrand F, Ustinov AV, et al. Loss Mechanisms and Quasiparticle Dynamics in Superconducting Microwave Resonators Made of Thin-Film Granular Aluminum. *Physical Review Letters*. 2018;121(11):117001. Available from: <https://doi.org/10.1103/PhysRevLett.121.117001>.
- [238] Villiers M, Smith WC, Petrescu A, Borgognoni A, Delbecq M, Sarlette A, et al.. Dynamically enhancing qubit-photon interactions with anti-squeezing; 2023. Available from: <https://arxiv.org/abs/2212.04991>.
- [239] Xu K, Sun ZH, Liu W, Zhang YR, Li H, Dong H, et al. Probing dynamical phase transitions with a superconducting quantum simulator. *Science Advances*. 2020;6(25):eaba4935. Available from: <https://www.science.org/doi/abs/10.1126/sciadv.aba4935>.
- [240] Song C, Xu K, Li H, Zhang YR, Zhang X, Liu W, et al. Generation of multicomponent atomic Schrödinger cat states of up to 20 qubits. *Science*. 2019;365(6453):574-7. Available from: <https://www.science.org/doi/abs/10.1126/science.aay0600>.
- [241] Adam JD, Birabeau JP, Guerin J, Pousse S. Procédes de preparation de sur-

- face de cuivre compatibles avec un depot de niobium realise par pulverisation cathodique. 1985. Available from: <http://cds.cern.ch/record/2646136/files/85-SB-AC-B-3199-gp.pdf>.
- [242] Pei T, Pályi A, Mergenthaler M, Ares N, Mavalankar A, Warner JH, et al. Hyperfine and Spin-Orbit Coupling Effects on Decay of Spin-Valley States in a Carbon Nanotube. *Phys Rev Lett*. 2017 Apr;118:177701. Available from: <https://link.aps.org/doi/10.1103/PhysRevLett.118.177701>.
- [243] Hartmann U, Wilhelm FK. Decoherence of Charge States in Double Quantum Dots Due to Cotunneling. *physica status solidi (b)*. 2002;233(3):385-90. Available from: <https://onlinelibrary.wiley.com/doi/abs/10.1002/1521-3951%28200210%29233%3A3%3C385%3A%3AAID-PSSB385%3E3.0.CO%3B2-7>.